

**DAMAGE, COLLAPSE POTENTIAL AND LONG DURATION EFFECTS
OF SUBDUCTION GROUND MOTIONS ON STRUCTURAL SYSTEMS**

by

Ilaria Capraro

B.Sc., University of Padova, Italy, 2010

M.Sc., University of Bologna, Italy, 2012

A THESIS SUBMITTED IN PARTIAL FULFILLMENT OF
THE REQUIREMENTS FOR THE DEGREE OF

DOCTOR OF PHILOSOPHY

in

THE FACULTY OF GRADUATE AND POSTDOCTORAL STUDIES
(Civil Engineering)

THE UNIVERSITY OF BRITISH COLUMBIA
(Vancouver)

June 2018

© Ilaria Capraro, 2018

The following individuals certify that they have read, and recommend to the Faculty of Graduate and Postdoctoral Studies for acceptance, the dissertation entitled:

Damage, Collapse Potential and Long Duration Effects of Subduction Ground Motions on Structural Systems

submitted by Ilaria Capraro in partial fulfillment of the requirements for

the degree of Doctor of Philosophy

in Civil Engineering

Examining Committee:

Carlos Estuardo Ventura, Civil Engineering
Supervisor

Liam Finn, Civil Engineering
Supervisory Committee Member

Ricardo Foschi, Civil Engineering
Supervisory Committee Member

Annalisa Meyboom, School of Architecture and Landscape Architecture
University Examiner

Tsung Yuan (Tony) Yang, Civil Engineering
University Examiner

Additional Supervisory Committee Members:

Ron DeVall, Read Jones Christoffersen Ltd.
Supervisory Committee Member

Abstract

Current code designs are based on design spectrum which does not account adequately for long duration shaking and therefore they do not reflect the duration effects of subduction earthquakes on seismic demands. The 2015 edition of the National Building Code of Canada (NBCC) probabilistically includes the effects of subduction earthquakes in developing the Uniform Hazard Spectrum (UHS), thus leading to increased interest in the impact of subduction ground motions on seismic demands for design.

The research aim of this thesis is to investigate in detail the impact of subduction motions on design, particularly the effect of duration and the evaluation of the damage potential of the subduction motions.

The evidence of structural damage observed during reconnaissance after the 2011 Tohoku and 2010 Maule subduction earthquakes was used to investigate the characteristics of ground motions that could be used as consistent indicators of damage potential. Characteristics considered were basic shaking parameters, as well as spectral parameters. Among the parameters considered, the constant strength spectrum appeared to be the best indicator.

The effects of the long duration shaking due to subduction motions on the dynamic performance of structures was investigated using Incremental Nonlinear Dynamic Analysis (IDA). The response of several nonlinear Single-Degree-of-Freedom (SDOF) systems designed using a force-reduction factor of 5.0, covering a wide range of fundamental periods and ductility capacities was studied. The effect of duration was isolated by compiling two suites of spectrally compatible motions representing crustal and subduction earthquakes. Based on the drift ratios from IDAs, fragility curves were developed giving the probability of exceeding a prescribed drift ratio. The study clearly showed that the conditional probability of exceeding a prescribed drift for subduction earthquakes is higher than the probability associated with crustal motions. However, the magnitude of this effect depends on the fundamental period, the ductility of the building and the shaking intensity.

In order to investigate how the above findings apply to a Multi-Degree-of-Freedom (MDOF) building, the same pair of input motions were used to run IDA on a 6-storey reinforced concrete (RC) moment frame. The resulting fragility curves confirmed the findings obtained with the SDOF analyses.

Lay summary

Megathrust earthquakes are usually associated with large magnitude subduction earthquakes and long duration of shaking. Current design procedures are based on design spectra which do not reflect adequately the effects of subduction earthquakes on the seismic demand. Moreover, recent subduction events showed that structural damage from earthquake shaking is not always directly correlated only with seismic intensity, but also depends on the building type and the dominant periods of the ground motion.

An investigation was first conducted to explore which characteristics of subduction motions consistently reflect the damage observed during post-earthquake reconnaissance. Secondly, the effects of long duration were studied by running time history analyses on simplified structural models, covering a wide range of fundamental periods and ductility capacities, and quantifying the effects on the structural fragility. A similar dynamic analysis was conducted on a 6-storey reinforced concrete frame building. The results showed that long duration motions significantly increase the demands on the structures and leads to higher probabilities of collapse.

Preface

This thesis presents the research conducted on the damage, collapse potential and long duration effect of subduction ground motions on structures. The research was conducted at the University of British Columbia in Vancouver under the supervision of Prof. C.E. Ventura.

Together with Prof. Ventura, Profs. L. Finn and R. Foschi and Dr. R. DeVall are members of the supervisory committee and provided guidance and feedback during the development of this thesis.

I, Ilaria Capraro, am the primary author of this thesis. I was responsible for the literature review and for deciding the line of thoughts behind this research study.

The study presented in Chapter 2 was motivated by the initial investigations by Prof. C.E. Ventura. The author conducted the selection of subduction ground motions (Chapter 3) from the S2GM online database with permission of Dr. Bebamzadeh, who developed the database. The crustal motions for analysis were selected from the PEER database. The author compiled the Matlab routine for the identification of the spectrally compatible pairs of subduction and crustal motions.

The code for parallel processing used in the parametric analysis of SDOF systems (Chapter 4) was kindly provided by Michael Fairhurst, PhD student at UBC. The code was then modified by the author to fit for the purpose of this research. I conducted the numerical analysis and wrote the Matlab codes for fragility analyses of the data (Chapter 5).

The computer model for the RC moment frame used in Chapter 6 was generously provided by Prof. Abbie Liel of the University of Colorado, Boulder. The OpenSees model was then adapted by David Chin, MSc at the University of British Columbia. I conducted the numerical analysis and post-processed the data.

All the seven Chapters were written by the author. The manuscript was reviewed by Profs. Ventura, Finn and Foschi and Dr. DeVall.

Part of Chapter 2 was published in the following paper:

Capraro, I., Ventura, C.E., Finn, L. (2017), “*Understanding Subduction Ground Motions and their Relation to Structural Damage*”, Proceedings of the 6th Structural Engineers World Congress. Cancún, Mexico, 10 pp.

I conducted all the numerical analysis and wrote the draft of the paper. Profs. Ventura and Finn provided feedback and guidance during the study and helped editing the manuscript.

Papers on the other thesis findings will be published in peer-reviewed journals.

Table of contents

Abstract	iii
Lay summary	v
Preface	vi
Table of contents	viii
List of tables	xi
List of figures	xiii
List of symbols	xx
List of abbreviations	xxii
Acknowledgements	xxiii
Dedication	xxvi
1. Introduction	1
1.1. Overview.....	1
1.2. Background and literature review	6
1.2.1 Observations from past subduction earthquake events.....	6
1.2.2 Seismic parameters and damage potential of earthquake ground motions	8
1.2.3 State-of-the-art on the evaluation of long duration effect of ground motions.....	11
1.3. Research goal, objectives and scope.....	15
1.4. Thesis organization	17
2. Damage potential of subduction ground motions: case studies	19
2.1. Introduction.....	19
2.2. Maule 2010 earthquake.....	21
2.2.1 Post-earthquake field observations	21
2.2.2 Ground motions parameters and structural damage.....	21

2.2.3	Elastic response spectra analysis	24
2.3.	Tohoku 2011 earthquake.....	26
2.3.1	Post-earthquake field observations	26
2.3.2	Ground motions parameters and structural damage.....	29
2.3.3	Elastic response spectra analysis	33
2.3.4	Constant ductility spectra analysis.....	38
2.3.5	Insight from nonlinear response.....	41
2.3.6	Constant strength spectra analysis	43
2.4.	Ductility demands for other Tohoku ground motions.....	46
2.5.	Discussion.....	50
3.	Selection and scaling of ground motions for Victoria, British Columbia.....	53
3.1.	Introduction.....	53
3.2.	Seismic hazard in southwestern British Columbia	54
3.3.	Consideration of subduction earthquakes in the Building Code.....	56
3.4.	Selection and scaling of ground motions for time history analysis	57
3.4.1	Selection and scaling of subduction ground motions	58
3.4.2	Selection and scaling of short-duration ground motions	62
3.4.2.1	Example of spectrally equivalent records pair.....	64
3.5.	Results of ground motions pairing.....	66
4.	Nonlinear Incremental Dynamic Analysis (IDA).....	70
4.1.	Introduction.....	70
4.2.	Description of the computational method.....	71
4.3.	Modeling of SDOF systems.....	71
4.4.	Results of IDA	76
4.5.	Discussion.....	78
5.	Fragility analysis and assessment of duration effect	80
5.1.	Fragility analysis.....	80
5.2.	Effects of structural period on probability of collapse.....	83
5.3.	Effects of long duration on the probability of collapse.....	89
5.4.	Discussion.....	97
6.	Effects of long duration shaking on buildings: a case study	100

6.1.	Introduction.....	100
6.2.	Description of the model.....	101
6.3.	Results of the IDA and fragility curves	103
6.4.	Discussion	105
7.	Summary and conclusions.....	108
7.1.	Summary and conclusions	108
7.2.	Recommendations for future research	111
	Bibliography	114
	Appendices.....	126
	Appendix A Spectrally equivalent ground motion pairs	127
	Appendix B Fragility curves	148
	Appendix C Contour plots of the probability of collapse.....	155
	Appendix D Duration effect plots	161

List of tables

Table 2-1: Summary of the characteristics of the motions at Maipu and Curico	23
Table 2-2: Summary of the characteristics of the motions at Tsukidate and Sendai.....	32
Table 2-3: Summary of the suitability of the considered parameters as indicators for damage potential of subduction earthquakes.....	51
Table 3-1: UHS Spectral acceleration values for Victoria, BC 2015 hazard calculations.	58
Table 3-2: Summary of the parameters considered during selection and scaling of ground motion records.....	59
Table 3-3: Summary of the ground motions characteristics for the record pair # 6.	65
Table 3-4: Summary of spectrally equivalent records pairs.	67
Table 6-1: Backbone curve parameters.....	103
Table A- 1: PAIR # 1 - Spectrally equivalent records.....	128
Table A- 2: PAIR # 2 - Spectrally equivalent records.....	129
Table A- 3: PAIR # 3 - Spectrally equivalent records.....	130
Table A- 4: PAIR # 4 - Spectrally equivalent records.....	131
Table A- 5: PAIR # 5 - Spectrally equivalent records.....	132
Table A- 6: PAIR # 6 - Spectrally equivalent records.....	133
Table A- 7: PAIR # 7 - Spectrally equivalent records.....	134
Table A- 8: PAIR # 8 - Spectrally equivalent records.....	135
Table A- 9: PAIR # 9 - Spectrally equivalent records.....	136
Table A- 10: PAIR # 10 - Spectrally equivalent records.....	137
Table A- 11: PAIR # 11 - Spectrally equivalent records.....	138
Table A- 12: PAIR # 12 - Spectrally equivalent records.....	139
Table A- 13: PAIR # 13 - Spectrally equivalent records.....	140
Table A- 14: PAIR # 14 - Spectrally equivalent records.....	141

Table A- 15: PAIR # 15 – Spectrally equivalent records.	142
Table A- 16: PAIR # 16 - Spectrally equivalent records.	143
Table A- 17: PAIR # 17 - Spectrally equivalent records.	144
Table A- 18: PAIR # 18 - Spectrally equivalent records.	145
Table A- 19: PAIR # 19 - Spectrally equivalent records.	146
Table A- 20: PAIR # 20 - Spectrally equivalent records.	147

List of figures

Figure 1-1: Acceleration response spectra of sinusoidal signals with varying number of cycles ($\xi = 5\%$).....	2
Figure 1-2: Velocity response spectra of sinusoidal signals with varying number of cycles ($\xi = 5\%$).....	3
Figure 1-3: Displacement response spectra of sinusoidal signals with varying number of cycles ($\xi = 5\%$).....	3
Figure 1-4: Effect of number of cycles of sinusoidal motion on fraction of steady-state response for a SDOF oscillator and 5% damping.....	4
Figure 1-5: Acceleration response spectra at Tsukidate station (MYG004) during the 2011 Tohoku earthquake.....	4
Figure 2-1: Location of the Maule epicenter and the stations of Curico and Maipu (USGS).....	20
Figure 2-2: Location of the Tohoku epicenter and the stations of Tsukidate and Sendai.....	20
Figure 2-3: Damage to the church of San Francisco (Curico, Maule region).....	22
Figure 2-4: Damage in La Prensa in Curico (Courtesy of Decofrut/Flickr; NASA, 2017).....	22
Figure 2-5: Damage to masonry low-rise buildings in Talca, Maule region (EERI, 2010).....	22
Figure 2-6: Damaged building in Maipu, Santiago region (Courtesy of Jorge Barrios; Wikipedia, 2010).....	22
Figure 2-7: NS - Acceleration time history at Curico and Maipu stations.....	24
Figure 2-8: Arias intensities for the NS records at Curico and Maipu.....	24
Figure 2-9: Comparison of frequency content at Curico (green) and Maipu (magenta).....	24
Figure 2-10: Acceleration response spectra for Curico and Maipu records ($\xi = 5\%$).....	25
Figure 2-11: Velocity response spectra for Curico and Maipu records ($\xi = 5\%$).....	26
Figure 2-12: Displacement response spectra for Curico and Maipu records ($\xi = 5\%$).....	26
Figure 2-13: Overturned objects in Tsukidate - example 1 (Ventura, 2011).....	27

Figure 2-14: Not overturned objects in Tsukidate – example 1 (Ventura, 2011).	27
Figure 2-15: Not overturned objects in Tsukidate - example 2 (Ventura, 2011).	27
Figure 2-16: Damage to reinforced concrete walls in Sendai - example 1 (Ventura, 2011).	27
Figure 2-17: Damage to reinforced concrete building in Sendai - example 2 (Ventura, 2011). ..	27
Figure 2-18: Collapse of a mid-story of a reinforced concrete building in Sendai (Ventura, 2011).	27
Figure 2-19: Shear cracks on first-storey column in Sendai (Nishiyama et al., 2011).	28
Figure 2-20: Shear cracks on first-storey column in Sendai caused by aftershocks (Nishiyama et al., 2011).	28
Figure 2-21: Elevation view of the 9-storey shear wall building in Sendai (Nishiyama et al., 2011).	28
Figure 2-22: Crushing at the base of the RC column (modified from: Nishiyama et al., 2011). .	28
Figure 2-23: Elevation view of the 8-storey shear wall building in Sendai (Nishiyama et al., 2011).	29
Figure 2-24: Damaged boundary beams with openings (Nishiyama et al., 2011).	29
Figure 2-25: Particle acceleration at Tsukidate.	30
Figure 2-26: Particle acceleration motion at Sendai.	30
Figure 2-27: Particle velocity at Tsukidate.	30
Figure 2-28: Particle velocity at Sendai.	30
Figure 2-29: Particle displacement at Tsukidate.	31
Figure 2-30: Particle displacement at Sendai.	31
Figure 2-31: Comparison of time histories at Tsukidate (red) and Sendai (blue).	32
Figure 2-32: Comparison of frequency contents at Tsukidate (red) and Sendai (blue).	32
Figure 2-33: Comparison of Arias intensities at Tsukidate (red) and Sendai (blue).	32
Figure 2-34: Soil profile at MYG004 - Tsukidate station (NIED).	33
Figure 2-35: Soil profile at MYG013 - Sendai station (NIED).	33
Figure 2-36: Elastic pseudo-acceleration response spectra for Tsukidate and Sendai ($\xi = 5\%$). .	34
Figure 2-37: Elastic pseudo-velocity response spectra for Tsukidate and Sendai ($\xi = 5\%$).	34
Figure 2-38: Elastic displacement response spectra for Tsukidate and Sendai ($\xi = 5\%$).	35
Figure 2-39: Comparison between acceleration response spectra of the isolated pulses in Tsukidate ($\xi = 5\%$).	36

Figure 2-40: Comparison between acceleration response spectra of the isolated pulses in Sendai ($\xi = 5\%$).....	36
Figure 2-41: Comparison between velocity response spectra of the isolated pulses in Tsukidate ($\xi = 5\%$).....	36
Figure 2-42: Comparison between velocity response spectra of the isolated pulses in Sendai ($\xi = 5\%$).....	36
Figure 2-43: Comparison between displacement response spectra of the isolated pulses in Tsukidate ($\xi = 5\%$).....	37
Figure 2-44: Comparison between displacement response spectra of the isolated pulses in Sendai ($\xi = 5\%$).....	37
Figure 2-45: Constant ductility spectra for Tsukidate ($\xi = 5\%$).	39
Figure 2-46: Constant ductility spectra for Sendai ($\xi = 5\%$).	39
Figure 2-47: Comparison of constant ductility spectra for displacement response ($\xi = 5\%$).	39
Figure 2-48: Acceleration time history of a simple sinusoidal signal.	40
Figure 2-49: Acceleration response spectra of the sinusoidal signal for different ductilities ($\xi = 5\%$).....	40
Figure 2-50: Velocity response spectra of the sinusoidal signal for different ductilities ($\xi = 5\%$).	41
Figure 2-51: Displacement response spectra of the sinusoidal signal for different ductilities ($\xi = 5\%$).....	41
Figure 2-52: Acceleration and yielding time history for Bilinear SDOF at 0.2 sec (Tsukidate in red, Sendai in blue).	42
Figure 2-53: Hysteresis loop for Bilinear SDOF at 0.2 sec (Tsukidate in red, Sendai in blue)....	42
Figure 2-54: Acceleration and yielding time history for Bilinear SDOF at 1.0 sec (Tsukidate in red, Sendai in blue).	42
Figure 2-55: Hysteresis loop for Bilinear SDOF at 1.0 sec(Tsukidate in red, Sendai in blue)....	42
Figure 2-56: Acceleration and yielding time history for Clough SDOF at 0.2 sec (Tsukidate in red, Sendai in blue).	43
Figure 2-57: Hysteresis loop for Clough SDOF at 0.2 sec (Tsukidate in red, Sendai in blue)....	43
Figure 2-58: Acceleration and yielding time history for Clough SDOF at 1.0 sec (Tsukidate in red, Sendai in blue).	43

Figure 2-59: Hysteresis loop for Clough SDOF at 1.0 sec (Tsukidate in red, Sendai in blue).....	43
Figure 2-60: Constant strength spectra for Tsukidate (red) and Sendai (blue) for a Bilinear system.	44
Figure 2-61: Spectral ratios for ductility demands for a Bilinear system.	44
Figure 2-62: Constant strength spectra for Tsukidate (red) and Sendai (blue) for a Clough system.	45
Figure 2-63: Spectral ratios for ductility demands for a Clough system.	45
Figure 2-64: Ductility demands of unscaled Sendai and Tsukidate records and comparison with unscaled subduction motions ($C_y = 0.1$).	47
Figure 2-65: Ductility demands of unscaled Tsukidate and Sendai records and comparison with scaled subduction motions ($C_y = 0.1$).	48
Figure 2-66: Ductility demands of unscaled Tsukidate and Sendai records and comparison with unscaled subduction motions ($C_y = 0.2$)	49
Figure 2-67: Ductility demands of unscaled Tsukidate and Sendai records and comparison with scaled subduction motions ($C_y = 0.2$).	49
Figure 2-68: Ductility demands of unscaled Tsukidate and Sendai records and comparison with unscaled subduction motions ($C_y = 0.3$).	49
Figure 2-69: Ductility demands of unscaled Tsukidate and Sendai records and comparison with unscaled subduction motions ($C_y = 0.3$).	49
Figure 3-1: Example of unscaled crustal and subduction response spectra of paired ground motions.....	54
Figure 3-2: Example of scaled crustal and subduction response spectra of paired ground motions.	54
Figure 3-3: Tectonics of Pacific north-west.....	55
Figure 3-4: Cross-section of the tectonic setting of southwest British Columbia.	55
Figure 3-5: Design spectrum and target period range.....	58
Figure 3-6: Response Spectra of unscaled subduction ground motions.	61
Figure 3-7: Response spectra of the subduction ground motions scaled to the target spectrum. .	61
Figure 3-8: Response spectra of unscaled short duration crustal motions.....	63
Figure 3-9: Response spectra of short-duration motions scaled to the target spectra.....	63
Figure 3-10: Acceleration time histories for record pair # 6.	64

Figure 3-11: Example of spectrally equivalent records for pair # 6 and matching to the target spectrum.....	65
Figure 3-12: Number of records for significant duration intervals.....	68
Figure 3-13: Comparison between mean and standard deviation of the two spectrally equivalent suites of motions.	69
Figure 4-1: SDOF system with rigid rod and rotational inelastic spring at the base.	72
Figure 4-2: Definition of the backbone curve.....	73
Figure 4-3: Illustration of deterioration modes (Modified from: Ibarra et al., 2005).	75
Figure 4-4: IDA curves obtained with crustal motions, for SDOF with $T = 1.2$, $R = 5$ sec and ductility 11.	77
Figure 4-5: IDA Curves obtained with subduction motions, for SDOF with $T = 1.2$ sec, $R = 5$ and ductility 11.	78
Figure 5-1: Fragility curves for $T = 1.2$ sec SDOF with ductility 11 and $R = 5$	81
Figure 5-2: Fragility curves for $T=1.2$ sec structure calculated for different ductility levels $D = 3, 5, 7, 9, 11$	82
Figure 5-3: Fragility curves envelope for crustal motions and ductility 11.....	83
Figure 5-4:: Surface plot and projection of the contour in the shaking level-period plane.	84
Figure 5-5: Contour plot of the envelope of the fragility curves for crustal motions and ductility 11.....	85
Figure 5-6: Contour plot showing the probability of collapse for the crustal suite of motions and ductility 11.	86
Figure 5-7: Contour plot of the probability of collapse for the subduction suite of motions and ductility 11.	88
Figure 5-8: The effect of long duration shaking on structural systems with ductility 11.	90
Figure 5-9: Contour plot and evaluation of long duration effect on structural systems with ductility 11.....	92
Figure 5-10: Long duration effect for ductility 3.....	94
Figure 5-11: Long duration effect for ductility 5.....	94
Figure 5-12: Long duration effect for ductility 7.....	95
Figure 5-13: Long duration effect for ductility 9.....	95
Figure 5-14: Duration effect at base design shaking intensity.....	96

Figure 6-1: 3D view of the prototype building (ATC 78, 2011; ATC 78-1, 2012).....	101
Figure 6-2: Elevation view of the external perimeter frame of the building (ATC 78-1, 2012). 102	
Figure 6-3: Elevation view and modeling scheme of the RC frame (Chin, 2017).	102
Figure 6-4: IDA curves obtained with crustal motions.....	104
Figure 6-5: IDA curves obtained with subduction motions.....	104
Figure 6-6: Fragility curves for crustal and subduction motions.....	105
Figure 6-7: Fragility curves for the 6-storey RC moment frame.....	107
Figure 6-8: Fragility curves for a SDOF system of $T = 1.5$ sec and ductility 7.	107
Figure B- 1: Fragility curves for $T = 0.1$ sec.	148
Figure B- 2: Fragility curves for $T = 0.2$ sec.	148
Figure B- 3: Fragility curves for $T = 0.3$ sec.	148
Figure B- 4: Fragility curves for $T = 0.4$ sec.	148
Figure B- 5: Fragility curves for $T = 0.5$ sec.	149
Figure B- 6: Fragility curves for $T = 0.6$ sec.	149
Figure B- 7: Fragility curves for $T = 0.7$ sec.	149
Figure B- 8: Fragility curves for $T = 0.8$ sec.	149
Figure B- 9: Fragility curves for $T = 0.9$ sec.	150
Figure B- 10: Fragility curves for $T = 1.0$ sec.	150
Figure B- 11: Fragility curves for $T = 1.1$ sec.	150
Figure B- 12: Fragility curves for $T = 1.2$ sec.	150
Figure B- 13: Fragility curves for $T = 1.3$ sec.	151
Figure B- 14: Fragility curves for $T = 1.4$ sec.	151
Figure B- 15: Fragility curves for $T = 1.5$ sec.	151
Figure B- 16: Fragility curves for $T = 1.6$ sec.	151
Figure B- 17: Fragility curves for $T = 1.7$ sec.	152
Figure B- 18: Fragility curves for $T = 1.8$ sec.	152
Figure B- 19: Fragility curves for $T = 1.9$ sec.	152
Figure B- 20: Fragility curves for $T = 2.0$ sec.	152
Figure B- 21: Fragility curves for $T = 2.5$ sec.	153
Figure B- 22: Fragility curves for $T = 3.0$ sec.	153

Figure B- 23: Fragility curves for T = 3.5 sec.	153
Figure B- 24: Fragility curves for T = 4.0 sec.	153
Figure B- 25: Fragility curves for T = 4.5 sec.	154
Figure B- 26: Fragility curves for T = 5.0 sec.	154
Figure C- 1: Contour plot for ductility 3 and crustal suite of motions.	155
Figure C- 2: Contour plot for ductility 3 and subduction suite of motions.....	155
Figure C- 3: Contour plot for ductility 5 and crustal suite of motions.	156
Figure C- 4: Contour plot for ductility 5 and subduction suite of motions.....	156
Figure C- 5: Contour plot for ductility 7 and crustal suite of motions.	157
Figure C- 6: Contour plot for ductility 7 and subduction suite of motions.....	157
Figure C- 7: Contour plot for ductility 9 and crustal suite of motions.	158
Figure C- 8: Contour plot for ductility 9 and subduction suite of motions.....	158
Figure C- 9: Contour plot for ductility 11 and crustal suite of motions.	159
Figure C- 10: Contour plot for ductility 11 and subduction suite of motions.....	159
Figure D- 1: Contour plot showing the difference in probability of collapse due to long duration effect for ductility 3.	161
Figure D- 2: Contour plot showing the difference in probability of collapse due to long duration effect for ductility 5.	162
Figure D- 3: Contour plot showing the difference in probability of collapse due to long duration effect for ductility 7.	162
Figure D- 4: Contour plot showing the difference in probability of collapse due to long duration effect for ductility 9.	163
Figure D- 5: Contour plot showing the difference in probability of collapse due to long duration effect for ductility 11.	163

List of symbols

C_y	Constant strength coefficient
D_{5-95}	Significant duration calculated between 5-95% of the Arias intensity
f	Scale factor
F	Fraction of steady-state maximum response
F_y	Normalized yield capacity
h, ξ	Damping ratio
K_0	Initial elastic stiffness
K_s	Strain-hardening stiffness
Λ, λ	Deterioration parameter
Λ_A	Acceleration reloading stiffness deterioration parameter
Λ_C	Post-capping strength deterioration parameter
Λ_K	Unloading stiffness deterioration parameter
Λ_s	Cyclic strength deterioration parameter
μ, D	Ductility
M_r	Residual moment strength
M_y	Yield moment resistance
M_w	Moment magnitude
N	Number of cycles of a sinusoidal motion
$P_{Crustal}$	Probability of collapse for crustal motions
$P_{Subduction}$	Probability of collapse for subduction motions
$P-\Delta$	P-Delta effect
R	Reduction Factor
$SA^{RECORD}(T_i)$	Reference record spectral acceleration at i^{th} period
$SA^{TARGET}(T_i)$	Target spectral acceleration at i^{th} period

$S_a(T_i)$	UHS spectral acceleration at i^{th} period
S_{di}	Inelastic spectral displacement
SF	Scale factor
θ_p	Pre-capping rotation capacity
θ_{pc}	Post-capping rotation capacity
θ_y	Yield rotation
T_1	First natural period
T_2	Second natural period
T_3	Third natural period
$V_b(T_i)$	Base shear at i^{th} period
$V_{s,20}$	Average shear wave velocity of the top 20 m of soil
$V_{s,30}$	Average shear wave velocity of the top 30 m of soil
W	Weight
$w(T_i)$	Weight function at i^{th} period

List of abbreviations

IDA	Incremental Dynamic Analysis
JMA	Japan Meteorological Agency
MDOF	Multi-Degree-of-Freedom
MRF	Moment Resisting Frame
MSE	Mean Square Error
NBCC	National Building Code of Canada
OSDI	Overall Structural Damage Index
PBEE	Performance Based Earthquake Engineering
PGA	Peak Ground Acceleration
PGD	Peak Ground Displacement
PGV	Peak Ground Velocity
PSA	Pseudo Spectral Acceleration
PSV	Pseudo Spectral Velocity
RC	Reinforced Concrete
SDOF	Single-Degree-of-Freedom
SSI	Soil-Structure-Interaction
UHS	Uniform Hazard Spectrum
URM	Unreinforced Masonry

Acknowledgements

Firstly, I would like to express my gratitude to my supervisor, Prof. Carlos E. Ventura. He patiently guided and supported me through the complexities of earthquake engineering, yet giving me the freedom of investigating on my own. He saw the potential of my ideas before I realized it, inspired me to pursue my research with passion and purpose and motivated me to give my very best during my PhD studies. I feel truly honored of having the opportunity to work with him.

I would also like to acknowledge Prof. Liam W.D. Finn, not only for all time and energy he dedicated in helping editing this thesis, but also for sharing his immense knowledge and experience in the field of earthquake engineering and for instilling his enthusiasm for teaching.

I would like to thank the members of my thesis committee: Dr. Ron DeVall from Read Jones Christoffersen Ltd. and Prof. Ricardo Foschi, for their deep interest, dedication and constant encouragement throughout the evolution of the thesis. Their comments and enlightening questions sharpened my understanding and helped me improving my research findings.

I am truly thankful to Drs. Yavuz Kaya, Jason Dowling and Martin Turek, for their availability and expert advice in answering my many questions.

I would like to thank Dr. Armin Bebamzadeh, for sharing his extensive knowledge and expertise in the field of nonlinear structural analysis. His passion for learning was a motivating factor for me.

I am deeply indebted to Michael Fairhurst for his time, infinite patience and dedication in sharing his knowledge of Opensees and Matlab. He helped me to explore the mysteries of numerical computing.

A special thanks goes to my office mates and beautiful minds at UBC: Alexander Mandler, Marco Galaviz and Niels Savnik, for the everyday companionship and for patiently enduring my many quirks. The Office was not only just a workplace, but rather a special environment where we shared what we knew best, learned about what we did not know that well, with the right balance of laughter and focus.

My appreciation goes also to the staff of the Civil Engineering Department: Terry Moser, Glenda Levins, Felix Yao, Shannon Remillong, Kevin Veltheer, Elnaz Mani and Louise Fogarty, for all their help and patience in accommodating my requests and for solving my bureaucratic dilemmas.

A huge thank you goes to my friends here in Vancouver: Javi Miguelez, Marta Carrasco, Andres Barrero, Pablo Carrasco, Ignacio San Miguel, Carla Hilario, Giona Matasci, William Fritzberg, Andressa Coope and Diego Botezelli, for all the food, music and dancing. They dragged me along quite unexpected adventures and hilarious hobbies. These are memories I will treasure forever.

I would also like to acknowledge especially Simone Tengattini, for his honest friendship and the relaxing strolls along Commercial Drive on Sunday afternoons.

I would like also to give a heartfelt *grazie* to my friends Davide Donati and Alessandra Venturelli. They have been my safe heaven here in Vancouver. With their sense of humor and constant optimism, they helped me during my frustrations at critical stages of my PhD. I feel very lucky our paths crossed.

I would like to thank Cristina Zanotti, a life coach and authentic Friend, for her understanding, emotional support and for tolerating my musical taste... *#PantaRhei*.

I would also like to extend my gratitude to Rita Marchesini and Guido Garzitto, not only for giving me unlimited access to their vegetable garden, but for their unconditional and affectionate care during these last three years: I truly felt an extended member of their family.

I cannot thank enough my girlfriends scattered all over Europe: Pamela Attavilla, Emily Rose Ciscato, Silvia Bordignon and Amaia Martinez; who gave me continual encouragement and shared my hopes and dreams during the ups and downs of my research program.

A special thanks to my dear brother Gabriele, a role model and everlasting source of inspiration and encouragement. He taught me to strive for my ideas, aim for progress and always be strong in my purposes to achieve my goals.

To my parents, Valeria and Daniele, I owe my deepest gratitude. Without their absolute love, support and encouragement I could not have gone this far. They never questioned my life choices and trustfully supported my decisions.

Finally, I would like to acknowledge the Natural Sciences and Engineering Research Council of Canada (NSERC) for providing financial funding to study the effect of subduction earthquakes on buildings.

Dedication

To Gabriele, Valeria and Daniele

Chapter 1

Introduction

“He who loves practice without theory is like the sailor who boards ship without a rudder and compass and never knows where he may cast.”

Leonardo da Vinci (1452 – 1519)

1.1. Overview

Southwestern British Columbia is a region characterized by a very complex tectonic environment. Contribution to the seismic hazard is given by three different types of seismic sources: crustal, subcrustal and subduction earthquakes. While crustal and subcrustal earthquakes are usually characterized by low/intermediate magnitudes and short durations, subduction earthquakes are associated with larger magnitudes and longer duration of shaking. Because of the proximity of two major cities in Canada (Victoria and Vancouver) to the Cascadia Subduction Zone, it is of interest to study the effects of subduction ground motions on the seismic performance of structural systems.

Current building code designs are based on design spectra which give the spectral acceleration as a function of the building period. However, these spectra do not reflect adequately the effects of long duration motions. Long duration is, among other aspects, a unique characteristic that differentiates subduction ground motions from the other earthquake motions. If long duration

subduction earthquakes are a significant component of the hazard, it is important to assess the effects of duration on the seismic performance of structural systems.

Long duration of shaking may consist of frequency components that are repeated for many cycles. This, in turn, might lead to resonant response of structures with the same frequency (or period) as the ground motion. As a result, the associated response spectra might show sharp peaks of high spectral values at those frequencies and one might conclude that systems with such frequency might experience large demands, hence damage. The effect of a large number of motion cycles dominated by a certain frequency can be better understood by reference to the response of a Single-Degree-of-Freedom (SDOF) system to sinusoidal excitation of limited number of cycles.

In order to understand the effect of large number of cycles of motion dominated by a certain frequency, a study on the response of a SDOF systems to sinusoidal excitation with limited number of cycles was conducted by the author. To this end, response spectra of simple sinusoidal signals have been developed by increasing the number of cycles of the excitation. The response spectra have been calculated for sinusoidal signals with period of 1 sec, acceleration amplitude equal to 0.2 g and 5% damping ($\xi = 5\%$). Figure 1-1, 1-2 and 1-3 show the spectra for acceleration, velocity and displacement respectively. Six sinusoidal signals have been considered for analysis and are characterized by 1, 2, 3, 4, 5, 10 cycles. The response spectrum of a sinusoidal signal of 300 cycles is plotted for comparison in Figures 1-1 to 1-3.

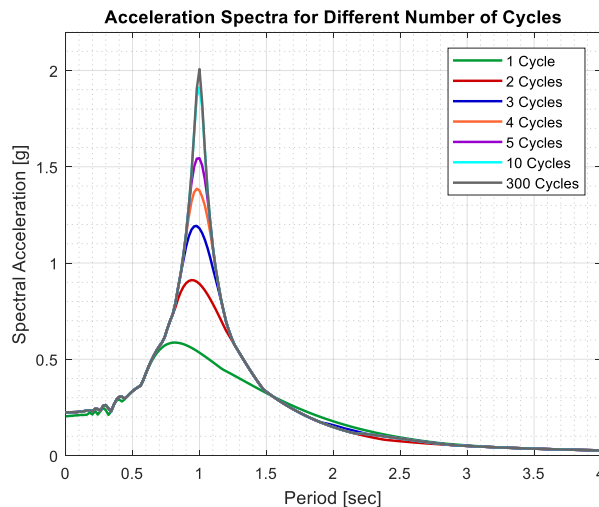


Figure 1-1: Acceleration response spectra of sinusoidal signals with varying number of cycles ($\xi = 5\%$).

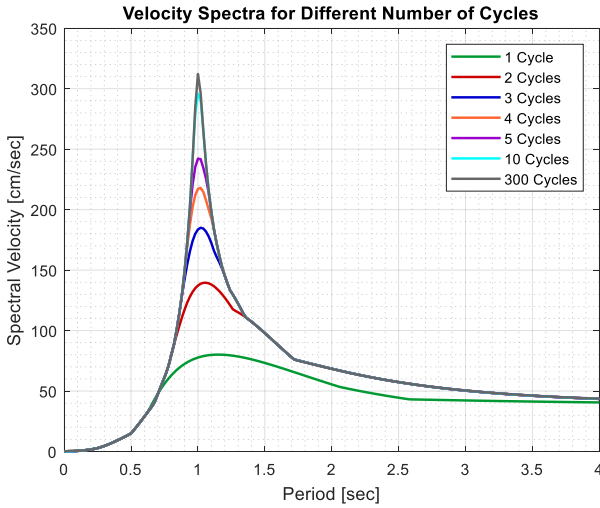


Figure 1-2: Velocity response spectra of sinusoidal signals with varying number of cycles ($\xi = 5\%$).

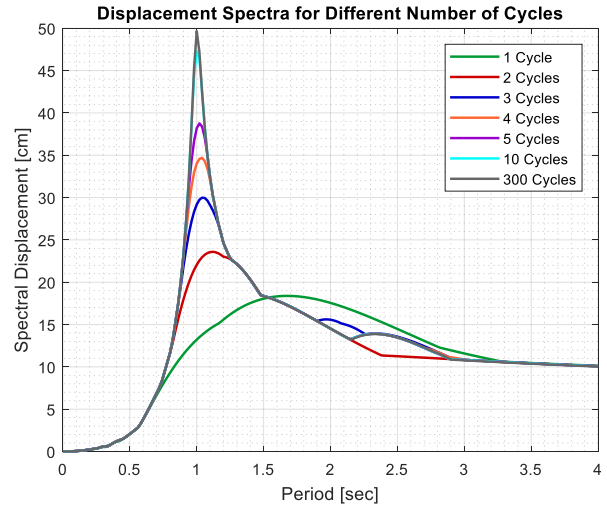


Figure 1-3: Displacement response spectra of sinusoidal signals with varying number of cycles ($\xi = 5\%$).

As the number of cycles increases, the spectral amplitude at resonance becomes progressively larger. Eventually, after 10 cycles of motion, the response spectrum of the sinusoidal signal will reach the 300 cycles spectrum. This example clearly shows that the duration of the signal is well represented, up to 10 loading cycles, at structural periods close to resonance. However, signals with more than 10 cycles will result in a response spectrum corresponding to the 300 cycles spectrum. Similar conclusion can be drawn also from the velocity and displacement elastic response spectra. Thus, elastic response spectra do not reflect adequately the effects of long duration.

Murphy and O'Brien in 1978 gave a mathematical interpretation of this limitation. They presented Equation 1-1 which defines the number of cycles, N , of a sinusoidal motion with a damping ratio h to reach a given fraction F of the maximum steady state response.

$$N = \frac{\ln(1 - F)}{-h \cdot 2 \cdot \pi} \quad (1-1)$$

This equation is plotted in Figure 1-4. It can be observed that after about 7 cycles the response has reached 90% of what it will ever reach, regardless of how many cycles are input. At 10 cycles, the maximum response would closely reach the steady-state response. The additional

energy being put into the system by prolonging the shaking will be only marginally represented by the spectrum.

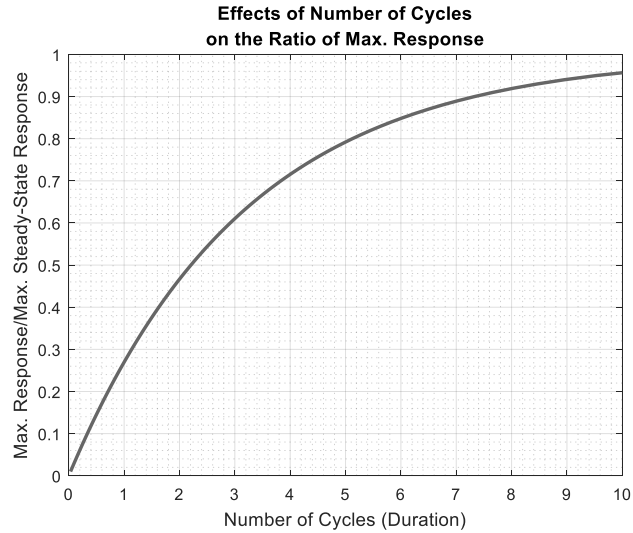


Figure 1-4: Effect of number of cycles of sinusoidal motion on fraction of steady-state response for a SDOF oscillator and 5% damping.

The sharp peaks due to the repetition of many loading cycles with the same frequency can be observed also in response spectra generated by real ground motion records. An example is provided in Figure 1-5, which shows the acceleration response spectra at Tsukidate station (Japan) during the 2011 Tohoku earthquake. At a period of 0.24 sec, the spectrum shows a very sharp peak and is associated with a spectral amplitude of 13 g. The peak in the spectrum is due to the repetition of loading cycles of period of about 0.24 sec. It is of interest then, to study the effects of the number of loading cycles on the structural response and damage potential.

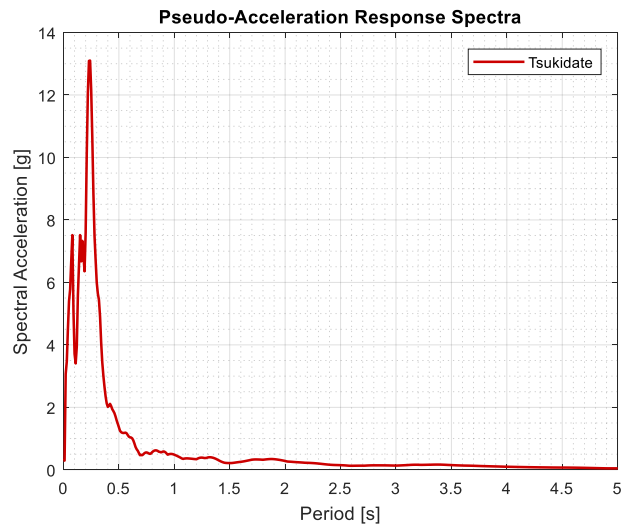


Figure 1-5: Acceleration response spectra at Tsukidate station (MYG004) during the 2011 Tohoku earthquake.

In the past five years, three major studies have been conducted to evaluate the effect of long duration ground motions on the seismic performance against collapse of a variety of structural systems (Raghunandan and Liel (2013), Chandramohan et al. (2016) and Fairhurst et al (2017)). These investigations clearly showed that the demands imposed on the structures are significantly higher when considering long duration motions compared to the ones obtained with shorter duration motions, thus leading to higher probabilities of collapse. Moreover, these studies not only demonstrated the importance of the effects of long duration shaking, but also that these effects are more significant for structures characterized by significant stiffness and strength degradation.

After recent large magnitude subduction events (2011 Tohoku and 2010 Maule earthquakes), engineers and seismologists conducted extensive post-earthquake field investigations with the goal of collecting valuable technical data and developing a better understanding of the structural damage associated with subduction earthquakes. These investigations showed how structural damage from earthquake shaking is not always directly correlated to seismic intensity, but is also dependent on the building type and the dominant periods of the ground motion. A striking example is given by the field evidence at Sendai and Tsukidate stations during the 2011 Tohoku Earthquake. According to the JMA (Japan Meteorological Agency) intensity scale, the maximum seismic intensity was 7 in the city of Kurihara (K-NET Tsukidate) and the rating in Sendai was 6+ (Ochi & Suzuoki, 2011). A Peak Ground Acceleration (PGA) of 3.0 g was recorded in Tsukidate (MYG004), while at Sendai (MYG013) the PGA was 1.5 g. Post-earthquake field investigations showed that the damage at Tsukidate was not as severe as expected given the extremely high intensity rating. On the other hand, the damage in Sendai was more severe than expected given the lower intensity rating.

Moreover, it has been observed that subduction ground motions can be also associated with response spectra characterized by very large spectral amplitudes at short periods. This is in contrast to the traditional belief that large magnitude earthquakes at long distance from the site would commonly generate a flatter spectrum at short period and larger amplitudes at longer periods (Ch. 6, Chopra A.K., 2016). The ground motion recorded at Tsukidate offers a good example of this behavior. The repetition of many short-period cycles resulted in a spectrum with high demands in the low-period range.

This thesis sheds light on these apparent paradoxes and attempts to explain the relationship between the damage and ground motion characteristics.

1.2. Background and literature review

1.2.1 Observations from past subduction earthquake events

The *Michoacán Earthquake*, which hit Mexico in 1985, caused dramatic amplifications of the horizontal components of motion in the period range 2-3s in the area of Mexico City underlain by soft lake sediments (Campillo et al., 1989). Extensive damage was caused by resonance between the 2 sec period of the lake sediments and buildings characterized by a similar fundamental period. Investigations on this coupling effect between high-rise buildings and the soft basin response was possible through the study of several long duration accelerograms recorded in Mexico City (Wirgin & Bard, 1996). In addition, in the lake bed basin the duration increased due to the waves being reflected back and forth from the walls of the basin. The main finding from the Michoacán Earthquake was the significant impact of the soil conditions in both the amplification and duration of the ground shaking and the magnifying effects on the dynamic response of moderate period structures.

On December 26th, 2004 the *Sumatra-Andaman Earthquake* was triggered where the Indian and Australian plates subduct beneath the Sunda plate. With a 1300-1500 km long fault and a rupture duration of 500 seconds, the Sumatra Andaman earthquake was classified as a moment magnitude M_w 9.1-9.3 event (Shearer & Burgmann, 2010).

A reconnaissance survey was conducted in the coastal region of Banda Aceh in the northern tip of Sumatra, where the shaking was strongest (Saatcioglu et al., 2006). The main types of construction in this area were low-rise timber frame buildings and non-engineered RC buildings with unreinforced masonry infill walls. Where the low-rise timber buildings survived the seismic shaking, they collapsed under the water pressure of the tsunami waves (Cluff, 2008). Non-engineered RC buildings suffered total or partial collapse because of the lack of ductile detailing and poor seismic design. Unreinforced Masonry (URM) walls were used as infills for the RC frame structures and experienced out-of-plane failures due to the wave pressure of the tsunami.

Post-earthquake field investigations were also conducted in Port Blair, capital of the Andaman and Nicobar Islands. Low-rise traditional timber and masonry structures performed very well during the earthquake shaking. Interestingly, an old mosque built in 1913 with masonry domes and minarets and retrofitted in 2001-2002 did not suffer any structural damage, except the collapse of few slender minarets. On the other hand, several low-rise RC frames experienced

substantial damage during the earthquake. As in the case for Banda Aceh, the structural damage was mostly attributed to poor construction and lack of ductile detailing (Kaushik & Jain, 2007).

The M_w 8.8 *Maule earthquake* occurred on February 27th 2010 in central Chile. With a rupture area of 81500 km², it affected a vast region of the country. Post-earthquake field investigations were conducted by international teams of engineers to assess the damage caused by the earthquake.

Besides the failure of a few engineered buildings caused by structural irregularities and limited ductility capacity, the reconnaissance team reported that the performance of engineered buildings in Santiago was quite good. Masonry construction in the Maule region suffered the most damage. For instance, in the city of Talca, 80% of the buildings were damaged and 50% were slated for demolition. The variable damage distribution patterns were attributed in part to local site conditions (GEER Association, 2010). At Curico and three other locations (Maipu, Concepción and Melipilla) the recorded motions resulted in seismic demands exceeding the design spectra (Elnashai et al., 2010). In the city of Curico, 90% of the adobe construction was destroyed and structural damage was observed also in hospitals, schools and churches.

The 2011 *Tohoku Earthquake* off the Sanriku coastline in Japan was a M_w 9.0 event and has been ranked as the 4th largest event ever in terms of magnitude (USGS, 2012). Japan has a long history of large magnitude earthquakes, but when the Tohoku earthquake hit Japan, the consequences in terms of scale of earthquake, tsunami's height, flooding extension, human and economic losses, greatly exceeded any expectations. The fault rupture of the Tohoku involved three different segments in sequence, resulting in a maximum slip of about 40 m and a significant amount of energy released in a three-minute span. These characteristics made the earthquake not only powerful, but also extremely long in duration. As a proof that the event was beyond any expectations of the authorities, the recording capacity of several seismographs was exceeded and therefore the data stored was partially incomplete (Shojiro et al., 2011).

Far away from the epicenter, at Tokyo and Osaka Bay stations, the recordings showed long period earthquake motions (Nishiyama et al., 2011). The effects of long period motions were different depending on the location and structures involved. For instance, it was found that a 37 story RC building in Tokyo experienced a maximum displacement at the top of about 17 cm, while

the ground displacement was 20 cm. On the other hand, a 55 story steel building in the Osaka Bay area which was 770 km distant from the epicenter, showed a zero-to-peak maximum displacement at the top floor of more than 130 cm, while at ground, the maximum displacement observed was less than 10 cm. This means that, in one cycle of vibration, the building experienced a total amplitude of about 260 cm (Nishiyama et al., 2011). The tall building in Osaka showed from resonance between the fundamental natural period of the building (around 6.5-7.0 seconds) with the predominant period of the ground motion (6-7 sec).

The extraordinary long duration of the shaking subjected structural systems to several cycles of deformation. A direct observation of this phenomena is given by records obtained from an instrumented 9-story shear wall building, which made it possible to track the change in its fundamental period every 10 seconds. Before the earthquake hit, the first natural period was estimated to be 0.7 sec in both principal directions. During the shaking, due to the progress of damage and flexural failure in members and connections, the period increased to 1 sec during the first wave and then from 1.2 to 1.5 sec during the second wave. As a result, the fundamental natural period was elongated to twice the initial period and the stiffness reduced by a factor of 4 (Nishiyama et al., 2011).

1.2.2 Seismic parameters and damage potential of earthquake ground motions

The identification of parameters reflecting the damage potential of earthquake strong ground motions is a topic that has challenged the research community for the past three decades. Early research was conducted on the correlation between ground motions damage potential with simple parameters, such as peak parameters (PGA, PGV, PGD), Arias Intensity and spectral parameters (S_a , S_v , S_d). Later, several studies explored the utility of more advanced, structure-specific seismic parameters to represent the damage potential of earthquake motions.

Although it is a common opinion that PGA is not a reliable index for reflecting the damage potential of ground motions, PGA is one of the most common ground motion parameter used in engineering practice. PGV instead is considered a much more representative measure for earthquake intensity as it is directly related to energy demand (Cosenza and Manfredi, 2000).

Research on the statistical correlation between seismic parameters and damage potential of earthquake ground motions were conducted by Elenas (2000) and Elenas et al. (2001) by

investigating the nonlinear response of an 8-storey RC frame considering different sets of real records. The damage was measured in terms of Overall Structural Damage Index (OSDI) by calculating the Park-Ang (Park & Ang, 1985) damage parameter. They showed that the spectral acceleration, spectral velocity and spectral displacement at the first mode ($S_a(T_1)$, $S_v(T_1)$ and $S_d(T_1)$ respectively) overall well correlate with the damage imparted to the structure. Peak ground parameters such as PGV and PGD were found to have medium correlation with the structural damage. Interestingly, within the parameters considered, the Arias Intensity was found to be the structural-independent parameter that better represented the overall structural damage, ranking either 'high' or 'medium' correlation. On the other hand, as expected, PGA ranked within 'medium to poor' correlation, proving once again the PGA is not a suitable parameter to reflect the damage potential of a ground motion.

Later in 2011 Elenas conducted a similar study investigating the damage imparted to a 6-storey RC frame by a set of 75 synthetic accelerograms. Similar seismic parameters were considered and supported the findings shown by the author's previous studies based on real accelerograms.

Further studies on the correlation between seismic parameters and damage on reinforced concrete frames were conducted by Cantagallo et al (2012), Kadas and Yakut (2014) and Cao and Ronagh (2014). These studies confirmed PGA and other peak parameters not to be suitable as damage indicators. The seismic parameters that demonstrated the best correlation with damage were spectral and energy indices.

A step ahead in the study of ground motion damage potential was taken by Luco et al. (2005). Their study focused on the damage potential of ground motions on steel moment resisting frames. Luco et al. supported the usefulness of $S_a(T_1)$ as a measure for damage potential, but only for not highly inelastic systems which are dominated by a single-mode vibration. As already showed by Bazzurro and Cornell (2002), assessment based on $S_a(T_1)$ only would not be appropriate for long period buildings which may be dominated by higher modes. As a result, Luco et al. proposed a new, vector-based, index which positively correlates to the structural damage. This index is a combination of $S_a(T_1)$ with higher-mode spectral acceleration and the 1st mode inelastic spectral acceleration. Later in 2007, Luco and Cornell demonstrate the efficiency of advanced intensity measures which reflects the effects of nonlinearity and the contribution of higher modes.

Later research explored the utility of advanced, structure-specific ground motions intensity measures. For instance, studies conducted on reinforced concrete moment frames were conducted by Fontara et al. (2012), Kostinakis et al. (2014) and by Kostinakis and Athanatopoulou (2015). Their research overall agreed on the better suitability of structure-specific ground motion intensity measures against the traditional simple parameters. The authors also showed that, once again, $S_a(T_1)$ is reasonably a good indicator for damage potential for low-rise buildings subjected by low-intensity motions.

Although most of the studies classified peak ground motion parameters to be unsuitable measures to discriminate the damage potential of the motions, past investigations identified lower bounds for damage. Such lower bound for PGA was identified to be 0.2 g by Martinez-Pereira (1999). The thresholds for other peak parameters were also investigated. For example, the lower bound for PGV was found to be 20 cm/sec for the motion to be potentially damaging to structural systems (Bommer & Martinez-Pereira, 2000).

Some of the studies cited above, explored the suitability of duration as seismic parameter to represent the damage potential of the ground motions. In particular, the earlier studies by Elenas (2000), Elenas et al. (2001) and Elenas (2011) demonstrated a poor correlation between the duration, evaluated as the time interval between 5% and 95% of the Arias Intensity (Trifunac and Brady, 1975), and the structural damage. A later study conducted by Nanos et al. (2008) explored the suitability of different duration metrics along PGA and Arias Intensity, to reflect the motion damage potential. The investigation was done considering a six storey reinforced concrete frame and a suite of 450 synthetic accelerograms. Nanos et al. confirmed the high correlation between Arias Intensity and structural damage, while the correlation for PGA was medium-ranked. Most interestingly, they demonstrated that, within the range of duration definitions, the duration proposed by Trifunac and Brady (1975) showed the weakest correlation to the damage imparted to the structure. The duration metric which correlated best was found to be the bracketed duration (Bolt, 1973), which is defined as the time elapsed between the first and the last excursion beyond a specific threshold acceleration.

This finding strongly contradicts with other studies that indicated the duration evaluated as per Trifunac and Brady is the most appropriate duration metric for assessing the response of structural systems (Hancock & Bommer, 2006; Foschaar et al., 2012; Liel & Raghunandan, 2013;

Chandramohan et al., 2016). It is important to note that these correlation studies were conducted with a limited database of records, mostly from crustal events. Even when synthetic motions were used for analysis, the duration range considered was between 20 sec to 40 sec. Clearly, if subduction motions are not considered, this duration range would be very limiting.

Moreover, several researchers also pointed out that the correlation between seismic parameters and ground motion damage potential is conditional on the structural typology considered, the damage parameter used for analysis, and the level of seismic intensity (Fontara et al., 2012; Kostinakis et al., 2015).

1.2.3 State-of-the-art on the evaluation of long duration effect of ground motions

Research on the effect of long duration ground motions on seismic performance of structures has developed over the last 15 years. In the early years, the study on long duration ground motions was mainly conducted by performing time history analysis on inelastic structures and comparing the correlations between the damage measures with the motions duration.

One of the first studies was conducted by Bommer et al (2004) at Imperial College on the influence of long duration motions on the response of masonry structures. They considered seven structural models with different period and characterized by strength and stiffness degradation. The failure mode in these models was primarily controlled by in-plane mechanisms. By running time history analysis with almost 500 records, they found out that longer duration motions led to greater strength degradation than shorter records. They also observed that, for their models, Arias Intensity (AI) (Arias, 1970) and spectral acceleration at the fundamental period of the structure were good indicators of structural damage (Bommer et al., 2004). However, this study had no access to records from later subduction earthquakes that became available after 2004, especially after the 2011 Tohoku earthquake. The records they used were mainly recordings from crustal events.

A particularly good review of the correlation between duration and damage measure was conducted by Bommer et al. (2006). In their analysis, they investigated past studies by grouping them according to the damage measures used, the type of structural model and the metric chosen for duration. They finally classified each and every study according to a rating scheme and found out that studies considering peak response as a damage measure generally correlated poorly with

duration, while studies considering energy measures proved the influence of duration to be significantly important. The duration effect was dominant when the structural systems were modeled accounting for strength and stiffness degradation and considering the destabilizing effect of gravity loads (P- Δ effect) (Hancock & Bommer, 2006).

The same authors also conducted a study on an 8 storey RC-wall frame building, which was subjected by a series of time history analyses. In this investigation, a total of thirty records of various durations was used for analysis. The motions were all spectrally matched to the same target spectrum. The time history analyses highlighted that fatigue and energy damage measures correlated well with longer durations (Hancock & Bommer, 2007).

Further investigation on the influence of duration on RC structures was conducted in 2013 by Raghunandan and Liel at the University of Colorado. In particular, they used a set of 17 RC frame buildings, representative of modern and older construction, to run nonlinear Incremental Dynamic Analysis (IDA) using 76 ground motions of varying duration. Results of this study showed that the collapse capacity of each structure, quantified as the median ground motion intensity causing collapse, decreased as the duration of the motion increased. It is important to note that in their study, Raghunandan and Liel (2013) used inelastic spectral displacement, S_{di} , as the ground motion intensity measure. In previous studies conducted by Tothong et al., S_{di} was shown to be a suitable intensity measure for nonlinear dynamic analysis, demonstrating the effectiveness of S_{di} in reflecting both ground motion intensity as well as spectral shape effect for structural systems dominated by first mode response (Tothong & Cornell, 2006; Tothong & Luco, 2006). Moreover, to quantify the influence of ground motion duration on collapse capacity, Raghunandan and Liel fitted a multivariate regression model to the analysis result to predict collapse capacity as a function of ground motion duration, structural period, ductility capacity and lateral load resisting system. The results showed, once again, that longer duration leads to a decrease in median collapse capacity. As the duration increases, the ability of structures to withstand higher intensities of ground motions becomes less as a larger part of their energy dissipation capacity has been utilized. Their analysis also showed that highly ductile structures could withstand greater motion intensities before collapse when subjected to shorter duration earthquakes. The effect of duration on collapse capacity was found to be more significant for highly ductile systems, as their capacity to withstand longer duration motions diminishes as a larger part of the energy dissipation capacity is utilized due to the larger number of cycles. The authors indeed pointed out how for less ductile structural

systems, characterized by less energy dissipation capacity, even a short duration motion could have a detrimental effect as the structure has not enough capacity to withstand even a low number of cycles. Raghunandan and Liel also investigated the impact of the energy dissipation capacity and P- Δ deformations on the duration effect. Results demonstrated that, in general for any duration, systems with less energy dissipation capacity (more degradation) showed a decrease in the collapse capacity. In addition, they found out that collapse capacity decreases for higher gravity loads due to the P- Δ effect for short duration records. Contrarily, for long duration motions, this finding did not seem to hold: the collapse capacities calculated with different levels of P- Δ deformation were very close, thus suggesting that P- Δ does not critically affect the collapse capacity at that duration range. The authors also concluded that the effects of P- Δ on the results is not as significant as the influence of cyclic deterioration and ductility capacity parameters. The study conducted by Raghunandan and Liel (2013) showed also that an increase on the fundamental period of the structure is generally associated with an increase in the collapse capacity values.

In 2013, Raghunandan carried out a study using 36 buildings of varying heights and belonging to 4 different design periods (ICBO 1967, 1973, 1944 and ICC 2012) to run IDA. These analyses were conducted using two record suites: a set of 35 crustal motions and a set of 42 subduction ground motions. In addition, a third set of records comprising 30 simulated motions generated by subduction earthquakes with magnitude greater than 8.5 was used for comparison. This study confirmed that the building median collapse capacity was significantly reduced when considering subduction motions. Moreover, Raghunandan confirmed how the rate of reduction in the collapse capacity due to duration is higher for ductile buildings as compared to non-ductile. Raghunandan and Liel research supported the significant influence of ground motion duration on the structural collapse capacity. (Raghunandan, 2013; Raghunandan & Liel, 2013; Liel & Raghunandan, 2014).

A step forward towards the isolation of ground motion duration from the other shaking parameters was taken by Baker and his research group at Stanford University. Chandramohan et al. (2016) performed IDA on a 5 storey steel moment frame and on a RC bridge pier. They also advanced the concept of spectrally equivalent records according to which, for each long duration motion, a corresponding short duration record having a compatible (similar) spectral shape was paired. This selection process led to the creation of two suites of ground motions, one for long and one for short duration, showing similar mean response spectra. In this way, the use in their IDA of

$S_a(T_1)$ as measure for ground motion intensity was considered a suitable option to isolate the effect of duration from ground motion spectral shape. They found that the effect of long duration reduced the median collapse capacity of the 5 steel story frame by 27% and the capacity of the RC column by 17% (Chandramohan et al. 2014; Chandramohan et al., 2013; Chandramohan et al., 2016). Chandramohan also conducted a parametric study on the RC bridge pier to assess the impact of different levels of degradation and of different plastic rotational capacities. The sensitivity study showed that the increase in rotational capacity lead to an increase in the difference in the median collapse capacity between long and short duration motions. Moreover, Chandramohan also showed that, for systems experiencing more severe degradation, the influence of duration resulted in a more pronounced decrease in the median collapse capacity. Despite similarities in the findings by Chandramohan (2016) to the trends shown by Raghunandan and Liel (2013), it is important to note that these studies cannot be directly correlated due to fundamental differences in the procedure of selecting the ground motions and the choice of intensity measure for IDA.

Another study was conducted by Fairhurst et al. (2017) at the University of British Columbia. Their study focused on the influence of long duration motions on RC shear wall buildings. To this end, they considered five prototypes of Vancouver coupled shear wall buildings of different height, specifically 6, 12, 18, 24 and 30 story, and these models were subjected to two spectrally equivalent suites of motions representing long and short duration respectively. The spectrally equivalent motions were scaled to the UHS for a site in Vancouver, BC. The analysis conducted for the collapse level of shaking confirmed that the long duration records tended to impose greater drift demands than short duration records. Fairhurst et al. found out that at levels of shaking where little damage was expected, such as 100% UHS design level, the duration of ground motions may not be important as input motion parameter to consider. On the other hand, they verified the significant influence of ground motion duration in the evaluation of the median collapse capacity at higher shaking levels, thus confirming the findings of previous studies on the effects of long duration ground motions on collapse capacity (Raghunandan & Liel, 2013; Chandramohan, 2016).

Later in 2017, Chin published a study on the effects of long duration motions on the probability of drift exceedance of RC frames. In his study, Chin investigated the performance of both a RC shear wall and a MDOF RC frame. These two models have been used to conduct IDA to generate fragility curves for collapse. Moreover, a sensitivity analysis for different values of degradation and deformation capacities was conducted for each model. The two sets of ground

motions used by Chin were not spectrally equivalent (i.e. the motions were not selected following the approach first introduced by Chandramohan in 2016), but they were independently scaled to the UHS for Victoria, BC. Results showed that an increase in the ductility capacity allows reaching the median collapse capacity at higher shaking levels for both crustal and subduction fragility curves. Moreover, long duration subduction ground motions generated the same probability of collapse of crustal motions, but at lower levels of shaking.

Clearly over the years the approach to long duration has evolved. The latest approach by Chandramohan et al (2015) based on the compatible spectral pair concept offers a clear way to isolate the effects of duration from the influence of spectral shape. The present study extends this work utilizing the concept of spectrally equivalent records and exploring the influence of building period and ductility capacity on the duration effect on structural collapse.

1.3. Research goal, objectives and scope

The main **goal** of this research is to understand the effects of subduction ground motions on structural systems and identify which structures are more exposed to these effects. This research has three objectives:

1. The **first objective** is to investigate the damage level observed during the 2010 Maule earthquake (stations of Maipu and Curico) and the 2011 Tohoku earthquake (stations of Tsukidate and Sendai) using the characteristics of the ground motions recorded at the sites;
2. The **second objective** is the investigation of the impact of long duration subduction motions on the seismic performance of structural systems dominated by a single-mode response;
3. The **third objective** is to investigate the effects of long duration subduction motions on the response of an existing Multi-Degree-of-Freedom (MDOF) structure.

The investigation on the damage observed during the 2010 Maule and the 2011 Tohoku earthquake was conducted using the shaking characteristics of the ground motions recorded. During the 2010 Maule earthquake, the Peak Ground Acceleration (PGA) recorded at Maipu was 0.56 g, while the PGA in Curico was 0.47g. Despite quite similar shaking intensities, the structural

damage observed in Curico was far more severe and widespread than what observed in Maipu. Another interesting case is the one associated to the field observations at Tsukidate and Sendai (Japan) after the 2011 Tohoku earthquake. The shaking intensity at Tsukidate was classified as JMA 7, which is the largest intensity level in the Japanese scale. Yet suffered little damage, whereas the damage in Sendai, rated JMA 6+, was quite substantial. The motion recorded in Tsukidate featured an extremely high PGA (about 3 g), while the PGA at Sendai was 1.5 g. An investigation was carried out to understand what characteristics of the subduction ground motions contributed most to the damage potential.

The investigation of the impact of long duration subduction motions on the seismic performance of structural systems dominated by a single-mode response was conducted comparing the probability of collapse associated with long duration subduction motions to the probability resulting from short duration motions. The study also focuses on developing the effect of structural periods and ductility capacities on the impact of long duration shaking on structural collapse.

The investigation of the effects of long duration subduction motions on the response of an existing Multi-Degree-of-Freedom (MDOF) structure was conducted considering a 6-storey RC moment frame. This study was carried out by conducting a nonlinear IDA, using the compatible motion pairs scaled to the 100% hazard level.

The **scope** of this thesis is limited to study:

- The suitability of selected shaking parameters and response spectra (i.e. PGA, PGV, SD, frequency content, Arias Intensity, elastic response spectrum, inelastic response spectrum and time history analysis) to explain the relationship with the observed structural damage;
- The effects of long duration subduction motions on collapse of structures dominated by one mode, the influence of structural period and ductility on the long duration effects;
- The effects of long duration subduction motions on collapse performance of a 6-storey RC frame building.

1.4. Thesis organization

This thesis is organized into seven Chapters. The first objective is addressed in Chapter 2, the second objective in Chapters 3, 4, and 5 and the third objective in Chapter 6. Overall, the main focus of the dissertation is on the study of the effects of long duration subduction motions (Chapters 3 to 6).

A summary of the key findings and limitations of this study is presented in Chapter 7. Recommendations are made also for future research.

The content of each Chapter is outlined below.

- **Chapter 2.** Two case studies were presented to explain the relationship between observed damage and associated shaking intensity. One case study investigated the difference on the damage pattern during the 2010 Maule Earthquake at the stations of Maipu and Curico. The second study presents the detailed analysis done for the records at the stations Tsukidate and Sendai during the Tohoku 2011 earthquake;
- **Chapter 3.** This Chapter presents the methodology for selecting and scaling the strong ground motions for time history analysis. Two suites of 20 acceleration records each were selected to represent long duration subduction and short duration crustal ground motions respectively. In order to isolate duration from the other shaking parameters, the records have been selected and scaled so that, the subduction and crustal motions are spectrally compatible. The subduction motions were linearly scaled to the UHS for Victoria, BC in the period range of interest. Each crustal motion was linearly scaled to the scaled subduction motion, thus providing a compatible spectral pair of input motions;
- **Chapter 4.** Nonlinear IDA (IDA) on SDOF systems to develop mean structural drifts at different periods and ductility capacities is described;
- **Chapter 5.** Fragility curves for probability of collapse and of exceeding specified drift limits are developed on the basis of the IDA analyses. The comparison between crustal and subduction fragility curves clearly shows the effect of duration and

enhances significantly the understanding of its dependence on structural period and ductility level considered;

- **Chapter 6.** The two suites of motions defined in Chapter 3 were used in this Chapter as input ground motions for time history analysis of a 6-storey reinforced concrete moment frame building. The IDA analysis was conducted for different levels of shaking. The structural response obtained with the short duration crustal motions is compared with the results generated with the long duration ground motions to determine the effect of duration on the probability of collapse;
- **Chapter 7.** A summary of the key findings and limitations of this study is presented in this Chapter. Recommendations were advanced for future research in this area.

Chapter 2

Damage potential of subduction ground motions: case studies

“Every block of stone has a statue inside it and it is the task of the sculptor to discover it.”

Michelangelo Buonarroti (1475 – 1564)

2.1. Introduction

This Chapter presents an exploratory study about the damage potential of subduction earthquakes with the intention of tentatively identifying ground motion parameters which would better relate to the damage observed during post-earthquake field investigations. To this end, two case studies are presented. The first study is a comparison between the damage observed at Curico and Maipu stations during the 2010 Maule earthquake. The second study presents the investigation on the damage observed at Tsukidate and Sendai during the 2011 Tohoku earthquake.

During the 2010 Maule earthquake, similar intensities of shaking were recorded at the stations in Curico (Maule region) and Maipu (Santiago region): the PGA in Curico was 0.47 g and was 0.56 at Maipu. Both locations are at a comparable distance from the rupture zone (Figure 2-1). Post-earthquake field inspections documented much more severe and widespread damage in Curico despite having slightly lower PGA.

In the case of Tsukidate and Sendai, mentioned earlier, there was a striking paradox between observed damage and the JMA shaking intensity. In Japan, the JMA seismic intensity is a common seismic scale used to measure the strength of an earthquake ground motion. This intensity is expressed in *shindo* levels which range from 0 to 7 and describes the degree of shaking at various locations on the surface. The JMA seismic intensity was estimated to be 6+ in Sendai while at the Tsukidate station it reached the highest scale degree of 7. As shown in Figure 2-2, both sites are at comparable distances from the rupture (Nishiyama et al., 2011). The station of Tsukidate recorded an extremely high PGA, about 3 g, while the PGA in Sendai was 1.5 g. Despite this extremely large difference in PGA, the damage was much greater in Sendai than in Tsukidate, confirming that the PGA is not a good index of damage potential. Similar consideration holds for the Peak Ground Velocity (PGV). While the PGV at Tsukidate reached 110 cm/sec, the PGV intensity in Sendai was of about 86 cm/sec. The maximum displacement (PGD) were roughly 22 cm at both stations. Neither the PGV, nor the PGD provided useful information about the damage observed at the site.

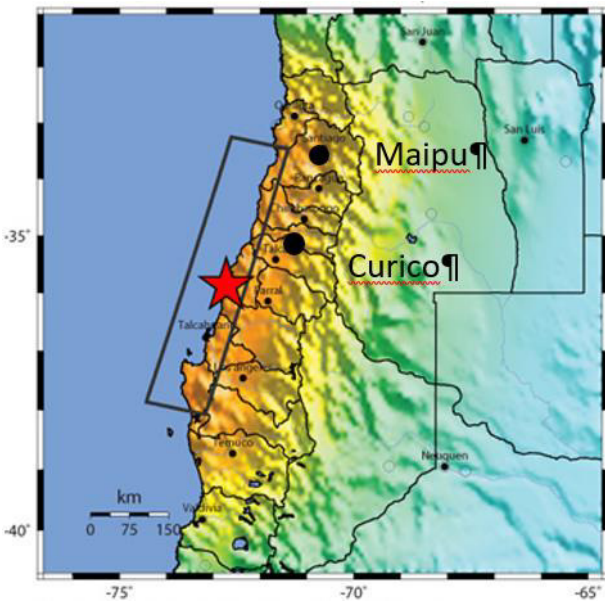


Figure 2-1: Location of the Maule epicenter and the stations of Curico and Maipu (USGS).

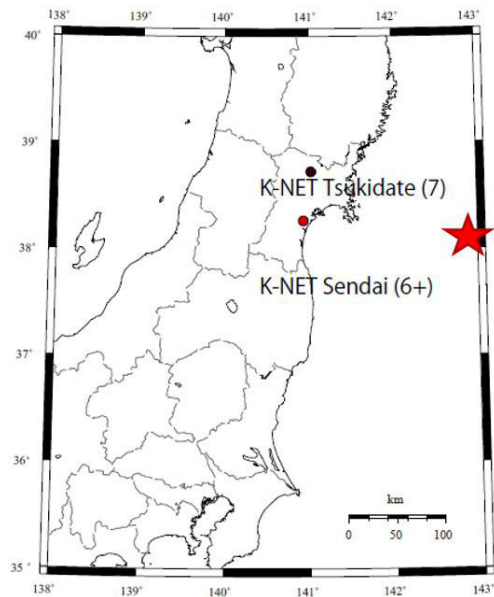


Figure 2-2: Location of the Tohoku epicenter and the stations of Tsukidate and Sendai.

This Chapter investigates what other characteristics of the ground motion record may significantly contribute to structural damage. Specifically, the effects of frequency content, Arias Intensity and spectra such as elastic, constant ductility and constant strength are explored and the impact of these parameters will be assessed using reported structural damage data. It is important to note that, the rationale behind the selection of parameters chosen for analysis is not to provide a comprehensive review of all the seismic parameters discussed in Section 1.2.2 to reflect the damage potential of ground motions. The parameters used were selected as measures and indices commonly used in civil engineering practice.

2.2. Maule 2010 earthquake

2.2.1 Post-earthquake field observations

Post-earthquake field investigations were conducted in several regions of Chile to assess the damage caused by the earthquake and tsunami to buildings and infrastructure. The adobe construction in the Maule region suffered the most damage. In the city of Curico, 90% of the masonry construction was destroyed. Damage was not only associated with housing construction, but was also observed in hospitals, schools and churches (GEER Association, 2010). Examples of damage to adobe construction is given in Figure 2-3, Figure 2-4 and Figure 2-5. Figure 2-3 shows the collapse of the church of San Francisco in the city of Curico (Wikipedia, 2010), while Figure 2-4 provides an example of the extensive damage to low-rise masonry constructions. Similar structural damage was observed in other areas of the Maule region, in particular in the capital city Talca (Figure 2-5). In the metropolitan region of Santiago, the reconnaissance team reported a generally good performance for engineered buildings. Just few engineered constructions failed because of poor ductile detailing and design irregularities. An example of damaged building in Maipu (Metropolitan Region) is shown in Figure 2-6.

2.2.2 Ground motions parameters and structural damage

This Section illustrates the shaking characteristics of the motions in Maipu (less damage) and Curico (more damage) during the 2010 Maule Earthquake, used to investigate the damage observed during the post-earthquake reconnaissance.



Figure 2-3: Damage to the church of San Francisco (Curico, Maule region).



Figure 2-4: Damage in La Prensa in Curico (Courtesy of Decofrut/Flickr; NASA, 2017).



Figure 2-5: Damage to masonry low-rise buildings in Talca, Maule region (EERI, 2010).



Figure 2-6: Damaged building in Maipu, Santiago region (Courtesy of Jorge Barrios; Wikipedia, 2010).

The records at Curico and Maipu were obtained from the COSMOS database for analysis (COSMOS, 2017). The largest acceleration recorded was in the north-south direction for both sites (Elnashai et al., 2010) and therefore it was selected for this study. Both sites were located at similar distances from the fault rupture, about 65 km. The station at Maipu recorded a PGA of 0.56 g, while the PGA at Curico was 0.47. Figure 2-7 shows the acceleration time histories at the two stations, which are both characterized by a two-waves group. Although the PGA at Curico is less than Maipu, the acceleration history at Curico was generally greater than at Maipu.

A summary of the ground motion characteristics at Maipu and Curico sites is provided in Table 2-1. There is a significant difference between the PGV values: at Maipu the PGV was 40% higher than at Curico, although registered less structural damage. Conversely, Curico recorded a

higher PGD (about 8 cm) than at Maipu, where the PGD was 6.2 cm. Even though one could argue that PGD could potentially explain the major structural damage at Curico, it is important to remember that, as shown earlier, that this finding did not hold for Tsukidate and Sendai. The comparison between shaking parameters at Maipu and Curico shows that peak ground parameters are not suitable for discriminating the damage potential of the recorded motions at these sites.

The significant duration at Curico (50 sec) is much larger than the duration at Maipu (32 sec). This could support the greater damage observed at Curico, as structures excited by longer motions would experience more loading cycles.

Table 2-1: Summary of the characteristics of the motions at Maipu and Curico

	Maipu	Curico
Record Name	MAIPU S/N 663	CURICO S/N 499
Max. Acceleration	0.56 g	0.47 g
Max. Velocity	41.87 cm/sec	29.7 cm/sec
Max. Displacement	6.2 cm	8.05 cm
Waveform	2-wave groups	2-wave groups
Period (Frequency)	Intermediate Period 0.5 sec (2 Hz)	Short/Intermediate Period 0.1 – 0.5 sec (2 – 10 Hz)
D ₅₋₉₅	32.19	50.19 sec

The Arias Intensity is a common measure of the energy content of the ground motion (Bommer & Boore, 2004) and it is defined as the time integral of the ground acceleration squared (Arias, 1970). Figure 2-8 shows the comparison between Arias intensities at Curico and Maipu. The Arias intensity at Curico is larger than the one generated at Maipu, signifying a higher energy imparted by the motion to the structures. Therefore, in this case, the Arias intensity may seem to be a good indicator of potential damage. However, the study on the two Japanese sites described later shows that in that case the Arias intensity was not a good measure of structural damage.

The frequency content of the motions at Curico and Maipu is shown for comparison in Figure 2-9. The record in Maipu shows a predominant frequency at about 2 Hz. On the other hand, the motion in Curico features an important component at lower frequencies (about 0.07 Hz) and also shows large amplitudes for a range of frequencies from 2 Hz to 10 Hz. Buildings in Curico are mainly low-rise unreinforced masonry constructions and are therefore particularly vulnerable to seismic shaking. The presence of non-ductile adobe construction along with a motion with

frequency components 2-10 Hz that are in the range of frequencies of low-rise buildings justifies the extensive damage at Curico.

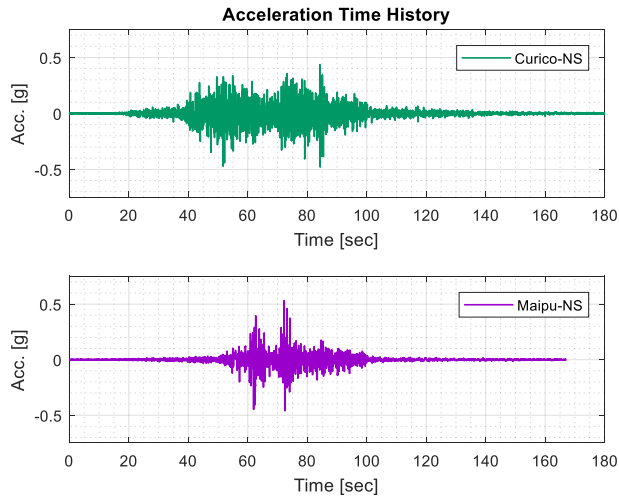


Figure 2-7: NS - Acceleration time history at Curico and Maipu stations.

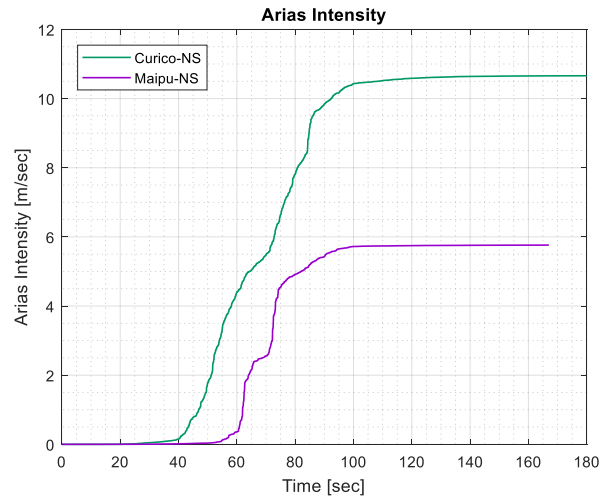


Figure 2-8: Arias intensities for the NS records at Curico and Maipu.

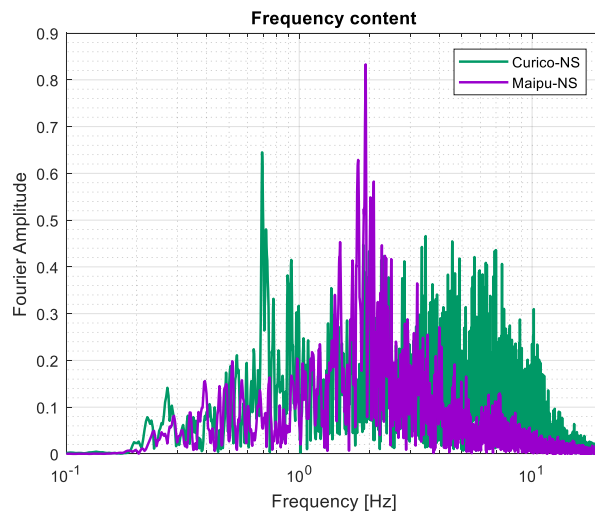


Figure 2-9: Comparison of frequency content at Curico (green) and Maipu (magenta).

2.2.3 Elastic response spectra analysis

Next, the relationship between the elastic response spectra of the motions and the damage observed is investigated. Spectral amplitudes for accelerations, velocities and displacements have been calculated for 5% damping and shown in Figure 2-10, 2-11 and 2-12 respectively.

While in the period range below 0.4 sec the amplitudes in terms of velocity and displacements are quite comparable, the acceleration spectrum for the motion in Curico shows a very sharp peak at a period of 0.16 sec. The spectral amplitude associated with this period is 2 g. In this period range the acceleration amplitudes at Maipu are lower than at Curico. This is the period range of interest typical of those low-rise non-ductile constructions that suffered the greatest damage at Curico during the 2010 Maule Earthquake. The elastic spectra generated by the motion at Maipu show a dominant amplitude at about 0.5 sec for both acceleration and velocity, suggesting that buildings in that period range would experience very large demands. This is the period associated with mid-rise constructions in Chile and does not correspond to those low-rise structures which experienced damage, such as shown in Figure 2-6. Moreover, the elastic displacement spectra show generally larger peak spectral demands than the PGD for a period range between 0.5 and 5 sec. This observation is particularly evident for the spectrum generated with the Curico motion which is characterized by very large demands at 1.5 and 3.7 sec.

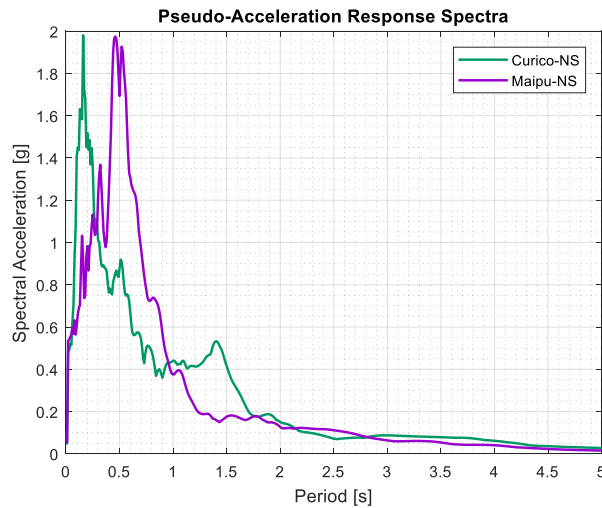


Figure 2-10: Acceleration response spectra for Curico and Maipu records ($\xi = 5\%$).

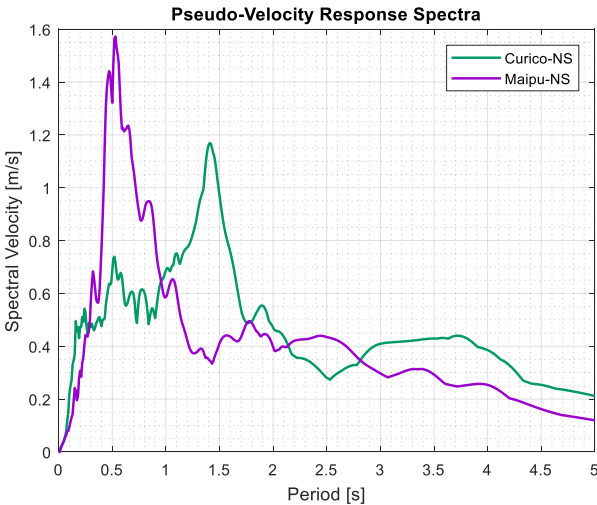


Figure 2-11: Velocity response spectra for Curico and Maipu records ($\xi = 5\%$).

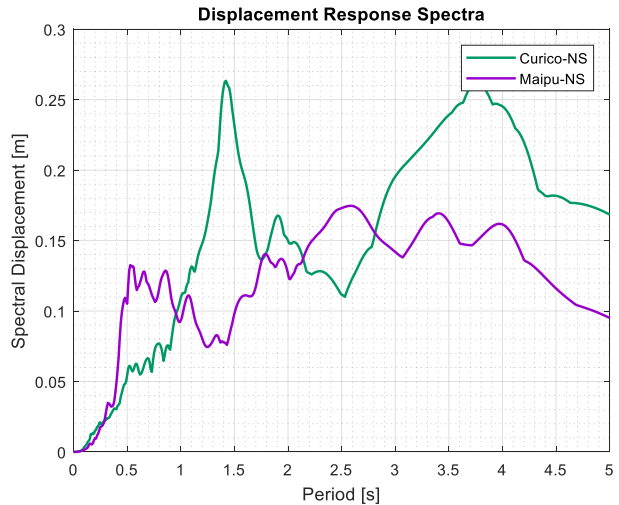


Figure 2-12: Displacement response spectra for Curico and Maipu records ($\xi = 5\%$).

2.3. Tohoku 2011 earthquake

2.3.1 Post-earthquake field observations

Limited damage was observed in wood houses in Tsukidate, but it was not as severe as expected given the high JMA seismic intensity rating. In some cases, where the damage was substantial, it was caused by ground liquefaction and soil failure and was not directly related to poor structural performance under ground shaking. Figure 2-13 shows a typical example of damage in Tsukidate, where the objects on the sideboard overturned during the shaking. On the other hand, the containers shown in Figure 2-14 with high aspect ratios and many stacked items did not overturned despite the very high acceleration (Figure 2-15).

In the city of Sendai, significant damage was observed in wooden houses. Reinforced concrete buildings suffered severe damage as well. Post-earthquake evaluations reported several types of damage patterns in reinforced concrete buildings. Figure 2-16 shows evidence of shear failure of reinforced concrete walls, while Figure 2-17 provides evidence of shear failure in perimeter columns. An example of mid-story collapse in a reinforced concrete building is shown in Figure 2-18. Damage in terms of shear failure was observed in first storey columns of a low rise building. Figure 2-19 shows shear cracks on the columns that were reported to suffer additional damage during aftershocks (Figure 2-20).



Figure 2-13: Overturned objects in Tsukidate - example 1 (Ventura, 2011).



Figure 2-14: Not overturned objects in Tsukidate – example 1 (Ventura, 2011).



Figure 2-15: Not overturned objects in Tsukidate - example 2 (Ventura, 2011).



Figure 2-16: Damage to reinforced concrete walls in Sendai - example 1 (Ventura, 2011).



Figure 2-17: Damage to reinforced concrete building in Sendai - example 2 (Ventura, 2011).



Figure 2-18: Collapse of a mid-story of a reinforced concrete building in Sendai (Ventura, 2011).



Figure 2-19: Shear cracks on first-storey column in Sendai (Nishiyama et al., 2011).



Figure 2-20: Shear cracks on first-storey column in Sendai caused by aftershocks (Nishiyama et al., 2011).

Significant damage was observed also in intermediate period RC buildings. An example is given by the 9-story RC shear wall building (Figure 2-21) which suffered structural damage. The crushing of the concrete is evident at the third floor, as shown in Figure 2-22 by the red arrow (Shojiro, 2011). Damaged in boundary beams was reported as well in shear wall buildings. Figure 2-23 shows an example of 8-story shear wall building where significant damage was localized around the openings in the coupling beams (Figure 2-24).



Figure 2-21: Elevation view of the 9-storey shear wall building in Sendai (Nishiyama et al., 2011).



Figure 2-22: Crushing at the base of the RC column (modified from: Nishiyama et al., 2011).



Figure 2-23: Elevation view of the 8-storey shear wall building in Sendai (Nishiyama et al., 2011).

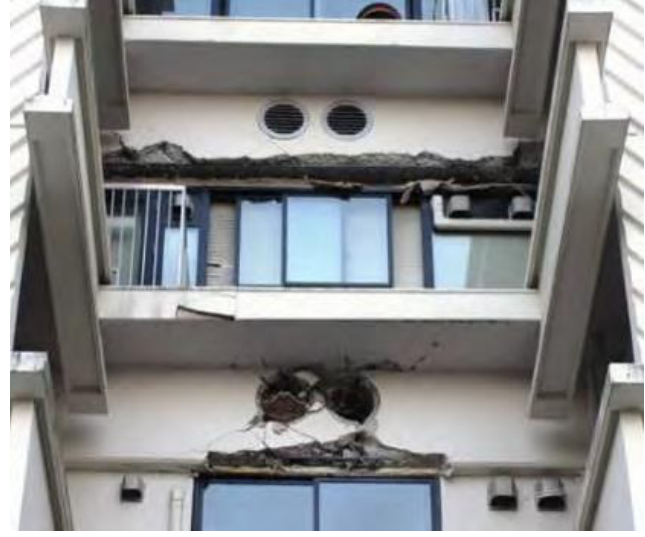


Figure 2-24: Damaged boundary beams with openings (Nishiyama et al., 2011).

2.3.2 Ground motions parameters and structural damage

As reported, there was much greater damage in Sendai than in Tsukidate despite the fact that Tsukidate had a higher JMA intensity rating. A detailed study was conducted to explain the difference in damage potential of the two site records by examining the different ways of characterizing ground motion intensity.

The ground motion records for Tsukidate and Sendai were downloaded from the Japanese Kyoshin networks K-NET and KiK-net database of the National Research Institute for Earth Science and Disaster Prevention (NIED). In order to understand the contributions of each component to the ground motions, the 3D particle motions were generated for accelerations, velocities and displacements. The acceleration motions are shown for Tsukidate and Sendai in Figure 2-25 and Figure 2-26 respectively. The velocities are represented in Figure 2-27 and Figure 2-28, while the particle displacement motions are shown in Figure 2-29 and Figure 2-30.

While displacement particle motions are quite comparable at Tsukidate and Sendai (Figure 2-29 and Figure 2-30), the particles velocities in Tsukidate (Figure 2-27) are greater than in Sendai (Figure 2-28). It is the acceleration time histories which show the most evident difference. The particle acceleration at Tsukidate (Figure 2-25) is significantly higher than the particle acceleration in Sendai (Figure 2-26), regardless of the direction considered. A significant vertical component

is also present at Tsukidate, while in Sendai the vertical amplitude is much lower. This suggests that the vertical component did not have a major contribution to the extended damage in Sendai. The main direction of the acceleration motion is the North-South (NS), where Tsukidate registers a PGA close to 3 g and Sendai 1.5 g. For this reason, the investigation about the damage potential at the two stations was carried out considering the NS component.

Clearly, PGA is a poor indicator of damage potential: PGA was 3.0g in Tsukidate and only half as large at Sendai at 1.5 g, yet Sendai had much greater damage. In addition to the traditional ground motion parameters, such as PGA, PGV and maximum displacement, attention was focused on the frequency content and the significant duration. Significant duration is defined as the time from 5% to 95% of the Arias Intensity and it is traditionally designated D_{5-95} .

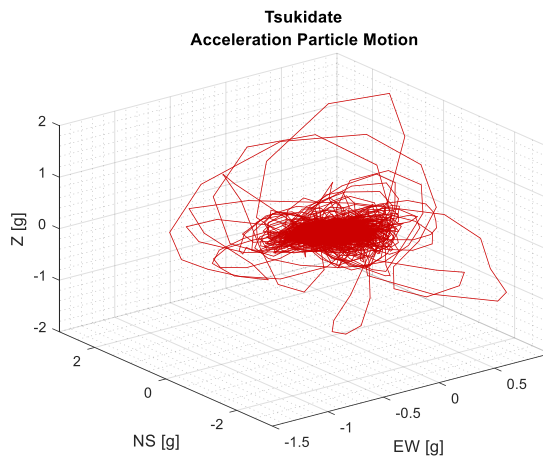


Figure 2-25: Particle acceleration at Tsukidate.

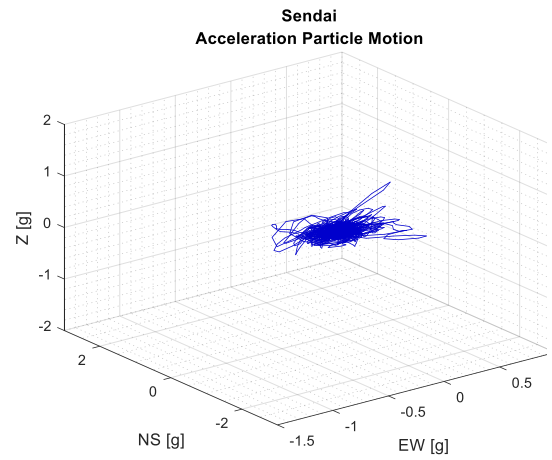


Figure 2-26: Particle acceleration motion at Sendai.

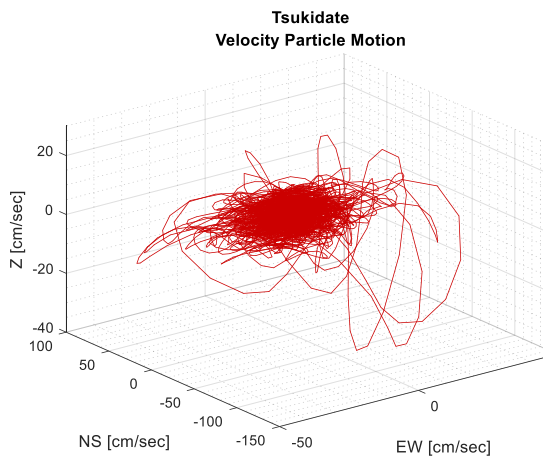


Figure 2-27: Particle velocity at Tsukidate.

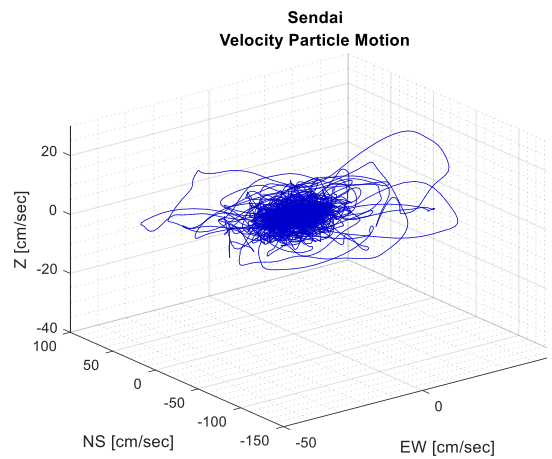


Figure 2-28: Particle velocity at Sendai.

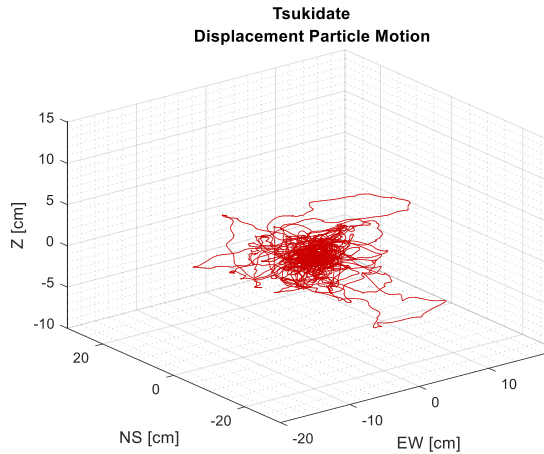


Figure 2-29: Particle displacement at Tsukidate.

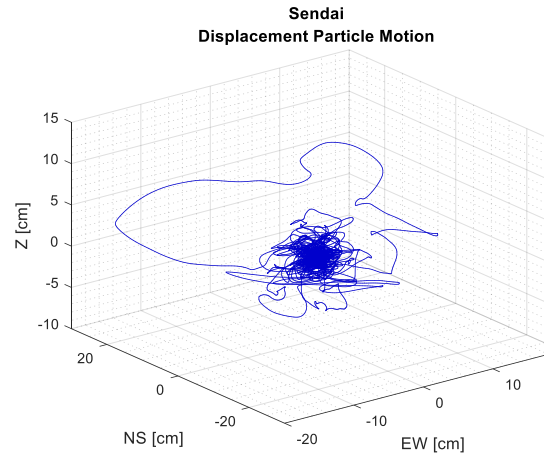


Figure 2-30: Particle displacement at Sendai.

Table 2-2 provides a summary of the main characteristics of the motions recorded at Tsukidate and Sendai stations. It can be noted that although the PGV at Tsukidate is higher (110 cm/sec) than at Sendai (86 cm/sec), much more damage was observed at Sendai. The maximum ground displacements were similar at about 22 cm for both stations. It appears clear that peak ground parameters do not reflect adequately the damage potential of ground motions. From a qualitative point of view, both records have similar time history shapes, which can be described by two waves groups as shown in Figure 2-31. One of the characteristics of the records which underlines the different nature of the ground motions is the frequency content (Figure 2-32). Tsukidate motions have a much higher frequency content, with higher amplitudes at short periods (about 0.2 sec), while the motion at Sendai generates a much wider frequency spectrum within the period range 0.5 and 1.0 sec. The significant duration at Sendai is about 89 sec, while the motion at Tsukidate has a duration of 80 sec. It seems unlikely that the small difference (about 10%) in duration would explain the much greater and widespread damage in Sendai respect to Tsukidate.

The Arias Intensities of Tsukidate and Sendai are shown in Figure 2-33. It is clear that the Arias intensity for Sendai is only a small fraction of the Arias Intensity of the Tsukidate record. However, the damage in Sendai was much greater than the damage in Tsukidate, despite the fact that the Arias Intensity is supposed to be a measure of the energy in the ground shaking. Clearly, the Arias Intensity is not a good measure of potential damage to structures in this case in contrast to the findings from Curico and Maipu discussed earlier.

Table 2-2: Summary of the characteristics of the motions at Tsukidate and Sendai.

	Tsukidate	Sendai
Record Name	MYG0041103111446-NS	MYG0131103111446-NS
JMA Seismic Intensity	7	6+
Max. Acceleration	2.91 g	1.46 g
Max. Velocity	110 cm/sec	86 cm/sec
Max. Displacement	22.5 cm	22.4 cm
Waveform	2-wave groups	2-wave groups
Period (Frequency)	Short Period 0.2 sec (5 Hz)	Intermediate period 0.5 – 1.0 sec (1 – 2 Hz)
D ₅₋₉₅	80.85 sec	89.72 sec

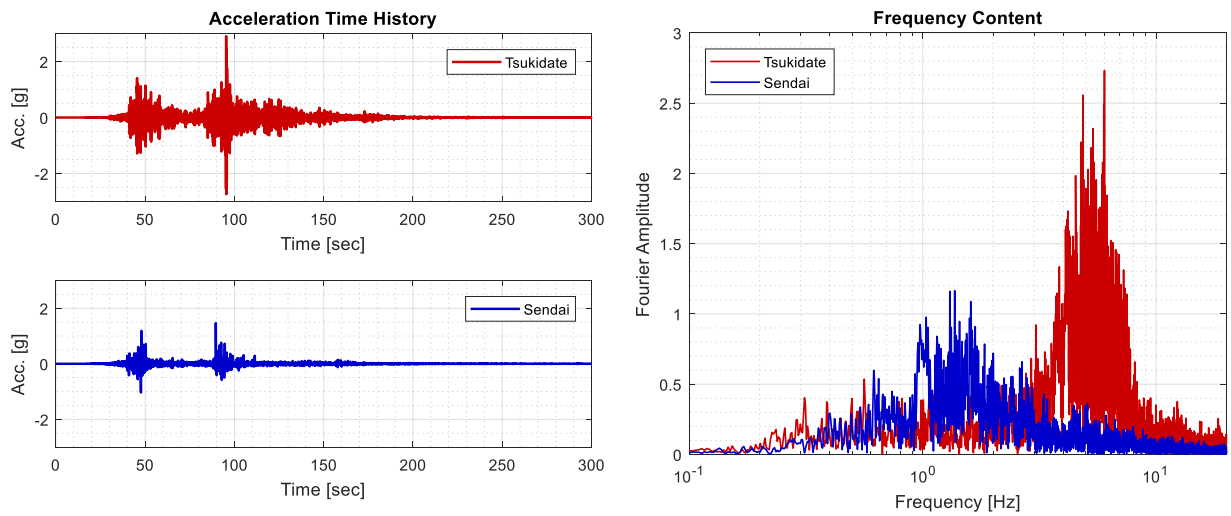


Figure 2-31: Comparison of time histories at Tsukidate (red) and Sendai (blue).

Figure 2-32: Comparison of frequency contents at Tsukidate (red) and Sendai (blue).

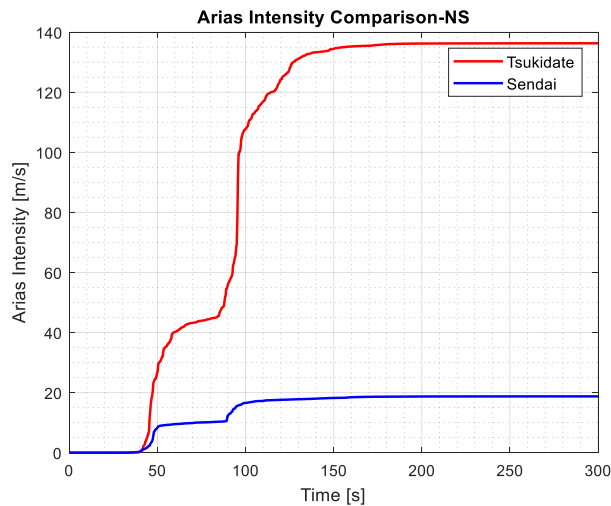


Figure 2-33: Comparison of Arias intensities at Tsukidate (red) and Sendai (blue).

Soil profiles for the station at Tsukidate and Sendai are shown in Figure 2-34 and Figure 2-35 respectively (NIED). The soil profile at Tsukidate shows alternating of sandy soil and silt layers up to 10 m of depth, while from 10 to 20 m deep the sandy soil is alternated with gravelly soil. On the other hand, the site conditions at Sendai are represented by a thin layer of clay within the first 1.5 m of depth, followed by about 4-meter-thick layer of silt. At the depth of 5 m the profile shows a very deep (about 9-meter-thick) layer of gravelly soil and then at the depth of 14 m reaches rock.

The mean shear wave velocity over the top 20 m, $V_{s,20}$, was calculated based on the borehole data from the NIED website (http://www.kyoshin.bosai.go.jp/kyoshin/db/index_en.html?all). At the station of Tsukidate, the $V_{s,20}$ is 252 m/sec, while it is 333 m/sec at Sendai. The difference in average shear wave velocities over the 20 m depth of the holes are not significant enough to have a major impact on site response.

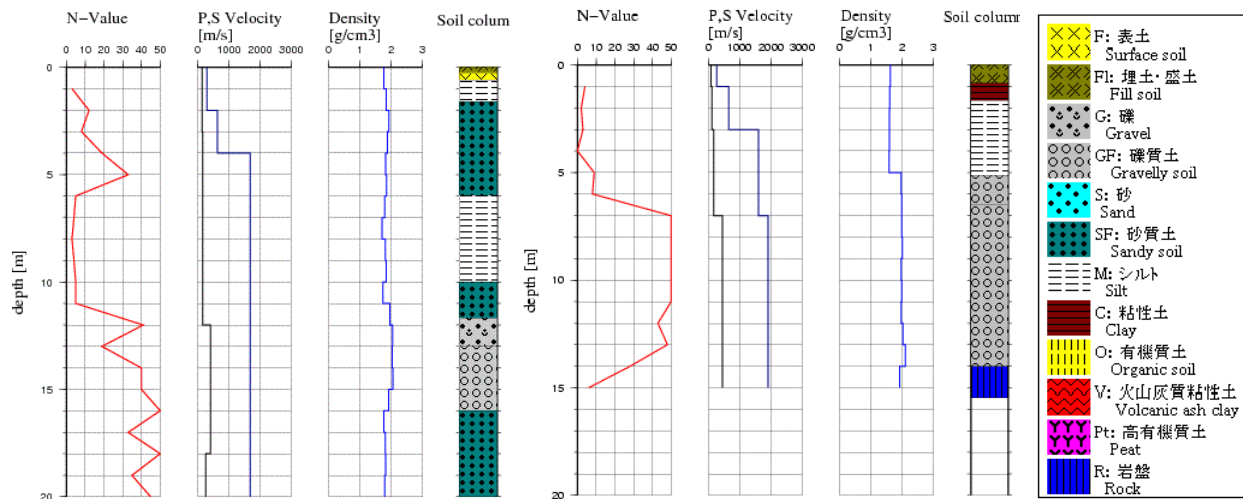


Figure 2-34: Soil profile at MYG004 - Tsukidate station (NIED). Figure 2-35: Soil profile at MYG013 - Sendai station (NIED).

2.3.3 Elastic response spectra analysis

Next, the relevance of the elastic response spectrum as an index of damage potential is investigated. This is a logical step because the elastic spectrum is commonly used as the basis for design in current building code provisions. Elastic response spectra for pseudo acceleration (PSA), pseudo velocity (PSV) and spectral displacements have been calculated and plotted for both sites as showed respectively in Figure 2-36, Figure 2-37 and Figure 2-38.

The motion recorded in Tsukidate is associated with a spectral shape featuring a very sharp spike at 0.24 sec in the acceleration response spectrum with the maximum response reaching 13 g and much lower amplitudes at other spectral periods. The high peak ground acceleration of about 3 g recorded in Tsukidate resulted from a single pulse with high frequency components. There is very little impulse associated with the spike and therefore is not capable of driving the system to significant displacements. This was very evident in the subsequent dynamic analysis presented below where the responses reversed very quickly and the displacements were quite insignificant. On the other hand, the spectrum associated to the motion recorded in Sendai shows significantly lower amplitudes but features a broader spectral shape. It should be noted that, although much less than the peak spectral acceleration at Tsukidate, these amplitudes are still significant at about 1.7 g over a fairly broader period range from 0.1 to 5.0 sec. These motions have the capacity of generating higher elastic displacements demands as shown in Figure 2-38.

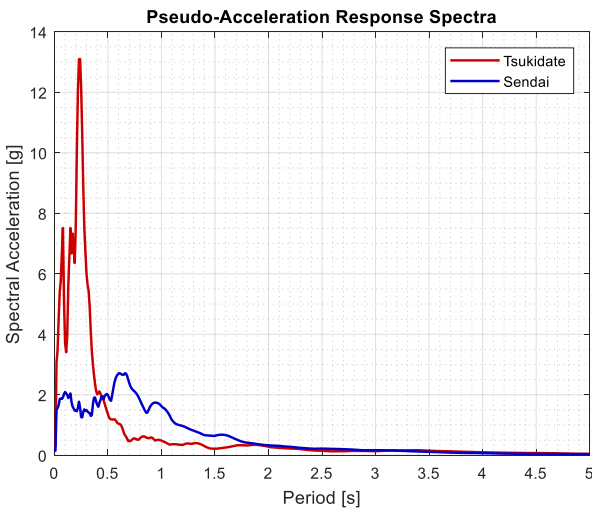


Figure 2-36: Elastic pseudo-acceleration response spectra for Tsukidate and Sendai ($\xi = 5\%$).

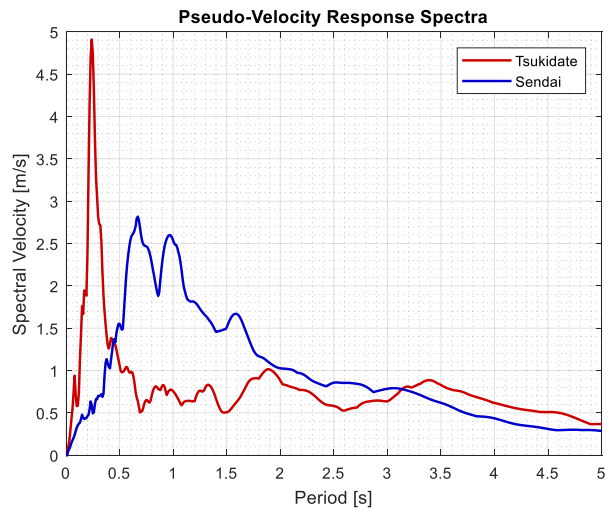


Figure 2-37: Elastic pseudo-velocity response spectra for Tsukidate and Sendai ($\xi = 5\%$).

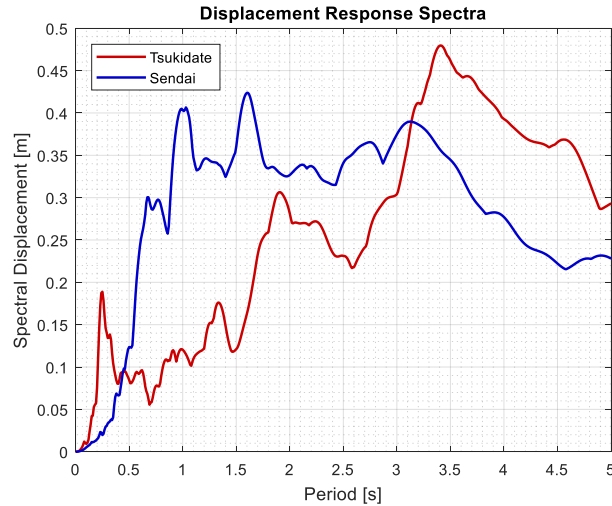


Figure 2-38: Elastic displacement response spectra for Tsukidate and Sendai ($\xi = 5\%$).

The difference in velocity and displacement spectra supports the greater damage observed at Sendai. This is particularly evident in the period range of 0.4 to 2 sec (Figure 2-37), where the Sendai velocity and displacement spectra are much greater than the Tsukidate spectrum and therefore imparts greater energy to the system. This is supported by the post-earthquake field observations which reported significant damage in low and intermediate period buildings in the Sendai area. A similar observation can be made about the elastic displacement response. As shown in Figure 2-38 the motion at Sendai generates higher displacement demands than at Tsukidate in a period range from 0.5 to 3 sec.

Elastic response spectra have been generated isolating the contribution of the first and second clusters of seismic waves (hereafter named pulses) in both Tsukidate and Sendai records. For each record, the first pulse was isolated by extracting the first 75 seconds of the acceleration time history and the remaining part of the motion is the second pulse. Zeros were added at the end/beginning of the cropped records and the response spectra were calculated for each pulse independently and plotted for comparison. Figure 2-39 and Figure 2-40 shows the acceleration spectra for Tsukidate and Sendai respectively. Similarly, Figure 2-41 and Figure 2-42 describe the velocity response spectra, while the displacement spectra are given in Figure 2-43 and Figure 2-44. All the response spectra have been generated for 5 % damping ($\xi = 5\%$). In the Figures, a darker color is assigned to the spectrum calculated with the first pulse, while a lighter color is associated with the contribution of the second pulse (dark red and light red are assigned to Tsukidate, dark blue and

light blue to Sendai). The scattered spectrum represented by gray dots represents the response spectrum considering the whole record.

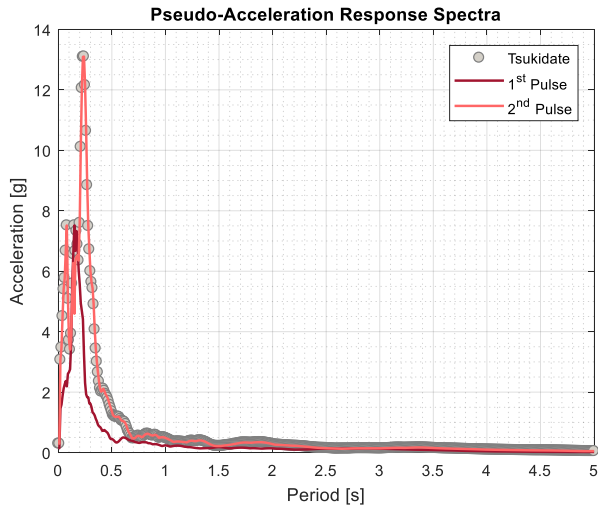


Figure 2-39: Comparison between acceleration response spectra of the isolated pulses in Tsukidate ($\xi = 5\%$).

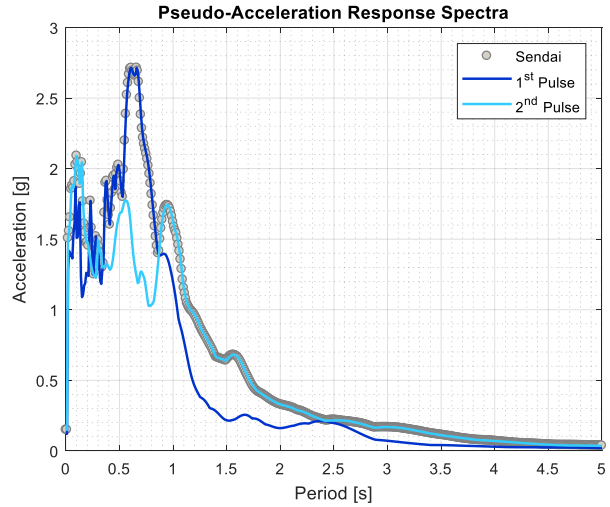


Figure 2-40: Comparison between acceleration response spectra of the isolated pulses in Sendai ($\xi = 5\%$).

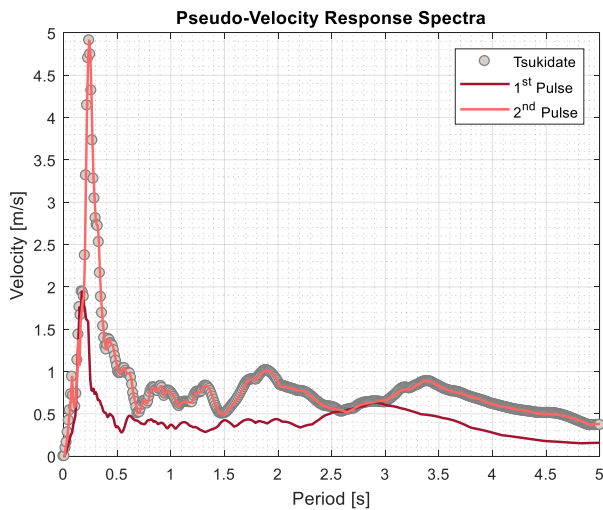


Figure 2-41: Comparison between velocity response spectra of the isolated pulses in Tsukidate ($\xi = 5\%$).

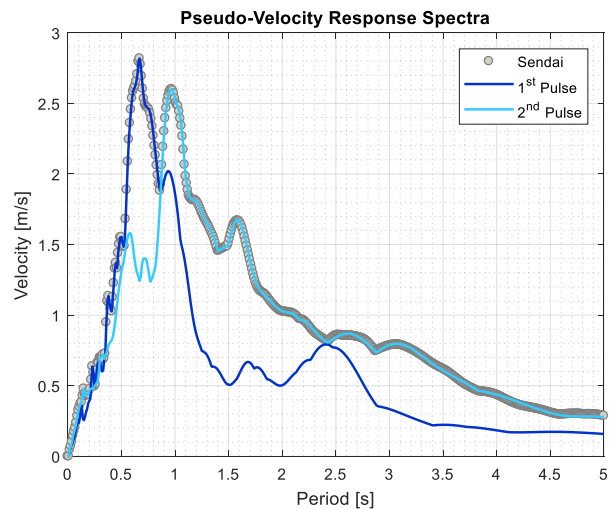


Figure 2-42: Comparison between velocity response spectra of the isolated pulses in Sendai ($\xi = 5\%$).

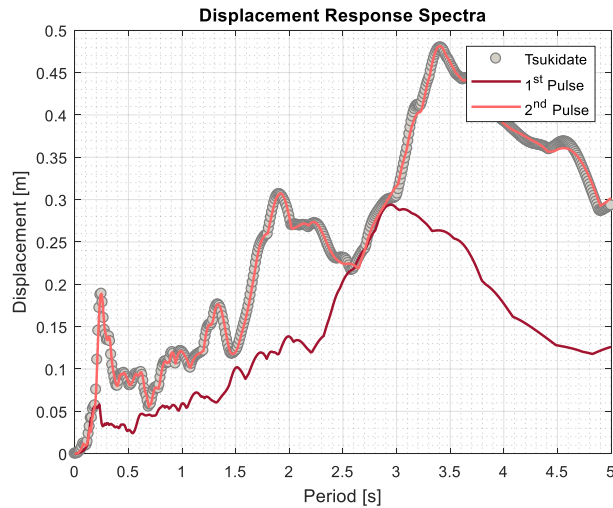


Figure 2-43: Comparison between displacement response spectra of the isolated pulses in Tsukidate ($\xi = 5\%$).

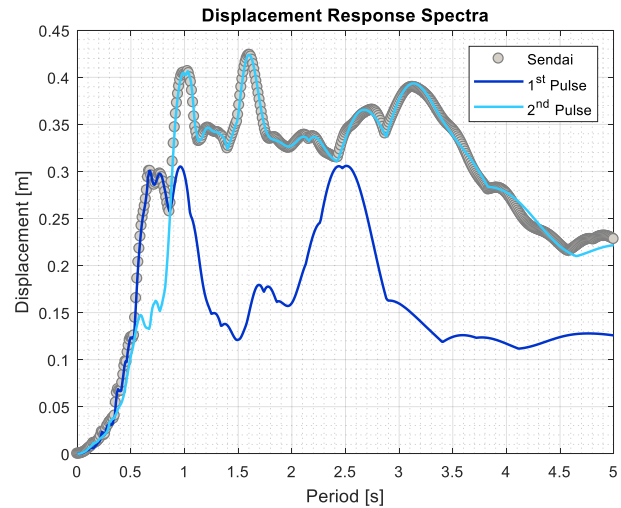


Figure 2-44: Comparison between displacement response spectra of the isolated pulses in Sendai ($\xi = 5\%$).

The spectra generated at Sendai shows how both the first and second pulses contribute to the overall response spectrum (Figure 2-40, Figure 2-42, Figure 2-44). On the other hand, the analysis of the Tsukidate response spectra (Figure 2-39, Figure 2-41, Figure 2-43) shows how the second pulse (light red color) dominates the response and that the seismic information of the first pulse is not significant when calculating the overall response spectrum. This holds also for the acceleration, velocity and displacement spectra. This observation leads to the conclusion that a hypothetical ground motion featuring a time history given by the second pulse only, would result in the same response spectra as the complete 300 sec long motion. This finding confirms again the observations previously made in Chapter 1: the elastic response spectrum does not reflect adequately the duration of the motion.

As previously mentioned in Section 1.2.2, past studies showed that elastic spectral demands (i.e.: $S_a(T_1)$, $S_d(T_1)$) do not correlate well with inelastic seismic responses.

As a consequence, researchers advanced alternative, vector-based intensity measures which include inelastic spectral demands (Luco et al., 2005). As reported, intensity measures which consider the effects of inelastic behaviour through the spectral shape were found to indicate the strongest correlation with structural damage (Fontara et al., 2012). For instance, Tothong and Cornell (2006) proposed the use of the inelastic spectral displacement S_{di} for better predicting

nonlinear structural response than commonly used parameters such as $S_a(T_1)$ and PGA. In particular, S_{di} was found to capture the effect of period elongation of inelastic systems and therefore better represent the record's spectral shape and to be preferred to $S_a(T_1)$ for structures dominated by a first mode response (Tothong & Luco, 2007). Later in 2007, Luco and Cornell (2007) further developed advanced intensity measures which reflected the contribution of both higher modes as well as nonlinear behavior.

As supported by the studies mentioned above, it is clear that inelastic intensity measures have significant advantages over indices based exclusively on elastic response. For this reason, the suitability of inelastic spectral displacement (S_{di}) to reflect structural damage, specifically through constant-ductility and constant-strength spectra, is investigated in the following Sections.

2.3.4 Constant ductility spectra analysis

The Constant ductility spectrum is a tool used to calculate the lateral resistance of a system to ensure that a target ductility is achieved in design (Scott & Mason, 2017). Constant Ductility spectra have been calculated for Tsukidate and Sendai using Bispec V2 computer program (Earthquake Solutions).

The Constant ductility spectra have been generated considering the Bilinear Plastic Model implemented in Bispec. The bilinear system is characterized by a linear behavior up to the yield limit and then exhibit a softer post-yield response, characterized by a hardening stiffness ratio (post-yielding stiffness/elastic stiffness) equal to 0.05. All the spectra have been obtained considering a damping ratio equal to 5%. Different levels of ductility (1.5, 2 and 3) were analyzed.

Figure 2-45 and Figure 2-46 show the constant ductility acceleration spectra for Tsukidate and Sendai respectively. The nonlinear spectra for the motions recorded in Tsukidate show how the spectral shape significantly changes for each level of ductility when considering a nonlinear system. This rapid decrease in spectral amplitudes is particularly significant in comparison with the very sharp peak at the period of 0.24 sec. A slight increase of ductility to 1.5, results in a decrease of about 60% in spectral amplitude, reaching a spectral acceleration of about 5 g, much less than the elastic spectral value of 13 g. This shows that even a small amount of inelastic behavior would reduce high intensity short period peaks to significantly lower values. As for the inelastic spectra generated with the Sendai record, the spectral ordinates decrease in amplitudes (up to 40%).

In general, it can be seen that the displacement demands of the Sendai motion are greater than the demands at Tsukidate for a period range from 0.4 to 3.3 sec, for the ductility capacities under consideration. Based on the results shown in Figure 2-47, it would seem that the constant ductility displacement spectra may be a useful tool for discriminating between the damage potential of the different earthquake records.

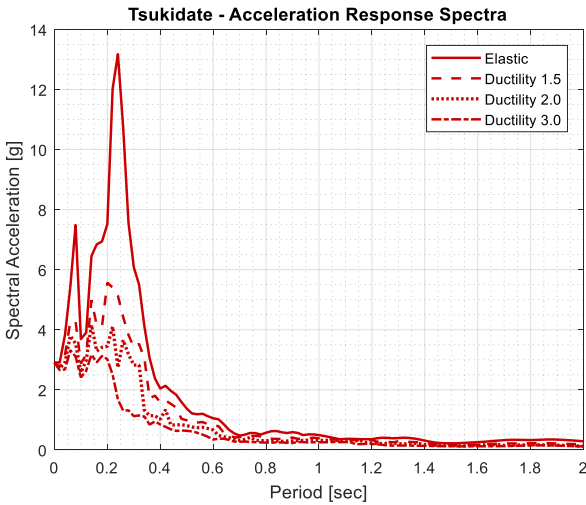


Figure 2-45: Constant ductility spectra for Tsukidate ($\xi = 5\%$).

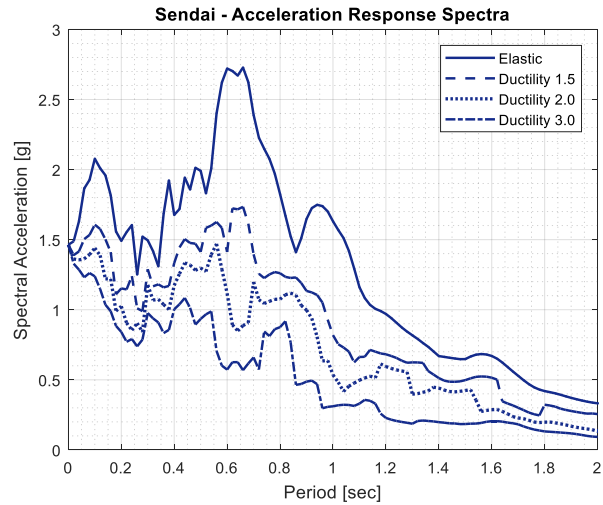


Figure 2-46: Constant ductility spectra for Sendai ($\xi = 5\%$).

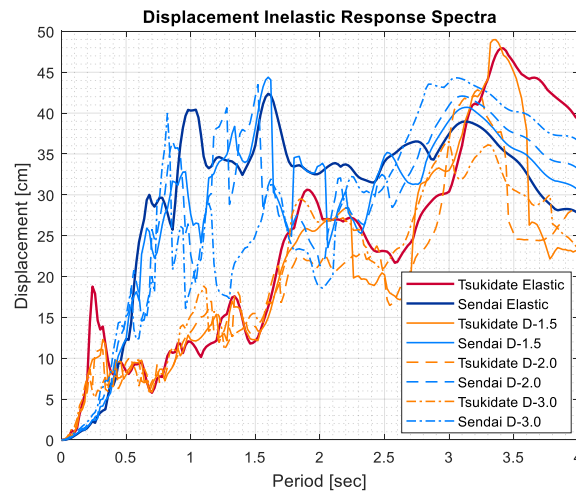


Figure 2-47: Comparison of constant ductility spectra for displacement response ($\xi = 5\%$).

The rapid decrease in spectral amplitudes at 0.24 sec period observed in the constant-ductility spectra generated with the motion in Tsukidate can be explained by considering the

inelastic spectra of a simple sinusoidal signal (Figure 2-48). The sinusoidal signal considered has an acceleration amplitude of 0.2 g and a period equal to 1.0 sec. The constant ductility spectra have been generated for acceleration, velocity and displacement and are shown in Figure 2-49, Figure 2-50 and Figure 2-51 respectively. The ductility values considered for analysis are 1.5, 2.0 and 3.0. The results of the analyses are compared with the elastic spectra in each Figure. For each of acceleration, velocity and displacement responses, it can be observed that when the structural period is in resonance with the period of the signal, a similar drop in amplitude occurs for three ductility levels. For instance, when the ductility capacity of the system is 1.5, the inelastic acceleration amplitude at resonance decreases to about 25% of the elastic response. Similar behavior is also shown in the velocity and displacement spectra. This trend is clearly reflected in the constant-ductility spectra presented in Figure 2-45, confirming what previously observed in the Fourier spectrum: the record at Tsukidate is characterized by the repetition of loading cycles of period about 0.2 sec.

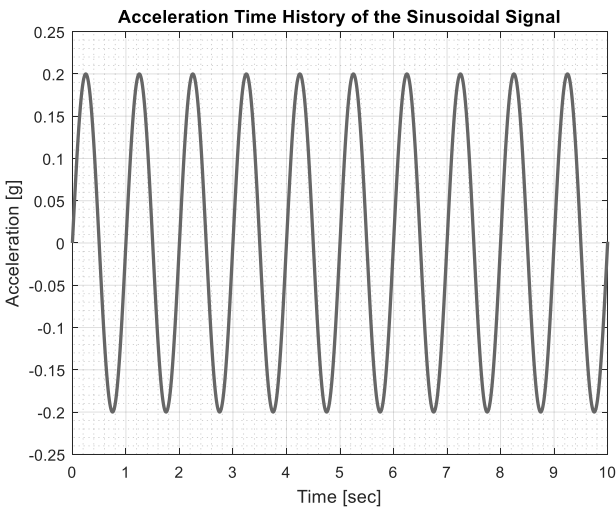


Figure 2-48: Acceleration time history of a simple sinusoidal signal.

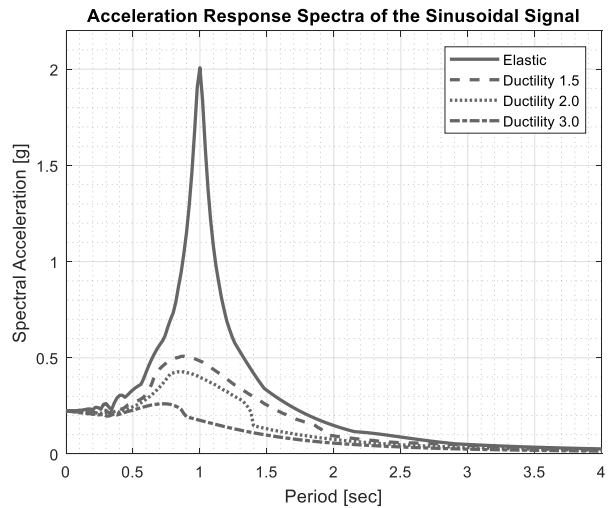


Figure 2-49: Acceleration response spectra of the sinusoidal signal for different ductilities ($\xi = 5\%$).

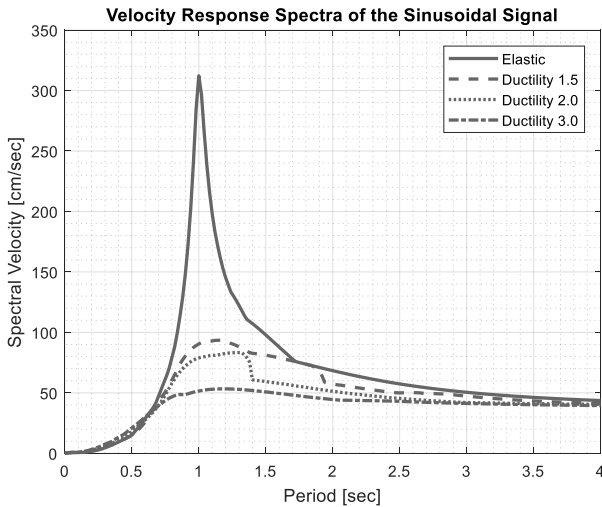


Figure 2-50: Velocity response spectra of the sinusoidal signal for different ductilities ($\xi = 5\%$).

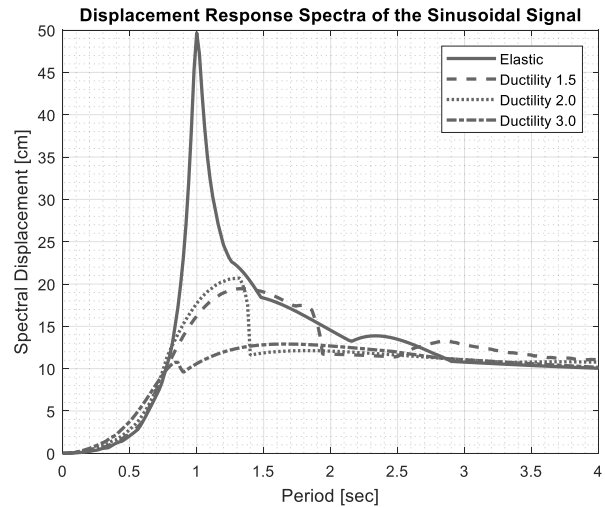


Figure 2-51: Displacement response spectra of the sinusoidal signal for different ductilities ($\xi = 5\%$).

2.3.5 Insight from nonlinear response

A number of nonlinear time history analyses were performed using the Bispec V2 computer program (Earthquake Solutions). The structural models were represented by SDOF systems with fundamental periods of 0.2 and 1.0 sec to represent short and intermediate period structures.

The material models selected for analyses were the Bilinear and Clough models (Earthquake Solutions) with no limitation on the ductility capacity. A description of the Bilinear model was given in Section 2.3.4. The Clough model, referred as Clough Bilinear Stiffness Degrading Model in Bispec, is a hysteretic model that exhibits a degraded stiffness during unloading which is dependent on the current state of the model and on the largest displacement previously reach in each direction. This stiffness change occurs when the system force crosses the zero force line (Earthquake Solutions; Clough, 1966). As in the case for the constant ductility spectra, the hardening stiffness ratio consider for analysis was 0.05. The damping ratio ξ was equal to 5%.

The input motions were the recorded Tsukidate and Sendai records. For each analysis, displacement response time history, yielding events time history and force-displacement hysteretic loops were plotted for comparison. Results of these analyses are presented in Figure 2-52 to Figure 2-59. The results at Tsukidate are shown in red, while Sendai results are shown in blue.

For a short period structure (0.2 sec) represented by a Bilinear model, the number of yielding events generated by the motion at Tsukidate (Figure 2-52) is much higher than at Sendai (Figure 2-52). On the other hand, the maximum displacement response associated with Tsukidate record

(Figure 2-53) is lower than the one in Sendai (Figure 2-53). The analysis of an intermediate period structure (1.0 sec) using the same material model results in more yielding episodes in Sendai (Figure 2-54) and the displacements are higher (Figure 2-55). It seems clear that the motion at Tsukidate, even though it generates more yielding events at short periods, does not push the system as far into the inelastic range as the motion recorded at Sendai. Similar results were found using a nonlinear Clough-type material model (Figure 2-56 to Figure 2-59), with the exception that at short period (0.2 sec), the motion at Sendai generates not only larger deformations, but also a greater number of yielding cycles than at Tsukidate (Figure 2-56 and 2-57).

Nonlinear analysis allows the evaluation of the nonlinear displacement demands that a particular structural system is expected to withstand during an earthquake. Therefore, nonlinear analysis can give some useful insights into damage potential.

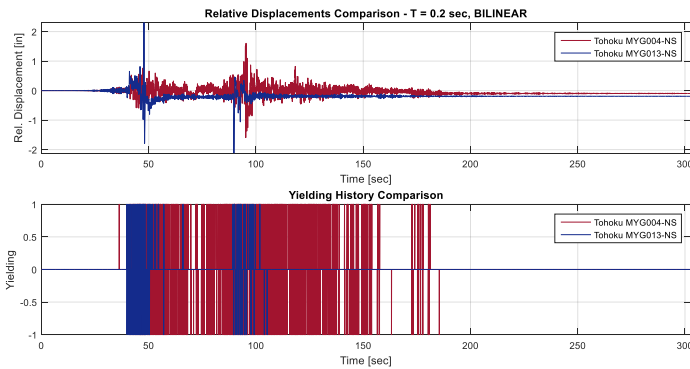


Figure 2-52: Acceleration and yielding time history for Bilinear SDOF at 0.2 sec (Tsukidate in red, Sendai in blue).

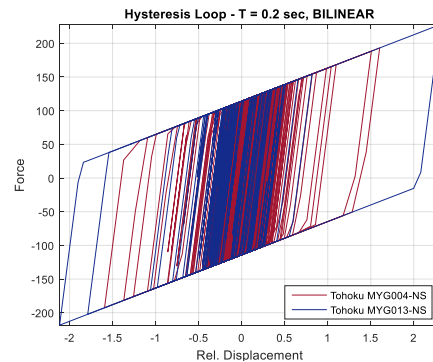


Figure 2-53: Hysteresis loop for Bilinear SDOF at 0.2 sec (Tsukidate in red, Sendai in blue).

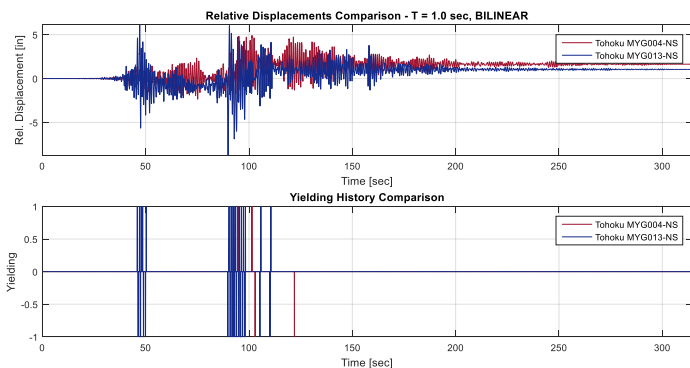


Figure 2-54: Acceleration and yielding time history for Bilinear SDOF at 1.0 sec (Tsukidate in red, Sendai in blue).

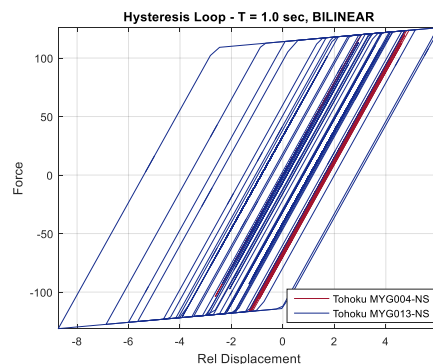


Figure 2-55: Hysteresis loop for Bilinear SDOF at 1.0 sec (Tsukidate in red, Sendai in blue).

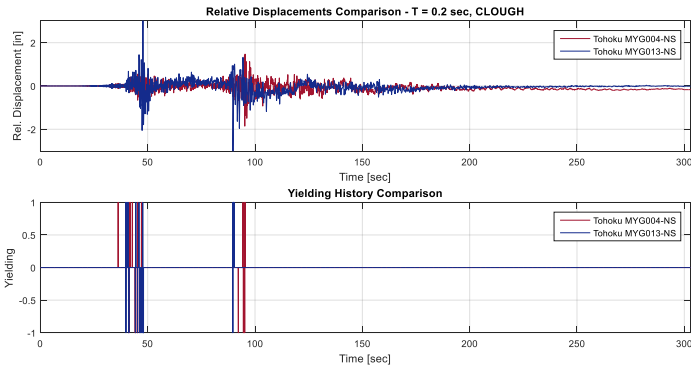


Figure 2-56: Acceleration and yielding time history for Clough SDOF at 0.2 sec (Tsukidate in red, Sendai in blue).

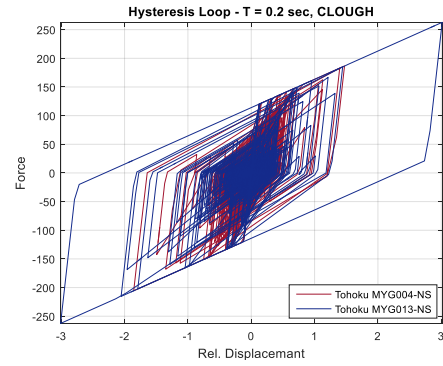


Figure 2-57: Hysteresis loop for Clough SDOF at 0.2 sec (Tsukidate in red, Sendai in blue).

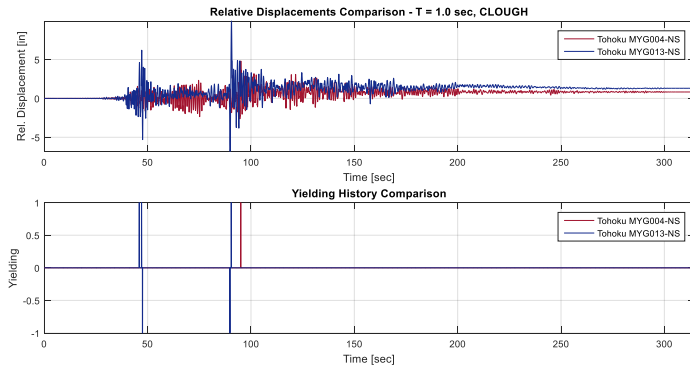


Figure 2-58: Acceleration and yielding time history for Clough SDOF at 1.0 sec (Tsukidate in red, Sendai in blue).

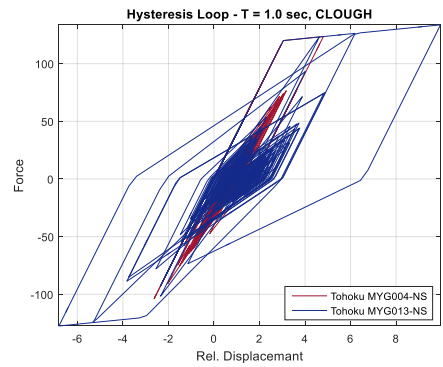


Figure 2-59: Hysteresis loop for Clough SDOF at 1.0 sec (Tsukidate in red, Sendai in blue).

2.3.6 Constant strength spectra analysis

Constant strength spectra have been generated with Bispec V2 for both records. This type of spectrum considers a system with constant strength regardless its natural period. In this case, the constant strength has been represented with the coefficient C_y , which can be defined as a normalized yield capacity, F_y , defined by:

$$C_y = \frac{F_y}{W} \quad (2-1)$$

where W is the weight of the building.

Two values of C_y , 0.1 and 0.3, were considered for analyses using both the Bilinear and the Clough hysteretic models. $C_y = 0.1$ is representative of low strength system, while $C_y = 0.3$ is associated with a conventionally designed system. The results for C_y equal to 0.1 and 0.3 for the Bilinear model are shown in Figure 2-60 and corresponding results for the Clough model in Figure 2-62. The constant strength spectra obtained with the motion at Tsukidate are shown in red, while the spectra generated at Sendai are shown in blue. The bold black dashed lines in Figure 2-60 and Figure 2-62 represent the threshold between elastic and inelastic behavior.

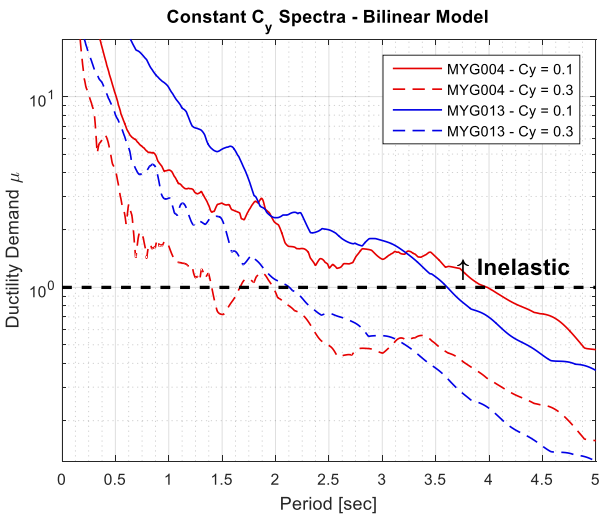


Figure 2-60: Constant strength spectra for Tsukidate (red) and Sendai (blue) for a Bilinear system.

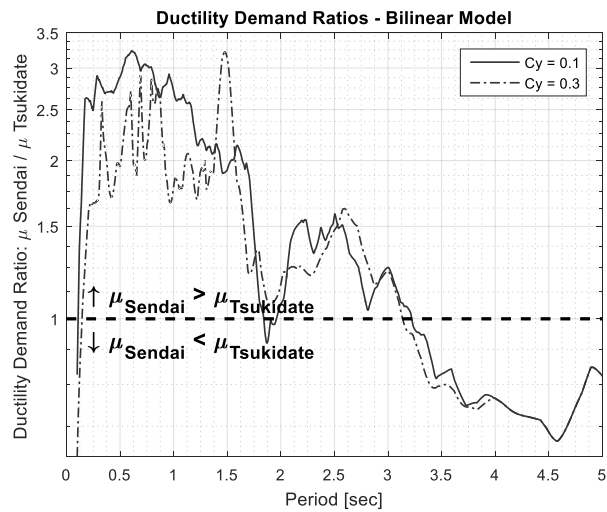


Figure 2-61: Spectral ratios for ductility demands for a Bilinear system.

These constant strength spectra give an indication of nonlinear ductility demands, which are directly related to the damage caused by the motions. The ductility demands imposed by the Sendai motion are consistently higher than the Tsukidate demands in the period range 0-3 sec. This means that the structural systems in this period range will be led further into the inelastic range in Sendai than in Tsukidate, provided that it has enough ductility capacity. This, in turn, implies that the structures in Sendai will experience more damage than those in Tsukidate. The conclusion holds for both the Bilinear and Clough material models and the different C_y levels. The only exception occurs at periods between 3.2 and 4.0 seconds, where the ductility demand in Tsukidate is slightly higher than the one in Sendai. However, both show ductility values lower than 2, suggesting a structural behavior close to linear elastic.

A building with fundamental period equal to 1 sec and a C_y factor equal to 0.3, is going to slightly exceed the elastic limit (ductility demand about 1.8) when subjected to the Tsukidate motion, while the ductility demand generated by the Sendai record is about 3. A building with the very same fundamental period but designed with a lower strength capacity ($C_y = 0.1$) is going to be pushed further into the inelastic range: the ductility demand at Tsukidate is about 4, while the motion in Sendai requires the structure to develop significant ductility (up to 10).

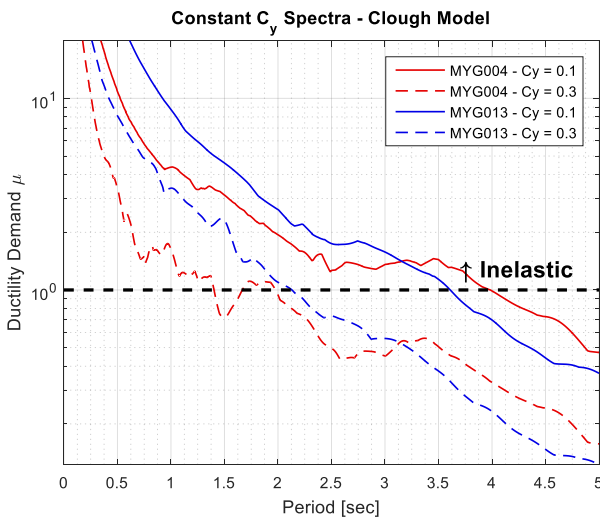


Figure 2-62: Constant strength spectra for Tsukidate (red) and Sendai (blue) for a Clough system.

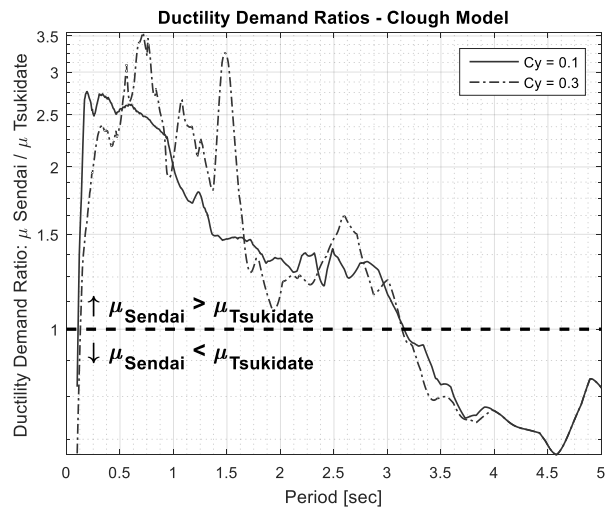


Figure 2-63: Spectral ratios for ductility demands for a Clough system.

The constant strength spectra can be interpreted also in terms of variation in the ductility demands with respect to different strength levels. As an example, let us consider Figure 2-60. The ductility demands generated by the Tsukidate motion are represented by a red solid line for weak systems ($C_y = 0.1$) and by a red dashed line for conventionally designed systems ($C_y = 0.3$). Comparing the values along the vertical ordinate, it can be inferred that weaker systems ($C_y = 0.1$) have greater displacement demands compared to stronger systems ($C_y = 0.3$). The plot also shows how for weaker systems a broader part of the spectrum (i.e. a wider range of structures) is expected to develop inelastic deformations in comparison to a stronger system. This is quite understandable, as a weaker structural system would be expected to suffer greater deformations to withstand the energy imparted by the motion in comparison to the very same motion exciting a stronger system.

Figure 2-61 and Figure 2-63 give the spectral ratios of the ductility demand at Sendai to the one at Tsukidate. Therefore, these plots provide information on the relative damage potential of the two records in terms of ductility demands. The plot in Figure 2-61 confirms how the ductility demands and hence the damage to the bilinear system, are greater in Sendai than Tsukidate up to a period of 3.0 sec. In particular, in the low and intermediate period range (from 0.2 to 1.5 sec), the ductility demands at Sendai reach values up to three times higher than the ones at Tsukidate.

This finding is validated by the post-earthquake observations that the buildings that experienced damaged by the earthquake shaking in Sendai had periods in the range 0.2 to 3 sec. The relative difference of the ductility demands at the two sites decreases for period range between 1.5 and 3.2 sec, where the displacement demands in Sendai are still higher than the ones in Tsukidate, but with less significant relative difference (about 1.5 times greater). These observations also hold for the Clough material model, as shown in Figure 2-63.

2.4. Ductility demands for other Tohoku ground motions

It was considered of interest to compare the demands of Sendai with the demands of the motions linearly scaled to the Victoria (BC) UHS, as it is a location prone to subduction earthquakes. Therefore, the scaled and unscaled subduction ground motions selected in Chapter 3, were used to develop constant-strength spectra. The analyses were run for three different C_y values, specifically $C_y = 0.1, 0.2, 0.3$ representing systems with different strength capacities for the bilinear model. The ductility demands were calculated for both unscaled and scaled subduction motions. Figure 2-64 and 2-65 show the results for C_y equal to 0.1. In these plots the blue line refers to the ductility demands at *Sendai* for the unscaled motion, while the red line shows the unscaled demands at *Tsukidate*. The grey lines show the ductility demands of the individual unscaled (Figure 2-64) and scaled subduction motions (Figure 2-65). The dashed black line represents the elastic limit.

The ductility demands of the unscaled subduction motions (Figure 2-64) are found to be lower than the demands at both Tsukidate and Sendai. When the subduction motions are scaled to the Victoria UHS (Figure 2-65), the ductility demands are significantly higher than the ones generated by the unscaled motions. In the period range between 0.3 and 1 sec, the demands of the subduction suite fall between the ones at Tsukidate and Sendai. For structural periods between 1 and 2 sec, the constant C_y spectra lead to demands compatible to the ones at Sendai, while for

periods above 2 sec, the demands of the subduction suite of motions are higher than the ones in Sendai. The process of ground motions scaling clearly increased the damage potential of the subduction suite of unscaled motions. It can also be observed that the ductility demands at a specific structural period cover a wider range of values for scaled records than for the unscaled motions. For instance, at $T = 1.0$ sec, ductility demands for the unscaled suite of motions varies between 1.2 and 3.9, while for scaled motions, the ductility demand ranges from 6.4 to 10.9.

The analyses for the other C_y values are shown in Figure 2-66 and 2-67 ($C_y = 0.2$) and Figure 2-68 and 2-69 ($C_y = 0.3$) and confirm the observations made for $C_y = 0.1$.

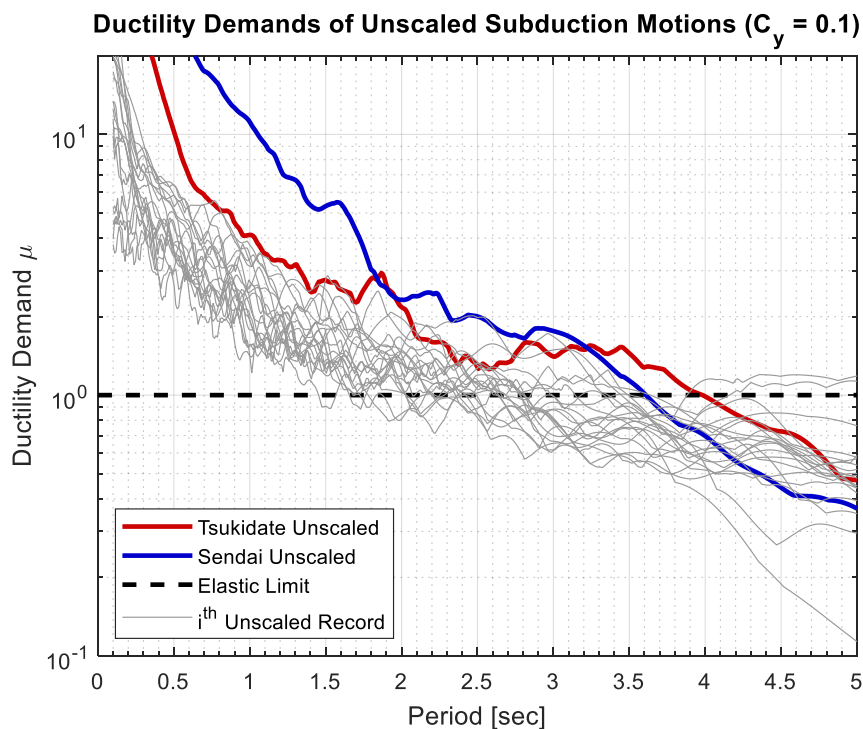


Figure 2-64: Ductility demands of unscaled Sendai and Tsukidate records and comparison with unscaled subduction motions ($C_y = 0.1$).

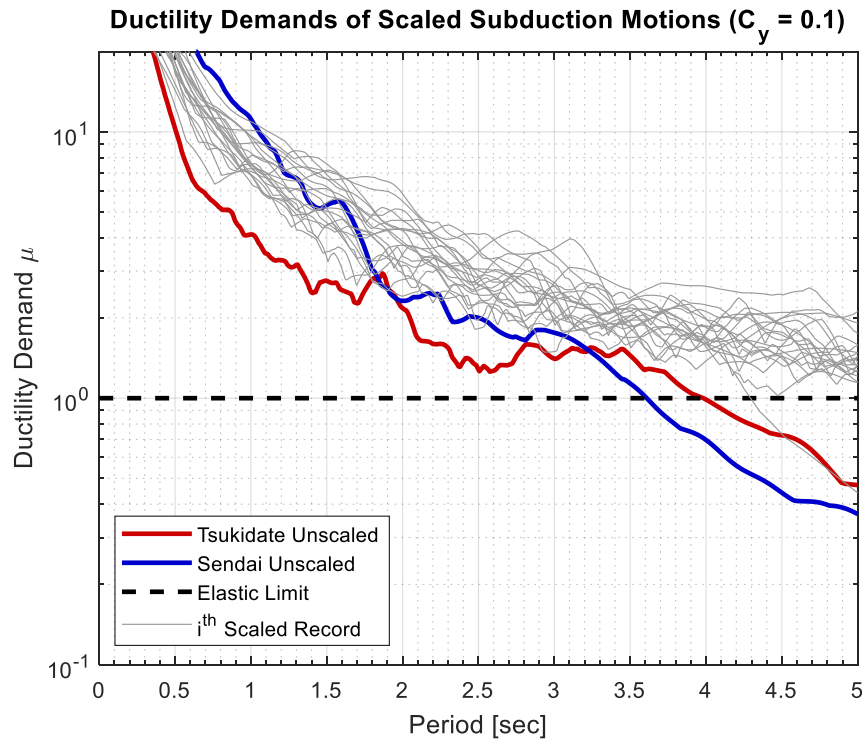


Figure 2-65: Ductility demands of unscaled Tsukidate and Sendai records and comparison with scaled subduction motions ($C_y = 0.1$).

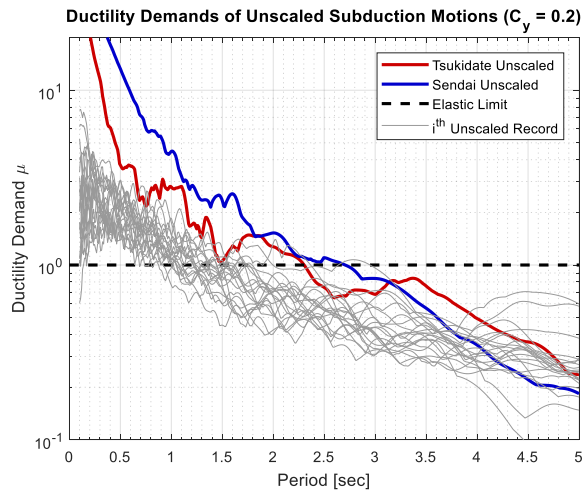


Figure 2-66: Ductility demands of unscaled Tsukidate and Sendai records and comparison with unscaled subduction motions ($C_y = 0.2$)

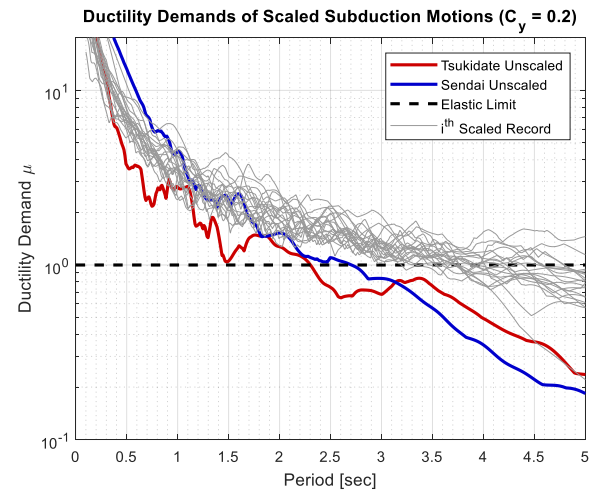


Figure 2-67: Ductility demands of unscaled Tsukidate and Sendai records and comparison with scaled subduction motions ($C_y = 0.2$).

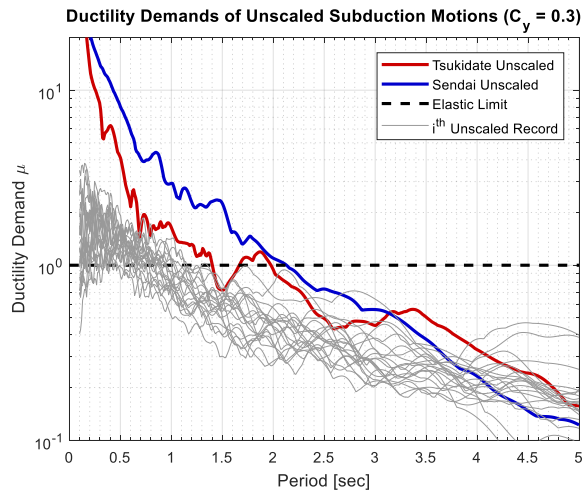


Figure 2-68: Ductility demands of unscaled Tsukidate and Sendai records and comparison with unscaled subduction motions ($C_y = 0.3$).

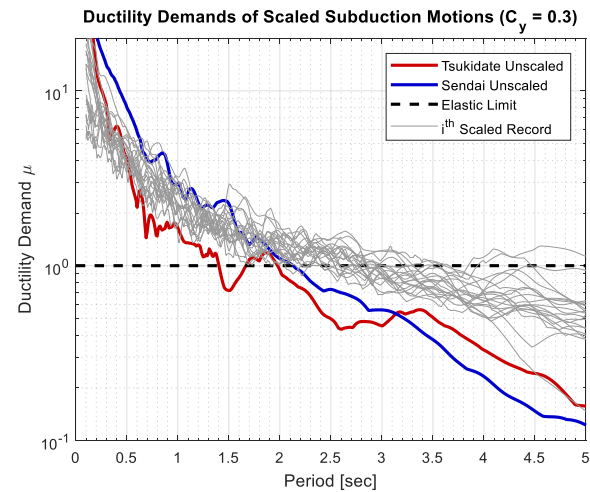


Figure 2-69: Ductility demands of unscaled Tsukidate and Sendai records and comparison with unscaled subduction motions ($C_y = 0.3$).

2.5. Discussion

This Chapter explores how different characteristics of the subduction ground motions affect the associated damage potential. The relationship between structural damage and associated shaking intensities was investigated for motions recorded during the 2010 Maule earthquake (Curico and Maipu stations) and the 2011 Tohoku earthquake (Tsukidate and Sendai station).

In particular, for the Tsukidate and Sendai sites, the study on the relationship between damage to shaking parameters was conducted in great detail. To this purpose, several characteristics have been considered for comparison. Peak responses such as PGA, PGV, SD and frequency contents were considered for comparison. These parameters did not fully explain the damage potential of the ground motions. Therefore, these indices have been shown not to be good measures for structural damage potential. This finding supports the conclusions presented by previous researchers on the suitability of peak ground motion parameters to reflect the damage potential of ground motions (Elenas, 2011; Cantagallo et al., 2012; Kadas & Yakut, 2014). In this study, the Arias intensity was found to be poorly related to the structural damage observed at the two stations. This finding is in contrast with the literature review, as past studies showed that Arias Intensity had an overall good correlation with the damage potential of the ground motions (Elenas, 2000; Elenas, 2001; Nanos et al., 2008). Moreover, contrarily to what demonstrated by previous studies (Elenas, 2000, Elenas et al., 2011; Kadas & Yakut, 2014), elastic response spectra and constant ductility spectra were generated for the two ground motions under consideration but they provided only limited information about the structural demands and the associated damage. In particular, the very sharp peak characterizing the elastic acceleration demands at Tsukidate is a poor indicator of damage because the mobilization of a small amount of ductility in the system drastically reduced the spectral demands.

It is through the implementation of constant strength spectra that the relative damage potential of the Tsukidate and Sendai ground motions can be explained more fully. These spectra provide the ductility demand imposed by a given ground motion on a variety of systems with different fundamental periods and for two specific constant strength conditions. The analysis of the constant strength spectra showed that the ductility demands (hence, deformation demands) at Sendai were consistently larger than at Tsukidate over a wide period range (0.15-3.2 sec). The most useful way of representing the relative ductility demands of the Sendai and Tsukidate motions is in terms of ductility demand ratios. The constant strength spectrum for $C_y = 0.3$ generated by

the ground motion recorded at Sendai led to higher demands than the spectrum generated by the record at Tsukidate in the period range from 0 to approximately 3.0 seconds. The ductility demand ratios are significantly higher in the period range of 0 to 1.5 sec. This observation holds for each fundamental period and for the different constant strength levels considered.

Based on the two case studies presented in this Chapter, the suitability of the considered parameters to represent a good (or poor) indicator for damage potential of subduction ground motions is summarized in Table 2-3.

Table 2-3: Summary of the suitability of the considered parameters as indicators for damage potential of subduction earthquakes.

Parameter	Poor	Good	Comments
PGA	✓		
PGV	✓		
PGD	✓		
Frequency content	✓		
Arias Intensity			Inconsistent results
D ₅₋₉₅	✓		
Elastic acc. spectrum	✓		
Elastic vel. spectrum	✓		
Elastic displ. spectrum	✓		
Acc. constant- μ spectrum	✓		
Vel. constant- μ spectrum	✓		
Displ. constant- μ spectrum		✓	
Nonlinear time history analysis		✓	
Constant-C_y spectrum		✓	

As the data used for analysis is limited to two cases, it is not possible to generalize the findings of this Chapter. However, these findings provide a comparison between field observations and ground motion parameters commonly used in civil engineering practice. Therefore, the study offers an insight on the evaluation of damage potential of subduction ground motion records and also shows that nonlinear displacement spectra for constant strength is a reliable indicator of damage potential.

The ductility demands and damage potential of the ground motions used in the following chapters lie between the ductility demands of the ground motions at Tsukidate and Sendai at periods less than 1 sec, and above both Tsukidate and Sendai at periods greater than 1 sec.

Chapter 3

Selection and scaling of ground motions for Victoria, British Columbia

“There are no rules here – we are trying to accomplish something.”

Thomas Edison (1847 – 1931)

3.1. Introduction

This Chapter describes the process of selecting and scaling the ground motions to be used to perform the time history analyses required to establish the effect of long duration time histories on structural response. Victoria BC has been chosen as the location of interest because Victoria is the major city closest to the Cascadia Subduction Zone which can generate earthquakes with magnitudes up to M_w 9. A brief introduction to the seismicity at the site of interest is provided in Section 3.2.

Two suites of ground motions records have been selected in this study to represent short duration crustal and long duration subduction motions respectively. As described in Chapter 1, the evaluation of the effects of duration of shaking by subduction ground motions is based on the concept of compatible long and short duration spectra as introduced by Chandramohan et al., according to which each subduction motion is paired with a crustal motion characterized by similar spectral shape (Chandramohan et al., 2015) as shown in Figure 3-1. The subduction motion has been linearly scaled to match the target UHS for Victoria, BC and the crustal motion has been then

linearly scaled to match the subduction scaled spectrum (Figure 3-2). A pseudo-static code design using these compatible spectral pairs would result in the same seismic demand for each spectrum. Thus, the effect of duration will show up only if a non-linear dynamic analysis is conducted using the ground motions underlying each spectrum. Details about the applied procedure for selecting and scaling of motions and a step-by-step application of the method are presented in Section 3.4, while a summary of the selected suites of motions is provided in Section 3.5.

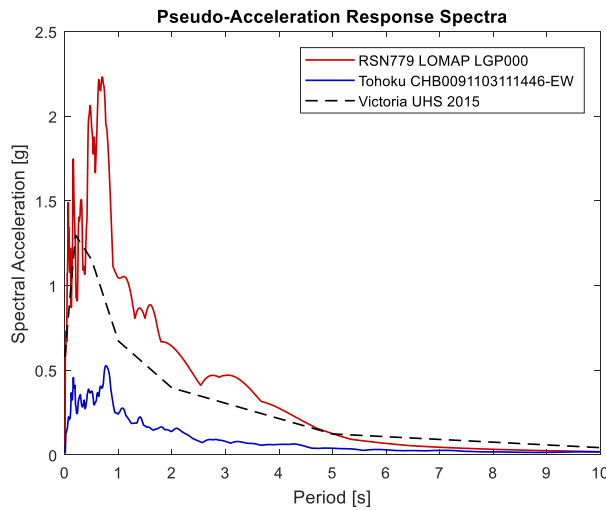


Figure 3-1: Example of unscaled crustal and subduction response spectra of paired ground motions.

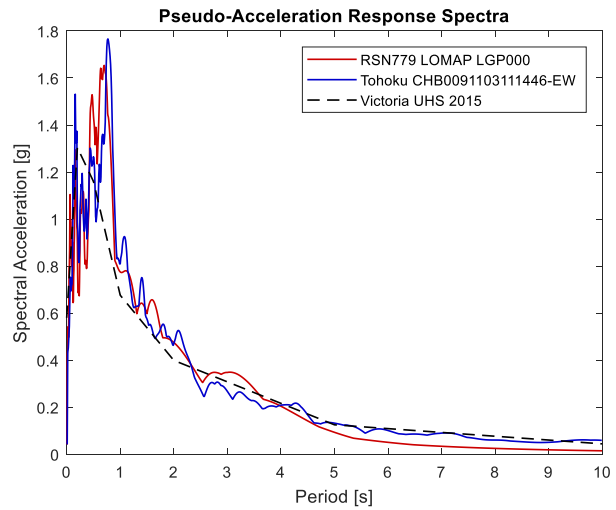


Figure 3-2: Example of scaled crustal and subduction response spectra of paired ground motions.

3.2. Seismic hazard in southwestern British Columbia

As a segment of the Pacific Ring of Fire and involving four tectonic plates and three different type of boundaries, the southwest of British Columbia is a region characterized by a unique tectonic environment. This area is one of the few of the world where all these three types of plate movements occur. Therefore, seismic hazard in British Columbia results from the combination of these three different seismic sources. Contribution to seismic hazard is given by shallow, crustal earthquakes, happening within the crust of the North American Plate; deep, subcrustal earthquakes (also called in-slab) triggered within the sinking Juan de Fuca Plate and subduction (interplate) earthquakes triggered at the interface between Juan de Fuca and the continental North American plate. Two smaller plates are subducting below the continental plate besides the Juan de Fuca: the Explorer Plate and the Gorda Plate (Clague, 1997, Atkinson & Boore, 2003, Oppenheimer, et al.,

1993, Natural Resources Canada, 2011, The Cascadia Region Earthquake Workgroup, 2005). This area forms the so-called Cascadia Subduction Zone, a megathrust fault which stretches from Northern Vancouver Island to Cape Mendocino (California) for a length of approximately 1300 km. A plan view of the Cascadia subduction Zone is shown in Figure 3-3.

There is evidence that the Juan de Fuca and the North American Plate are currently locked together, causing the build-up of the strain in the crust (Murray & Lisowski, 2000). A cross section of the Cascadia subduction zone in the southwest region of Canada is given in Figure 3-4 and the interface between the oceanic and continental plate which is expected to trigger a magnitude M~9 earthquake, is highlighted in red (Natural Resources Canada, 2016, United States Geological Survey, 2017).

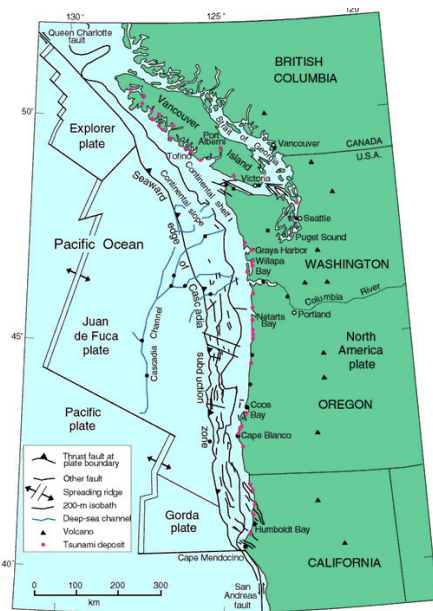


Figure 3-3: Tectonics of Pacific north-west.

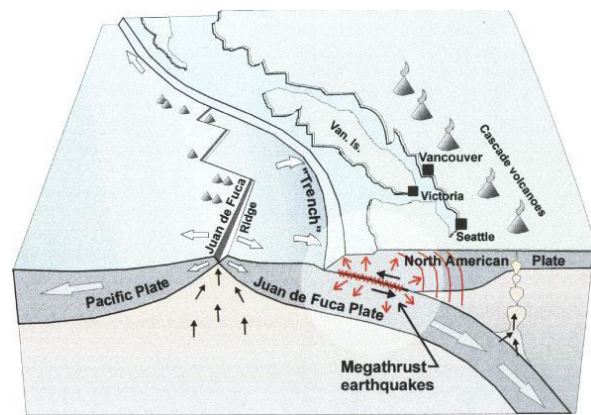


Figure 3-4: Cross-section of the tectonic setting of southwest British Columbia.

While many large subduction earthquakes have been historically documented or recorded in the regions such as Chile and Japan, no recent earthquake occurrence has been recorded in the Cascadia Subduction Zone. Thus, the Cascadia region is known to be the quietest of all Circum-Pacific subduction zones (Rong et al., 2014). Nevertheless, paleoseismological evidence, tree-ring dating and observations of sudden coastal subsidence and crustal uplift confirmed the occurrence of many major events in the past with an average recurrence interval of 550 years. Recent studies by Goldfinger (Goldfinger et al., 2017) revealed 4 additional events that have reduced the

recurrence interval to 430 years. The last major event has been dated to January 26th, 1700 on the basis of tsunami data from Japan. The observed wave heights were found to be compatible with a magnitude 9 event. Historical evidence of the 1700 Cascadia earthquake is also found in native American legends from northern California to British Columbia. Scientists support the idea that the earthquake ruptured the entire length of the Cascadia subduction zone. (Satake et al., 1996, Atwater B., 1987, and Satake & Atwater, 2007).

3.3. Consideration of subduction earthquakes in the Building Code

One of the major changes that followed the release of the NBCC 2015 regards the consideration of subduction ground motion in seismic design. In the 2015 version for the Building Code of Canada (NBCC, 2015), the contribution to the hazard from the subduction source is included in the probabilistic seismic hazard analysis along with crustal and subcrustal events (OPENFILE 7576, Halchuk et al., 2014).

The NBCC 2015 considers a probability of exceedance of 2% in 50 years (corresponding to a 2475-year return period), which is representative of “*rare events*”. This fully probabilistic model is referring to the use of mean hazard ground motions amplitudes in the determination of the target probability (Part 4 of Division B, 2015). As a result, the seismic hazard calculated with the NBCC 2015 resulted in much higher demands at sites close to the Cascadia Subduction Zone and this is why the study on long duration subduction ground motions is of utmost importance at sites in southwest of British Columbia.

The evaluation of seismic hazard in Canada is conducted by the Geological Survey of Canada (GSC). The OPENFILE 7576 report (Halchuk et al., 2014) describes the hazard model, provides technical files and look-up tables for the adopted Ground Motion Prediction Equations (GMPE) that produce the hazard values for the building and bridges codes in Canada.

In particular, for British Columbia, the OPENFILE 8090 report (Halchuk et al., 2016) provides the individual hazard contributions from the three seismic sources in the region (crustal, subcrustal, subduction) for different probability levels, allowing the construction of individual, scenario-specific UHS. Discussion about the GMPE used for seismic hazard assessment for each source and the adjustment of subcrustal and subduction GMPEs based on the Japanese data is provided in detail in the work done by Adams and Atkinson (Adams, 2011; Atkinson & Adams, 2013 and Ghofrani & Atkinson, 2013).

3.4. Selection and scaling of ground motions for time history analysis

The process of selection of ground motions and scaling to the UHS is outlined in this Section. The first step is the definition of a target spectrum which is specific for the site of interest and the considered hazard level. As standard practice in Canada¹, the spectrum chosen as target for selecting and scaling of strong ground motions is the 5% damped Uniform Hazard Spectrum (UHS) for a 2% in 50 years probability of exceedance. The site of interest is located in Victoria BC. The spectral accelerations are calculated based on hazard curves developed for an exceedance probability equal to 2% in 50 years, corresponding to a return period of 2475 years or, in other terms, an annual rate of exceedance equal to 1/2475. The site of interest is associated with soil conditions compatible with the code reference condition, Site Class C.

The spectral ordinates were obtained using the online Hazard Calculator on the Natural Resources Canada website http://www.earthquakescanada.nrcan.gc.ca/hazard-alea/interpolat/index_2015-en.php (Natural Resources Canada, 2016). Table 3-1 summarizes the acceleration values for a range in spectral periods. The period range targeted for selecting and scaling of ground motions covers structural periods between 0.1 sec to 4.0 sec. Figure 3-5 shows the UHS for Victoria and the green shaded region highlights the target period range chosen for scaling the motions.

¹ Although the UHS has been largely adopted as hazard standard, its suitability to serve as a base for selection and scaling of ground motions for time history analysis has been topic of discussion in recent research. For instance, Baker and Cornell (2006) and later Baker (2011) argue that it is questionable to use the UHS as a target spectrum for a single event as *'it conservatively implies that large-magnitude spectral values will occur at all periods within a single ground motion'*. To overcome this limitation, Baker (2011) proposed the Conditional Mean Spectrum (CMS) as a valid alternative for ground motion selection. The CMS gives the expected mean response spectrum conditioned on a target spectral acceleration value at the period of interest (Baker, 2011; Baker, 2015). Another option is the use the Conditional Spectrum (CS). Similarly to the CMS, the CS provides the expected response spectrum. Moreover, the CS accounts for the variability of the response spectra (Lin and Baker, 2015). Regardless of the difference of opinions on the use of UHS and the recent studies conducted by the GSC (Allen et al., 2015a; Allen et al., 2015b), the UHS is currently considered in the Canadian building code as the standard base for selecting and scaling ground motions.

Table 3-1: UHS Spectral acceleration values for Victoria, BC 2015 hazard calculations.

T [sec]	S _a (T) [g]
0.02	0.578
0.2	1.298
0.5	1.152
1.0	0.672
2.0	0.395
5.0	0.123
10	0.043

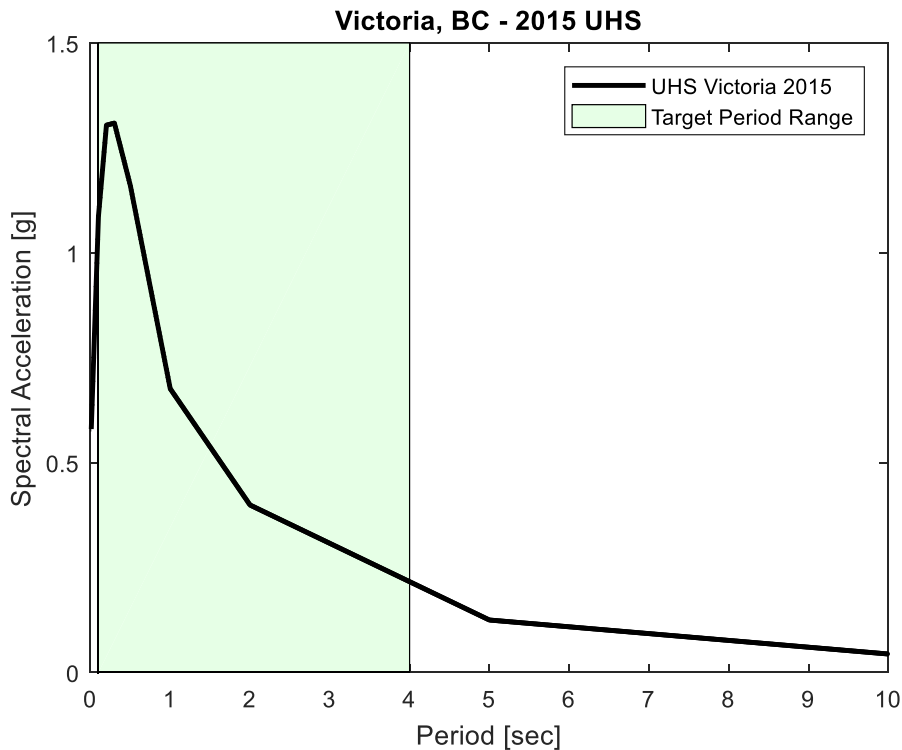


Figure 3-5: Design spectrum and target period range.

3.4.1 Selection and scaling of subduction ground motions

Long duration subduction ground motions have been selected via the S²GM Version 1.1 online database (Bebamzadeh et al., 2015). This database includes ground motions from 10 subduction events, for a total of 1161 recordings. Each horizontal component was selected independently and considering various ranges of magnitude. A first selection was conducted

considering a magnitude range between 7 and 9.5. The results showed a prevalence of records from the Japanese earthquakes of Hokkaido 2003 and Tohoku 2011. The search was repeated targeting a second magnitude range, between 8.1-8.5, to filter out the recordings from Hokkaido and Tohoku. The distance range for both searches was 50-500 km, while the interval for the average shear velocity was 120-700 m/sec. The longest usable period of each selected motion was checked to be equal or greater than the upper limit of the period range of interest. Table 3-2 summarizes the parameters considered during the process of selection and scaling of ground motions with details about the adopted scaling process.

Table 3-2: Summary of the parameters considered during selection and scaling of ground motion records.

Input parameters for selection and scaling of ground motions	
Magnitude, M_w	7 – 10; 8.1 – 8.5; 7 – 7.9
Epicentral distance [km]	50 – 500
Closest distance [km]	50 – 500
Average shear wave velocity, $V_{s,30}$ [m/sec]	120 – 700
Significant duration D_{5-95} [sec]	30 – 200
Spectral orientation	H1, H2
Max. number of records	15
Scaling method	MSE – Minimize the Square Error
Scale factor	0.5 – 4.0
Period range points [sec]	0.1 – 4.0
Weight of period points	1.0 (constant)
Period discretization	0.01

The selected records were linearly scaled to the UHS. The structural periods were assumed to be equally important, therefore the weight function was set constant and equal to 1. The periods were discretized using a 0.01 sec interval to improve the degree of fit as defined by the Mean Square Error (MSE).

MSE is evaluated as the weighted mean difference between the logarithmic values of the target response and the scaled record spectral amplitudes and it is considered therefore a

quantitative estimation of how well a time series conforms to the target spectrum. The MSE was calculated with the formula below (PEER, 2010):

$$MSE = \frac{\sum_i w(T_i) \{\ln[SA^{target}(T_i)] - \ln[f \times SA^{record}(T_i)]\}^2}{\sum_i w(T_i)} \quad (3-1)$$

where f is the linear scale factor applied to the motion response spectrum and $w(T_i)$ is the weight function, which assigns weights to different periods of the spectrum.

Linear scaling is accomplished by multiplying the spectrum by a scaling factor to match the target spectrum with minimum MSE. Such factor is defined in the equation below (PEER, 2010). Following the recommendations in the Commentary J (2015) of the NBCC, ground motions associated with scale factors below 0.5 or above 4 were neglected from the selection, as they do not adequately represent the magnitude and distance to the site.

$$\ln f = \frac{\sum_i w(T_i) \ln \left(\frac{SA^{target}(T_i)}{SA^{record}(T_i)} \right)}{\sum_i w(T_i)} \quad (3-2)$$

Figure 3-6 shows the pseudo acceleration (PSA) spectra of the unscaled subduction motions. The bold black line represents the 5% damped UHS for Victoria. It can be observed that the spectral amplitudes of the unscaled spectra fall below the target spectrum for the whole spectral period range. Figure 3-7 gives the acceleration spectra of the scaled records. The scaled spectra for each record is represented by grey lines, while the blue spectrum shows the mean spectral response. The target spectrum for Victoria BC is shown as a bold black line. A very good match was found between the mean spectrum and the UHS for structural periods above 0.5 sec, while the fit is not as good between mean response at periods shorter than 0.5 sec and the target spectrum.

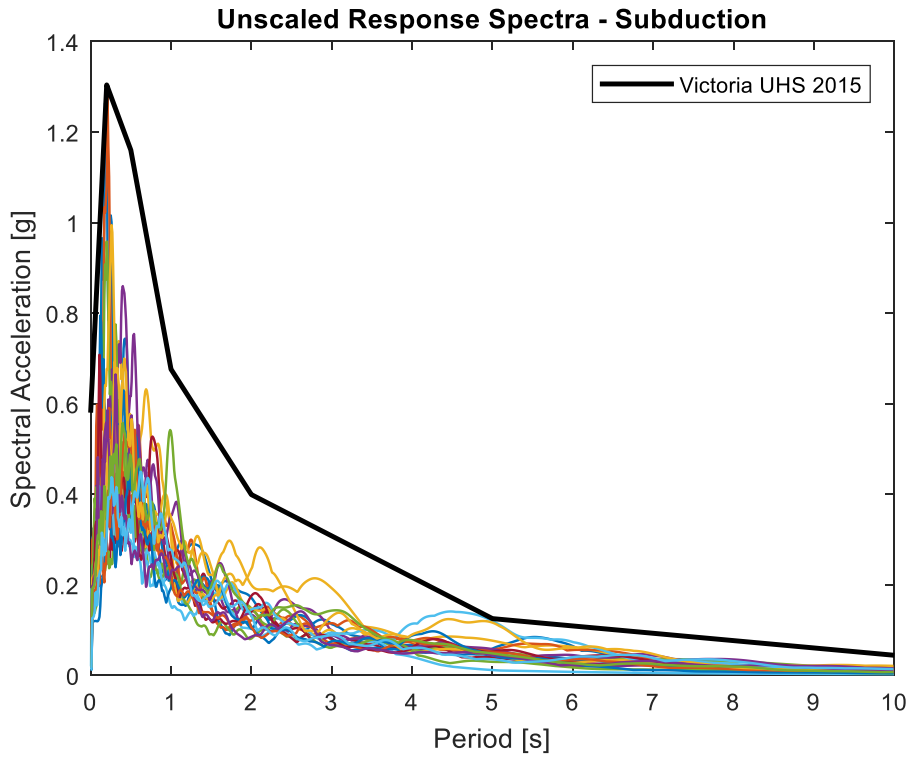


Figure 3-6: Response Spectra of unscaled subduction ground motions.

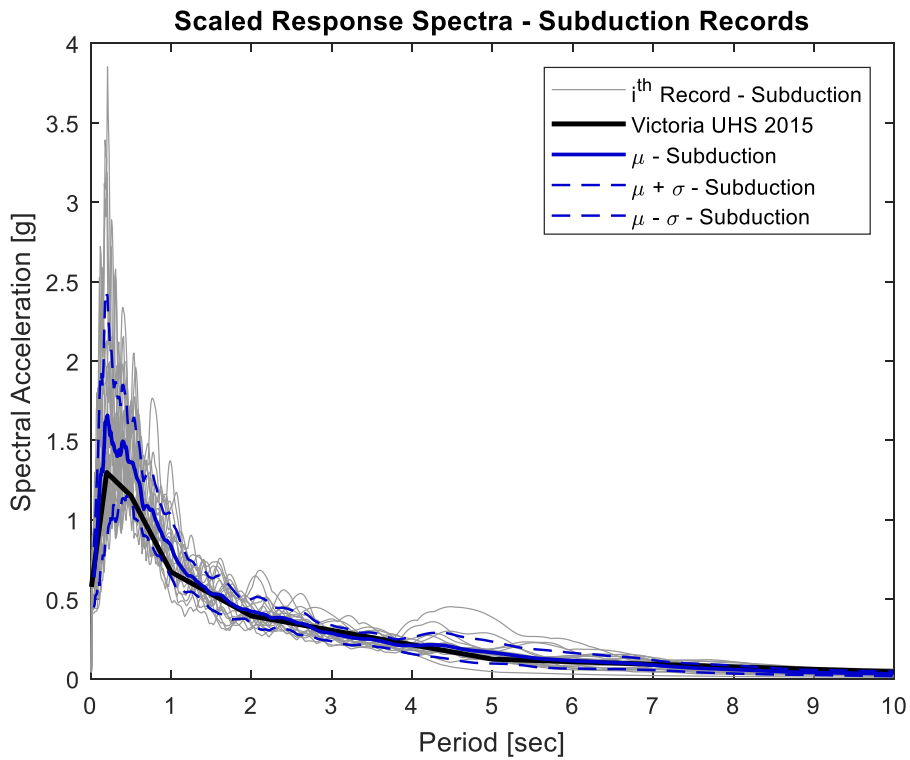


Figure 3-7: Response spectra of the subduction ground motions scaled to the target spectrum.

3.4.2 Selection and scaling of short-duration ground motions

The PEER Ground Motion Database was downloaded and compiled in Matlab to facilitate the ground motion selection. The NGA library includes records from 173 shallow crustal earthquakes and 1456 recording stations, for a total of 3551 multi-component ground motions (Baker et al., 2010; Baker et al., 2013, PEER, 2010, The MathWorks Inc., 2017). As the structural analysis to be carried out is one dimensional time history analysis, the search for crustal earthquake records was made treating the horizontal components as independent, resulting in a total of 7102 shallow crustal records available for selection. These ground motion records are corrected and filtered (Chiou et al., 2008).

Each of the scaled subduction motion spectra has been set as target spectrum in order to find a spectrally compatible short duration motion. This means that the subduction and compatible crustal motions will result in similar response spectra for the range of periods of interest. To this end, the ordinates of the subduction spectra have been recalculated based on a finer vector of fundamental periods with the intention of capturing more accurately the jagged shape characteristic of shorter periods. This resulted in a period vector of 301 points logarithmically distributed used for interpolation. Each of the 7012 crustal motions of the PEER database was linearly scaled to the target subduction response spectrum. The scaling process was performed following the same procedure for subduction records in terms of period range, scale factor limitations and weight function. Thus, each crustal record was then associated with a scale factor and MSE. In this process, the records with high velocity pulses were excluded from the selection.

The crustal motions have been sorted according lowest MSE values and the motion finally chosen for pairing was the one showing the best fit to the subduction scaled spectrum.

Figure 3-8 shows the acceleration response spectra of the unscaled records, while Figure 3-9 provides the response spectra obtained after the process of record pairing. In both plots the target spectrum for Victoria, BC is shown as a bold black line. The mean of the amplitudes of the scaled records amplitudes is represented as a red line, while the mean \pm standard deviations are given by the red dashed lines. The mean of the short duration motions closely matches the UHS target spectrum for period above 0.5 sec. Similarly to the matching for the subduction motions, the crustal suite results in a slight increase of the mean amplitude response at periods shorter than 0.5 sec.

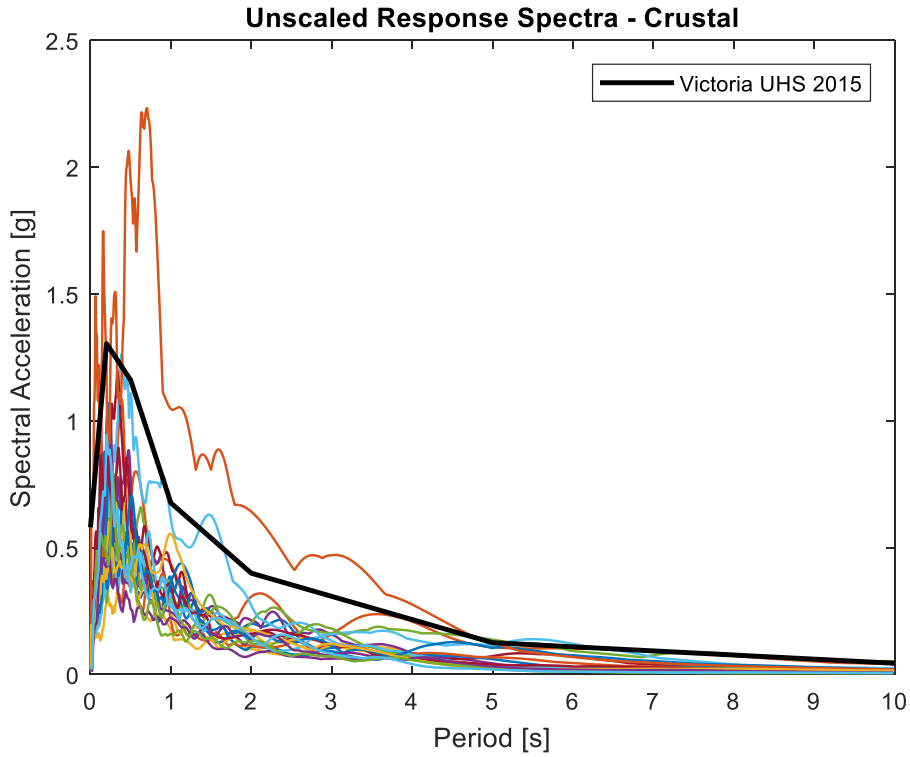


Figure 3-8: Response spectra of unscaled short duration crustal motions.

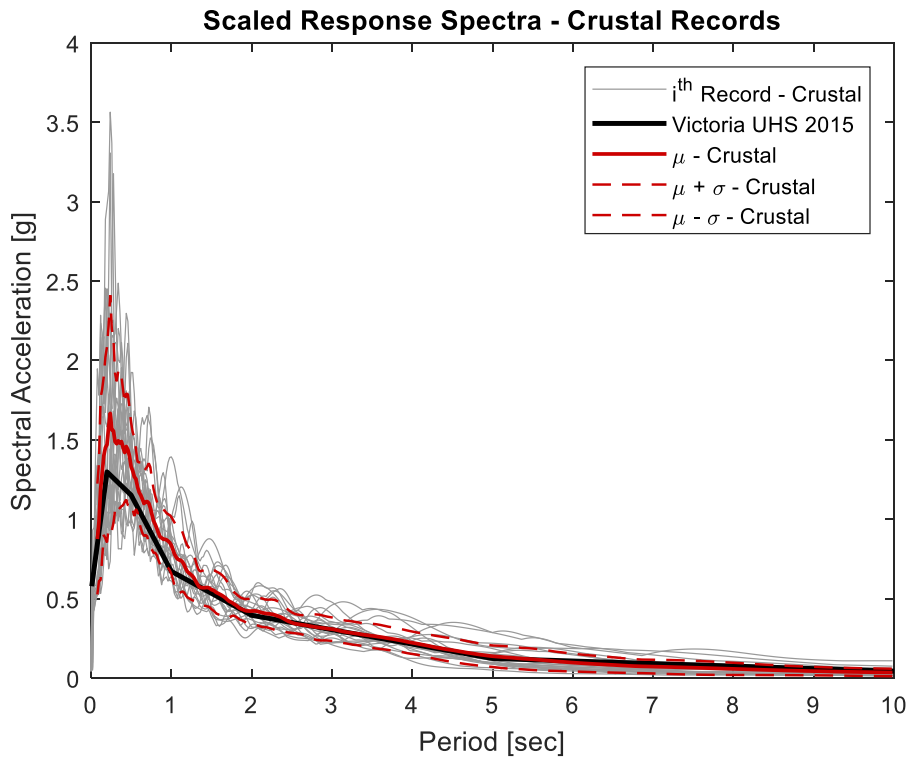


Figure 3-9: Response spectra of short-duration motions scaled to the target spectra.

3.4.2.1 Example of spectrally equivalent records pair

This Section illustrates an example of identification of a spectrally compatible pair of motions and is summarized in the following steps:

1. The long duration subduction motion considered in this example is a recording from Maule 2010 earthquake, which significant duration D_{5-95} is about 40.7 sec. This subduction motion has been first linearly scaled to match the UHS target spectrum over the period of interest. The associated scale factor was equal to 3.33;
2. Secondly, the *scaled* response spectrum of the subduction record has been uploaded in the Matlab platform as a target for pairing with a compatible crustal motion. Each of the 7012 PEER records has been linearly scaled to match the subduction spectrum;
3. The short duration crustal motion selected for pairing is a recording from the Northridge 1994 earthquake, which resulted in the best fit between spectral shapes and lowest MSE. The scaling procedure led to a scale factor equal to 3.99. The associated significant duration D_{5-95} is 16.5 sec: the subduction motion is 2.5 times longer than the crustal motion.

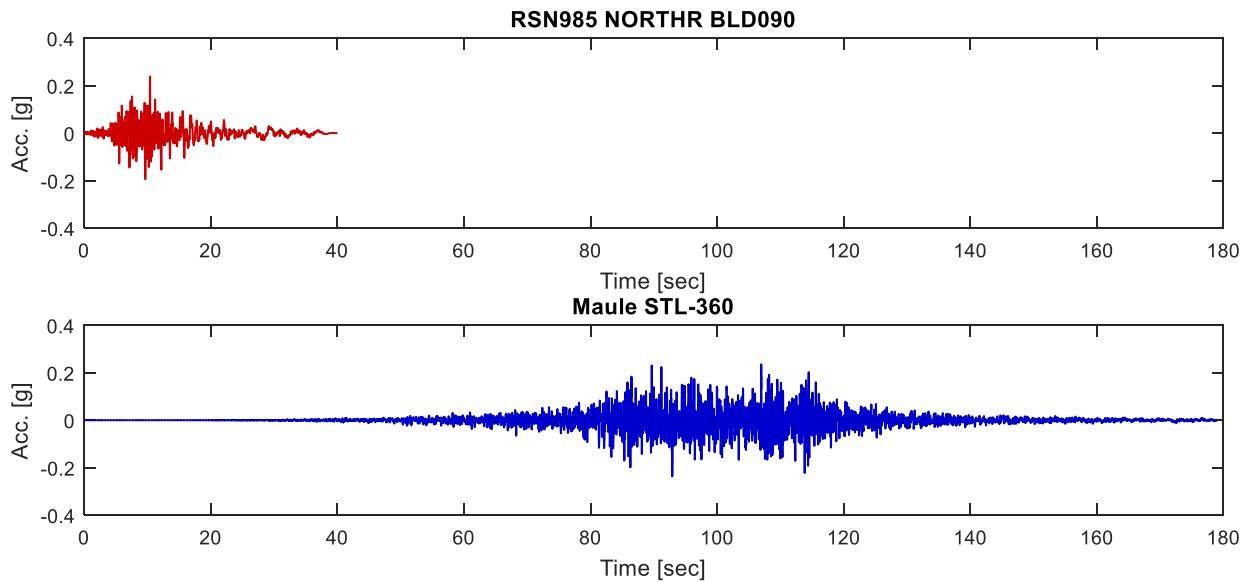


Figure 3-10: Acceleration time histories for record pair # 6.

Figure 3-10 shows the acceleration time histories of the unscaled records. The crustal motion recorded during the Northridge 1994 earthquake is plotted as the red time history, while the

subduction record for Maule 2010 earthquake is represented by the blue accelerogram. The crustal record from Northridge earthquake is characterized by strong shaking which last less than 20 sec, while the subduction motion shows significant shaking for over 40 sec. The comparison offers a clear example of difference in durations.

Table 3-3: Summary of the ground motions characteristics for the record pair # 6.

	Subduction	Crustal
Filename	STL-360	RSN985_NORTHR_BLD090
Event	Maule, Chile	Northridge-01, USA
Year	2010	1994
Magnitude	8.8	6.69
D ₅₋₉₅	40.70	16.56
SF	3.327	3.996
MSE	0.057	0.042

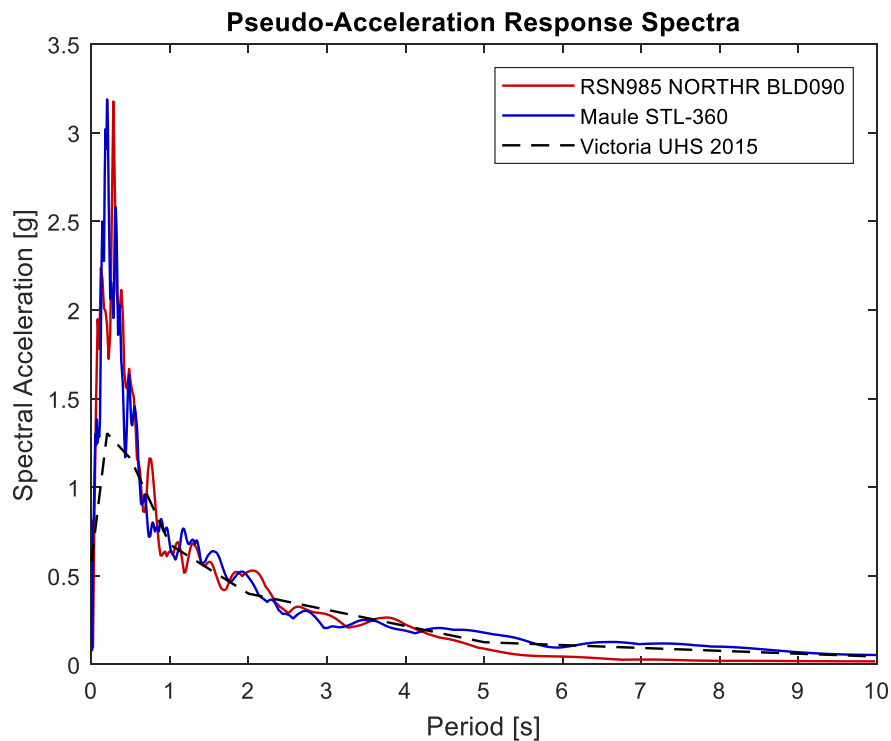


Figure 3-11: Example of spectrally equivalent records for pair # 6 and matching to the target spectrum.

Table 3-3 summarizes the parameters resulting from the selection and scaling of the spectrally equivalent record pair. The comparison between the response spectra generated by the subduction motion and the paired crustal is shown in Figure 3-11. The acceleration responses generated by the crustal record from Northridge 1994 are represented by the red spectrum, while the responses obtained with the subduction motion from Maule 2010 are expressed by the blue spectrum. The crustal response spectrum closely matches the spectrum for the subduction motion. The UHS target spectrum for Victoria BC is shown as a bold dashed line. This record pair represents a very good spectral match between them. Therefore, in a pseudo-static code design both spectra at any given period would give the same seismic demand. The effect of the longer duration can only be evaluated by running a nonlinear dynamic analysis, in which the longer record will result in larger drifts demands.

3.5. Results of ground motions pairing

As a result of the selection and pairing of the compatible ground motions, 20 record pairs have been identified and are summarized in Table 3-4. The suite of 20 long duration subduction ground motions includes 3 records from the Hokkaido 2003 earthquake, while 3 are motions from Maule 2010 and the remaining 14 are records from Tohoku 2011. The ground motions from Hokkaido 2003 are characterized by significant durations between 30 and 40 sec, while the Maule motions feature durations between 38 and 41 sec. The significant durations associated with the motions from Tohoku earthquake are considerably longer and range between 58 and 127 sec, with a mean duration of 93 sec. The overall average duration of the subduction suite is 77 sec. The magnitudes of the selected subduction motions range between M_w equal to 8 and 9.

The short duration crustal suite comprises motions from the following events: Chi-Chi 1999 (7 records), Taiwan 1986 (2 records), Chalafant Valley (1 record), Landers 1992 (1 record), Northridge 1994 (3 records), Loma Prieta 1989 (3 records), Superstition Hills 1987 (1 record), Kocaeli 1999 (1 record) and Hector Mine 1999 (1 record). The magnitude range is between M_w equal to 6.2 and 7.6. Both the motions featuring the longer and shorter duration within the crustal suite were recorded during the 1989 Loma Prieta earthquake. The longest duration is 28.8 sec (LOMAP_HSP090), while the shortest duration is 10.2 sec (LOMAP_LGP000). Altogether, the crustal motions have an average significant duration of 20 sec, which is about one fourth of the mean duration associated with the subduction suite.

Table 3-4: Summary of spectrally equivalent records pairs.

PAIR #	SUBDUCTION					CRUSTAL				
	SF	M	D ₅₋₉₅ (sec)	Event	File Name	SF	M	D ₅₋₉₅ (sec)	Event	File Name
1	2.68	8	38.18	Hokkaido, Japan, 2003	HKD0680309260450-EW	3.08	7.62	24.86	Chi-Chi, Taiwan, 1999	CHICHI_TCU089-N
2	3.02	8	30.52	Hokkaido, Japan, 2003	HKD0890309260450-EW	3.65	6.19	12.55	Chalfant Valley-02, 1986	CHALFANT.A_A-LAD180
3	2.10	8	39.16	Hokkaido, Japan, 2003	HKD1090309260450-NS	2.64	7.3	24.04	Taiwan SMART1(45), 1986	SMART1.45_45C00NS
4	2.72	8.8	38.43	Maule, Chile, 2010	ANT-360	3.14	6.3	18.08	Chi-Chi, Taiwan-06, 1999	CHICHI.06_CHY036E
5	3.89	8.8	39.87	Maule, Chile, 2010	stgolafloida1002271-NS	3.74	7.28	25.22	Landers, 1992	LANDERS_ABY090
6	3.33	8.8	40.70	Maule, Chile, 2010	STL -360	4.00	6.69	16.56	Northridge-01, 1994	NORTHR_BLD090
7	3.35	9	90.87	Tohoku, Japan, 2011	CHB0091103111446-EW	0.74	6.93	10.18	Loma Prieta, 1989	LOMAP_LGP000
8	3.43	9	58.14	Tohoku, Japan, 2011	CHB0101103111446-EW	2.51	6.54	13.65	Superstition Hills-02, 1987	SUPER.B_B-POE360
9	3.32	9	72.92	Tohoku, Japan, 2011	CHB0101103111446-NS	2.62	6.69	16.03	Northridge-01, 1994	NORTHR_CWC270
10	2.91	9	69.09	Tohoku, Japan, 2011	CHB0121103111446-EW	2.59	6.69	13.18	Northridge-01, 1994	NORTHR_CCN090
11	3.06	9	97.34	Tohoku, Japan, 2011	CHB0291103111446-NS	2.75	6.93	28.83	Loma Prieta, 1989	LOMAP_HSP090
12	3.85	9	90.85	Tohoku, Japan, 2011	FKS0221103111446-NS	1.82	7.51	11.79	Kocaeli, Turkey, 1999	KOCAELI_DZC180
13	3.22	9	93.18	Tohoku, Japan, 2011	IBR0091103111446-EW	2.08	7.62	26.81	Chi-Chi, Taiwan, 1999	CHICHI_TCU055-N
14	3.57	9	86.04	Tohoku, Japan, 2011	IBR0091103111446-NS	3.24	7.13	24.06	Hector Mine, 1999	HECTOR_ABY360
15	3.70	9	127.41	Tohoku, Japan, 2011	KNG2011103111446-EW	1.39	7.62	22.98	Chi-Chi, Taiwan, 1999	CHICHI_TCU067-N
16	3.28	9	116.66	Tohoku, Japan, 2011	KNG2051103111446-NS	3.97	7.62	25.48	Chi-Chi, Taiwan, 1999	CHICHI_HWA019-N
17	2.42	9	117.77	Tohoku, Japan, 2011	SIT0031103111446-EW	2.06	7.62	24.11	Chi-Chi, Taiwan, 1999	CHICHI_TCU055-E
18	3.80	9	79.42	Tohoku, Japan, 2011	TKY0071103111446-NS	2.10	7.62	24.11	Chi-Chi, Taiwan, 1999	CHICHI_TCU089-E
19	2.54	9	99.40	Tohoku, Japan, 2011	TKY0181103111446-NS	2.51	6.93	12.65	Loma Prieta, 1989	LOMAP_SLC270
20	3.40	9	107.02	Tohoku, Japan, 2011	TKY0241103111446-NS	3.02	7.3	21.17	Taiwan SMART1(45), 1986	SMART1/45I01EW

The histogram plot shown in Figure 3-12 illustrates the distribution of the durations in specified duration slots. Short duration crustal records, which have significant durations less than 30 sec, are shown as red bars. The long duration subduction motions have significant duration greater than 30 sec and are represented with blue bars. Almost half of the selected subduction records is characterized by significant durations greater than 90 sec. As for the short duration crustal records, 11 motions out of the total 20 have durations between 20 and 30 sec. Just a few of these motions are records from California events, while the majority are recordings from the Chi-Chi 1999 and Taiwan 1986 earthquakes.

Figure 3-13 shows the comparison of the mean spectral responses between the long duration subduction and the short duration crustal suites. It can be observed that the mean of the crustal suite matches very closely the mean response generated by the subduction suite in the period range of interest. The UHS target spectrum is represented by a bold black line. Although the records were scaled over a period of interest 0.1 and 4 sec, the matched pairs were found to closely match the target spectrum even at periods longer than 4 sec. Both mean spectra for subduction and crustal motions overlap the UHS target spectrum over the whole period range, with a slight increase of the mean amplitudes at shorter period, specifically from 0.1 to 0.5 sec.

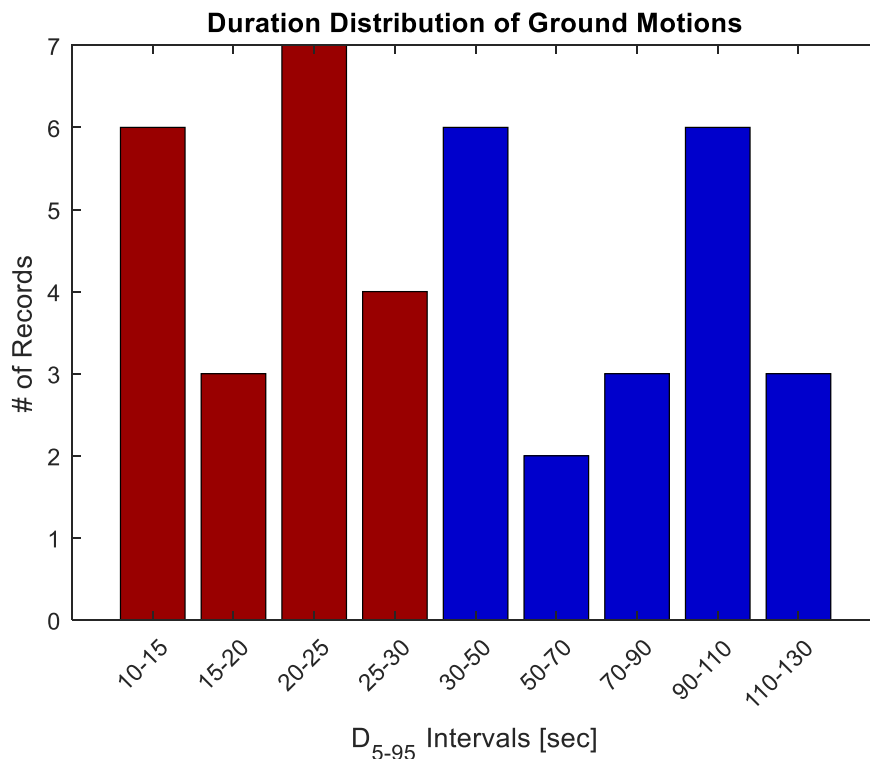


Figure 3-12: Number of records for significant duration intervals.

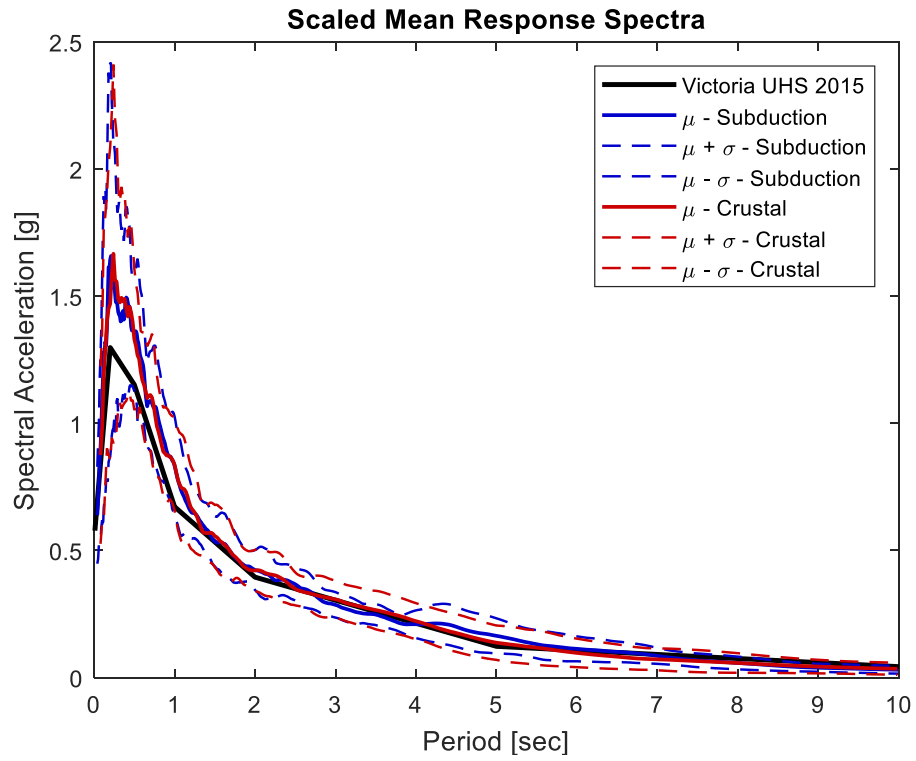


Figure 3-13: Comparison between mean and standard deviation of the two spectrally equivalent suites of motions.

Chapter 4

Nonlinear Incremental Dynamic Analysis (IDA)

“That’s been one of my mantras – focus and simplicity. Simple can be harder than complex: you have to work hard to get your thinking clean to make it simple. But it’s worth it in the end because once you get there, you can move mountains.”

Steve Jobs (1955 – 2011)

4.1. Introduction

Nonlinear Incremental Dynamic Analysis (IDA) was used to determine the probabilities of structural collapse under a variety of loading conditions.

Introduced in the late 70s by Bertero (1977), IDA is a parametric method of structural analysis which has become very popular in the engineering community within the framework of Performance-Based-Earthquake-Engineering (PBEE). IDA is considered a state-of-the-art procedure for estimating the collapse capacity of structural systems and has been included in FEMA guidelines since the year 2000 for determining the collapse prevention performance level (FEMA 350 and FEMA 351, 2000). IDA allows a comprehensive evaluation of the seismic performance of structures under different loading intensities (Villaverde, 2007) and therefore was chosen to study the effect of long duration ground motion on structural collapse. The current analysis follows the procedures developed by Vamvatsikos and Cornell (2002).

The purpose of this IDA study is to evaluate the effect of different structural periods and ductility capacities on the effects of long duration subduction motions on the probability of structural collapse. Because of the great computational effort associated with this extended parametric study, the IDA analyses were conducted on SDOF systems representing structural systems dominated by a single-mode response (Vamvatsikos & Cornell, 2004; Vamvatsikos & Cornell, 2005).

4.2. Description of the computational method

The compatible suites of motions developed in Chapter 3 are the baseline motions for the IDA analysis. The baseline motions identify the 100% hazard intensity scenario, which is hereafter called either “*Base Case*” or “*Base Design*” Scenario. Each of the 40 ground motions is then scaled to represent input motions that range from 10% to 250% of the Base motions in 10% increments. This results in 40x25 input motions representing low, moderate and high level seismic demands. As noted in Section 2.8, the ductility demands and damage potential of the ground motions used in this study lie between the demands at Tsukidate and Sendai at periods shorter than 1.0 sec, while they are above both Tsukidate and Sendai at periods between 1.0 sec and 5.0 sec. The objective of IDA analysis is to calculate the probability of exceeding a specified interstory drift limit. In this IDA study, the peak interstorey drift ratio was selected as the measure of damage.

The dynamic time history analyses were run for each motion using a Newmark integrator with γ and β parameters equal to 0.5 and 0.25 respectively (also known as Average Acceleration Method). The Modified Newton algorithm was chosen to solve the nonlinear equations resulting from the dynamic analyses. For each record, the integration time step used for analysis was equal to the time interval of the recorded motion.

4.3. Modeling of SDOF systems

SDOF systems with a range of fundamental periods have been used to model structures dominated by one mode. In most of the cases, the first natural mode is the one that controls the response. The period range of interest 0.1-5 sec was chosen to represent short, intermediate and long period structures. In the short and intermediate period ranges, i.e. up to 2 sec, the period interval for analysis was 0.1 sec, while at longer periods (from 2.0 to 5.0 sec), the interval for structural periods was 0.5 sec. This resulted in the identification of 26 different structural models.

Each SDOF system was modeled as a rigid cantilever oscillator with a rotational inelastic spring at the base, where the dissipation of hysteretic energy occurs. For this system, the drift ratio of the mass is equal to the rotation of the spring in radians. Figure 4-1 shows the representation of the SDOF systems.

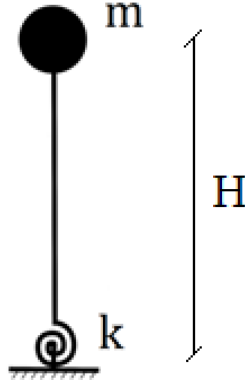


Figure 4-1: SDOF system with rigid rod and rotational inelastic spring at the base.

The *design base shear* for the i^{th} period SDOF is calculated using the following formula.

$$V_b(T_i) = \frac{S_a(T_i) \cdot W}{R} \quad (4 - 1)$$

Where $V_b(T_i)$ is the design base shear of the i^{th} period SDOF, T_i is the fundamental period of the SDOF system in seconds, $S_a(T_i)$ is the UHS spectral acceleration corresponding to the period T_i , W is the weight of the building and R is the force reduction factor and it is assumed to be equal to 5.

The moment resistance at the base is given by:

$$M_y(T_i) = V_b(T_i) \times H = \frac{S_a(T_i) \cdot W}{R} \times H \quad (4 - 2)$$

The *hysteretic response* for steel MRF has been simulated using the Modified Ibarra-Medina-Krawinkler Deterioration Model with Bilinear Hysteretic Response implemented in OpenSees and hereafter called *Bilinear Material Model* (OpenSees, 2017; Mazzoni et al., 2007).

The *backbone curve* is defined by the following parameters: yield moment resistance M_y , initial elastic stiffness K_0 , yield rotation θ_y , pre-capping inelastic rotation capacity θ_p , strain-hardening stiffness K_s , post-capping rotation capacity θ_{pc} and residual strength M_r (Ibarra et al., 2005). The pre-capping rotation capacity θ_p was evaluated as a multiple of the yield rotation θ_y . Specifically, it was calculated as a multiple of 2, 4, 6, 8 and 10. Therefore, the associated rotational ductility capacity values ($\mu = \theta_c/\theta_y$) were respectively 3, 5, 7, 9, 11. The analyses were performed for the five different levels of rotational ductility without changing the R-value to investigate the sensitivity of the effect of duration on different ductility capacity values and failure. In the course of this sensitivity study, the initial stiffness and yield moment resistance used to define the backbone curve were unchanged and the deterioration occurred during the loading cycles. This ductility range covers *low-ductile* (ductility 3), *intermediate-ductile* (ductility 5-7) and *very ductile* systems (ductility 9-11). In this study, strain hardening and residual strength were not considered, therefore K_s and M_r were set equal to 0. Figure 4-2 shows the backbone curve for a general Bilinear material model.

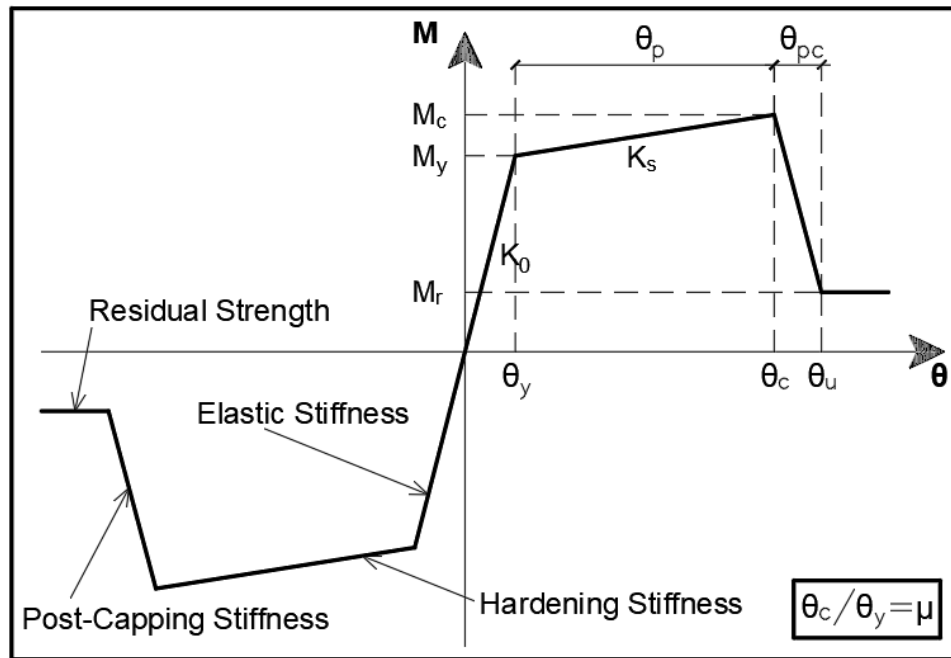


Figure 4-2: Definition of the backbone curve.

In order to illustrate the procedure followed on the calculation of the backbone parameters, an example is provided as a reference for the SDOF system characterized by a fundamental period

equal to 1.2 sec. For the purpose of the study, the weight W was assumed to be 100kN and the height H equal to 3 m. Similar calculation process was applied to the other structural periods.

$$T^* = 1.2 \text{ sec} \quad (4-3)$$

↓

$$S_a(T^*) = 0.62 \text{ g} ; R = 5 \quad (4-4), (4-5)$$

↓

$$V_b(T^*) = \frac{S_a(T^*) \cdot W}{R} = 12,412 \text{ N} \quad (4-6)$$

↓

$$M_y(T^*) = V_b(T^*) \cdot H = 37,236 \text{ Nm} ; K_r(T^*) = H^2 M \cdot \frac{4\pi^2}{(T^*)^2} = 2,516,215 \text{ Nm} \quad (4-7), (4-8)$$

↓

$$\theta_y(T^*) = \text{Drift Ratio}_{\text{Yield}} = \frac{M_y(T^*)}{K_r(T^*)} = 0.0147 \sim 1.5\% \quad (4-9)$$

↓

$$\theta_c(T^*, \mu) = \text{Drift Ratio}_{\text{Capping}} = \mu \cdot \theta_y(T^*) = 11 * \theta_y(T^*) = 0.162 \sim 16\% \quad (4-10)$$

The Bilinear material model accounts for both monotonic and in-cycle degradation. The Bilinear model was first introduced by Ibarra et al. (2005) and further developed by Lignos and Krawinkler (2010, 2012). Four different *deterioration modes* are implemented in the model and depend on energy-based deterioration parameters Λ (OpenSees, 2017, ATC-72-1, 2010). For illustrative purposes, these degradation modes are illustrated in Figure 4-3 where the monotonic load-displacement curve is shown in comparison to a quasi-static cyclic response for plywood shear wall panels (Ibarra et al., 2005). Description of the four degradation parameters is given in the following points:

- *Cyclic strength deterioration* Λ_S is the parameter accounting for the deterioration of structural strength with the number of cycles and amplitude of shaking. This deterioration mode can be illustrated as a translation and rotation towards the origin of the strength associated to the pre-capping stage and it is shown in Figure 4-3 as *Mode 1*;

- *Post-capping strength deterioration*: the strength can additionally deteriorate when the hysteresis reaches a negative tangent stiffness. This deterioration mode is shown as a translation of the post-capping bound to the origin and it is shown in Figure 4-3 as *Mode 2*. Post-capping strength deterioration is represented by the Λ_C deterioration parameter;
- *Unloading stiffness deterioration*: the stiffness can also deteriorate with increasing the number of cycles and the amplitude of motion. This deterioration mode can be illustrated as a clockwise rotation of the unloading slope and it is quantified by the parameter Λ_K . Figure 4-3 shows the effect of unloading stiffness deterioration as *Mode 3*.
- *Acceleration reloading stiffness deterioration*: Λ_A is the parameter that simulates this degradation mode. This degradation phenomenon is usually observed in reinforced concrete beams and it is not considered in the analysis (Ibarra et al., 2005) (*Mode 4*);

The value assigned to Λ_S , Λ_C and Λ_K is 0.897 when the dimensions of the structural model are given in *meters* (Liel et al., 2014 and Chin, 2017).

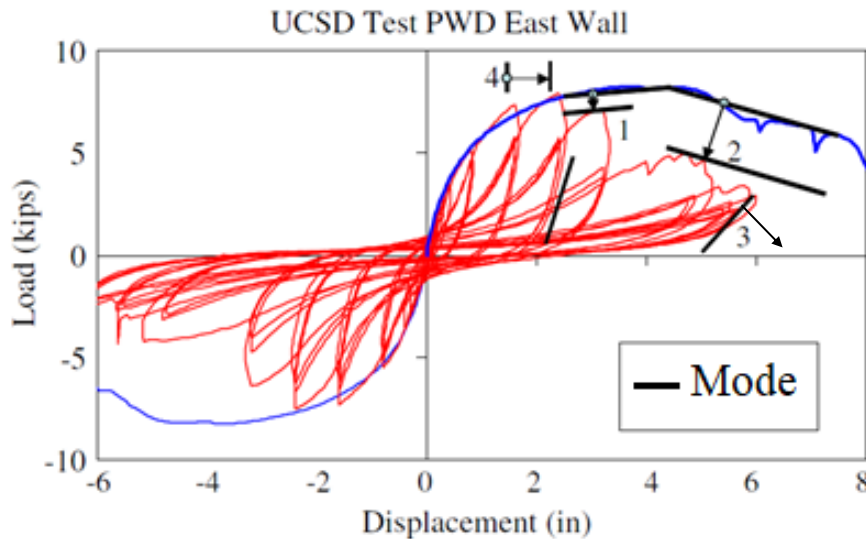


Figure 4-3: Illustration of deterioration modes (Modified from: Ibarra et al., 2005).

The structural response of the SDOF systems is closely related to the hysteretic behavior and the in-cycle degradation of the systems. Therefore, the cyclic deterioration modes are important

parameters in the modeling process. It is important to note that the results of the IDA study will be conditional on the type of hysteresis model and degradation modes considered.

Along with the deterioration characteristics of the system, P- Δ effects have been shown to play an important role in nonlinear dynamic analysis of SDOF systems as they reduce the effective stiffness of the system (Mahin, 1980). As a consequence, the yield strength decreases for loads in the direction of the offset. The importance of P- Δ and degradation effects on the influence of ground motion duration on structural collapse has been also supported by the work done by Chandramohan et al. (2016). Earlier studies conducted by Raghunandan and Liel (2013) showed that the level of P- Δ does not influence the effects on collapse capacity as significantly as deterioration and ductility. Moreover, Raghunandan and Liel (2013) showed how higher P- Δ effects resulted in a decrease in overall collapse capacities for short duration motions, but seemed not to have a significant effect for ground motions with long duration.

Since of P- Δ effects were found to have a different impact on structural collapse for short and long duration motions and because the objective of this study is to evaluate specifically the effects of duration and the influence of structural period and ductility capacity, P- Δ effects were not considered in the analysis.

4.4. Results of IDA

The result of a Single-Record IDA study, is represented in terms of an *IDA curve*, which shows the variation of the damage measure with shaking intensity. A detailed review of possible interpretations of an IDA curve is given by Vamvatsikos and Cornell (Vamvatsikos & Cornell, 2002). They generally considered that the global collapse capacity is achieved when the IDA curve becomes flat, as this flatline means that the deformation increases indefinitely with very small increments of ground motion intensity. On the other hand, FEMA 350 assumes their collapse point to occur when the tangent slope of an IDA curve reaches a value equal to the 20% of the elastic slope (FEMA 350, 2000). In this study, collapse is defined as the exceedance of the capping rotation θ_c .

Figure 4-4 and Figure 4-5 show the IDA curves set for a 1.2 sec period system and a ductility capacity equal to 11 generated respectively with the crustal and subduction motions. The x-axis shows the drift ratios, while the y-axis gives the shaking level. A shaking level equal to 100% refers to a shaking intensity given by the motions scaled to the Victoria UHS for a 2% in 50 years

probability of exceedance. Each grey dot refers to the computed maximum drift ratio of each record at each shaking level and the grey lines, obtained connecting the dots with a spline, represent the IDA curve for each ground motion record. The vertical dotted line indicates the capping rotation limit θ_c ($\theta_c = \mu \theta_y$). Such limit will be used as a definition of collapse during the fragility analyses in Chapter 5.

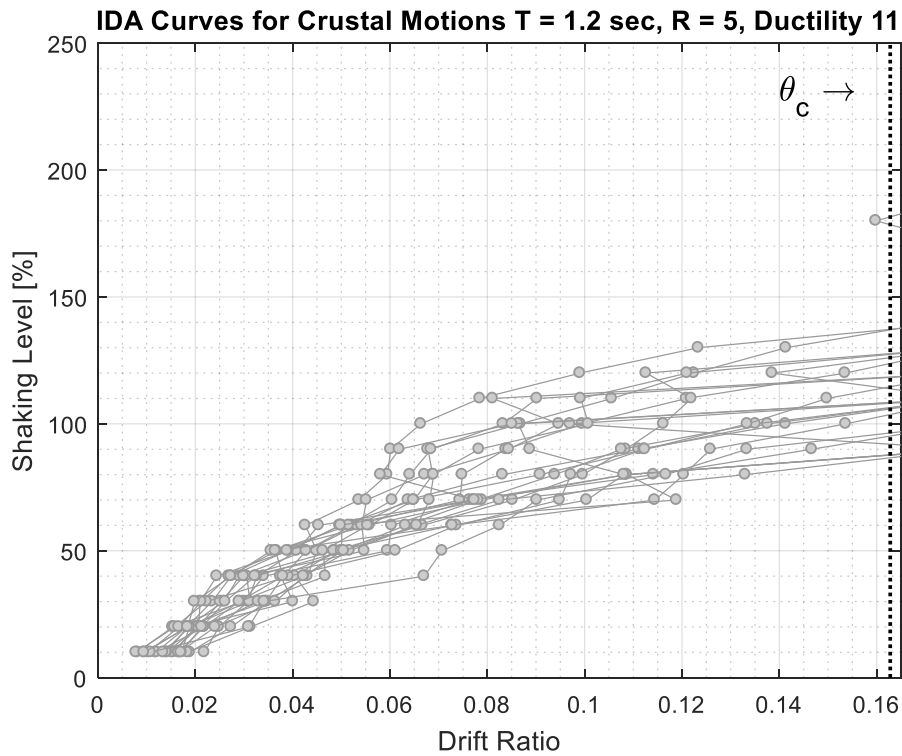


Figure 4-4: IDA curves obtained with crustal motions, for SDOF with T = 1.2, R = 5 sec and ductility 11.

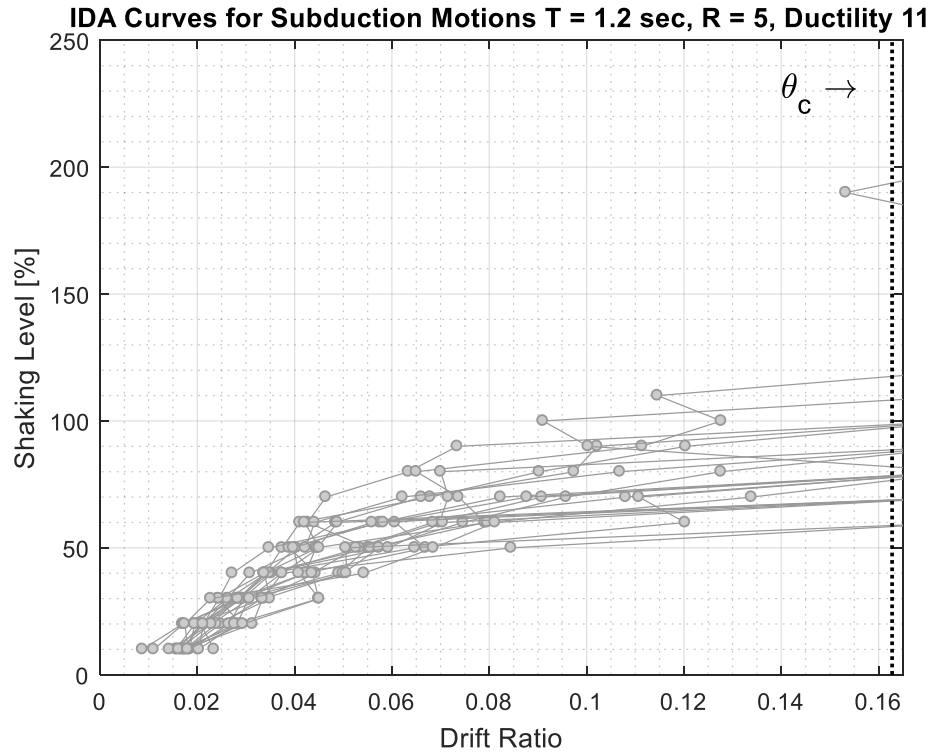


Figure 4-5: IDA Curves obtained with subduction motions, for SDOF with $T = 1.2$ sec, $R = 5$ and ductility 11.

4.5. Discussion

At very low levels of shaking, i.e. from 10% to 40% of the design intensity, the IDA curves show a quite compact trend, in both Figure 4-4 and Figure 4-5. The slopes of the IDA curves start diverging when the behavior becomes significantly nonlinear and the maximum drift ratio increases. The results show that the maximum drift ratio at the same intensity level also depends on the characteristics of the ground motion considered.

In Figure 4-4, it can be observed that the IDA curves for several crustal ground motions show drifts gradually increasing with shaking intensity and approaching the collapse limit state. On the other hand, for subduction ground motions (Figure 4-5), the IDA curves shift downwards towards lower intensity levels for a given drift ratio than crustal motions. This indicated the greater seismic demand from subduction motions. This result support the finding showed in previous studies conducted by Fairhurst et al. (2017) which reflect the higher demands imposed by subduction ground motions.

For both crustal and subduction suites of motions, some of the IDA curves show a *weaving* behavior. This phenomenon was first studied by Vamvatsikos and Cornell in 2002. This pattern is

can be recognized when an IDA curve exhibits successive segments of *softening* and *hardening*. This means that the slope of the IDA curve decreases and successively increases with higher shaking level. Therefore, system response at a specific shaking level, may show a similar (or even lower) demand at a higher shaking intensity. In their paper, Vamvatsikos and Cornell attribute this phenomenon to the great importance of *pattern* and *timing* of each ground motions, rather than shaking intensity.

It is important to recognize that the sensitivity analysis was conducted for variation in the ductility capacity only, considering a constant force reduction factor ($R = 5$).

Although the results of this study have been interpreted in terms of drift ratios, the results obtained from the IDA analyses could be also interpreted in terms of reactions (base shear and moments) of the SDOF systems. The drift ratios computed at each intensity level in IDA have been used to calculate the probability of collapse, as presented in Chapter 5.

Chapter 5

Fragility analysis and assessment of duration effect

“Logic will get you from A to Z; imagination will get you everywhere.”

Albert Einstein (1879 – 1955)

5.1. Fragility analysis

The drifts ratios from the IDA study have been used to generate fragility curves for collapse. To this end, *the drifts ratios have been assumed to be lognormally distributed over all the records at each shaking level*. Accordingly, the mean and standard deviation were estimated allowing the calculation of the probability of collapse (Porter, 2016). An alternative approach is the method developed by the Applied Technology Council in the FEMA P695 (2009). In this approach, the lognormal distribution function is used to fit the collapse shaking levels.

It is rather challenging to identify the occurrence of structural collapse, mainly because it is associated with multiple phenomena (large deformations, buckling, material degradation). As a result, the identification of structural collapse has led to contradictory opinions in past research (Villaverde, 2007, Araki & Hjelmstad, 2000). In this study, *collapse* is defined as the exceedance of the capping rotation capacity θ_c and, as such, depends on the structural period, the ductility capacity and the yield rotation (drift ratio).

The collapse fragility curves generated by the crustal and subduction motions are shown in Figure 5-1, specifically for a 1.2 sec-period SDOF system and a ductility level equal to 11. Fragility curves associated with other fundamental periods and ductility levels are included in Appendix B.

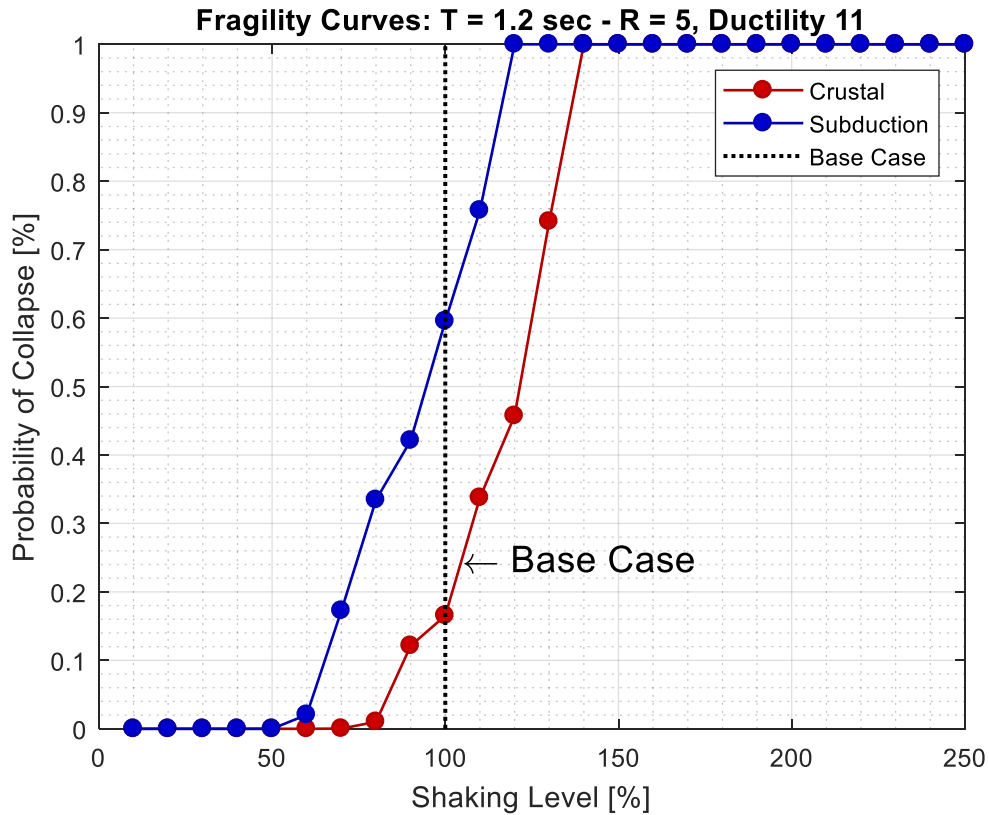


Figure 5-1: Fragility curves for T = 1.2 sec SDOF with ductility 11 and R = 5.

The fragility curve calculated using the subduction motions as input is represented by the blue line, while the red fragility curve is associated with the crustal motions. At shaking levels between 60% and 140% of the design intensity, the subduction fragility curve lies above the crustal fragility curve, signifying a higher probability of collapse. This higher probability of collapse is attributable to the difference in duration between crustal and subduction ground motions. At lower intensity levels (below 60%) and at extremely high levels (above 140%), the two fragility curves coincide, showing the same probability of collapse for long and short duration motions. At low levels of shaking in both cases, the probability of collapse is very low - close to zero. Conversely, above 140% shaking intensity the two curves reach both 100% probability of collapse. The vertical dotted line in Figure 5-1 represents the 100% intensity level scenario in which the motions are

scaled to match the UHS and therefore it refers to the *Base Case* motions. At this shaking intensity the increase in probability of collapse due to the longer duration of the subduction motions is estimated to be 44%. The effect of long duration motions becomes more significant in the range between 80 and 120% of the design intensity.

Fragility curves, calculated for other ductility levels, are compared in Figure 5-2, where bold lines represent subduction motions and dashed lines crustal motions. The fragility curves for subduction motions show a higher collapse rate than crustal motions at each ductility capacity considered. Structural systems characterized by lower ductility levels achieve the 100% probability of collapse at lower levels of shaking and the subduction fragility curve is very close to the crustal curve. Thus, the long duration shaking does not significantly influence the achievement of the collapse state at a low ductility level.

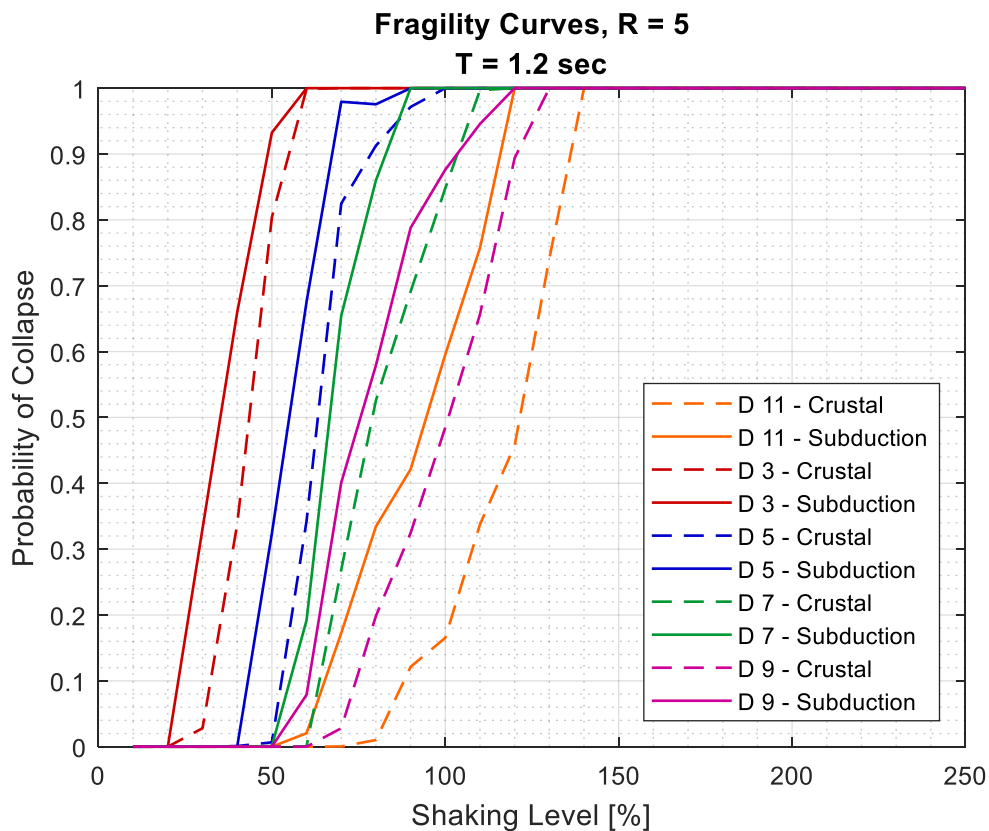


Figure 5-2: Fragility curves for T=1.2 sec structure calculated for different ductility levels D = 3, 5, 7, 9, 11.

The fragility analysis conducted on structural systems with period below 0.5 sec resulted in high probabilities of collapse associated with relatively low shaking intensity levels and are

illustrated by the fragility curves in Figure B-1 to Figure B-5 in Appendix B. Also, the increase in probability of collapse is particularly abrupt, with fragility curves are showing extremely steep slopes. This phenomenon is referred to as the *short period performance paradox*, because of the contradiction between the analytical prediction of higher collapse probabilities at short periods and the damage observed during post-earthquake field evaluations (Applied Technology Council, 2017).

5.2. Effects of structural period on probability of collapse

The effects of structural period (period secant to yielding) on the probability of collapse can be represented by the envelope of the fragility curves over the period range of interest. This interpretation leads to a surface plot in which the x and y axes represent structural period and shaking level respectively, while the z-ordinate gives the probability of collapse. Discussion of the results is given in considerable detail for ductility 11, thus to providing a model for interpreting the data resulted from the analysis conducted with ductilities 3, 5, 7 and 9. The discussion for these ductility levels is presented in Appendix C. Figure 5-3 provides the envelope of probabilities of collapse calculated with crustal motions for a ductility level equal to 11.

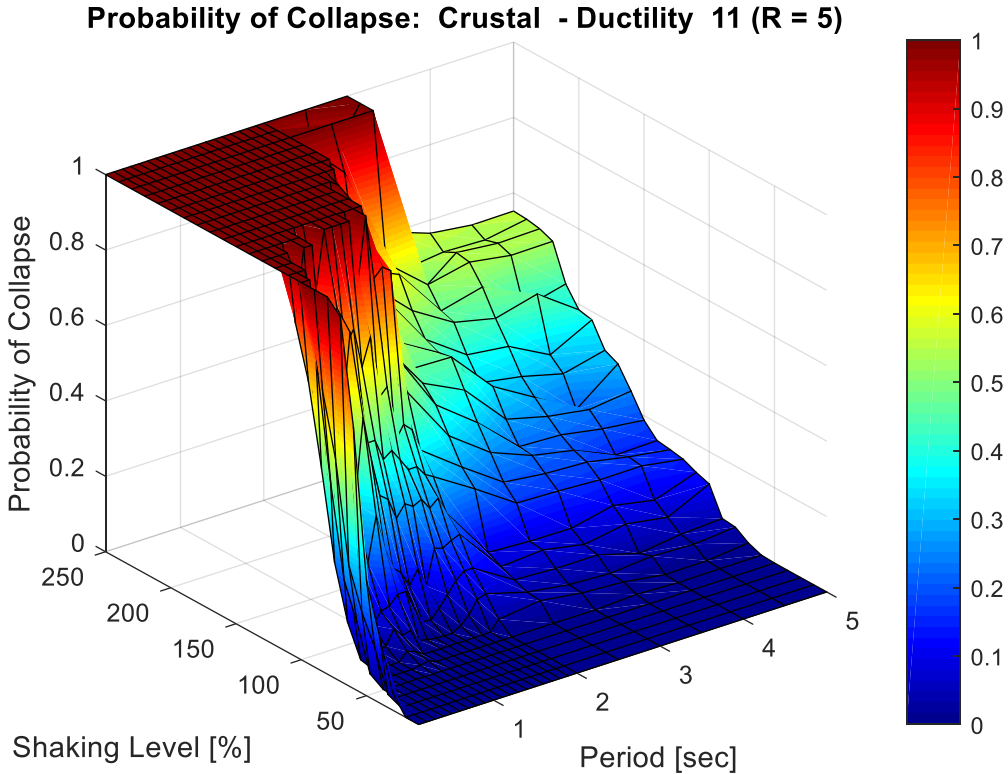


Figure 5-3: Fragility curves envelope for crustal motions and ductility 11.

The probability associated with each *period and intensity level pair* is assigned to the vertical axis. A color pattern has been used to identify different ranges of collapse probability. The color *dark blue* is associated with low probabilities (0-10%), while the color *dark red* refers to the achievement of high collapse probabilities (90-100%). Intermediate values are represented by a range of colors as shown in the colorbar. In particular, the mean (50%) probability of exceedance is associated with the color *green*. A contour plot of the surface can be generated with reference to the period-shaking level plane as shown in Figure 5-4. To appreciate at best the projection of the contour below the surface plot, a rotated view of Figure 5-4 is shown in Figure 5-5.

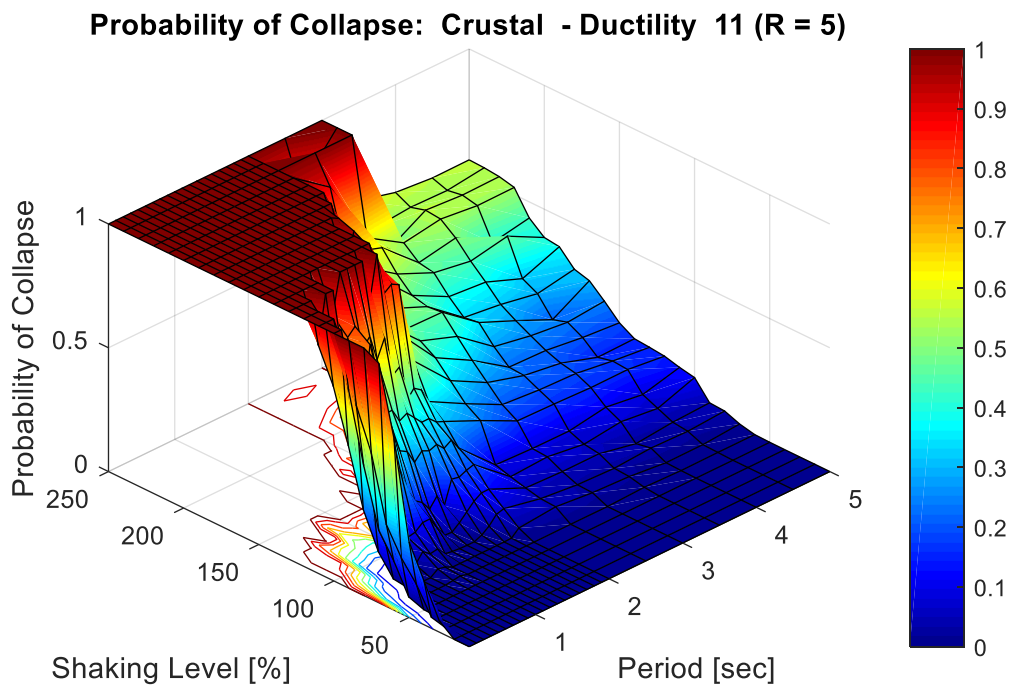


Figure 5-4:: Surface plot and projection of the contour in the shaking level-period plane.

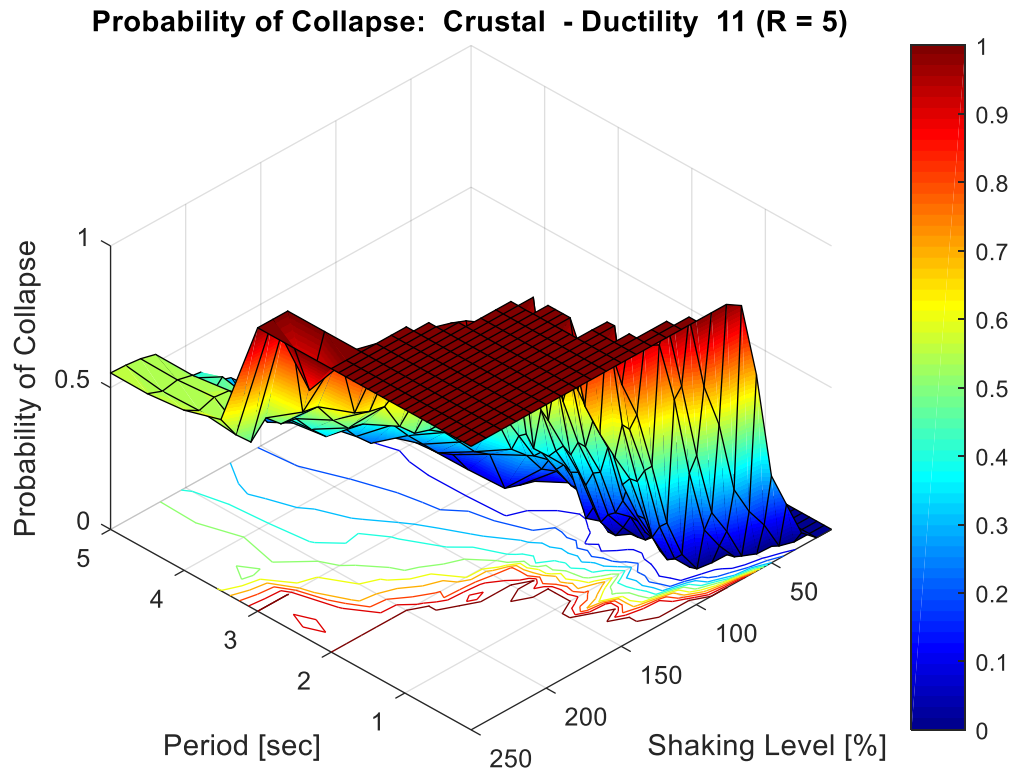


Figure 5-5: Contour plot of the envelope of the fragility curves for crustal motions and ductility 11.

Figure 5-6 shows the resulting contour plot. Each line in the contour plot is an *'equal probability of collapse line'*. The contour plots can be read as *elevation maps*. Each surface plot can be visualized as an uneven *terrain*. The surface is sliced with imaginary x-y planes at intervals of 10% probability of collapse, which represents the *contour interval*. Thus, the curves in the contour plot can be read as *topographic lines* and represent locations on the terrain (surface) with same *elevation*, which in our case, is same probability of collapse. This means that, if one follows a specific contour line, the elevation (probability of collapse) remains constant. The topographic lines describe not only the elevation, but also the *shape of the terrain*. The more the curves are close to each other, the steeper is the profile of the terrain, while lines spaced widely apart indicate more gentle slopes. The areas of the plot that have no contour lines at all, refer to relatively flat terrains, which are associated to 0% or 100% probability of collapse respectively.

The color legend assigned to Figure 5-3 has been applied also to the contour lines. Curves for 10% probability of collapse are shown in dark blue and for 100% probability in dark red. The probabilities in between these limits are shown in increments of 10% and are colored according to the colorbar. The area of the plot below the 10% (dark blue) collapse line is associated with 0%

probability of collapse, while the region above the 100% (dark red) collapse line refers to 100% probability of collapse. The mean probability of collapse (50%) is shown in green color.

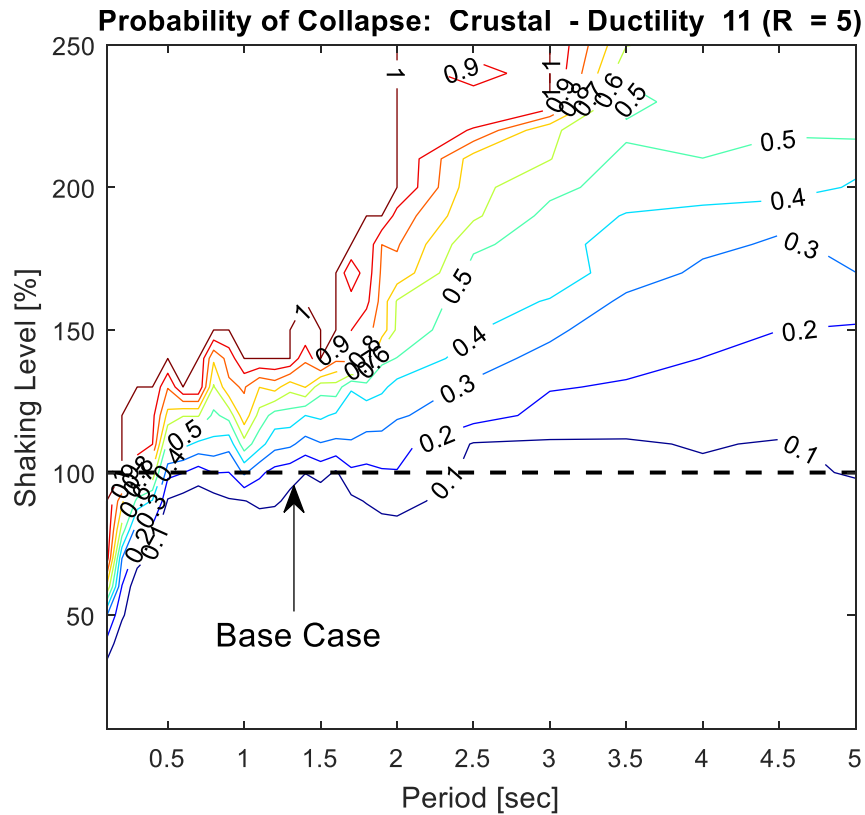


Figure 5-6: Contour plot showing the probability of collapse for the crustal suite of motions and ductility 11.

Several interpretations can be drawn from these contour plots. For instance, a horizontal contour line over a certain period range, means that the associated probability of collapse is constant for all the systems within that period range at that particular scaling level. If the equal collapse probability line is not horizontal, the probability of collapse is a function of the structural period and the shaking level. The *spacing* of the equal probability of collapse lines is also an important feature of this representation. If the lines are closely spaced, the probability of collapse is very sensitive to the increments in the motions intensity. On the other hand, if the lines are far apart, the increase in probability of collapse is gradual. The dashed black line marks the *Base Design* level and describes the structural performance in terms of probability of collapse when the motions are scaled to the 100% hazard intensity.

Figure 5-6 and Figure 5-7 show the contour plots for the crustal and subduction suite of motions respectively, for a ductility capacity equal to 11. From the contour plot for crustal motions (Figure 5-6), it can be observed that:

- At periods lower than 0.5 sec, high probabilities of collapse are observed at low and intermediate shaking intensities. This is at variance with findings on damage from post-earthquake field observations and therefore is an example of the paradox in the structural performance of short period structures mentioned in Section 5.1. In this period range, the contour curves are extremely close, emphasizing the strong dependence of the collapse performance to the intensity of the ground motions. A factor for this poor performance at short periods may be due to the fit of the motions in the period range 0.1-0.5 sec, where the mean response spectral amplitude was higher than the target Victoria UHS;
- In the period range between 0.5 and 1.5 sec, the contour curves assume a flatter trend and the structural period has little influence on the collapse performance. For SDOF system associated with periods above 1.5 sec, and at low levels of probability of collapse, the contour lines become horizontal. Therefore, in this region collapse depends on the shaking level only. For higher probability levels and periods above 1.5 sec, the contour curves spread apart and move towards the upper region of the plot. Therefore, the probability of collapse is a function of both shaking level and structural period;
- When the crustal motions are scaled to 250% intensity, structures of period between 3 and 5 sec do not reach 100% probability of collapse. This is probably due to the lack of correspondence between the typically short dominant periods of crustal motions and the structures with periods greater than 3.5 sec;
- The black dashed line refers to the shaking intensity which represents *Base Design*. Ignoring the region of the short period paradox below 0.5 sec, the probability of collapse at the 100% hazard intensity ranges from 10-20%. The 20% probability is associated to intermediate periods from 0.5 to 2 sec whereas for structural periods longer than 2 sec the probability of collapse is below 10%. This is found to be in line with the ASCE 7 (2016), where the probability of collapse evaluated through a PBEE design approach is expected to be within 10%.

The contour plot generated by the IDA study considering the subduction motions and a ductility level equal to 11 is shown in Figure 5-6.

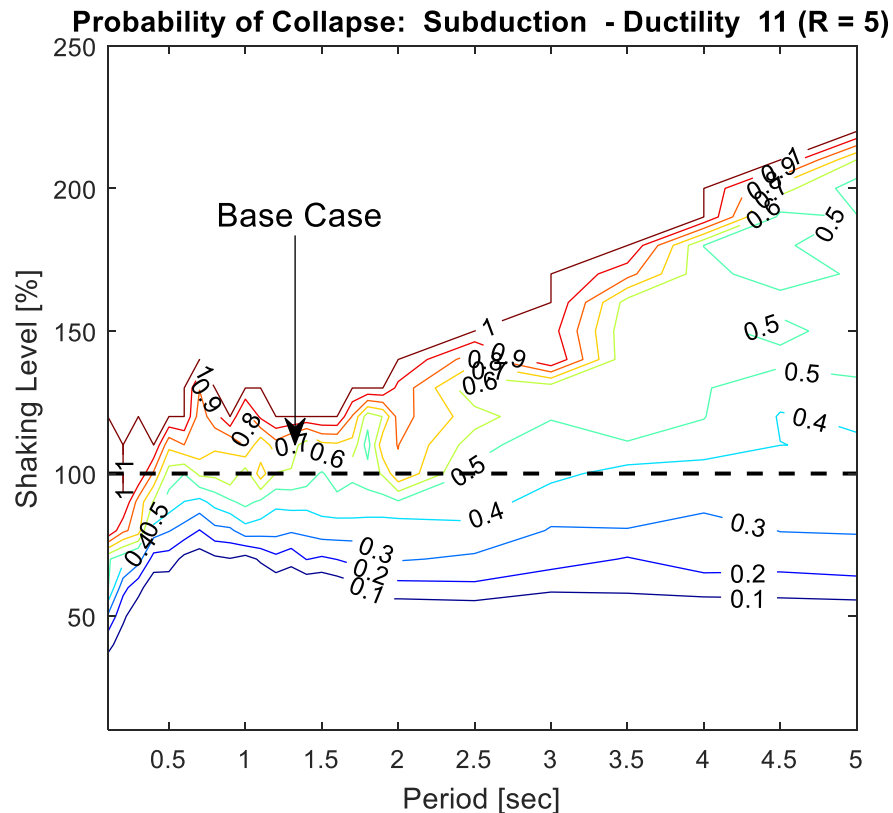


Figure 5-7: Contour plot of the probability of collapse for the subduction suite of motions and ductility 11.

It can be observed that:

- At structural periods below 0.5 sec, the presence of the short period paradox is present;
- The trend of the equal probability of collapse lines is similar to the previous case. After 0.5 sec, the equal probability curves are predominantly horizontal as in the case for crustal motions, but the corresponding probabilities of collapse are reached at lower shaking levels. Beyond 2 sec, the probability curves begin to climb indicating strong dependence on shaking level;
- At *Base Design* level, 100% shaking intensity, the probability of collapse generated by subduction motions is between 35% and 60%, and is higher than the probability

associated with the crustal motions. This difference is attributed to the longer duration of subduction ground motions;

- Consider a horizontal slice of each contour plots at 150% shaking intensity. For periods longer than 2.5 sec, the subduction ground motions lead to 50-100% probability of collapse, while the crustal suite of motions results in significantly lower probabilities, within the range of 20-40%.

Contour plots have been generated for each ductility level and they are shown in Appendix C in Figure C-1 to Figure C- 10. The effect of structural period on the probability of collapse at these ductility levels is also discussed in Appendix C.

5.3. Effects of long duration on the probability of collapse

The contour plots presented above provide significant insight into the variation of the probability of collapse with respect to shaking level and fundamental period. As the amount of detail and information carried by each contour plot is quite substantial, the contour plots have been merged to create a single plot summarizing the difference in the collapse performance due to the longer duration of the subduction motions.

Thus, the effect of the long duration of subduction motions can be interpreted as the difference, at each shaking level (SL^*), between the probability of collapse obtained with the subduction suite and the collapse probability calculated with the crustal motions (Equation 5-1).

$$Duration\ Effect(SL^*) = P_{Subduction}(SL^*) - P_{Crustal}(SL^*) \quad (5-1)$$

Figure 5-8 represents such comparison for ductility level 11. The x-ordinate refers to the structural period, while the y-axis represents the shaking level. This plot results in a set of data points (*period, shaking level*) corresponding to the difference in the calculated probability of collapse ($P_{Subduction} - P_{Crustal}$). A *colorbar* has been defined to cover a range of probability differences.

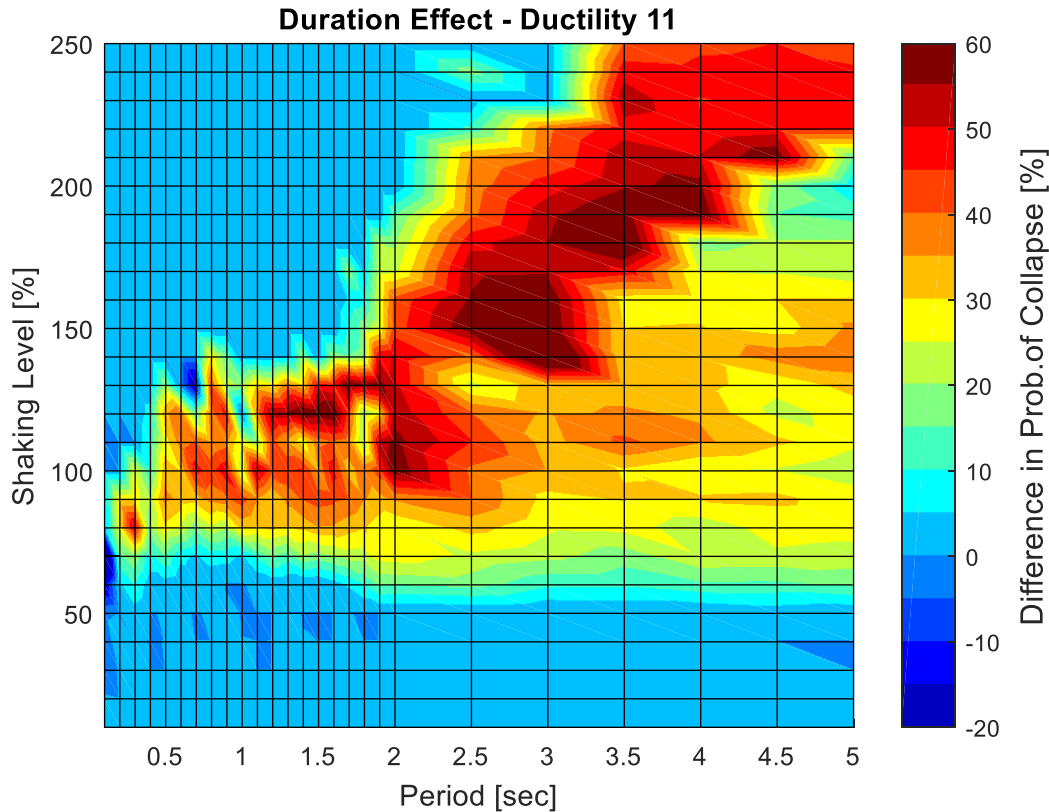


Figure 5-8: The effect of long duration shaking on structural systems with ductility 11.

The bin areas have been shaded applying linear interpolation of the colors between adjacent data points. A color *blue* was assigned to data points which did not register any difference in the probability of collapse between subduction or crustal motions while A *dark red* color was assigned to the maximum difference in probability of collapse. Other colors have been used to highlight intermediate values of the difference in probability of collapse: *cyan* (20%), *green* (30%), *yellow* (40%), *orange* (50%) and *bright red* (60%).

This representation provides information on the difference in the probabilities but, in order to gain a full understanding of the physical phenomena behind such differences, the plot should be always interpreted in conjunction with to the previous contour plots. Figure 5-8 shows the effect of duration for a ductility level equal to 11. It can be observed that:

- A rectangular portion of the plot can be isolated for shaking levels between 10 and 50% and for the whole period range between 0.1 and 5 sec. This area has been labeled by a blue color indicating no difference in the probability of collapse calculated with either crustal and subduction records. For this shaking interval, there is no influence

of the structural period. Moreover, this region refers to fragility curves where both suites of motions generate 0% probability of collapse;

- Another portion of the plot can be identified as a rectangular area which covers short and intermediate structural periods (specifically from 0.1 to 2 sec) and extreme shaking levels (from 150-200%). This region of the plot has been assigned a color blue and it refers to a '100% collapse' scenario;
- For structures characterized by periods between 0.2 to 2 sec, the duration of ground motions is found to be important for severe shaking levels, specifically from 70% to 120% of shaking intensity. The difference in probability of collapse reaches peaks of 30% to 60% at 100-110% shaking level. This phenomenon is quite consistent throughout the period range from 0.5 sec to 2 sec. For periods shorter than 0.5 sec, a similar trend is observed but limited to a much narrower range of intensity levels (60-100%);
- For structural systems with fundamental periods above 2 sec, the difference in the probability of collapse becomes significant at 60% intensity level and depends on both the structural period and shaking intensity considered. At 100% of shaking intensity, the difference in collapse probability reaches peaks above 60% for structural periods of 2 seconds, while for periods above 3 sec the difference is lower, about 30-40%. With increasing shaking levels, the difference in the probability of collapse is a function of the specific structural period. At intensities above 230% of shaking, the plot shows again an area labeled with blue color, meaning that at that shaking intensities, the effect of long duration motions fades away as both crustal and subduction motions result in 100% probability of collapse.

In order to facilitate the quantification of the surface plot shown in Figure 5-8, a corresponding contour plot can also be generated as shown in Figure 5-9.

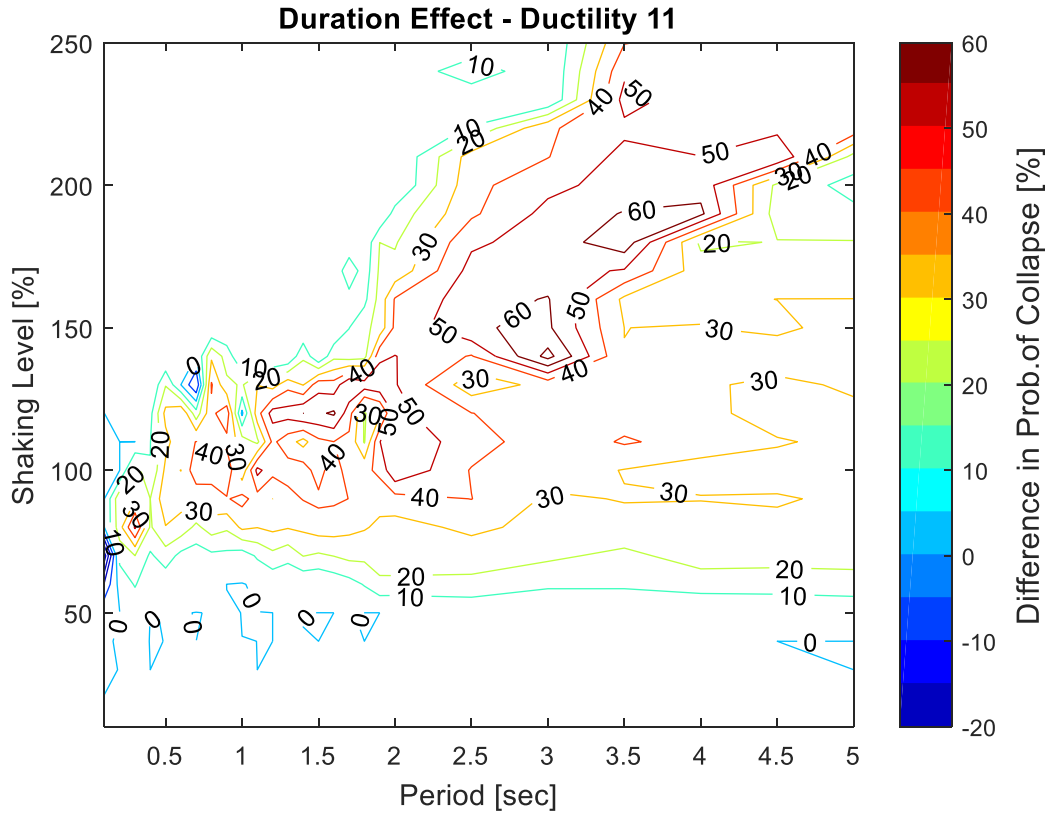


Figure 5-9: Contour plot and evaluation of long duration effect on structural systems with ductility 11.

The curves represent the set of data points (*period; shaking level*) which is associated with the same difference between the probability of collapse generated by subduction motions and crustal motions. The contour interval has been chosen equal to 10% and the same color legend as in Figure 5-8 was applied. The duration effect can be quantified and directly read from each line. The regions of the plot with no lines refer to set of data points, where the duration of ground motion is not significant with respect to the collapse performance. Plots similar to Figure 5-8 have been generated for the other ductility levels considered ($\mu = 3, 5, 7, 9$) and shown in Figures 5.10 to 5.13.

- At very low ductility level ($\mu = 3$), long duration subduction motions have little effect on the difference in probability of collapse. At shaking levels below 50%, there is only a 5 to 10% difference in the probability of collapse due to the longer duration of subduction motions;
- As the ductility increases and the systems reach a capacity equivalent to $\mu = 5$ (Figure 5-11), the difference between collapse probabilities for subduction and crustal

motions increases gradually. For periods between 0.2 to 2 sec, the increase in collapse probability for subduction motions is about 10-20%, with few peaks above 30% difference corresponding to structural periods of 0.6 and 1.6 to 1.9 sec. At periods above 2 sec, the difference in collapse rates becomes more significant. For periods between 2.5 and 5 sec and shaking intensities of 50 to 100%, the difference in probability of collapse is above 40%. A peak of 50% gap in the collapse probability is reached at 80% shaking intensity and at the specific structural period of 3.5 sec;

- Ductility level equal to 7 (Figure 5-12) establishes the threshold in which the duration of ground motions is most important when assessing the structural performance against collapse. For structural periods above 0.5 sec, differences above 30% pertain to the whole period range, and different intensity levels. A portion of the plot can be identified between 2.5 to 4.5 sec and for shaking intensities between 70 to 110%, where long duration motions increase of the collapse probability above 50%. A peak of 60% difference is observed for systems with fundamental periods of 3 and 3.5 seconds at 90% shaking level;
- At ductility capacity equal to 9 (Figure 5-13), the trend previously observed for ductility 7 is maximized, in particular for periods longer than 2 sec and for motions scaled to the 100% hazard intensity. In this portion of the plot, the 50% difference in probability of collapse expanded to longer periods (5 sec) and interests a wider range of shaking intensities (from 80% to 150%).

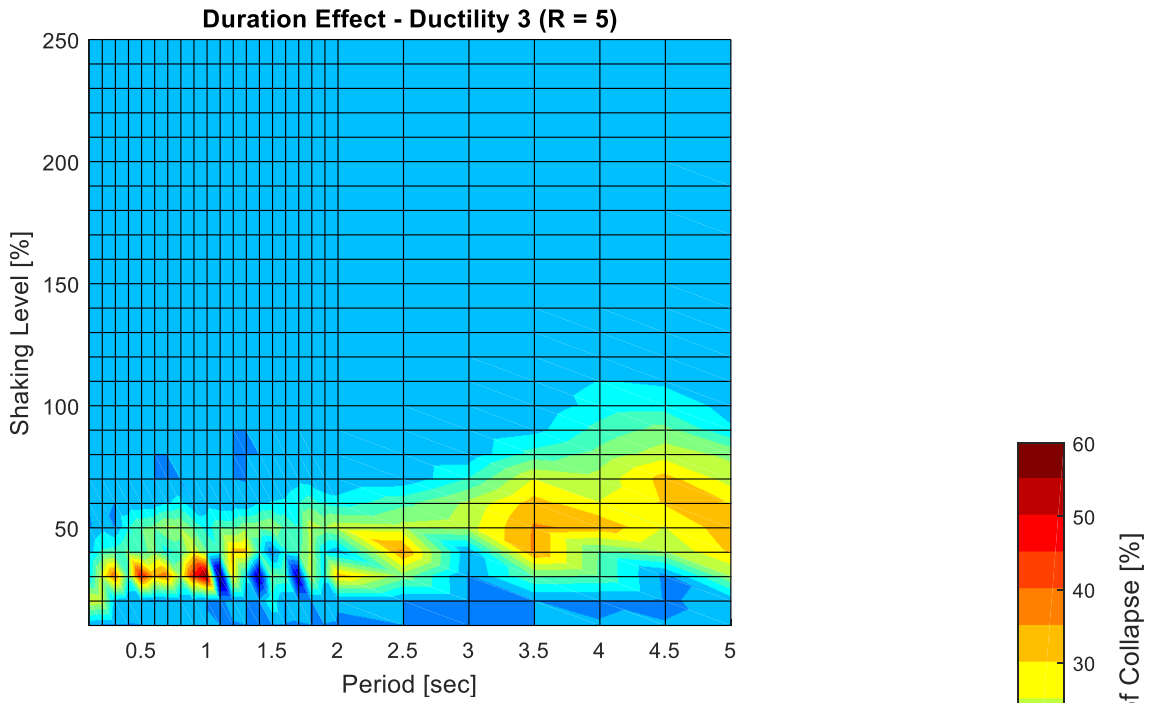


Figure 5-10: Long duration effect for ductility 3.

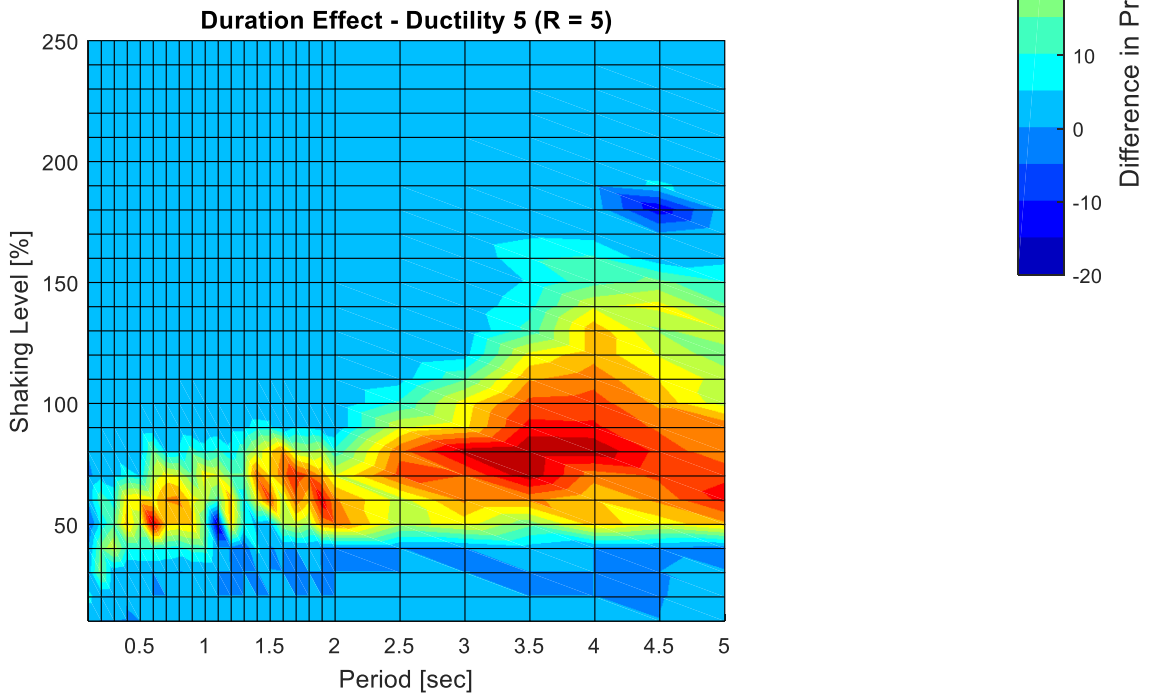


Figure 5-11: Long duration effect for ductility 5.

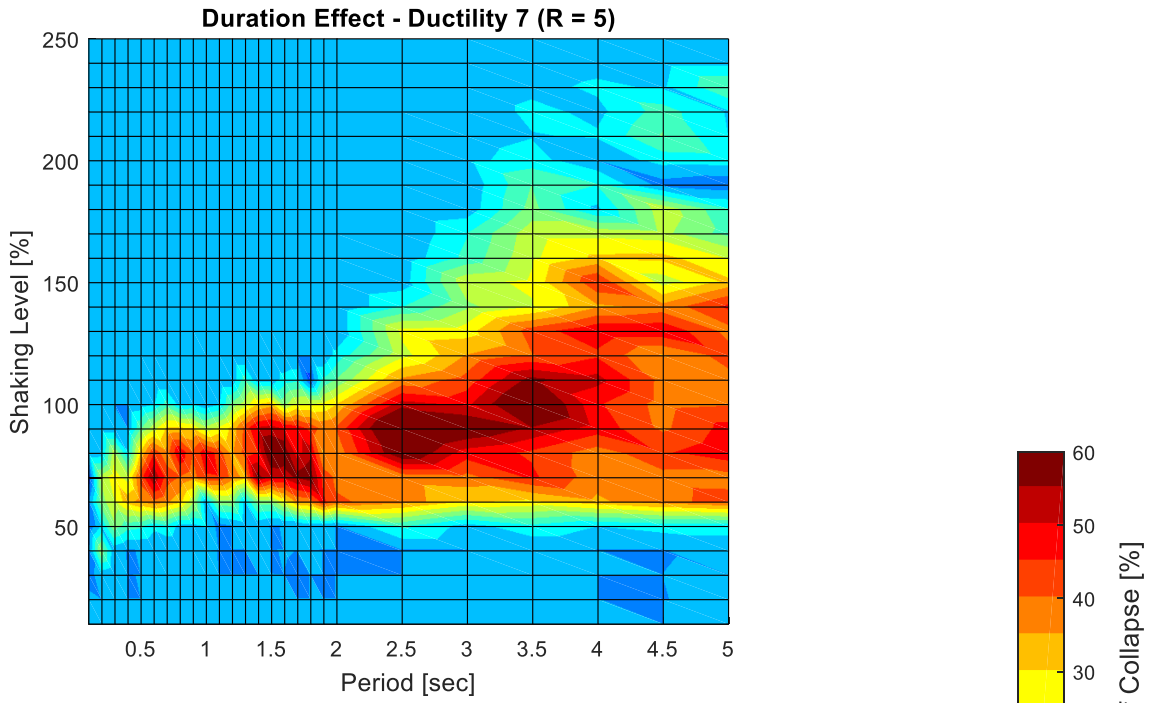


Figure 5-12: Long duration effect for ductility 7.

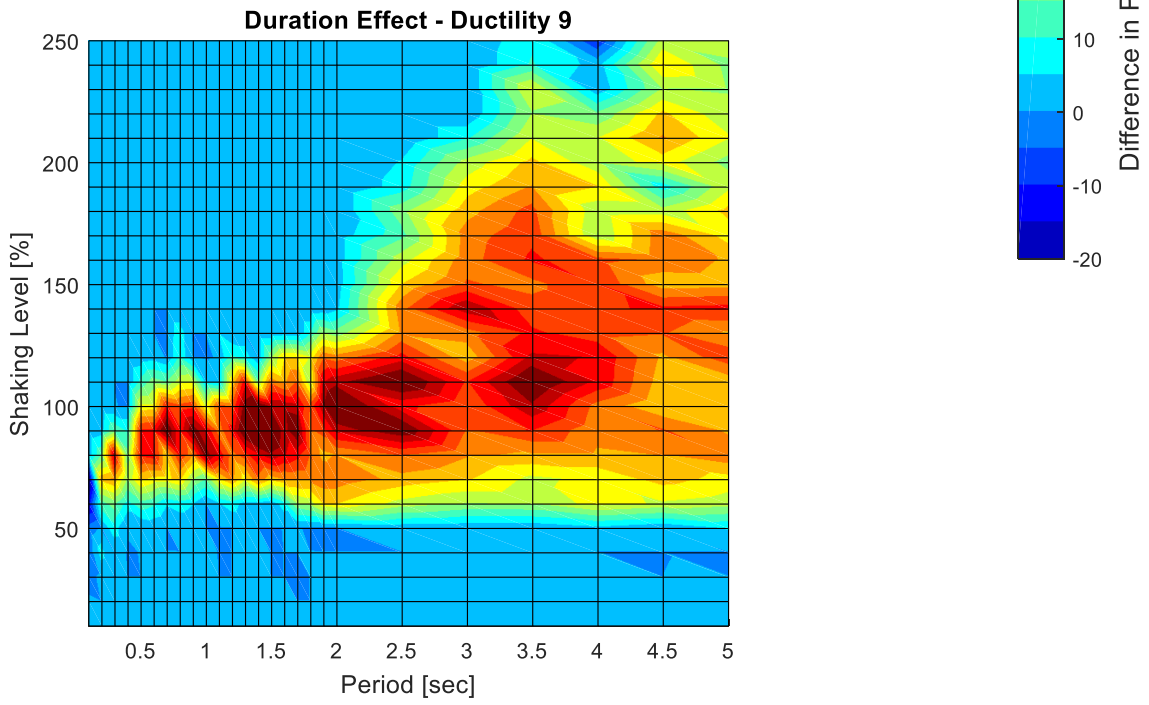


Figure 5-13: Long duration effect for ductility 9.

The companion contour plots similar to Figure 5-9 have been generated for the other ductility levels and included in Appendix D.

The influence of the longer duration of subduction motions on the probability of collapse for buildings designed according to the design UHS spectrum can be quantified retrieving the difference between collapse probabilities from the plot at 100% shaking level in Figure 5-8. The results are illustrated in Figure 5-14, where the collapse probability differences are plotted against the fundamental period for each ductility level considered. At low ductility capacity ($\mu = 3$), the effect of long duration motions at 100% hazard intensity is negligible. As the ductility level increases, the difference in the calculated probabilities becomes more significant. For ductility capacity equal to 5, the duration effect is recognizable at periods longer than 2.5 sec and leads to probability differences as high as 40%. Increasing the rotational capacity, at $\mu = 7$, the periods of interest are from 1.2 to 5 sec and the calculated difference in collapse probability is significantly higher, within 15-65%. If the system is characterized by very high ductility capacities, $\mu = 9$ and 11, the long duration effect pertains to the whole period range, from 0.5 sec to 5 sec, and it is associated with greater differences of probability of collapse.

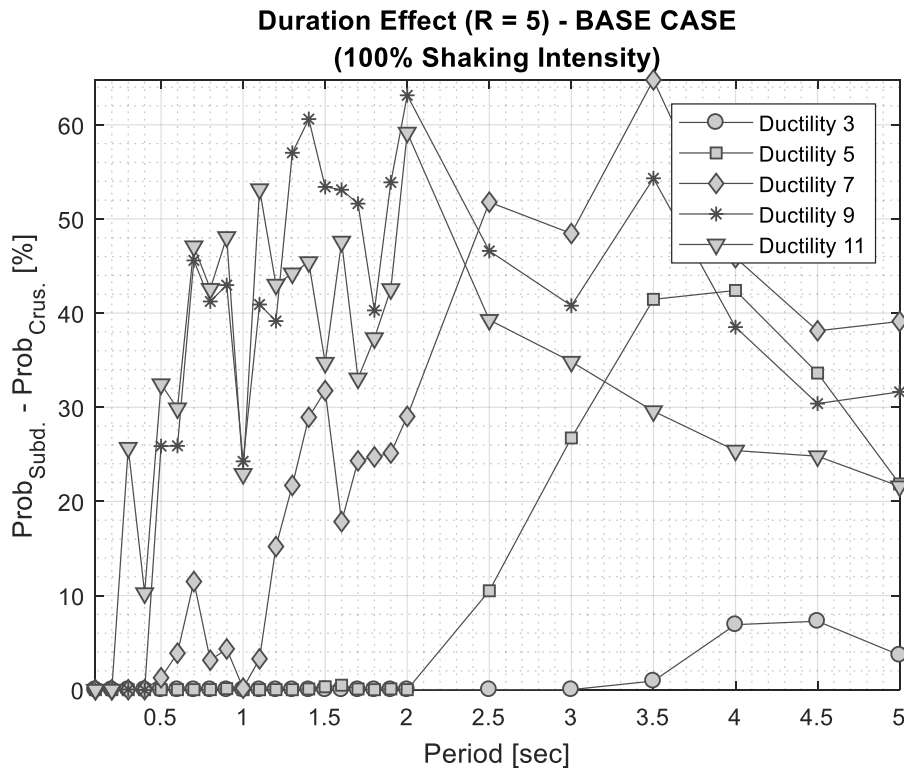


Figure 5-14: Duration effect at base design shaking intensity.

5.4. Discussion

In this Chapter the drifts ratios obtained from the IDA study were used to develop fragility curves for collapse. The fragility curves were developed for each structural period and each ductility level. The study offers insight on:

- the effects of ductility capacity on the probability of collapse;
- the influence of structural period on the probability of collapse;
- the effects of long duration ground motion on the probability of collapse and their variability with ductility capacity and structural period.

The sensitivity analysis showed that for a structure with a given stiffness, period, force reduction factor and yield moment, an increase in *ductility capacity* leads overall, regardless of the duration, to a translation of the fragility curves ‘to the right’, meaning that more ductile systems can withstand larger intensities of shaking compared to less ductile systems. This is quite intuitive; as more ductile systems have a larger capacity to dissipate the energy of the ground motion. Moreover, as shown in Figure 5-2 and in Appendix B, as the ductility of the system decreases, the fragility curves calculated with the subduction and crustal suites tend to get closer to each other. This means that the influence of duration is more evident for more ductile systems. This, again, can be explained as non-ductile systems are likely to reach collapse regardless of the duration of the ground motions, as their capacity is not enough to withstand even a lower number of cycles.

It is difficult to consistently connect the results of this thesis with the findings from previous studies because of differences in the approach followed, such as: the methodology for ground motions selection and scaling, the structural model analyzed, the choice of targeted hazard and intensity measure considered for IDA. Moreover, while in previous studies the effect of duration was evaluated as the difference in the median collapse capacity between long and short duration motions, in this study the effect of duration is quantified as the difference between the probability of collapse for subduction motions and the probability calculated with crustal motions at each specific shaking level.

However, these findings support overall both the results of the parametric study conducted by Raghunandan and Liel (2013) and the findings from the sensitivity analysis conducted on the SDOF bridge pier model by Chandramohan et al. (2015). The trends of the impact of ductility on

collapse performance agree as well with the results found by Chin (2017) on the analysis of a much more detailed model.

The sensitivity study on the *influence of structural period* on the probability of collapse presented in Section 5.2 provides a valuable contribution to knowledge. The influence of structural period is represented by the contour plots (Figures 5-6 and 5-7 and Figures C-1 to C-10). Appendix C illustrates the evolution of the contour plots, reflecting the impact of structural period on the probability of collapse for increasing ductility capacities. It was found that the effect of structural period is conditional on the ductility capacity considered. At low ductility level (ductility 3), the structural performance is quite similar regardless of the period range considered. This holds for the contour plots obtained for both crustal and subduction ground motions. As a consequence, long duration is found to be not a crucial factor in the evaluation of the collapse probability for low ductile systems. This finding reflects the consideration made earlier in this Section about the minor impact of long duration on the collapse probability for low-ductile systems. The contour plots (Figure 5-6, 5-7 and Appendix C) support this finding and the results of previous studies (Raghunandan, 2013; Chandramohan et al., 2015 and Chin, 2017) not only for a specific building (structural period), but extend the trend to a wider range of periods, i.e. 0.1 sec to 5 sec.

For higher ductility levels, the effect of structural period on the probability of collapse depends not only on the ductility level considered, but also on the shaking intensity of the ground motions. For intermediate period structures, i.e. from 0.5 sec to 1.5 sec, the contour plots show a compact, horizontal trend meaning that the structural period does not affect the variation on the structural performance, which is instead dependent on ductility and shaking level only. For systems characterized by periods above 2 sec, the contour curves spread out reaching higher levels of shaking, signifying an overall better performance against collapse. This is particularly emphasized in the contour generated with crustal motions. This might be related to the traditional belief that long period structures would be more likely to resonate with long period motions than short period motions, such as the ones generated from crustal earthquakes.

This finding overall agrees with the general trend indicated by the sensitivity analysis conducted by Raghunandan and Liel (2013).

The *effects of long duration* of subduction motions were evaluated as the difference, at each shaking level and specific structural period, between the collapse probability obtained with subduction motions and the collapse probability for crustal motions.

The parametric study on the SDOF systems showed that the effects of long duration subduction motions depend primarily on three variables: *fundamental period* of the structure, *ductility capacity* and *intensity of shaking*. It is at rotational capacities corresponding to ductility 11 that the effect of duration is maximized and is important for the period range of interest and a significant interval of shaking intensities. For low and intermediate period structures (below 2 sec period), the duration effect is found to be important in a narrower intensity range (60% to 140%), while for systems with periods above 2 sec, duration is important over a much wider range of shaking level, specifically from 60% to 250%. At 100% hazard intensity the results show that duration of ground motions does not affect the collapse performance at low ductilities, but results in a mean increase of 50 % for ductility capacity equal to 11.

For low ductility systems (ductility 3), the effect of the longer duration of ground motions on the probability of collapse is shown to have little effect. This quantifies the qualitative comparison of the contour plots generated for crustal and subduction motions (Figure C-1 and C-2) provided in Appendix C and discussed earlier in this Section.

To investigate the applicability of this approach to MDOF systems, a 6-storey RC moment frame was used to conduct a similar IDA and the results are presented in the following Chapter.

Chapter 6

Effects of long duration shaking on buildings: a case study

“Before I came here, I was confused about this subject. Having listened to your lecture, I am still confused. But on a higher level.”

Enrico Fermi (1901 – 1954)

6.1. Introduction

The two suites of ground motions selected in Chapter 3 and scaled to the Victoria UHS were used to conduct nonlinear IDA to evaluate the effects of long duration subduction motions on the probability of drift exceedance of a MDOF system. The IDA followed the same procedure as described in Chapter 4. In this analysis, the input motions were scaled from 10% to 250% of the design hazard intensity in increments of 10% shaking.

The structural model under consideration is the *Prototype 1* RC frame building developed by the Applied Technology Council and described in the ATC 78 (2011). The general configuration of the Prototype 1 refers to an existing RC frame building originally located in Seattle. For the purpose of this study, the building is assumed to be located in Victoria, BC. According to ATC- 78 (2011), the specific properties of Prototype 1 were those recommended by the American Concrete Institute in ACI 328-08 to ensure ductile performance (2008). This model was implemented in OpenSees computer program (OpenSees, 2017).

The IDA analysis led to the development of fragility curves which highlight the difference in probability of collapse under the crustal and the longer duration subduction motions.

6.2. Description of the model

The model configuration is a 6-storey, 5-bay RC frame building with a square plan area of 112ft x 112 ft. The height of the first storey is 13 ft, while the storey height of the other storeys is 11ft, leading to an overall building height of 68 ft. The building geometry is illustrated in Figure 6-1, where the perimeter frames are shown in blue and the interior frames in green. The perimeter frames were the Seismic Force Resisting System (SFERS), while the interior frames did not contribute to the lateral resistance. Therefore, the IDA analysis was conducted on the planar 2D perimeter frame. The elevation view of the external perimeter frame is shown in Figure 6-2. The end bays are 20 ft wide, while the width of each of the central bays is equal to 24 ft. The beams dimensions are illustrated in Figure 6-2 for the typical end and central bays. The columns dimensions at the first, second and third storey are equal to 28x28 in. The columns in the upper storeys are 24 x24 in. Description of the elements reinforcement is given in details in ATC 78-1 (2012).

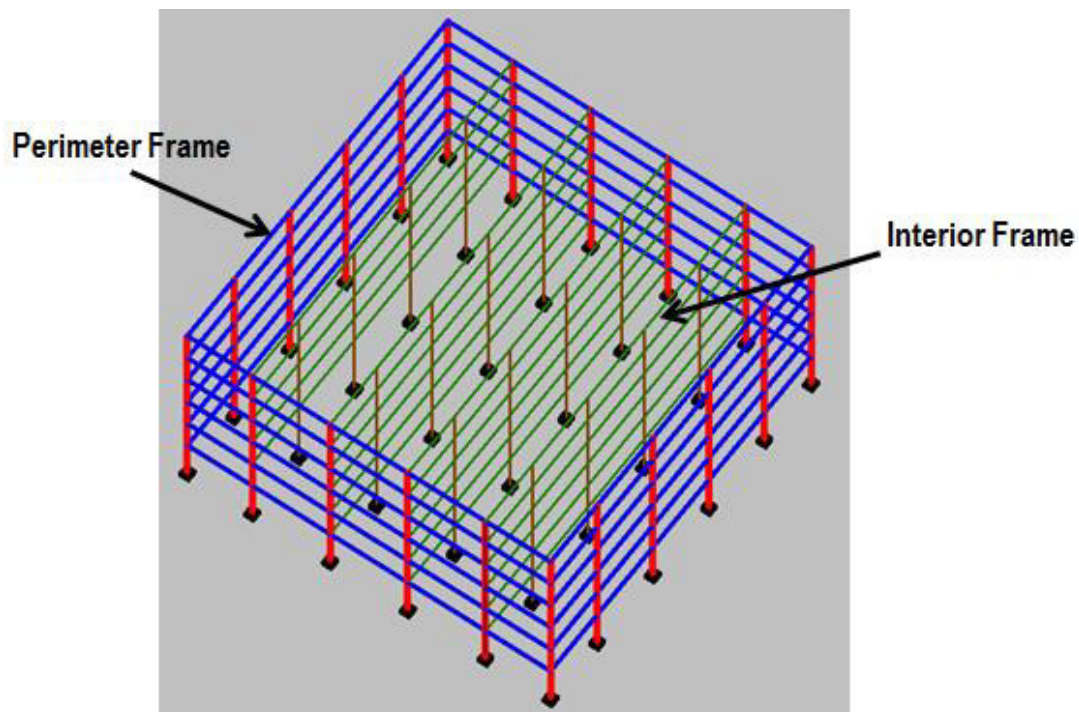


Figure 6-1: 3D view of the prototype building (ATC 78, 2011; ATC 78-1, 2012).

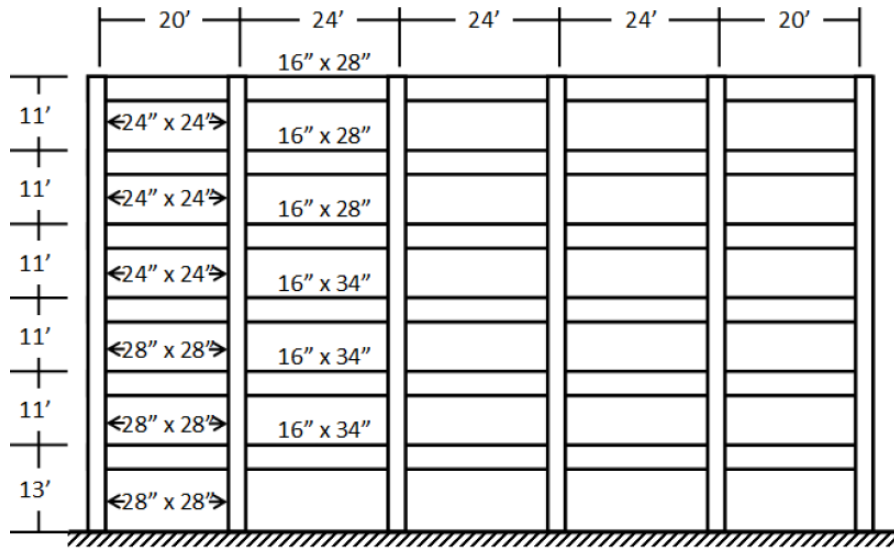


Figure 6-2: Elevation view of the external perimeter frame of the building (ATC 78-1, 2012).

Beams and columns were modeled by elastic line elements with plastic rotational hinges at each end of the line elements. The elastic flexural stiffness of the line elements was reduced for the analysis to take into account the cracked stiffness as described in ATC 78-1 (2012). The diaphragms were modeled as rigid bodies.

Geometrical nonlinearities caused by the P- Δ effect were modeled connecting a leaning column to the perimeter frame through axially rigid links.

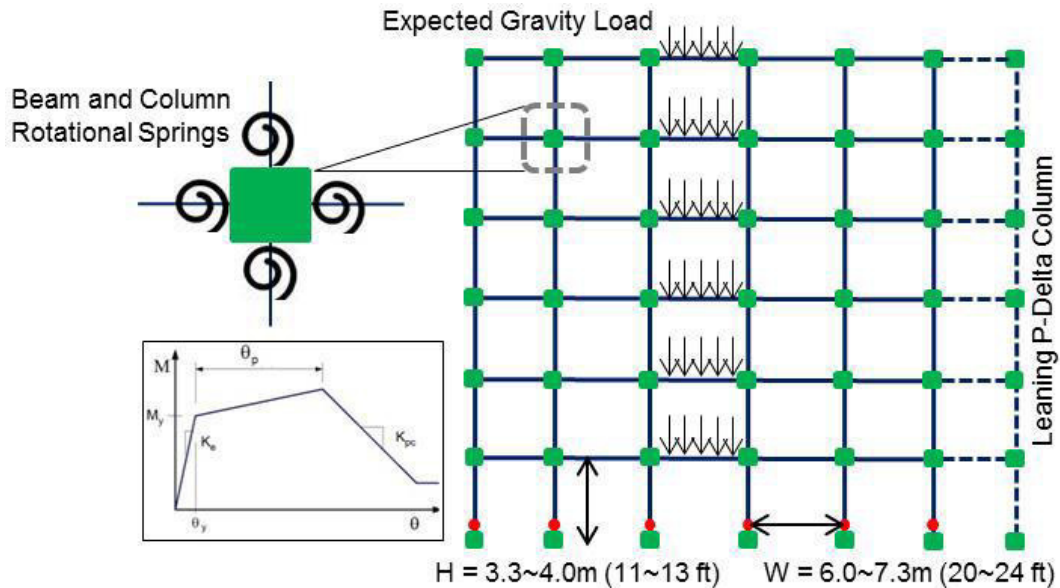


Figure 6-3: Elevation view and modeling scheme of the RC frame (Chin, 2017).

The rotational springs at each end of beam and column elements were modeled as zero-length elements constraining all degrees of freedom except rotation. Each rotational spring was modeled using the Bilinear hysteretic model developed by Ibarra et al. (2005). As in the case of the SDOF systems analyses (Figure 4-2, Chapter 4), the hysteretic model controlling the monotonic and the cyclic behavior of the rotational hinges depends on the parameters M_y , θ_y , θ_p , θ_{pc} and λ .

The values of yield moment M_y and yield rotation θ_y are reported in the ATC 78-1 (2012) for each beam and column cross section. The capping rotation capacity θ_p , post-capping rotation capacity θ_{pc} and deterioration parameter λ (in inches), were described in Chapter 4 and are listed in Table 6-1 (ATC 78-1).

Table 6-1: Backbone curve parameters.

Parameter	Columns	Beams
θ_p	0.06	0.05
θ_{pc}	0.1	0.15
λ	110	125

6.3. Results of the IDA and fragility curves

The first three natural periods of the building were determined by modal analysis to be $T_1 = 1.54$ sec, $T_2 = 0.54$ sec and $T_3 = 0.28$ sec.

The drift ratios from the IDA have been recorded for each building storey and the maximum of these drift ratios was used to generate the IDA curves. Figure 6-3 and Figure 6-4 show the IDA curves linking shaking levels and maximum drift ratios for crustal and subduction motions respectively. The vertical dotted line indicates drift ratio equal to 0.05. This value was chosen as the drift ratio corresponding to the flattening of the IDA curves. The fragility curves were calculated as the probability of exceeding this drift ratio.

A comparison of the IDA curves for crustal and subduction motions shows that the subduction motions reach maximum drift ratio at lower intensity of shaking than the crustal IDAs. This is due to the effect of the longer duration of shaking of the subduction motions.

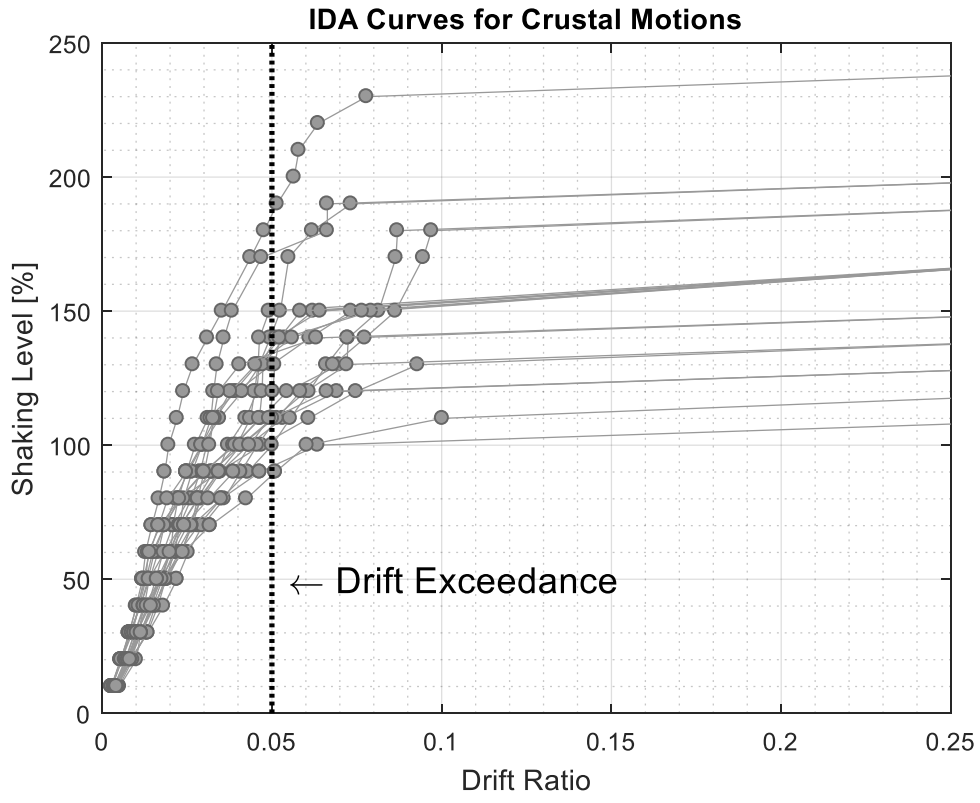


Figure 6-4: IDA curves obtained with crustal motions.

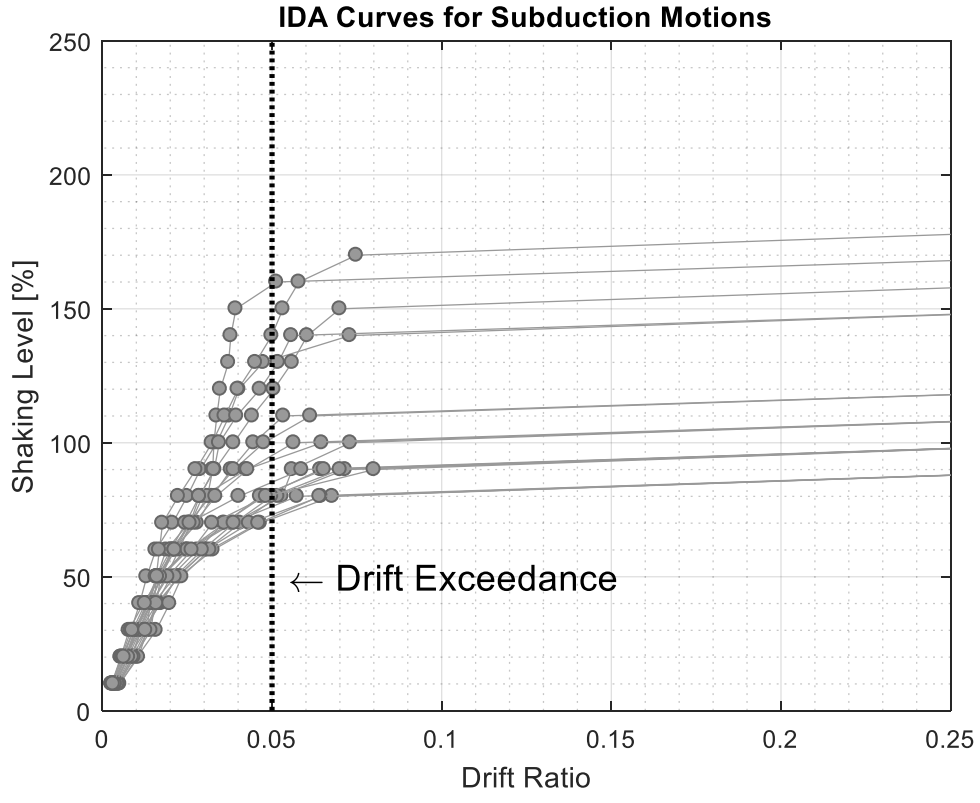


Figure 6-5: IDA curves obtained with subduction motions.

6.4. Discussion

This Chapter presents the results of a IDA study conducted on a MDOF system representing a 6-storey RC moment frame located in Victoria, BC. The motions selected in Chapter 3 and scaled to the Victoria UHS were used as input for dynamic analysis. The maximum drift ratios from the IDA have been assumed to be lognormally distributed at each shaking level and have been used to generate fragility curves showing the probability of the maximum drift exceeding the target ratio of 0.05. In Figure 6-5 the fragility curve from the crustal motions is shown in red and the subduction fragility curve in blue. At shaking levels between 70% and 180%, the subduction curve lies above the crustal one, leading to higher probabilities of drift ratio exceedance due to the longer duration of motions. For very high levels of shaking (above 190%) and shaking intensities below 60%, the two curves overlap indicating the same probability of drift ratio exceedance for crustal and subduction motions. When the crustal motions are scaled to match the Victoria UHS (100% shaking level), the probability of collapse is equal to 16%. On the other hand, at 100% of design hazard intensity, the subduction suite of motion leads to a probability of drift exceedance equal to 80%. This 64% increase in the probability reflects the effect of long duration of subduction ground motions. These conclusions confirm the findings illustrated in Chapter 4-5.

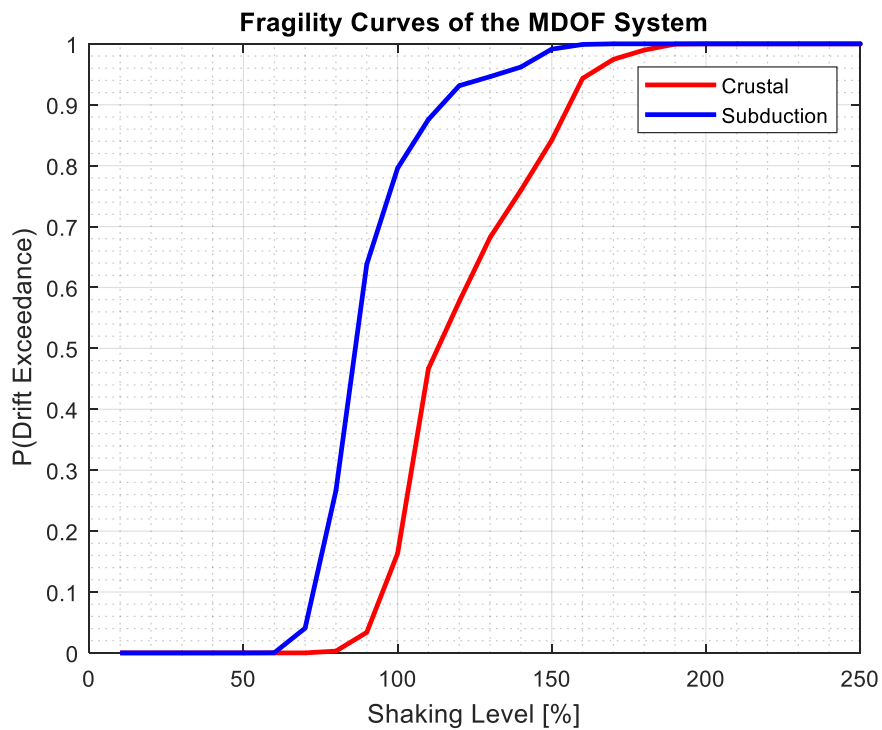


Figure 6-6: Fragility curves for crustal and subduction motions.

The trend of the fragility curves shown in Figure 6-6 supports the findings from previous studies on the effect of long duration motions on RC moment resisting frames which showed the fragility curves for long duration motions lying above the one for short duration motions. This resulted, at specific intensity levels, in higher probability of collapse for long duration motions (Raghunandan & Liel, 2013; Chin, 2017). Differences in the probability values are to be expected due to the difference in the models, the methodology of selection and scaling the ground motions and to the choice of intensity parameters for IDA. In particular, the study presented in this Chapter uses a structural model very similar to Chin (2017). The comparison between these results and Chin's shows a very similar trend, with the difference that in Chin's work the fragility curves shifted towards the right of the diagram (i.e. towards higher levels of shaking), signifying an overall better performance of the RC moment frame. It is important to note that the main difference between the two studies is that Chin scaled the motions to match a much narrow period range and the selection process was conducted independently for subduction and crustal motions.

It is of interest to tie this discussion with the results obtained in Chapter 5 for the SDOF analyses. As a preliminary study, the fragility curves obtained for the MDOF system (Figure 6-7) have been compared with the curves generated in Chapter 5 for a SDOF system with period equal to 1.5 sec and ductility capacity 7 (Figure 6-8). From the results of a pushover analysis conducted by Chin (2017), the system ductility of the RC moment frame was estimated to be about 6. Ductility 7 seemed to be a good compromise for comparison. The same pattern for the fragility curves applies to both cases: the subduction fragility curve lies above the crustal one at intermediate shaking intensities. At 100% shaking level, the duration effect evaluated for the RC moment frame was a difference in collapse probability of 64% (80%-16%). A similar probability was reached in the SDOF system at 80% shaking level and estimated to be 62% (=86%-24%). The fragility curves for the MDOF systems are shifted towards right as the degradation of the MDOF model is less severe than that for the SDOF system. The method based on SDOF system could be further improved and be used as a quick estimator of the effects of duration on more complex MDOF models. The modeling of the SDOF system should be enhanced according to:

- A correspondence between ductility of the SDOF and MDOF systems;
- Degradation parameters of the SDOF systems that reflect the degradation modeled in the corresponding real building.

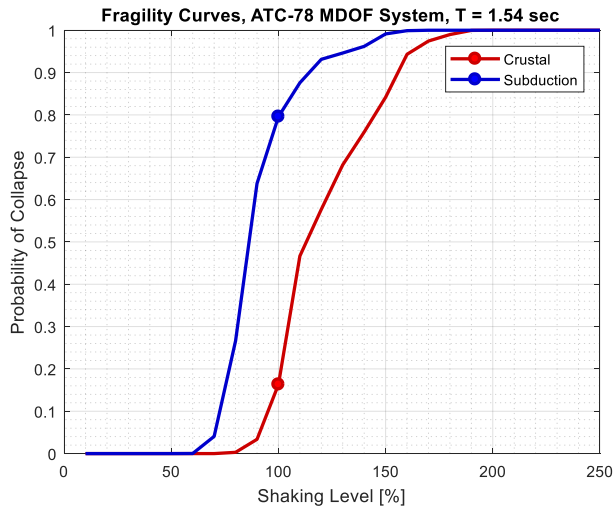


Figure 6-7: Fragility curves for the 6-storey RC moment frame.

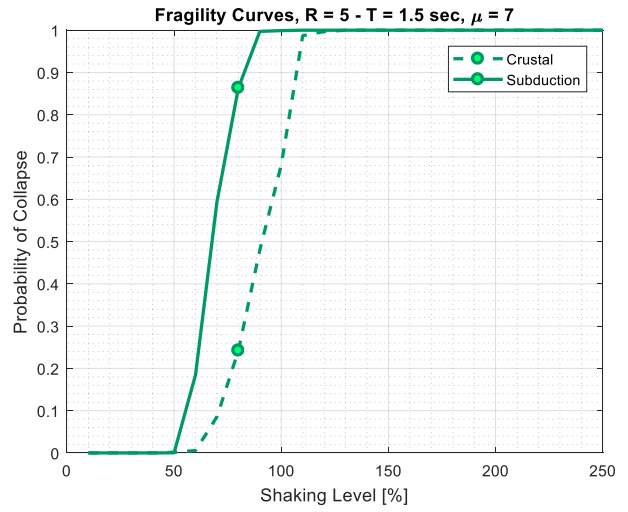


Figure 6-8: Fragility curves for a SDOF system of T = 1.5 sec and ductility 7.

Chapter 7

Summary and conclusions

“I put my heart and my soul into my work, and have lost my mind in the process.”

Vincent van Gogh (1853 – 1890)

7.1. Summary and conclusions

The *first objective* of this dissertation was to investigate the damage level observed during the 2010 Maule earthquake (stations of Maipu and Curico) and the 2011 Tohoku earthquake (stations of Tsukidate and Sendai) using the characteristics of the ground motions recorded at the sites. This was achieved in Chapter 2, where different characteristics of the subduction ground motions were considered to explore the relationship with the structural damage observed at the sites of interest.

The most striking example was the one concerning the damage observed at Tsukidate and Sendai stations after the 2011 Tohoku earthquake. The JMA intensity at Tsukidate was 7, while in Sendai the rating was 6+, yet much greater damage was observed at Sendai than at Tsukidate. Several shaking parameters were considered for analysis. PGA, Arias Intensity and frequency content did not relate well with the post-earthquake field observations. Elastic response spectra and constant-ductility response spectra provided only limited information about the damage potential of the records. Only the constant strength spectrum showed to be consistently related to the damage potential of the earthquake motions. The analysis of the constant strength spectra

showed that the ductility demands at Sendai were consistently larger than at Tsukidate over a wide period range (0.15-3.2 sec). Also, useful information can be obtained by the ratios between constant strength spectra ordinates, which give the relative damage potential of two different earthquake motions.

Overall, the study showed that among the parameters considered for analysis, the indices based exclusively on shaking characteristics proved not to relate well with the damage observed in the field. Damage measures reflecting both the ground motion shaking characteristics and the elastic structural response provide limited information and do not relate well to the observed damage. It is only when the inelastic response is considered (i.e. nonlinear time history analysis, displacement constant-ductility spectra and constant-strength spectra), that the damage potential of the motions can be better appreciated. In particular, the comparison of constant-strength spectra clearly showed that the Sendai motion has the potential to cause larger demands on structural systems than the motion at Tsukidate.

The *second objective* of this thesis was the investigation of the impact of long duration subduction motions on the seismic performance of structural systems dominated by a single-mode response. This objective was fulfilled in Chapters 3, 4 and 5 where an extensive parametric IDA study on single-mode dominated structures was conducted to investigate the effects of long duration subduction motion on the structural performance. Two suites of spectrally compatible ground motions have been used for analysis representing long duration subduction and short duration crustal motions respectively. The motions were scaled to match the UHS for a site in Victoria, BC and considering a probability of exceedance of 2% in 50 years. The drift ratios from IDA analyses were used to generate fragility curves to quantify the effect of duration of subduction motions. This effect was evaluated as the increase in the probability of collapse (or drift exceedance) obtained with the subduction motion against the crustal motions at each shaking level.

The *third objective* of this dissertation was to investigate the effects of long duration subduction motions on the response of an existing Multi-Degree-of-Freedom (MDOF) structure and was achieved in Chapter 6. To this end, the two sets of compatible motions obtained in Chapter 3 and previously used in the parametric study for the SDOF systems were used as input motions for a IDA on a 6-storey RC moment frame. The resulting drift ratios were used to develop fragility

curves to evaluate the effects of long duration subduction motions on the probability of drift exceedance.

The significant contributions of this study to the state-of-knowledge are:

- Constant strength spectrum showed a strong relationship to the damage potential of the earthquake motions investigated. These spectra allow the evaluation of the ductility, hence displacement demands, imposed by a given ground motion on a variety of systems covering a wide range of fundamental periods and specific constant strength conditions. Thus, constant strength spectra proved to be the best tool to evaluate the damage potential of earthquake motions.
- The parametric study on the SDOF systems showed that the effects of long duration subduction motions depend primarily on three variables: fundamental period, ductility capacity and intensity of shaking.
 - It is at very high rotational capacities ($\mu = 11$) that the effect of duration is maximized and is important for the whole period range of interest and a significant interval of shaking intensities. For systems characterized by low ductility capacities ($\mu = 3$), the effect of duration is not as pronounced;
 - The influence of structural period on the effect of long duration of subduction motions can be particularly appreciated at high ductility capacities ($\mu = 11$). For low and intermediate period structures (below 2 sec period), the duration effect is found to be important within a narrow intensity range (60% to 140%), while for systems with periods above 2 sec, duration is important over a much wider range of shaking level (60 to 250%);
 - When the motions are scaled to match the Victoria UHS, the results show that duration of ground motions, results in a mean increase of 50 % for ductility capacity equal to 11. On the other hand, duration does not significantly affect the collapse performance of systems characterized by low ductilities.

- The IDA analysis of the 6-storey RC moment frame confirmed the higher demands due to long duration of subduction ground motions as indicated by the SDOF IDA study. The fragility curves developed for crustal and subduction motions and indicated that the probability of drift exceedance is significantly higher when considering long duration subduction motions.
- The results of these studies show that the effect of long duration of subduction ground motions on the performance of structural systems is important for design and is a key factor to be considered during the selection of earthquake motions for analysis. This result is consistent with the findings obtained by previous researchers.

7.2. Recommendations for future research

The following bullet points summarize recommendations for future research in this area.

- *Further investigations on the damage potential of subduction ground motions.* More research is needed to further investigate the relationship between the damage observed during post-earthquake reconnaissance and subduction ground motion parameters. The study in Chapter 2 could be further expanded considering constant strength spectra developed with more refined hysteretic models including, for instance, strength degradation.
- *Creation of a comprehensive database of the results of nonlinear dynamic analyses on MDOF systems.* In this study, the investigation of the effects of long duration subduction motions on MDOF structures was conducted on the single example of a 6-storey RC moment frame building. Further analyses are needed on a more extensive database of MDOF structures, as to represent a much broader diversity of building typologies and structural periods. The analyses should consider also floor accelerations and inter-storey drift demands thus allowing some insight on the expected damage as well as on the probability of collapse. This investigation would enhance the understanding on the performance of each structural typology against long duration motions and on the impact of higher mode response on the duration effect.

- *Investigation on the effect of long duration subduction ground motions on performance states other than collapse.* Structures such as hospitals and other emergency facilities are currently treated in the Building Code as post-disaster buildings and have been assigned the highest Importance Category, involving stricter drift limits. The effect of long duration motions could be further investigated on these performance states. It would be also of practical interest to study the effects of long duration motions on a performance level representing the boundary between a feasible repair and a scenario where the building repair is impractical, that is irreparable damage. This would give a significant insight on decision making for post-earthquake retrofit interventions.
- *Investigation on the effects of long duration on non-structural damage.* The importance of non-structural damage is sometimes underestimated and attention is paid mostly to structural collapse. However, non-structural failures represent most of the earthquake damage and have costly consequences. Therefore, it is important to investigate the influence of long duration motions on non-structural failures and in the evaluation of seismic risk to limit losses.
- *Consideration of P- Δ effects on the SDOF study.* The parametric study on SDOF system illustrated in Chapter 4 and 5 was conducted without considering P- Δ effects which could potentially alter the results. The SDOF study can be further developed including such effects.
- *Consideration of different force reduction factor values on the SDOF study.* The SDOF system was modeled in Chapter 4 considering a force reduction factor R equal to 5. It would be of interest to investigate how the results of the study change when considering other values of R.
- *Extension of this study to other site locations.* This study was conducted considering ground motions scaled to the UHS for Victoria, BC. Further analyses should be

carried out for other sites that are exposed to significant seismic hazard to investigate in what measure the effects of long duration of subduction motions influence the seismic performance of structures.

- *Investigation on the influence of Soil-Structure-Interaction (SSI) on the effects of long duration subduction motions.* In this research, both the SDOF and MDOF systems were modeled considering a fixed-based condition. Further studies should be conducted on systems with a non-rigid foundation to understand in what measure the boundary condition at the base of the building influence the duration effect.
- *Incorporating duration effects in code design.* As pointed out earlier in the thesis, code design is based on design spectra that do not reflect the effects of long duration. One approach to account for long duration in design would be to develop a modification factor to be applied to the current code design forces. Extensive research would be required to establish the necessary database to support a modification factor.

Bibliography

- Adams, J., & Halchuk, S. (2003). *Fourth generation seismic hazard maps of Canada: Values for over 650 Canadian localities intended for the 2005 National Building Code of Canada*. Geological Survey of Canada, Open File 4459, Ottawa.
- Adams, J., Basham, P. W., & Halchuk, S. (1995). Northeastern North American earthquake potential - new challenges for seismic hazard mapping. *Current Research 1995-D*, 91-99.
- Allen, T. I., Adams, J., & Halchuk, S. (2015a). The seismic hazard model for Canada: Past, present and future. *Proceedings of the Tenth Pacific Conference on Earthquake Engineering*. Sydney, Australia.
- Allen, T., Luco, N., & Halchuk, S. (2015b). Exploring risk-targeted ground motions for the National Building Code of Canada. *Proceedings of the 11th Canadian Conference on Earthquake Engineering*. Victoria, Canada: Canadian Association for Earthquake Engineering.
- American Concrete Institute. (2008). *Building Code Requirements for Structural Concrete (ACI 318M-08) and Commentary*.
- Applied Technology Council. (2010). *ATC 72-1: Modeling and Acceptance Criteria for Seismic Design and Analysis of Tall Buildings*.
- Applied Technology Council. (2011). *ATC 78: Identification and mitigation of seismically hazardous older concrete buildings. Interim methodology evaluation*. Redwood City.
- Applied Technology Council. (2012). *ATC 78-1 Evaluation of the methodology to select and prioritize collapse indicators in older concrete buildins*. Redwood City.
- Applied Technology Council. (2017). *ATC 116: Developing solutions to the Short-Period Building Performance Paradox: Study for Wood Light-Frame Buildings*. Redwood City CA.
- Araki, Y., & Hjelmstad, K. (2000, February 29). Criteria for assessing dynamic collapse of elastoplastic structural systems. *Earthquake Engineering and Structural Dynamics*, 29, 1177-1198.
- Arias, A. (1970). A measure of earthquake intensity. (R. Hansen, Ed.) *Seismic Design for Nuclear Power Plants*, 438-483.
- ASCE 7. (2016). *Minimum Design Loads and Associated Criteris for Buildings and Other Structures*.

- Atkinson, G. M., & Adams, J. (2013). Ground motion prediction equations for application to the 2015 Canadian national seismic hazard maps. *Canadian Journal of Civil Engineering*, 40(10), 988-998. doi:10.1139/cjce-2012-0544
- Atkinson, G. M., & Boore, D. M. (2003). Empirical Ground-Motion Relations for Subduction-Zone Earthquakes and Their Application to Cascadia and Other Regions. *Bulletin of the Seismological Society of America*, 93(4), 1703-1729.
- Atwater, B. (1987). *Probable local precedent for earthquakes of magnitude 8 or 9 in the Pacific Northwest*. US Geological Survey.
- Atwater, B. F. (1987, May 22). Evidence for Great Holocene Earthquakes along the Outer Coast of Washington State. *Science*, 236(4804), 942-944.
- Backer, J. W., & Cornell, A. C. (2006). Spectral Shape, epsilon and record selection. *Earthquake Engineering and Structural Dynamics*, 35, 1077-1095. doi:10.1002/eqe.571
- Baker, J. W. (2011). Conditional Mean Spectrum: Tool for ground motion selection. *Journal of Structural Engineering*, 137(3), 322-331. doi:10.1061/(ASCE)ST.194-541X0000215
- Baker, J. W. (2015). Ground motion selection for performance-based engineering, and Conditional mean Spectrum as a selection tool. *Proceedings of the Tenth Pacific Conference on Earthquake Engineering*. Sydney, Australia.
- Baker, J. W., Jayaram, N., & Shahi, S. (2010). *rec_selection_meta_data*. Retrieved from <http://peer.berkeley.edu/transportation/projects/ground-motion-studies-for-transportation-systems/>
- Baker, J. W., Lin, T., Shahi, S. K., & Jayaram, N. (2013). *New Ground Motion Selection Procedures and Selected Motions for the PEER Transportation Research Program*. University of California, College of Engineering. Berkeley: Pacific Earthquake Engineering Center. Retrieved from http://peer.berkeley.edu/publications/peer_reports/reports_2011/webPEER-2011-03-BAKERetal.pdf
- Bazzurro, P., & Cornell, C. (2002). Vector-valued Probabilistic Seismic Hazard Analysis (VPSHA). *Proceedings of the 7th U.S. National Conference on Earthquake Engineering*. Boston, U.S.A.
- Bebamzadeh, A., Ventura, C. E., & Fairhurst, M. (2015). S2GM: Tool for Selection and Scaling of Ground Motions. *Los Angeles Tall Buildings Design Conference*. Los Angeles, CA.

- Bertero, V. V. (1977). Strength and deformation capacities of buildings under extreme environments. (P. KS, Ed.) *Structural Engineering and Structural Mechanics*, 211-215.
- Bolt, B. (1973). Duration of Strong Ground Motion. *5th World Conference on Earthquake Engineering*. Rome.
- Bommer, J. J., & Martinez-Pereira, A. (1999). The Effective Duration of Earthquake Strong Motion. *Journal of Earthquake Engineering*, 3(2), 127-172.
- Bommer, J. J., & Martinez-Pereira, A. (2000). Strong-motion parameters: definition, usefulness and predictability. *Proceedings of the 12th World Conference in Earthquake Engineering*. Auckland, New Zealand: Upper Hutt NZ.
- Bommer, J. J., Hancock, J., & Alarcon, J. E. (2006). Correlations between duration and number of effective cycles of earthquake ground motion. *Soil Dynamics and Earthquake Engineering*(26), 1-13.
- Bommer, J. J., Magenes, G., Hancock, J., & Penazzo, P. (2004). The Influence of Strong-Motion Duration on the Seismic Response of Masonry Structures. *Bulletin of Earthquake Engineering*, 2, 1-26.
- Bommer, J., & Boore, D. (2004). Engineering Seismology. In R. Selley, R. Cocks, & I. Plimer (Eds.), *Encyclopaedia of Geology* (pp. 499-514). Oxford: Elsevier.
- Campillo, M., Gariel, J., Aki, K., & Sanchez-Sesma, F. (1989, December). Destructive Strong Ground Motion in Mexico City: Source, Path and Site Effects During Great 1985 Michoan Earthquake. *Bulletin of the Seismological Society of America*, 79(6), 1718-1735.
- Cantagallo, C., Camata, G., Spacone, E., & Corotis, R. (2012). The variability of deformation demand with ground motion intensity. *Probabilistic Engineering Mechanics*, 28, 59-65. doi:10.1016/j.probengmech.2011.08.016
- Cao, V. V., & Ronagh, H. R. (2014). Correlation between seismic parameters of far-fault motions and damage indices of low-rise reinforced concrete frames. *Soil Dynamics and Earthquake Engineering*, 10-112. doi:10.1016/j.soildyn.2014.06.020
- Capraro, I., Ventura, C. E., & Finn, L. (2017). Understanding Subduction Ground Motions and their Relation to Structural Damage. *6th Structural Engineers World Congress*. Cancun, Mexico.

- Chandramohan, R., Baker, J. W., & Deierlein, G. G. (2014). Hazard-consistent ground motion duration: calculation procedure and impact on structural collapse risk. *10th U.S. National Conference on Earthquake Engineering*. Anchorage, Alaska.
- Chandramohan, R., Baker, J. W., & Deierlein, G. G. (2016). Quantifying the influence of ground motion duration on structural collapse capacity using spectrally equivalent records. *Earthquake Spectra*.
- Chandramohan, R., Lin, T., Baker, J. W., & Deierlein, G. G. (2013). Influence of Ground Motion Spectral Shape and Duration on Seismic Collapse Risk. *10th International Conference on Urban Earthquake Engineering*. Tokyo, Japan.
- Chin, D. H. (2017). *Effects of Long Duration Ground Motions on the Probability of Drift Exceedance for Reinforced Concrete Frames near the Cascadia Subduction Zone*. MSc Thesis, The University of British Columbia, Vancouver.
- Chiou, B., Darragh, R., Gregor, N., & Silva, W. (2008). NGA Project Strong-Motion Database. *Earthquake Spectra*, 24(1), 23-44.
- Chopra, A. K. (2016). *Dynamics of Structures: Theory and Applications to Earthquake Engineering*. (5th ed.). Upper Saddle River, New Jersey, USA: Pearson Prentice Hall.
- Clague, J. J. (1997). Evidence for large earthquakes at the Cascadia subduction zone. *Reviews of Geophysics*, 35(4), 439-460.
- Clough, R. (1966). *Effect of stiffness degradation on earthquake ductility requirements*. University of California, Department of Civil Engineering, Berkeley.
- Cluff, L. S. (2008). Effects of the 2004 Sumatra-Andaman Earthquake and Indian Ocean Tsunami in Aceh Province. *The Bridge*, 37(1), pp. 12-16. Retrieved from <https://www.nae.edu/File.aspx?id=7405&v=70df971>
- Cosenza, E., & Manfredi, G. (2000). Damage Indices and Damage Measures. (J. W. Ltd., Ed.) *Progress in Structural Engineering and Materials*(2), 50-59.
- COSMOS. (2017). *Strong-Motion Virtual Data Center (VDC)*. Retrieved July 06, 2017, from <http://www.strongmotioncenter.org/>
- Earthquake Solutions. (2017). *Providing State-of-the-Art Software for Structural and Earthquake Engineering*. Retrieved July 4, 2017, from Bispec 2.20: <http://www.eqsols.com/Pages/Bispec.aspx>

- EERI. (2010). *The Mw 8.8 Chile Earthquake of February 27, 2010*. Earthquake Engineering Research Institute.
- Elenas, A. (2000). Correlation between seismic acceleration parameters and overall structural damage indices of buildings. *Soil Dynamics and Earthquake Engineering*, 20(1-4), 93-100. doi:10.1016/S0267-7261(00)00041-5
- Elenas, A. (2011). Intensity parameters as damage potential descriptors of earthquakes. In M. Papadrakakis, M. Fragiadakis, & V. Plevris (Ed.), *Proceedings of the 3rd International Conference on Computational Methods in Structural Dynamics and Earthquake Engineering*. 26, pp. 327-334. Corfu, Greece: Springer, Dordrecht. doi:10.1007/978-94-007-5134-7_19
- Elenas, A., Lioios, A., Vasiliadis, L., Sakellari, M., & Koliopoulos, P. (2001). A numerical estimation of the interrelation between acceleration parameters and damage indicators in earthquake engineering. In E. Aifantis, & A. N. Kounadis (Ed.), *Proceedings of the 6th National Congress of Mechanics. I*, pp. 254-260. Thessaloniki, Greece: Hellenic Society of Theoretical and Applied Mechanics.
- Elnashai, A. S., Genturk, B., Kwon, O.-S., Al-Qadi, I. L., Hashash, Y., Roesler, J. R., . . . Valdivia, A. (2010). *The Maule (Chile) Earthquake of February 27, 2010*. Mid-America Earthquake Center.
- Fairhurst, M., Bebamzadeh, A., & Ventura, C. E. (2017). Collapse risk of tall concrete shearwall buildings under long duration ground motions. *Los Angeles Tall Buildings Structural Design Council Conference*, (p. 14). Los Angeles.
- FEMA 350. (2000). *Recommended Seismic Design Criteria for New Steel Moment-Frame Buildings*. Washington, DC: U.S. Federal Emergency Management Agency.
- FEMA 351. (2000). *Recommended Seismic Evaluation and Upgrade Criteria for Existing Welded Steel moment-Frame Buildings*. Washington, DC: U.S. Federal Emergency Management Agency.
- FEMA P695. (2009). *Quantification of Building Performance Factors*. Applied Technology Council, Washington, DC.
- Fontara, I. K., Athanatopoulou, A. M., & Avramidis, I. E. (2012). Correlation between advanced, structure-specific ground motion intensity measures and damage indices. *Proceedings of the 15th World Conference in Earthquake Engineering*. Lisbon, Portugal.

- Foschaar, J., Baker, J., & Deierlein, G. (2012). Preliminary assessment of ground motion duration effects on structural collapse. *Proceedings of the 15th World Conference on Earthquake Engineering*. Lisbon, Portugal.
- GEER Association. (2010). *Geo-Engineering Reconnaissance of the 2010 Maule, Chile Earthquake*.
- Ghofrani, H., & Atkinson, G. M. (2013). Ground-Motion Prediction Equations for Infrface Earthquake of M7 to M9 Based on Empirical Data from Japan. *Bulletin of Earthquake Engineering*. doi:0.1007/s10518-013-9533-5
- Goldfinger, C., Galer, S., Beeson, J., Hamilton, T., Black, B., Romsos, C., . . . Morey, A. (2017). The importance of site selection, sediment supply, and hydrodynamics: A case study of submarine paleoseismology on the northern Cascadia margin, Washington USA. *Marine Geology*, 384, 4-46.
- Halchuk, S., & Adams, J. (2008). *Fourth generation seismic hazard maps of Canada: Maps and grid values to be used with the 2005 National Building Code of Canada*. Geological Survey of Canada, Open File 5813. doi:10.4095/225402
- Halchuk, S., Adams, J., & Allen, T. (2016). *Fifth Generation Seismic Hazard Model for Canada: Crusta, In-slab, and Interface hazard values for Southwestern Canada*. Geological Survey of Canada, Open File 8090. doi:doi:10.4095/299244
- Halchuk, S., Allen, T., & Rogers, G. (2014). *Fifth Generation Seismic Hazard Model Input Files as Proposed to Produce Values for the 2015 National Building Code of Canada*. Geological Survey of Canada, Open File 7576. doi:10.4095/293907
- Hancock, J., & Bommer, J. J. (2006). A State-of-Knowledge Review of the Influence of Strong Motion Duration on Structural Damage. *Earthquake Spectra*, 22(3), 827-845.
- Hancock, J., & Bommer, J. J. (2007). Using spectral matched records to explore the influence of strong-motion duration on inelastic structural response. *Soil Dynamics and Earthquake Engineering*, 27, 291-299.
- Housner, G. W. (1965). Intensity of Ground Shaking Near the Causative Fault. *3rd World Conference on Earthquake Engineering*. New Zealand.
- Ibarra, L. F., & Krawinkler, H. (2005). *Global Collapse of Frame Structures under Seismic Excitations*. Stanford University, Department of Civil and Environmental Engineering. Stanford: John A. Blume Earthquake Engineering Center.

- Ibarra, L. F., Medina, R. A., & Krawinkler, H. (2005). Hysteretic models that incorporate strength and stiffness deterioration. *Earthquake Engineering and Structural Dynamics*(34), 1489-1511.
- Japan Meteorological Agency. (2017). *Tables explaining the JMA Seismic Intensity Scale*. Retrieved July 4, 2017, from <http://www.jma.go.jp/jma/en/Activities/inttable.html#ryuui>
- Kadas, K., & Yakut, A. (2014). Correlation of seismic demands with ground motion intensity parameters evaluated through different ground motion record sets. *Proceedings of the 10th U.S. National Conference on Earthquake Engineering*. Anchorage, Alaska.
- Kaushik, H. B., & Jain, S. K. (2007). Impact of Great December 26, 2004 Sumatra Earthquake and Tsunami on Structures in Port Blair. *Journal of Performance of Constructed Facilities*, 128-142.
- Kostinakis, K. G., & Athanatopoulou, A. M. (2015). Evaluation of scalar structure-specific ground motion intensity measures for seismic response prediction of earthquake resistant 3D buildings. (I. Takewaki, A. Stavros, Anagnostopoulos, & J. P. Lynch, Eds.) *Earthquakes and Structures*, 9(5), 1091-1114. doi:10.12989/eas.2015.9.5.1091
- Kostinakis, K., Papadopoulos, M., Athanatopoulos, A., & Morfidis, K. (2014). Correlation between structure-specific ground motion intensity measures and seismic response of 3D R/C buildings. *Proceedings of the 2nd European Conference on Earthquake Engineering and Seismology*. Istanbul, Turkey.
- Kramer, S. L. (1996). *Geotechnical Earthquake Engineering*. (W. J. Hall, Ed.) Upper Saddle River, New York, United States of America: Prentice-Hall.
- Liel, A., & Raghunandan, M. (2014). *Investigation of Structural Collapse Risk in the Cascadia Subduction Zone*. Boulder, Colorado, USA: U.S. Geological Survey (USGS).
- Lignos, D. G., & Krawinkler, H. (2010). Deterioration modeling of steel components in support of collapse prediction of steel moment frames under earthquake loading. (ASCE, Ed.) *Journal of Structural Engineering*, 137(11), 1291-1302. doi:10.1061/1943-541X.0000376
- Lignos, D., & Krawinkler, H. (2012). *Sideway Collapse of Deteriorating Structural Systems under Seismic Excitation*. Stanford University, department of Civil and Environmental Engineering. Stanford: John A. Blume Earthquake Engineering Center.

- Lignos, D., & Krawinkler, H. (2013). Development and Utilization of Structural Component Databases for Performance-Based Earthquake Engineering. *Journal of Structural Engineering*, 139(8).
- Lin, L. (2012). Probabilistic Seismic Demand Analysis Using Improved Intensity Measures. *Proceedings of the 15th World Conference in Earthquake Engineering*. Lisbon, Portugal.
- Lin, T., & Baker, J. W. (2015). Conditional Spectra. *Encyclopedia of Earthquake Engineering*. doi:10.1007/978-3-642-36197-5_386-1
- Luco, N., & Cornell, C. A. (2007). Structure-Specific Scalar Intensity Measures for Near-Source and Ordinary Earthquake Ground Motions. *Earthquake Spectra*, 23(2), 357-392. doi:10.1193/1.2723158
- Luco, N., Manuel, L., Baldava, S., & Bazzurro, P. (2005). Correlation of damage of steel moment-resisting frames to a vector-valued set of ground motion parameters. In G. Augusti, G. I. Schueller, & M. Ciampoli (Ed.), *Proceedings of the 2005 International Conference on Structural Safety & Reliability* (pp. 2719-2726). Rome, Italy: Millpress, Rotterdam.
- Mahin, S. A. (1980). Effects of duration and aftershocks on inelastic design earthquakes. *Proceedings of the 7th World Conference on Earthquake Engineering*, (pp. 677-680). Istanbul.
- Martinez-Pereira, A. (1999). *The characterization of near-field earthquake ground motions for engineering design*. PhD Thesis, Imperial College, University of London, London.
- Mazzoni, S., McKenna, F., Scott, M. H., & Fenves, G. L. (2007). *OpenSees Command Language Manual*.
- Murphy, J., & O'Brien, L. (1978). *Analysis of a Worldwide Strong Motion Sample to Develop an Improved Correlation Between Peak Acceleration, Seismic Intensity and Other Physical Parameters*. U.S. Nuclear Regulatory Commission.
- Murray, M. H., & Lisowski, M. (2000). Strain accumulation along the Cascadia subduction zone. *Geophysical Research Letters*, 27(22), 3631-3634.
- Nanos, N., Elenas, A., & Ponterosso, P. (2008). Correlation of different strong motion duration parameters and damage indicators of reinforced concrete structures. *Proceedings of the 14th World Conference on Earthquake Engineering*. Beijing, China.
- NASA. (2017). *Shake, rattle, and sink*. Retrieved December 12, 2017, from Earthdata: <https://earthdata.nasa.gov/user-resources/sensing-our-planet/shake-rattle-and-sink>

- National Research Institute for Earth Science and Disaster Prevention (NIED). (2017). Strong-motion eismograph networks (K-NET, Kik-net). Japan: National Research Institute for Earth and Disaster Resilience. Retrieved July 6, 2017, from <http://www.kyoshin.bosai.go.jp/>
- Natural Resources Canada. (2011). Plate Tectonics Shape (and Shake) British Columbia. (G. S. Canada, Ed.) Sidney, British Columbia, Canada. Retrieved from http://www.earthquakescanada.nrcan.gc.ca/pprs-pprp/pubs/GF-GI/GEOFACT_plate-tectonics_e.pdf
- Natural Resources Canada. (2016). *Determine 2015 National Building Code of Canada hazard values*. (Earthquakes Canada) Retrieved October 4, 2017, from http://www.earthquakescanada.nrcan.gc.ca/hazard-alea/interpolat/index_2015-en.php
- Natural Resources Canada. (2016). Seismic zones in Western Canada. *Background on Earthquakes in Western Canada*. Canada. Retrieved September 28, 2017, from <http://www.earthquakescanada.nrcan.gc.ca/zones/westcan-en.php>
- NBCC. (2005). *National Building Code of Canada*.
- NBCC. (2010). *National Building Code of Canada*.
- NBCC. (2015). *Annexure J: Guidelines for Selection and Scaling of Ground Motion Time Histories for Seismic Analysis*.
- NBCC. (2015). *National Building Code of Canada*.
- Nishiyama, I., Okawa, I., Fukuyama, H., & Okuda, Y. (2011). Building Damage by the 2011 off the Pacific coast of Tohoku earthquake and coping activities by NILIM and BRI collaborated with the administration. *43rd Joint Meeting of U.S.-Japan Panel on Wing and Seismic Effects*. Tsukuba, Japan: Public Works Research Institute.
- Ochi, S., & Suzuoki, M. (2011). The lessons of the Great East Japan Earthquake 2011 and the countermeasures against earthquakes and tsunamis in future - Fundamental Concepts behind Future Tsunami Disaster Prevention. *43rd Joint Meeting of U.S.-Japan Panel on Wing and Seismic Effects*. Tsukuba, Japan: Public Works Research Institute.
- OpenSees. (2017). "Open System for Earthquake Engineering Simulations". Pacific Earthquake Engineering Research Center (PEER). Retrieved October 17, 2017, from <http://opensees.berkeley.edu>

- Oppenheimer, D., Beroza, G., Carver, G., Dengler, L., Eaton, J., Gee, J. L., . . . Valentine, D. (1993). The Cape Mendocino, California, Earthquakes of April 1992: Subduction at the Triple Junction. *Science*, *261*(5120), 433-438. doi:10.1126/261.5120.433
- Park, Y.-J., & Ang, A. H. (1985). Mechanistic Seismic Damage model for Reinforced Concrete. *Journal of Structural Engineering*, *111*(4), 722-739. doi:10.1061/(ASCE)0733-9445(1985)111:4(722)
- PEER. (2010). *Technical Report for the PEER Ground Motion Database Web Application (Beta Version)*.
- Porter, K. (2016). *A Beginner's Guide to Fragility, Vulnerability and Risk*. Boulder: University of Colorado. Retrieved from <http://spot.colorado.edu/~porterka/Porter-beginners-guide.pdf>
- Raghunandan, M. (2013). *Influence of long duration ground shaking on collapse of reinforced concrete structures*. PhD Thesis, University of Colorado, Department of Civil, Environmental and Architectural Engineering, Boulder.
- Raghunandan, M., & Liel, A. B. (2013). Effect of ground motion duration on earthquake-induced structural collapse. *Structural Safety*, *41*, 119-133.
- Saatcioglu, M., Ghojarah, A., & Nistor, I. (2006). Performance of Structures in Indonesia during the December 2004 Great Sumatra Earthquake and Indian Ocean Tsunami. *Earthquake Spectra*, *22*(S3), S295-S319.
- Satake, K., & Atwater, B. F. (2007). Long-Term Perspectives on Giant Earthquakes and Tsunamis at Subduction Zones. *Annual Review of Earth and Planetary Sciences*, *35*, 349-374. doi:10.1146/35.031306.14030
- Satake, K., Shimazaki, K. T., & Ueda, K. (1996). Time and size of a giant earthquake in Cascadia inferred from Japanese tsunami records of January 1700. *Nature*, *379*, 246-249.
- Scott, M. H., & Mason, H. B. (2017). Constant-ductility response spectra for sequential earthquake and tsunami loading. *Earthquake Engineering and Structural Dynamics*.
- Shearer, P., & Burgmann, R. (2010). Lessons Learned from the 2004 Sumatra-andaman Megathrust Rupture. *Annual Review of Earth and Planetary Sciences*(38), pp. 103-31.
- Shojiro, K., Kazuhiro, N., Kazunari, M., & Masahiro, K. (2011). Strong Motion and Earthquake Response Records of the 2011 off the Pacific Coast of Tohoku Earthquake. *43rd Joint Meeting of U.S.-Japan Panel on Wind and Seismic Effects*. Tsukuba, Japan: Public Works Research Institute.

- Structural Engineers Association of BC. (2017). British Columbia Earthquake Fact Sheet. British Columbia, Canada. Retrieved September 28, 2017, from <https://www.egbc.ca/getmedia/4278c069-0374-4cc2-9e73-2b454a0f978a/SEABC-Eathquake-Fact-Sheet.pdf.aspx>
- The Cascadia Region Earthquake Workgroup. (2005). *Cascadia Subduction Zone Earthquakes: A magnitude 9.0 earthquake scenario*. Seattle: Oregon Department of Geology and Mineral Industries.
- The MathWorks Inc. (2017). MATLAB. 2017Ra. Retrieved from <http://mathworks.com/products/matlab>
- Tothong, P., & Cornell, C. A. (2006). An Empirical Ground-Motion Attenuation Relation for Inelastic Spectral Displacement. *Bulletin of the Seismological Society of America*, 96(6), 2146-2164. doi:10.1785/0120060018
- Tothong, P., & Cornell, C. A. (2007). *Probabilistic Seismic Demand Analysis Using Advanced Ground Motion Intensity Measures, Attenuation Relationship, and Near-Fault Effects*. Stanford University.
- Tothong, P., & Luco, N. (2007). Probabilistic seismic demand analysis using advanced ground motion intensity measures. *Earthquake Engineering and Structural Dynamics*, 36, 1837-1860. doi:10.1002/eqe.696
- Trifunac, M. D., & Brady, A. G. (1975). A Study on the Duration of Strong Earthquake Ground Motion. *Bulletin of the Seismological Society of America*, 65(3), 581-626.
- United States Geological Survey. (2017). *Cascadia Subduction Zone*. Retrieved September 28, 2017, from Two Contrasting Models of Lithospheric Structure: <https://earthquake.usgs.gov/data/crust/cascadia.php>
- USGS. (2012). *20 Largest Earthquakes in the World*. Retrieved December 10, 2017, from Earthquake List, Maps & Statistics: <https://earthquake.usgs.gov/earthquakes/browse/largest-world.php>
- Vamvatsikos, D., & Cornell, C. (2005). Direct estimation of the seismic demand of MDOF systems through Incremental Dynamic Analysis of an SDOF approximation. *Journal of Structural Engineering*, 131(4), 589-599.
- Vamvatsikos, D., & Cornell, C. A. (2002). Incremental dynamic analysis. (J. W. Ltd., Ed.) *Earthquake Engineering and Structural Dynamics*, 31, 491-514. doi:10.1002/141

- Vamvatsikos, D., & Cornell, C. A. (2004). Applied Incremental Dynamic Analysis. *Earthquake Spectra*, 20(2), 523-553.
- Ventura, C. (2011). Ground Shaking during the 2011 Japan Earthquake: what have we learned?
- Villaverde, R. (2007). Methods to Assess the Seismic Collapse Capacity of Building Structures: State of the Art. (ASCE, Ed.) *Journal of Structural Engineering*, 133(1), 57-66.
- Wikimedia Foundation Inc. (2017). *Wikipedia: the free encyclopedia*. Retrieved February 2016, from https://en.wikipedia.org/wiki/Lists_of_earthquakes
- Wikipedia. (2010). *2010 Chile earthquake*. Retrieved December 12, 2017, from https://howlingpixel.com/wiki/2010_Chile_earthquake
- Wikipedia. (2010). *Iglesia de San Francisco de Curico*. Retrieved December 12, 2017, from https://wikivisually.com/lang-es/wiki/Iglesia_de_San_Francisco_de_Curic%C3%B3
- Wirgin, A., & Bard, P.-Y. (1996). Effects of Buildings on the Duration and Amplitude of Ground Motion in Mexico City. *Bulletin of Seismological Society of America*, 86(3), 914-920.

Appendices

Appendix A Spectrally equivalent ground motion pairs

Appendix A provides a summary of the selected records. Each Table refers to a pair of spectrally compatible records and includes: response spectra of scaled records, acceleration time histories of unscaled records and a table with the important characteristics of each record.

Table A- 1: PAIR # 1 - Spectrally equivalent records.

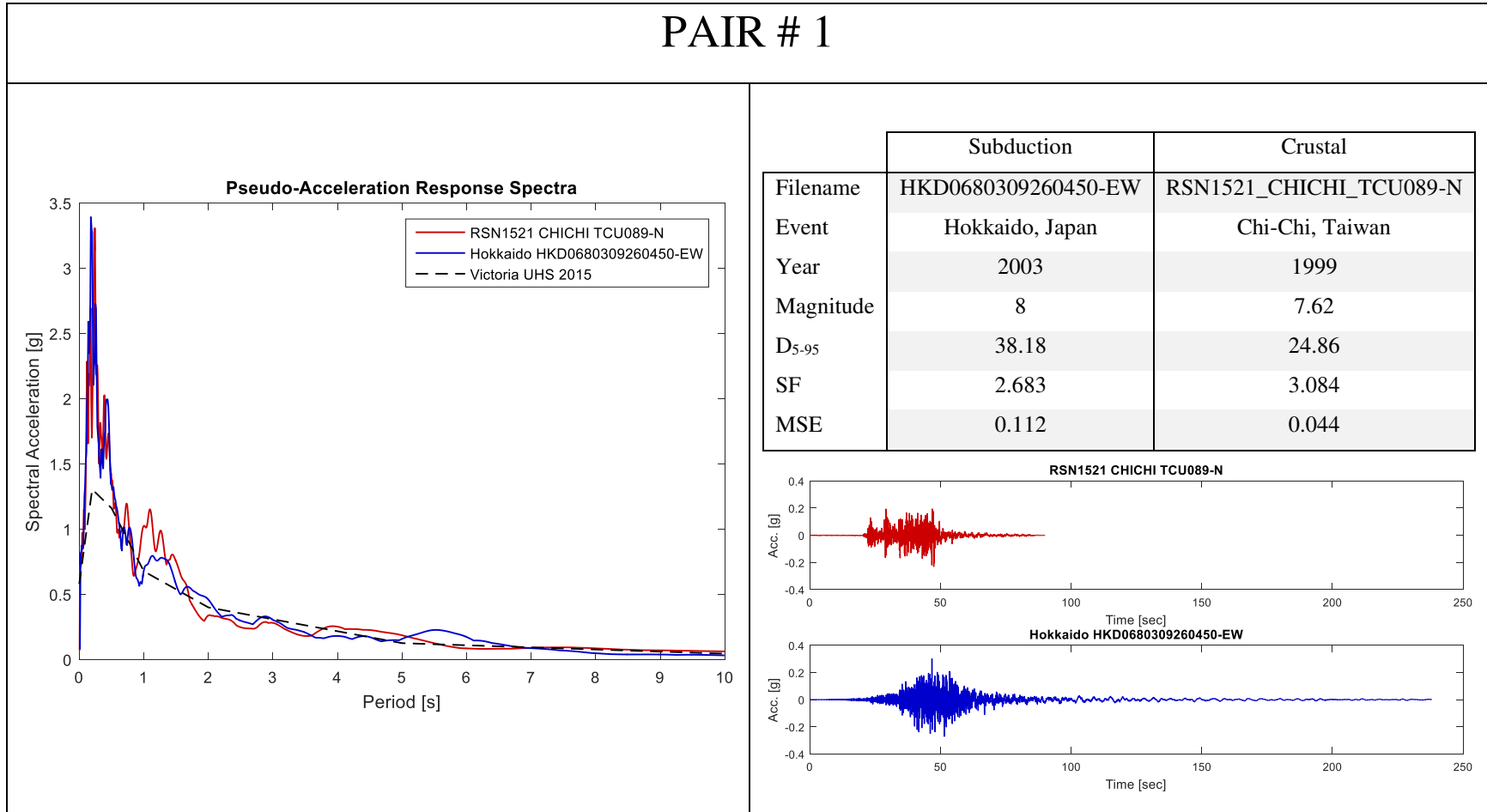


Table A- 2: PAIR # 2 - Spectrally equivalent records.

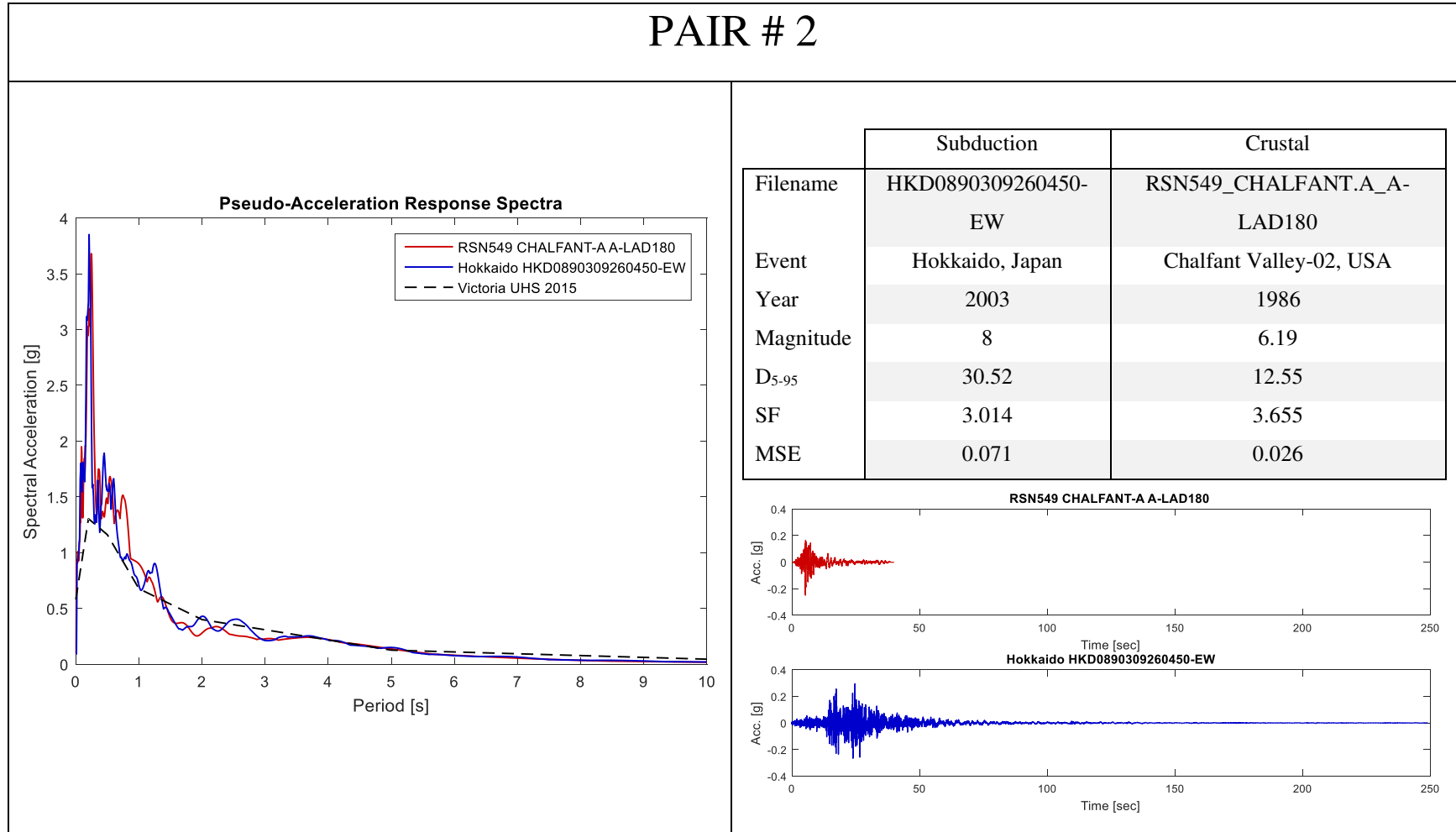


Table A- 3: PAIR # 3 - Spectrally equivalent records.

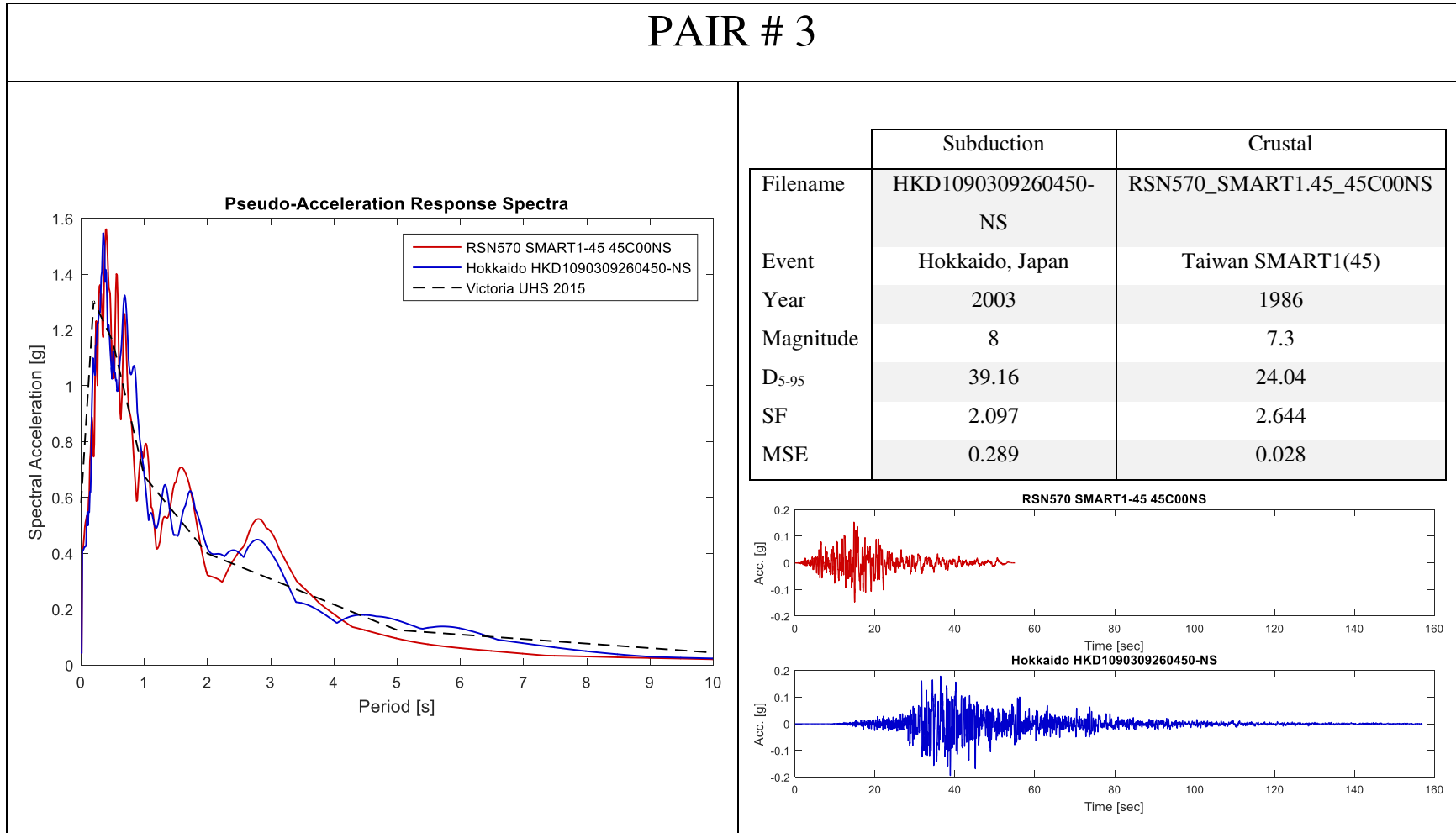


Table A- 4: PAIR # 4 - Spectrally equivalent records.

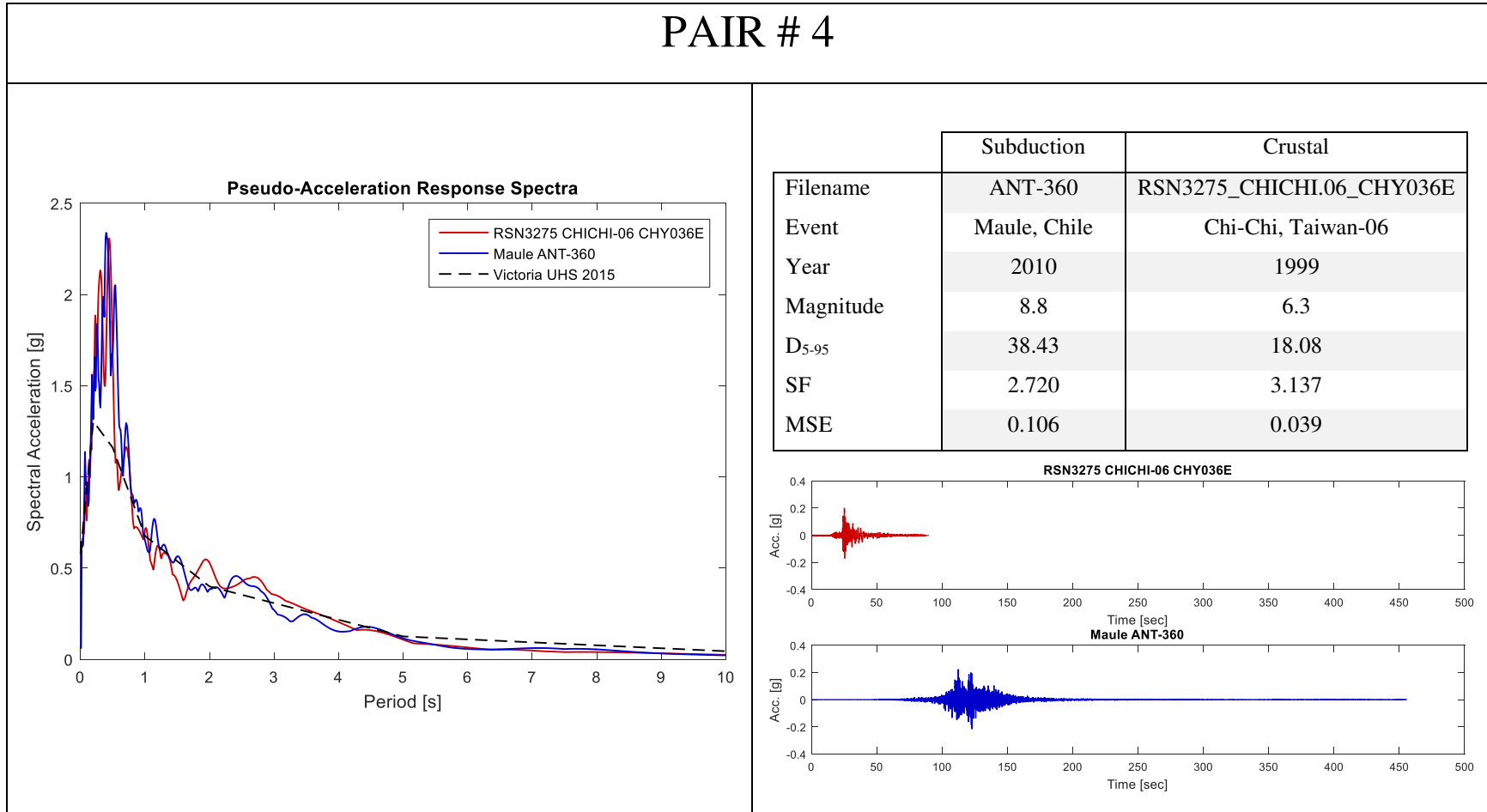


Table A- 5: PAIR # 5 - Spectrally equivalent records.

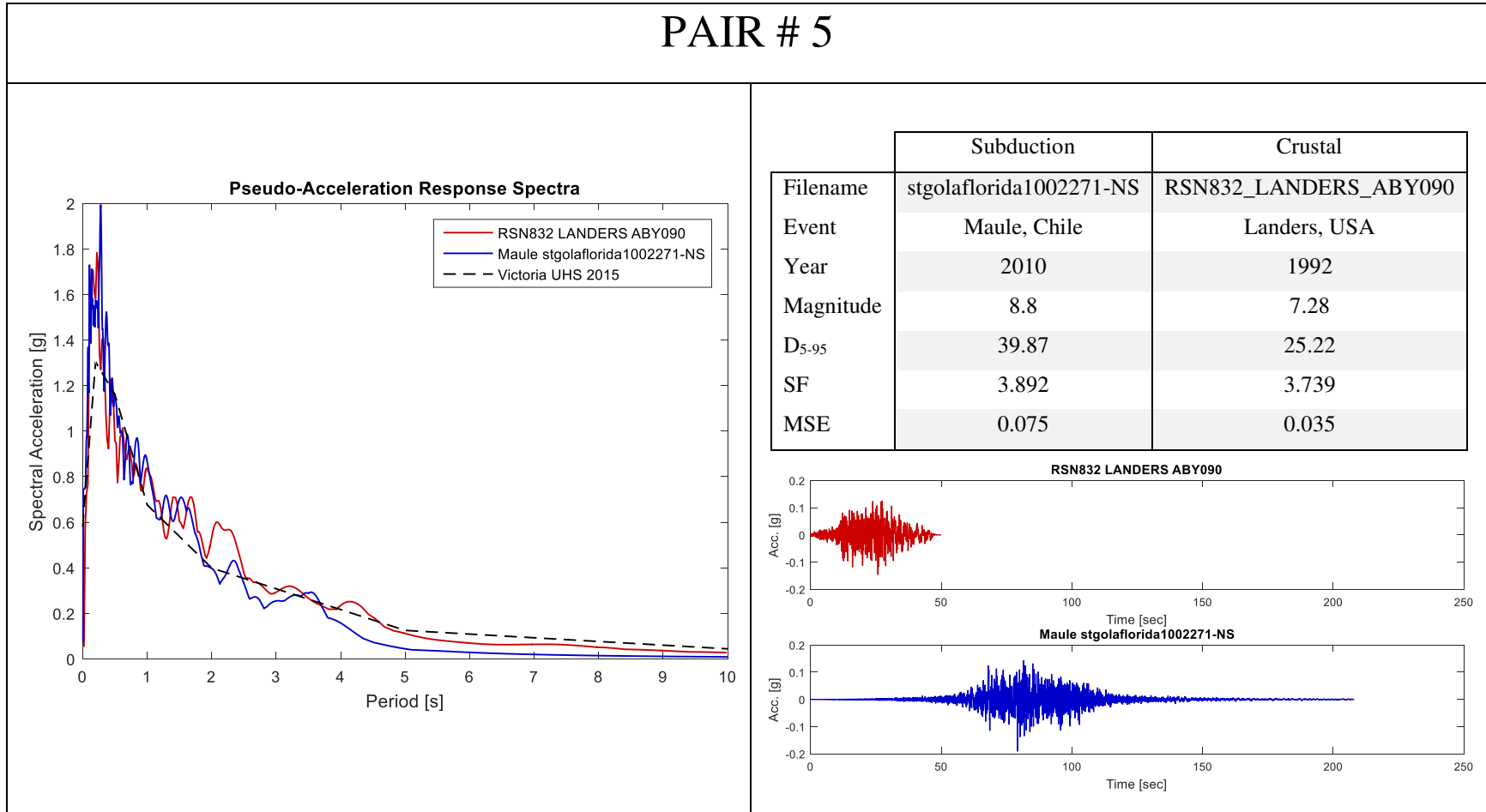
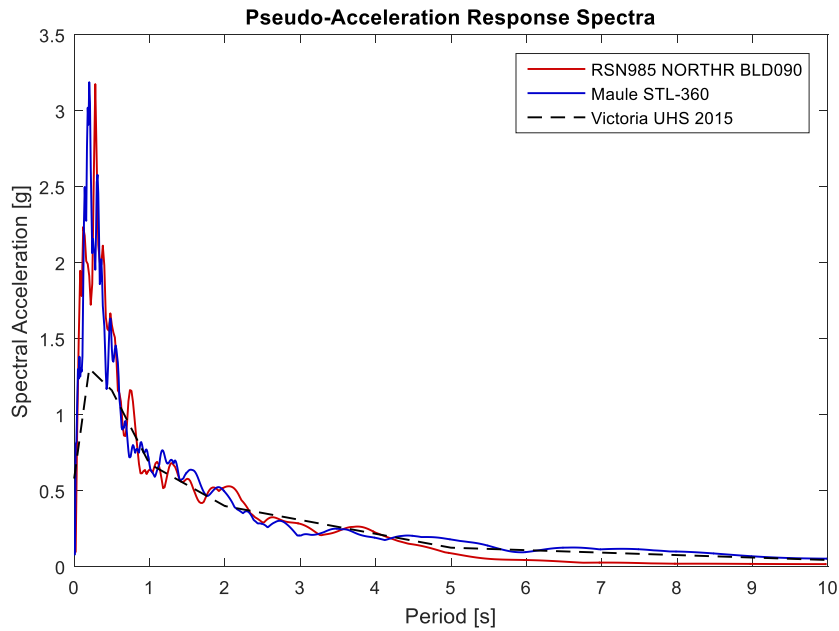


Table A- 6: PAIR # 6 - Spectrally equivalent records.

PAIR # 6



	Subduction	Crustal
Filename	STL-360	RSN985_NORTHR_BLD090
Event	Maule, Chile	Northridge-01, USA
Year	2010	1994
Magnitude	8.8	6.69
D ₅₋₉₅	40.70	16.56
SF	3.327	3.996
MSE	0.057	0.042

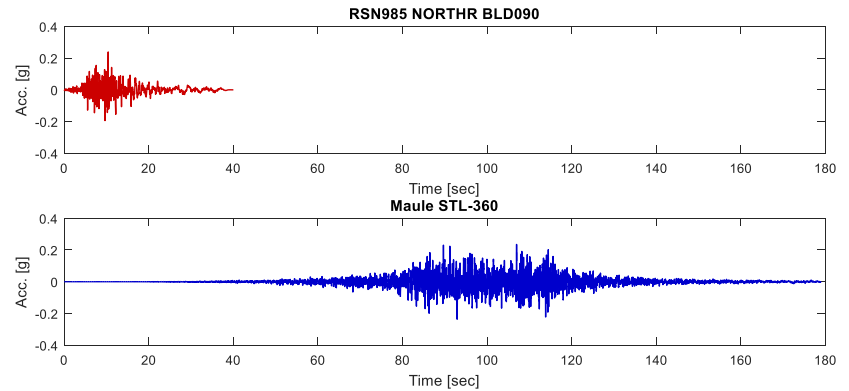


Table A- 7: PAIR # 7 - Spectrally equivalent records.

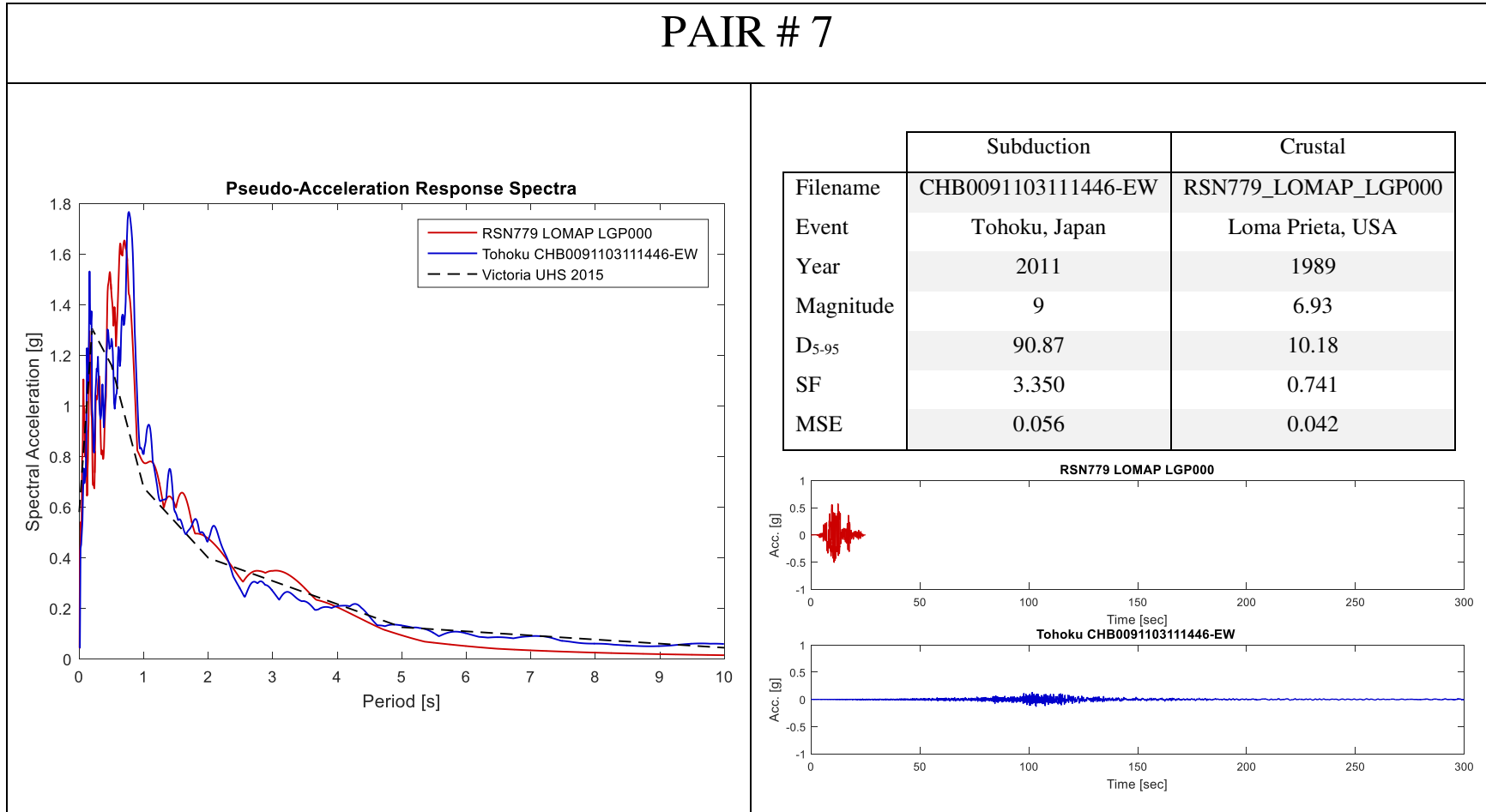
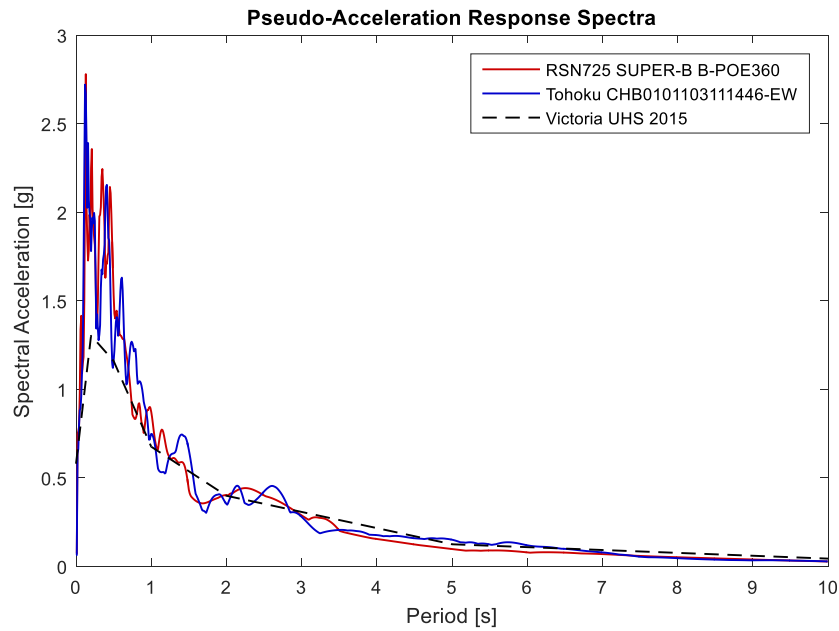


Table A- 8: PAIR # 8 - Spectrally equivalent records.

PAIR # 8



	Subduction	Crustal
Filename	CHB0101103111446-EW	RSN725_SUPER.B_B-POE360
Event	Tohoku, Japan	Superstition Hills-02, USA
Year	2011	1987
Magnitude	9	6.54
D ₅₋₉₅	58.14	13.65
SF	3.425	2.512
MSE	0.056	0.041

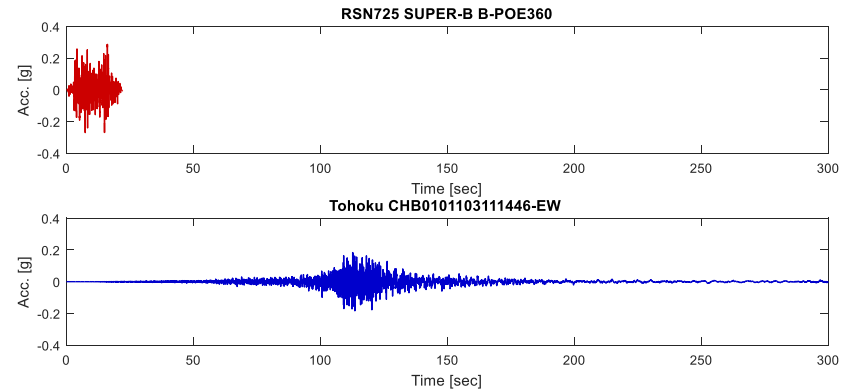


Table A- 9: PAIR # 9 - Spectrally equivalent records.

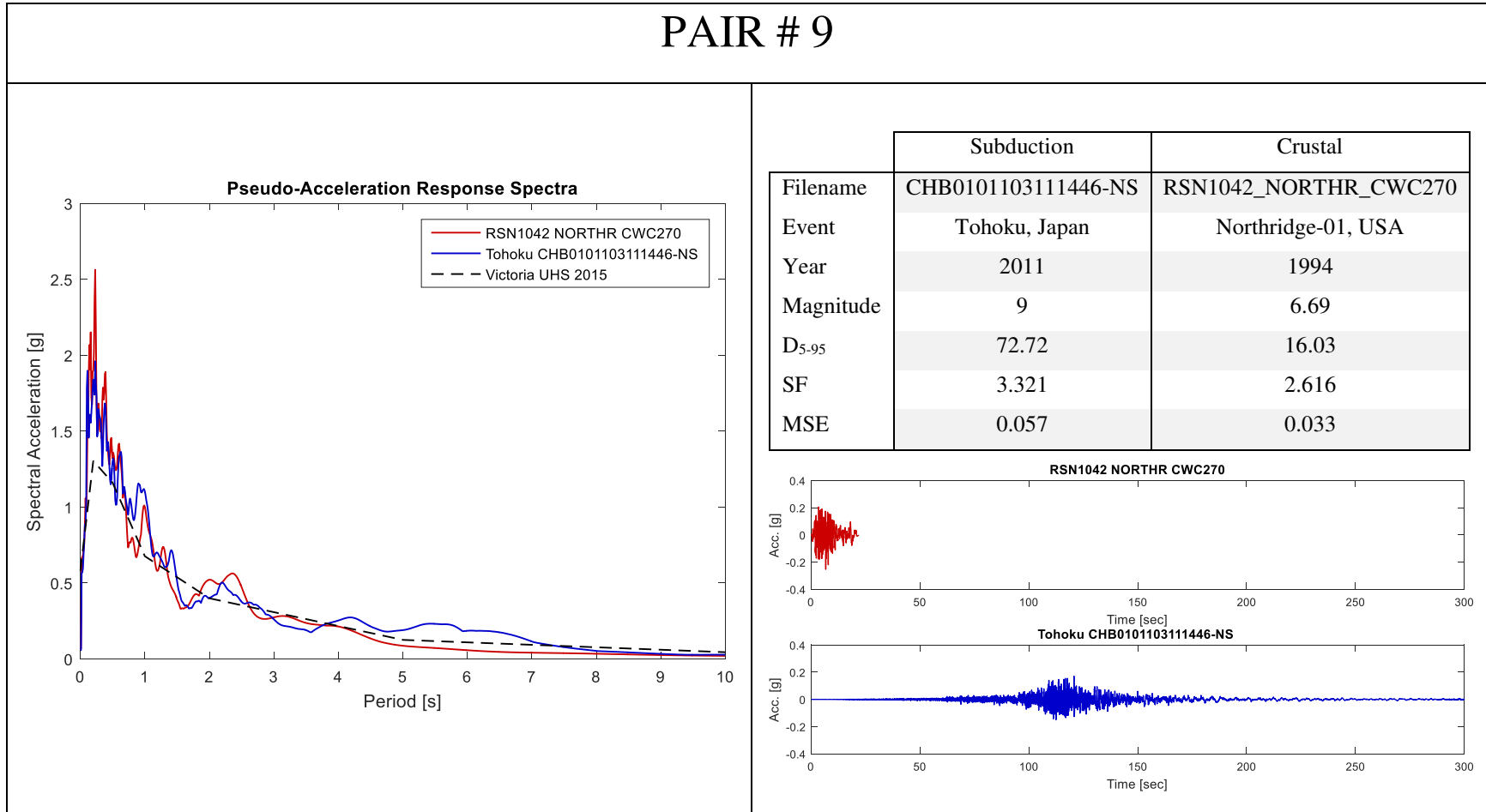
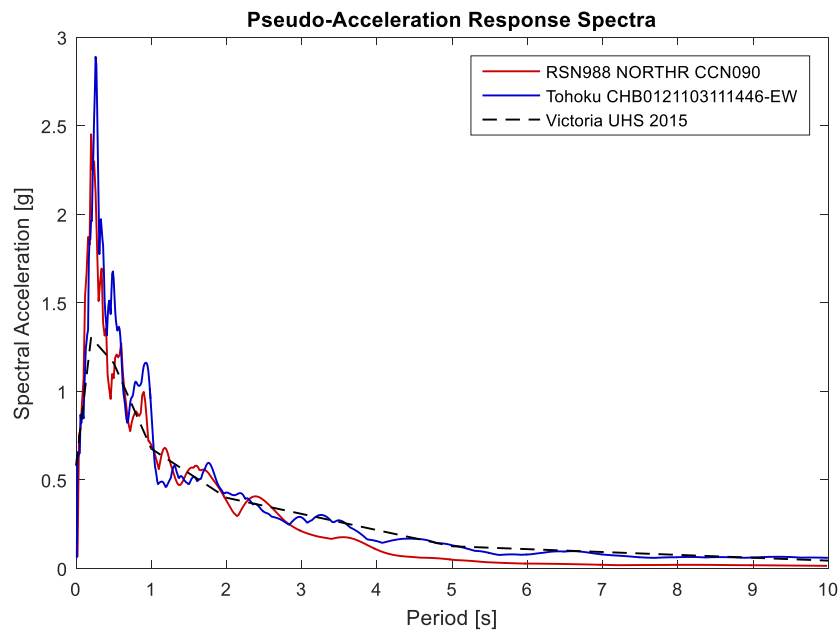


Table A- 10: PAIR # 10 - Spectrally equivalent records.

PAIR # 10



	Subduction	Crustal
Filename	CHB0121103111446-EW	RSN988_NORTHR_CCN090
Event	Tohoku, Japan	Northridge-01, USA
Year	2011	1994
Magnitude	9	6.69
D ₅₋₉₅	69.09	13.18
SF	2.905	2.594
MSE	0.081	0.043

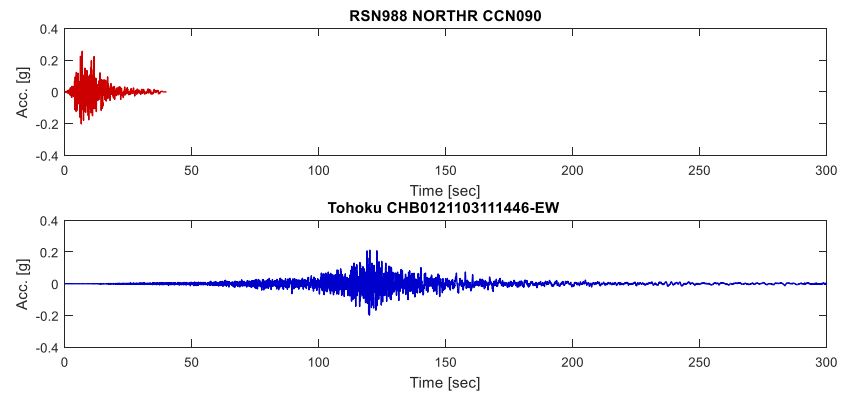
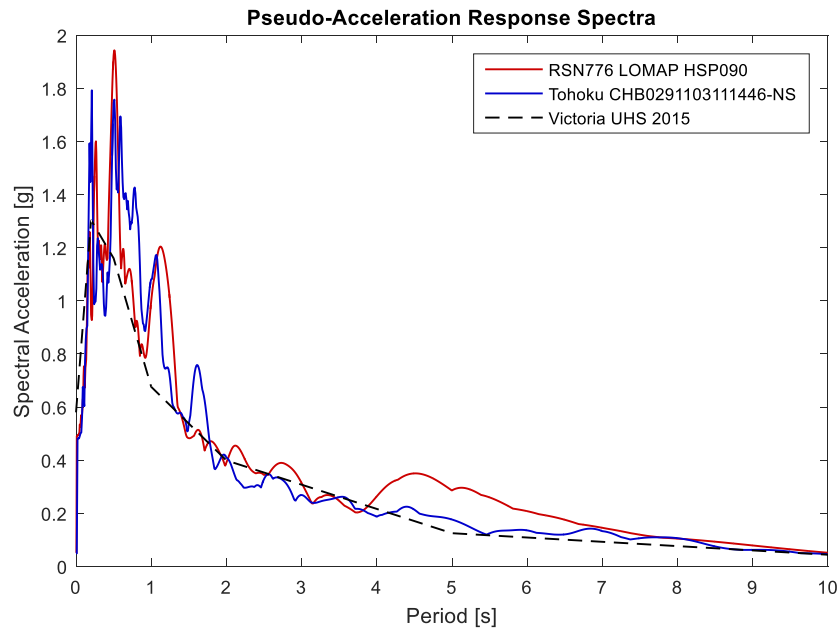


Table A- 11: PAIR # 11 - Spectrally equivalent records.

PAIR # 11



	Subduction	Crustal
Filename	CHB0291103111446-NS	RSN776_LOMAP_HSP090
Event	Tohoku, Japan	Loma Prieta, USA
Year	2011	1989
Magnitude	9	6.93
D ₅₋₉₅	97.34	28.83
SF	3.061	2.755
MSE	0.067	0.049

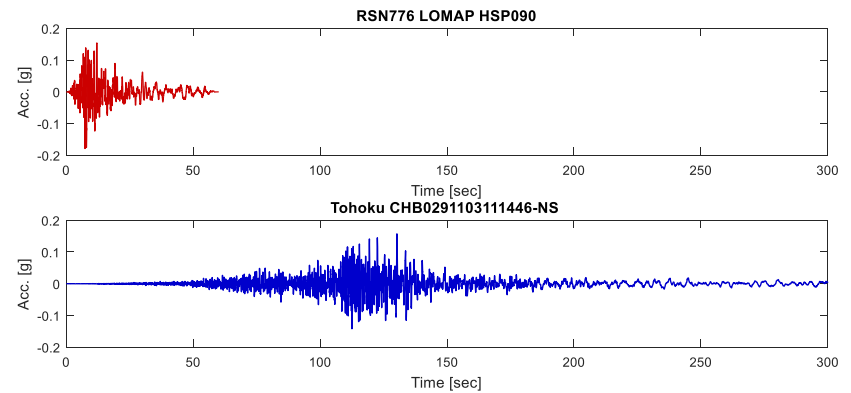
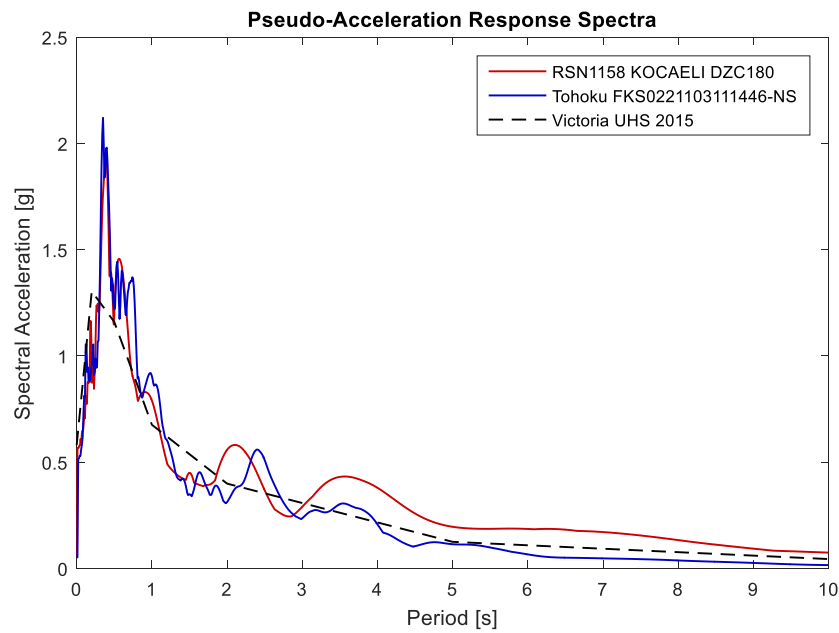


Table A- 12: PAIR # 12 - Spectrally equivalent records..

PAIR # 12



	Subduction	Crustal
Filename	FKS0221103111446-NS	RSN1158_KOCAELI_DZC180
Event	Tohoku, Japan	Kocaeli, Turkey
Year	2011	1999
Magnitude	9	7.51
D ₅₋₉₅	90.85	11.79
SF	3.850	1.821
MSE	0.072	0.041

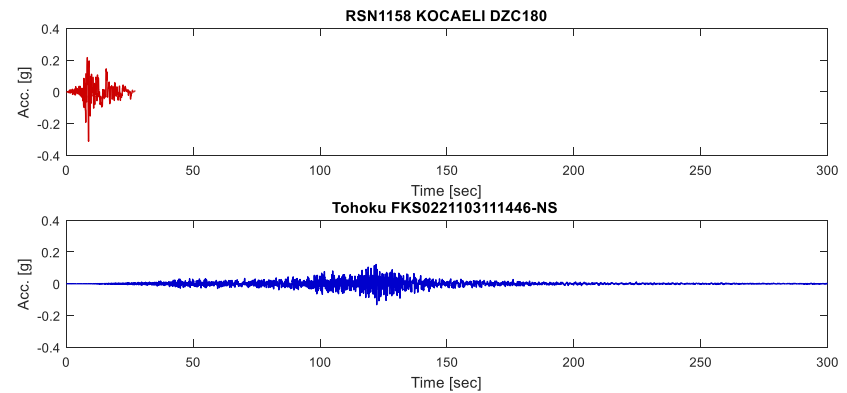


Table A- 13: PAIR # 13 - Spectrally equivalent records.

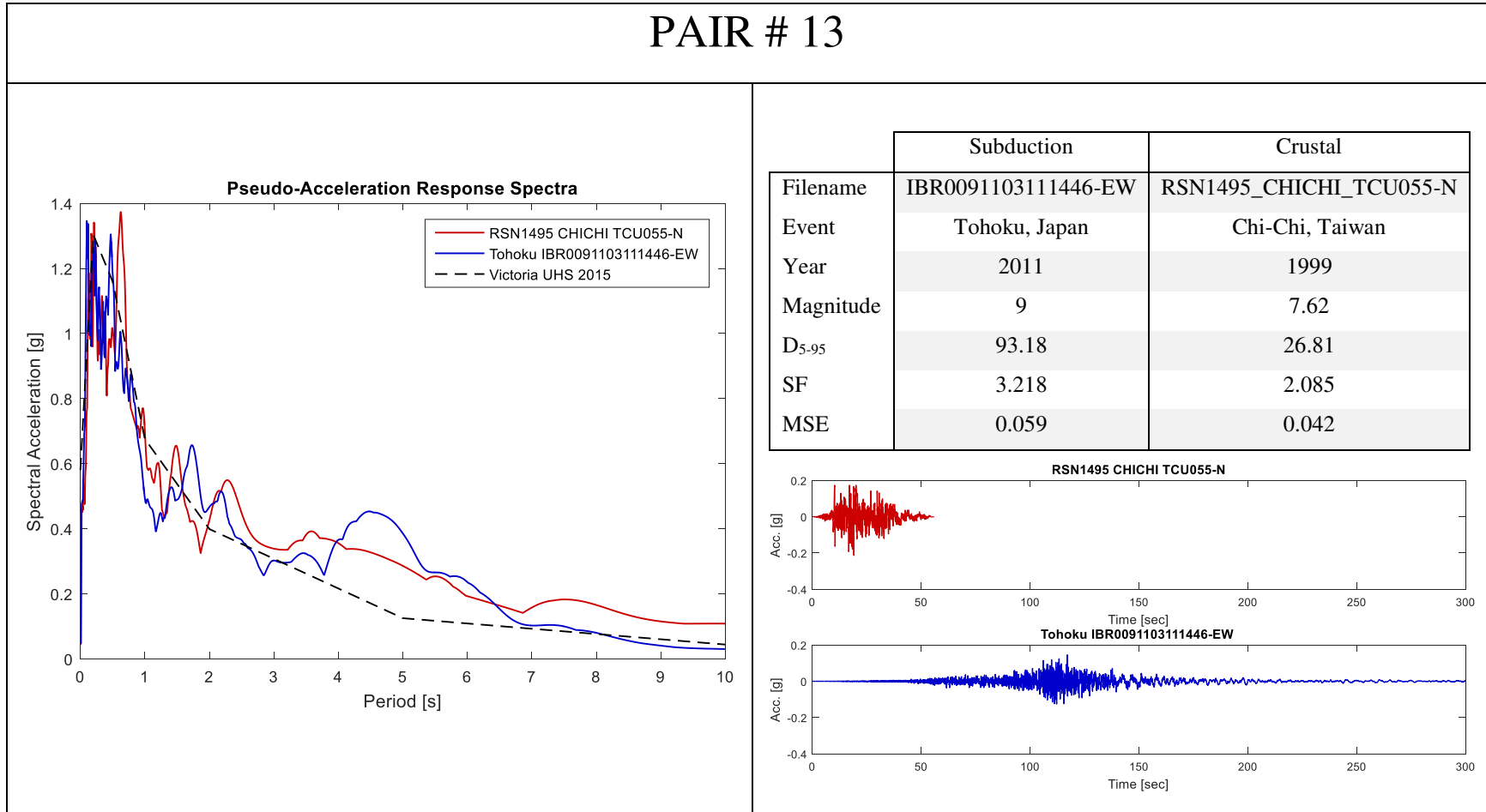


Table A- 14: PAIR # 14 - Spectrally equivalent records.

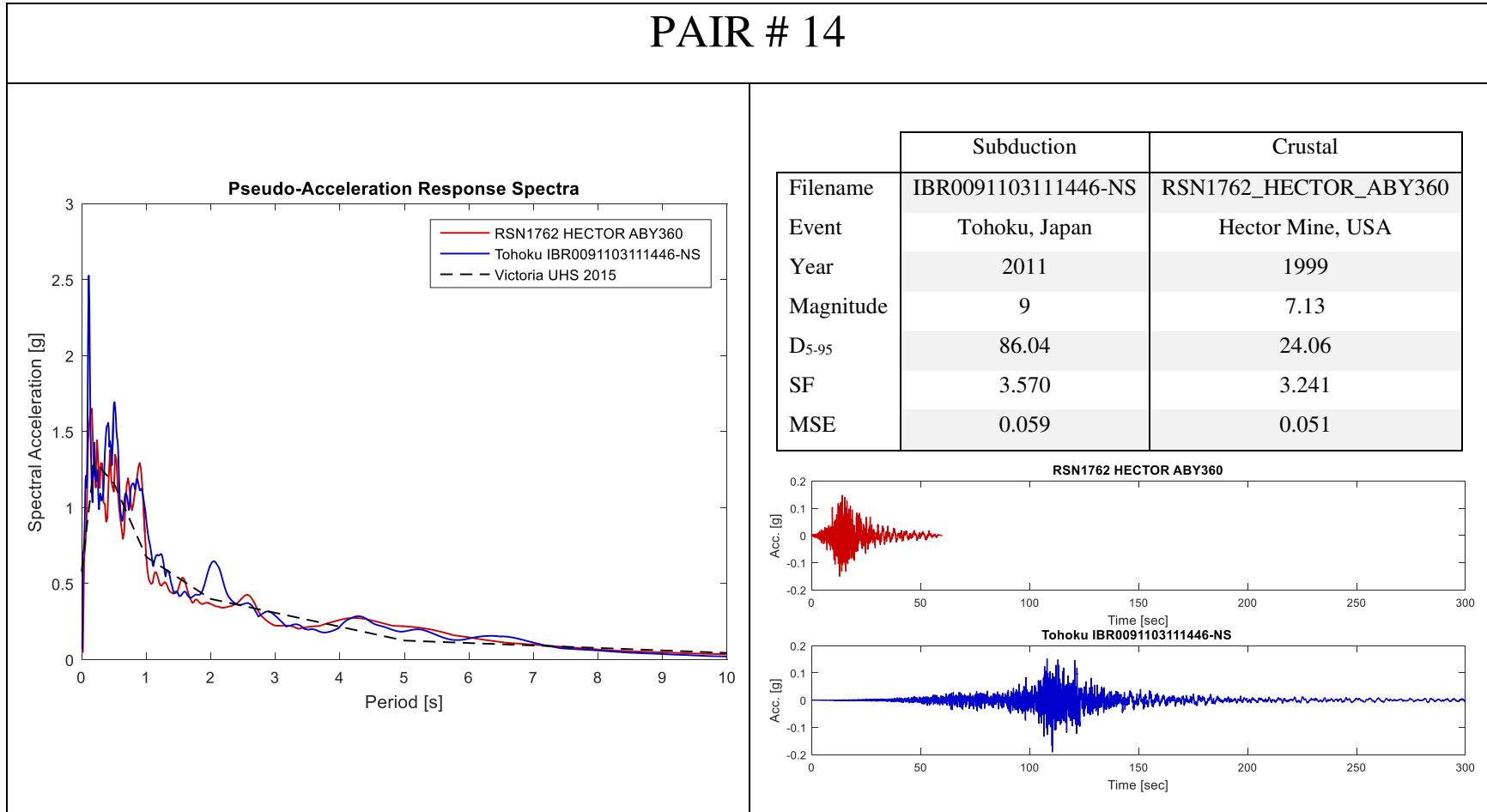


Table A- 15: PAIR # 15 – Spectrally equivalent records.

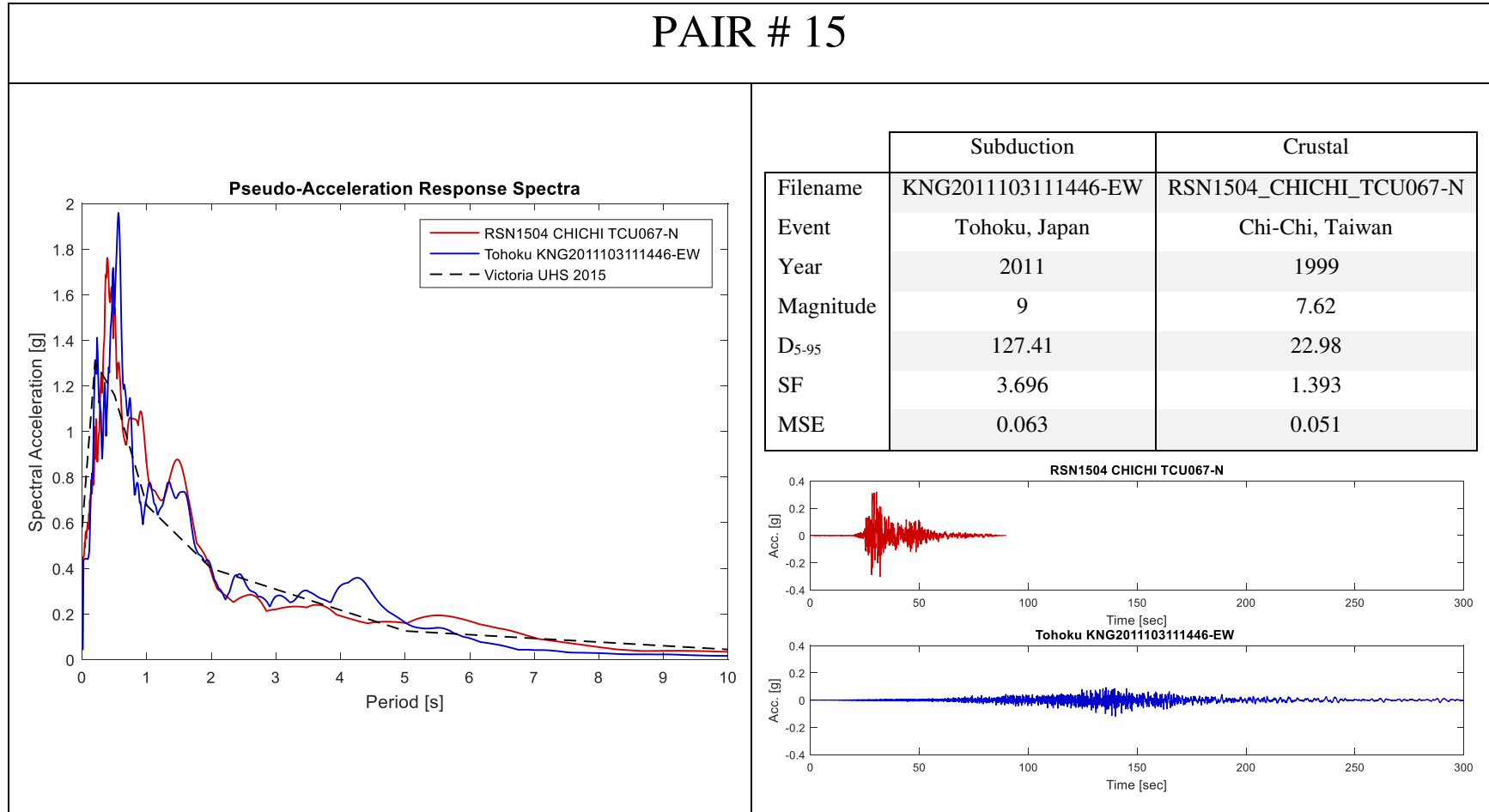


Table A- 16: PAIR # 16 - Spectrally equivalent records.

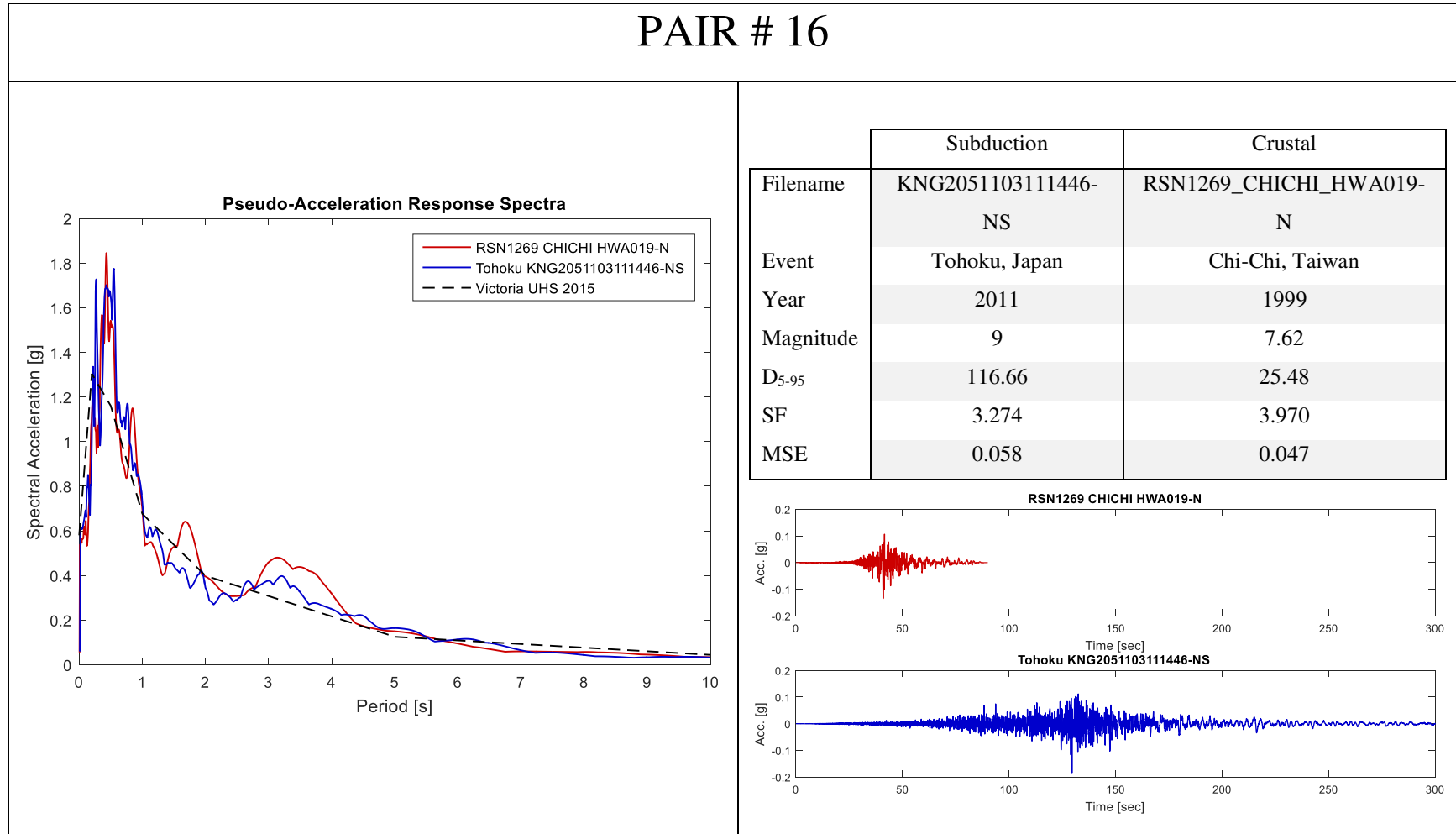


Table A- 17: PAIR # 17 - Spectrally equivalent records.

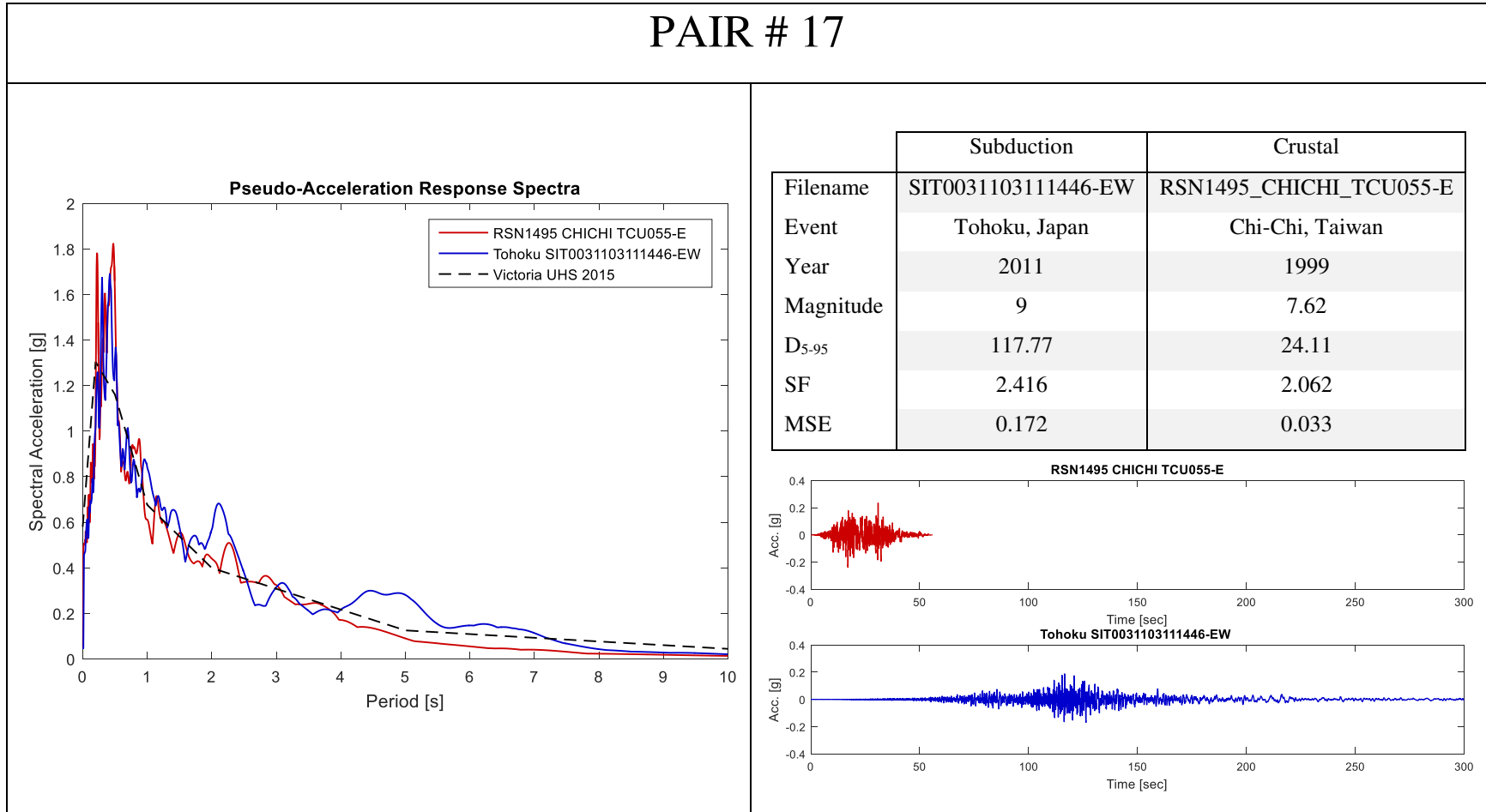


Table A- 18: PAIR # 18 - Spectrally equivalent records.

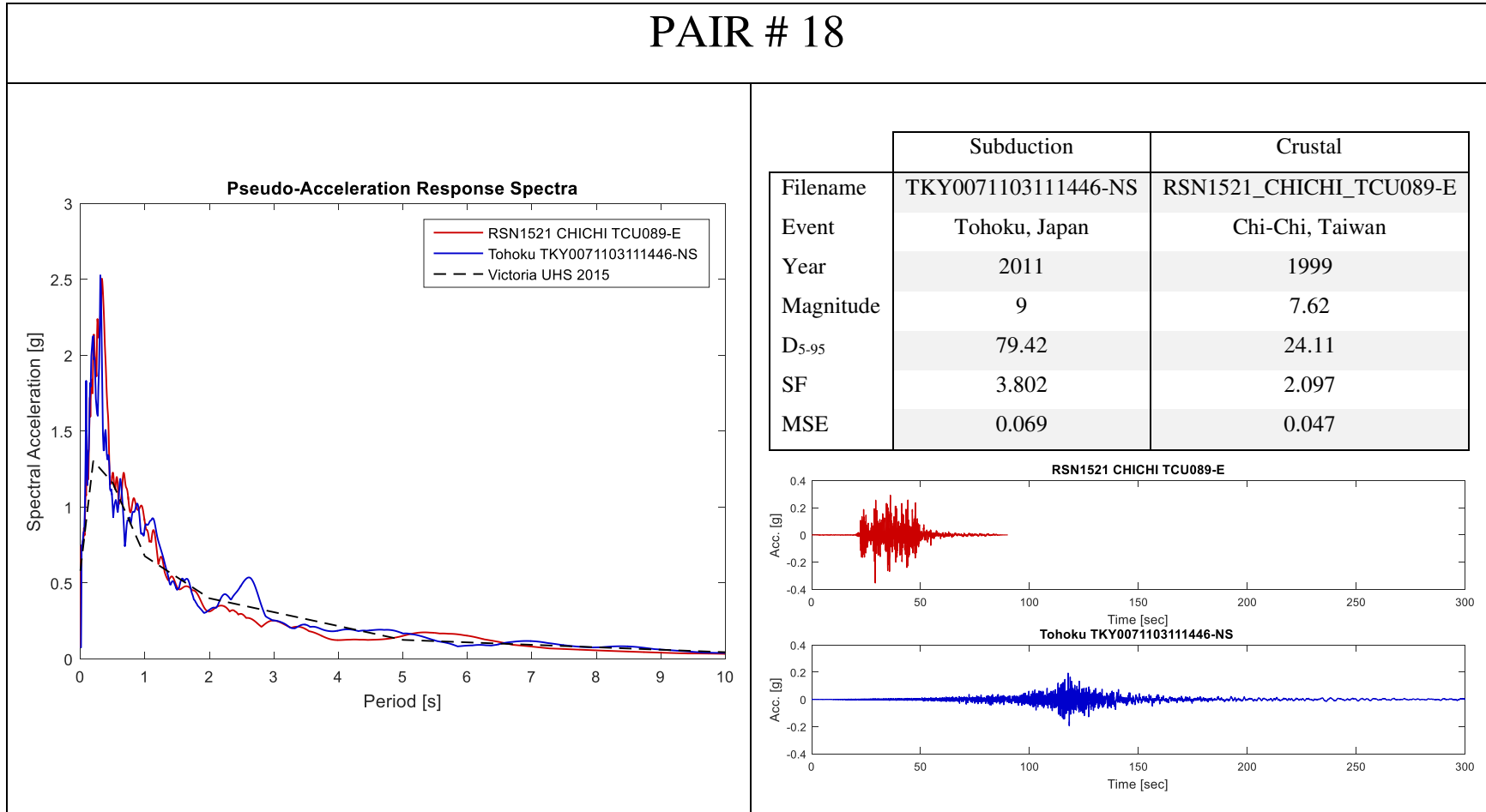
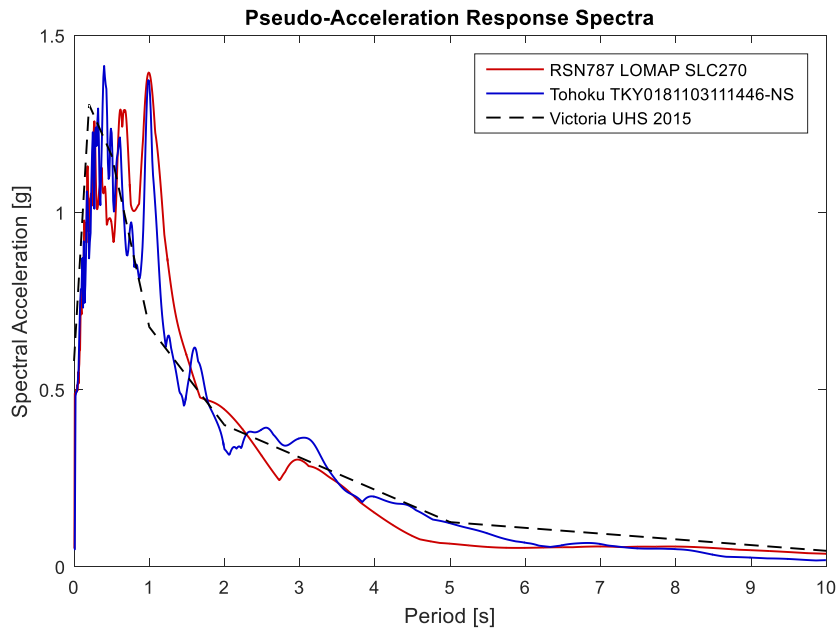


Table A- 19: PAIR # 19 - Spectrally equivalent records.

PAIR # 19



	Subduction	Crustal
Filename	TKY0181103111446-NS	RSN787_LOMAP_SLC270
Event	Tohoku, Japan	Loma Prieta, USA
Year	2011	1989
Magnitude	9	6.93
D ₅₋₉₅	99.40	12.65
SF	2.535	2.513
MSE	0.142	0.035

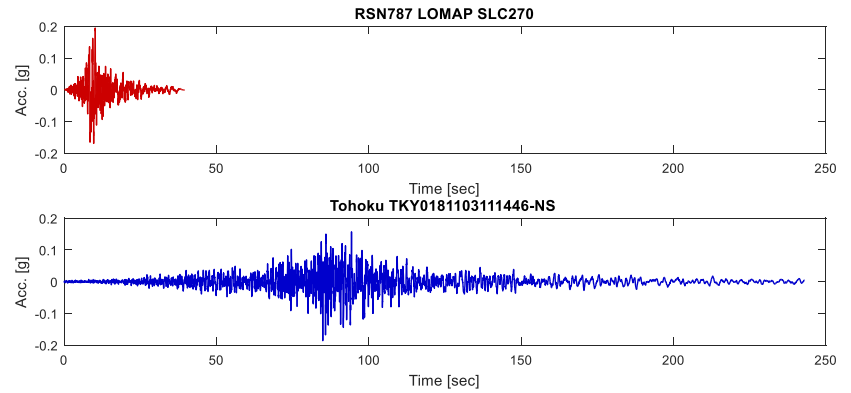
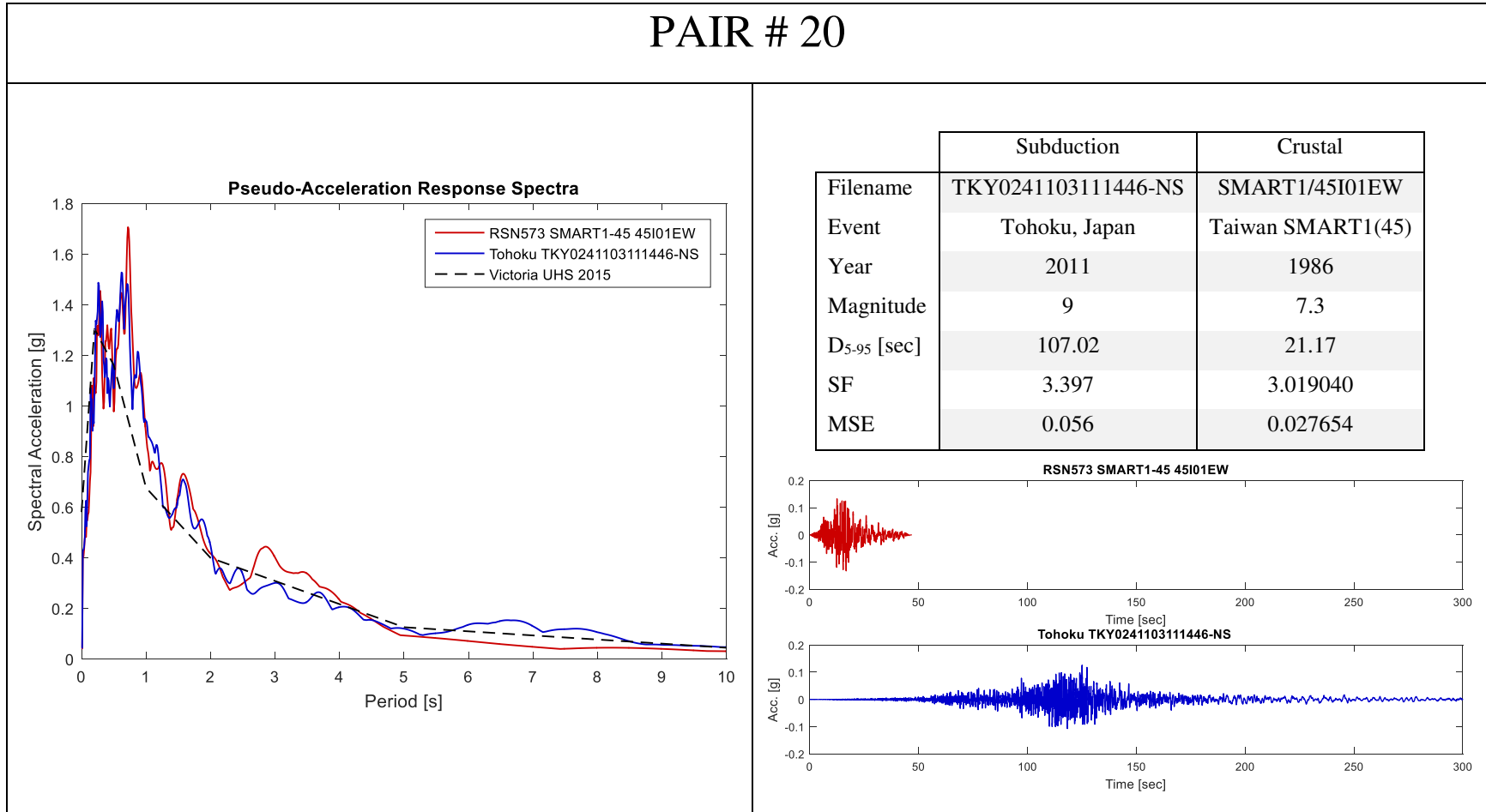


Table A- 20: PAIR # 20 - Spectrally equivalent records.



Appendix B Fragility curves

Appendix B shows the comparison between fragility curves calculated for the five ductility capacities corresponding to μ 3, 5, 7, 9 and 11. Each Figure refers to a specific structural period. Bold lines represent subduction motions, while dashed lines crustal motions.

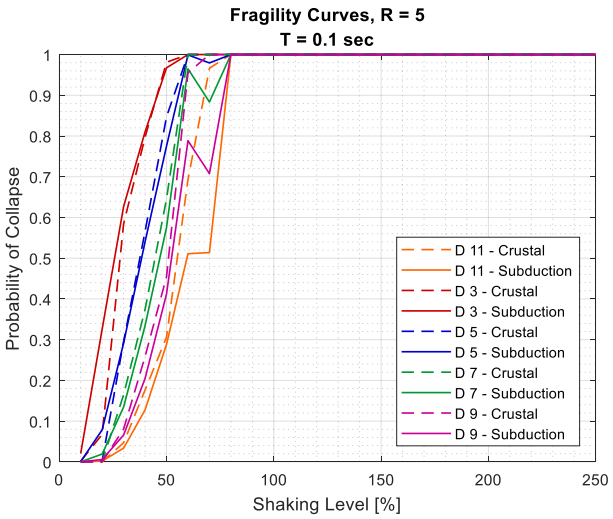


Figure B- 1: Fragility curves for T = 0.1 sec.

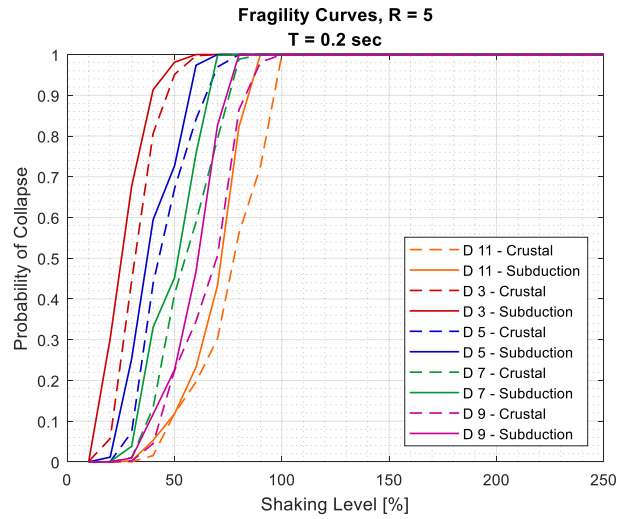


Figure B- 2: Fragility curves for T = 0.2 sec.

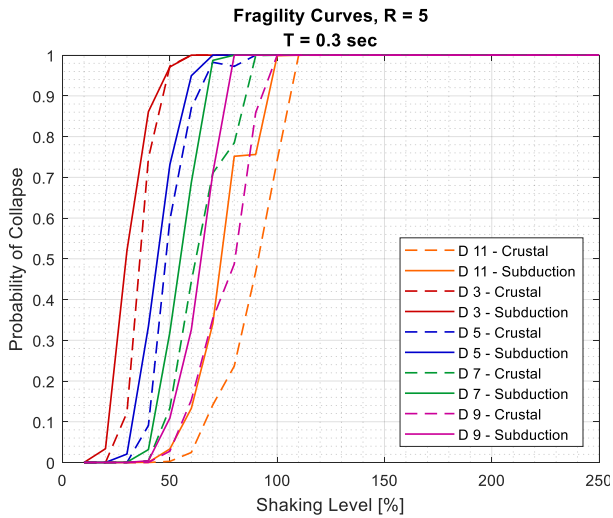


Figure B- 3: Fragility curves for T = 0.3 sec.

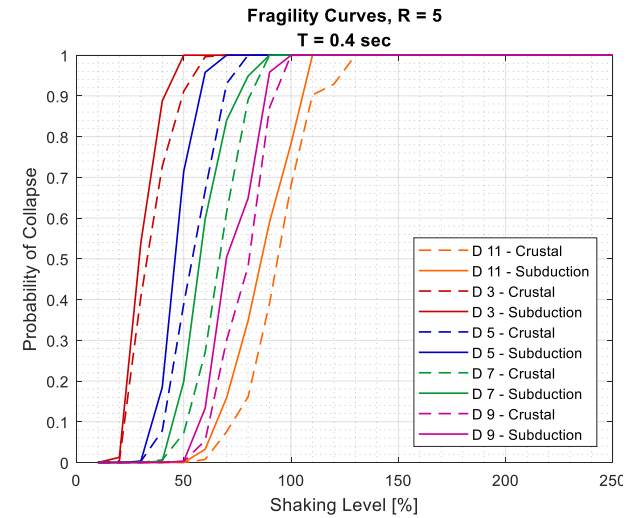


Figure B- 4: Fragility curves for T = 0.4 sec.

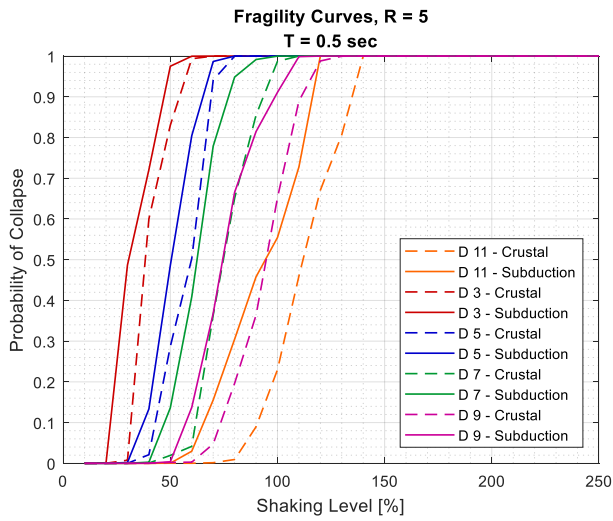


Figure B- 5: Fragility curves for T = 0.5 sec.

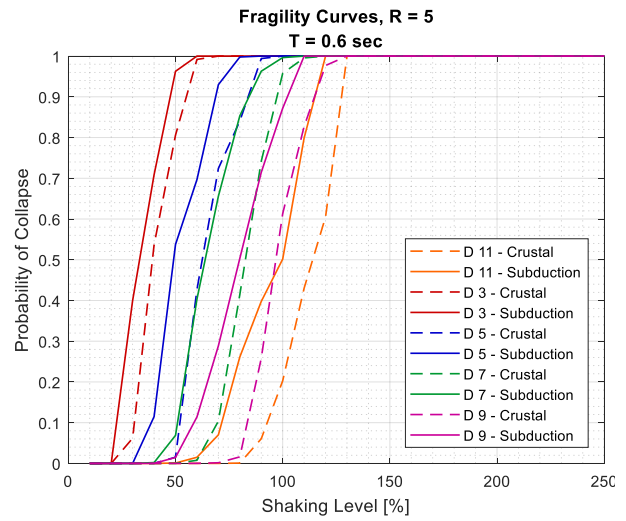


Figure B- 6: Fragility curves for T = 0.6 sec.

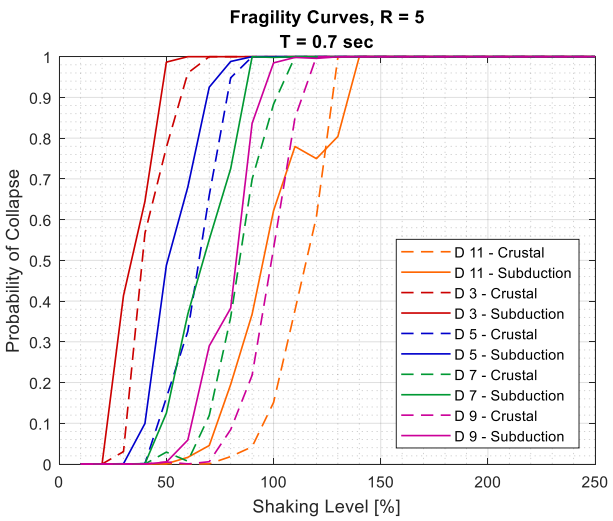


Figure B- 7: Fragility curves for T = 0.7 sec.

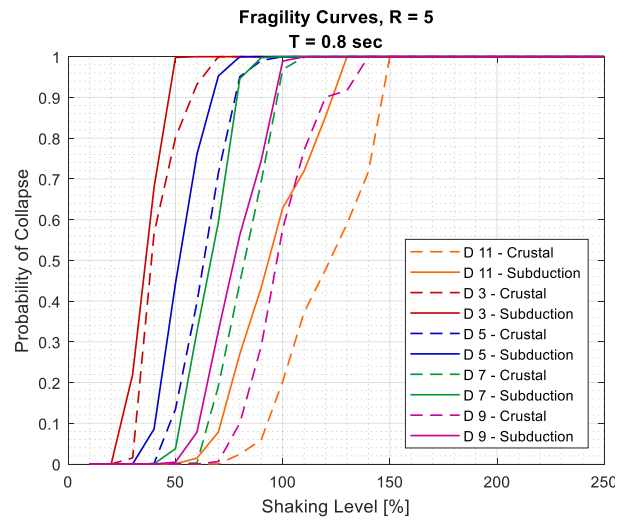


Figure B- 8: Fragility curves for T = 0.8 sec.

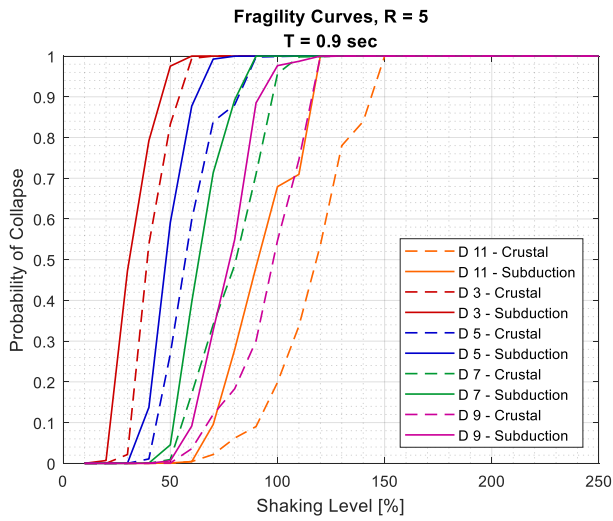


Figure B- 9: Fragility curves for T = 0.9 sec.

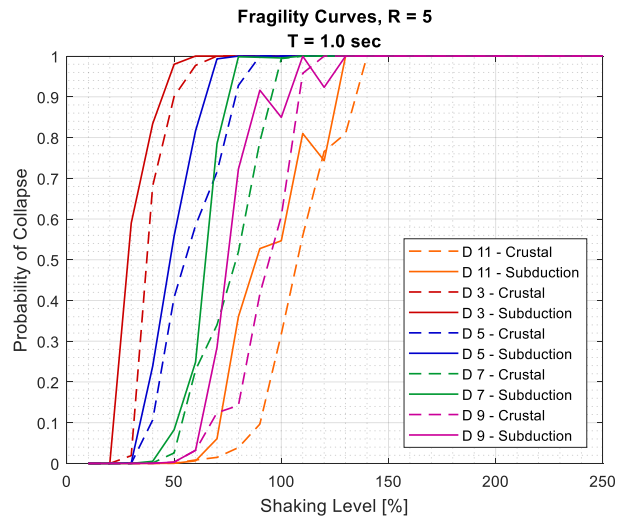


Figure B- 10: Fragility curves for T = 1.0 sec.

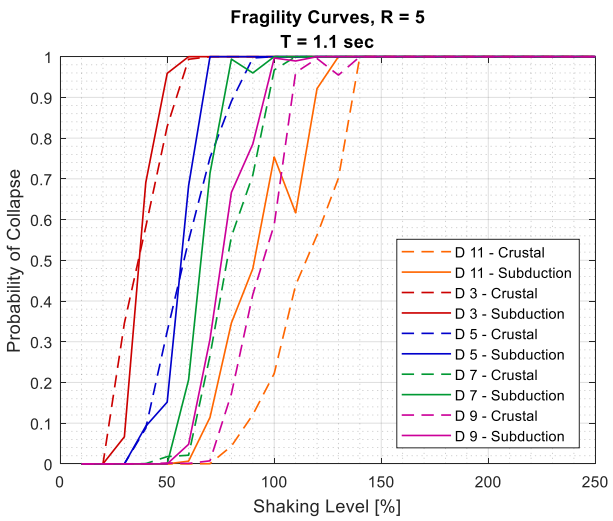


Figure B- 11: Fragility curves for T = 1.1 sec.

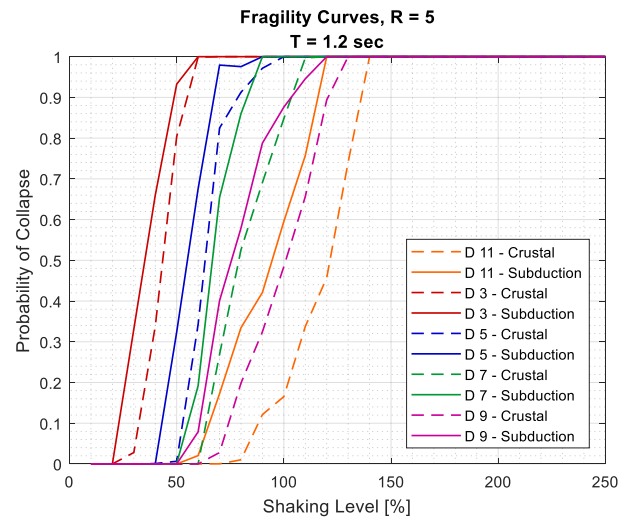


Figure B- 12: Fragility curves for T = 1.2 sec.

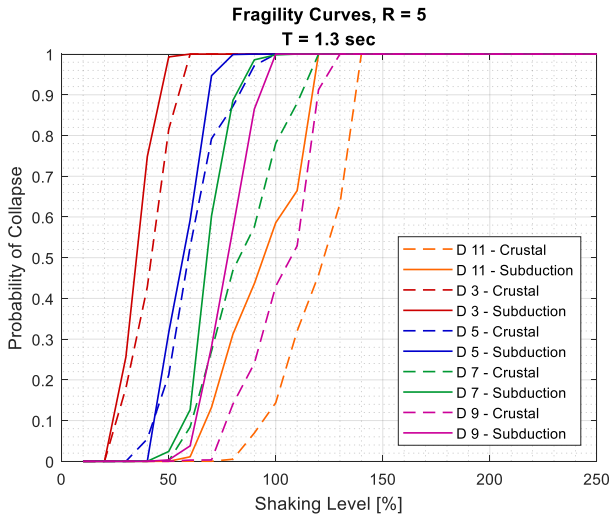


Figure B- 13: Fragility curves for T = 1.3 sec.

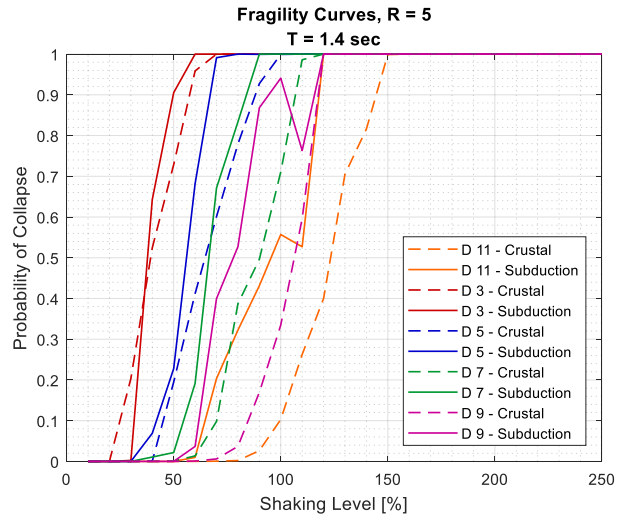


Figure B- 14: Fragility curves for T = 1.4 sec.

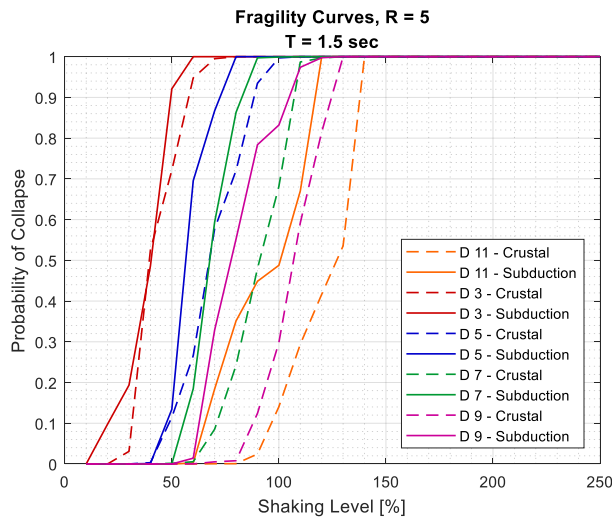


Figure B- 15: Fragility curves for T = 1.5 sec.

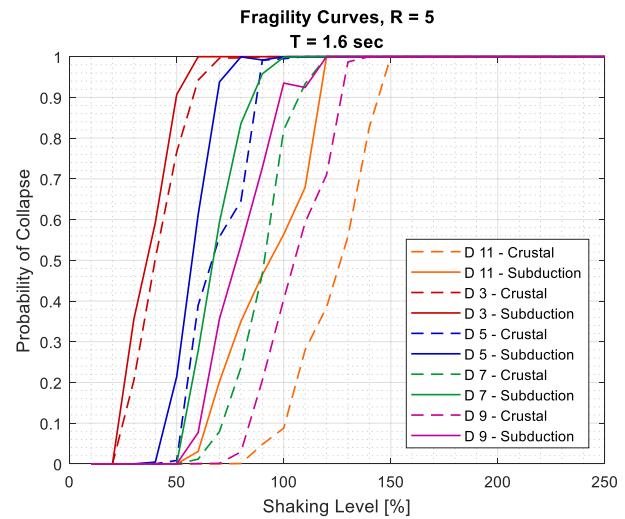


Figure B- 16: Fragility curves for T = 1.6 sec.

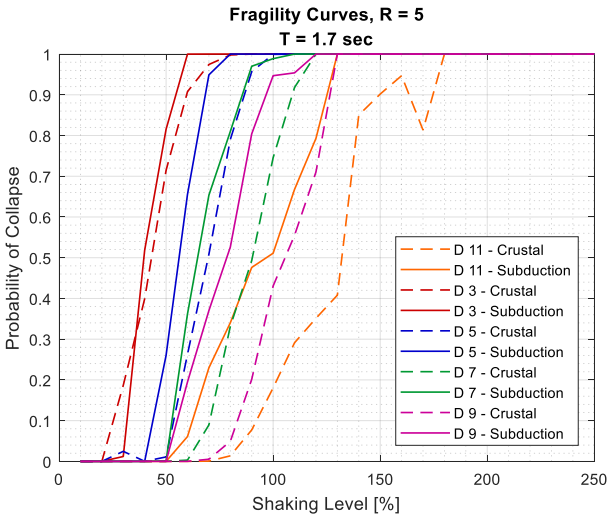


Figure B- 17: Fragility curves for T = 1.7 sec.

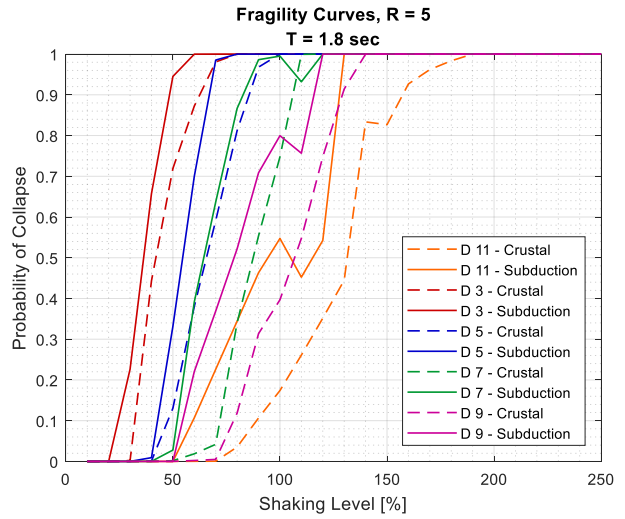


Figure B- 18: Fragility curves for T = 1.8 sec.

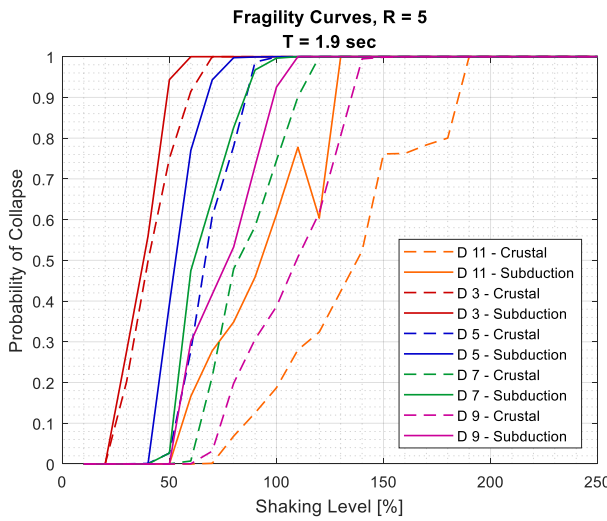


Figure B- 19: Fragility curves for T = 1.9 sec.

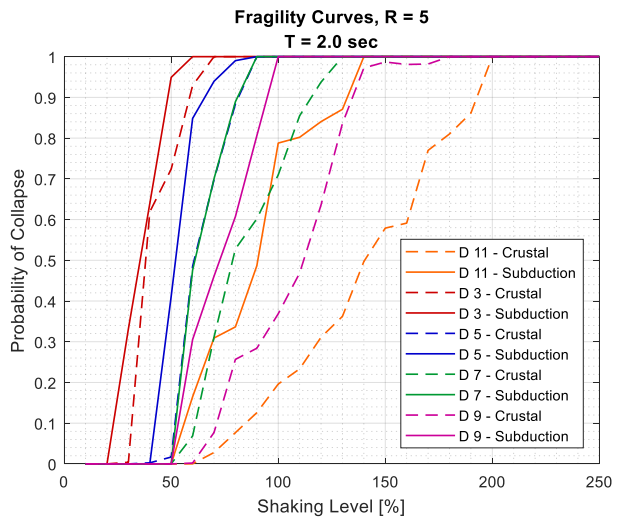


Figure B- 20: Fragility curves for T = 2.0 sec.

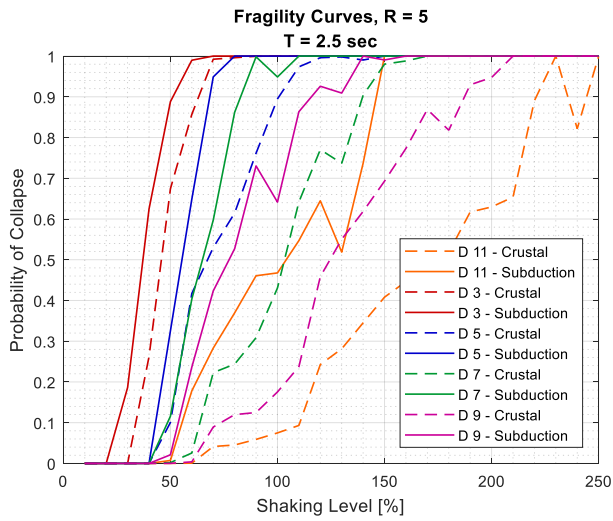


Figure B- 21: Fragility curves for T = 2.5 sec.

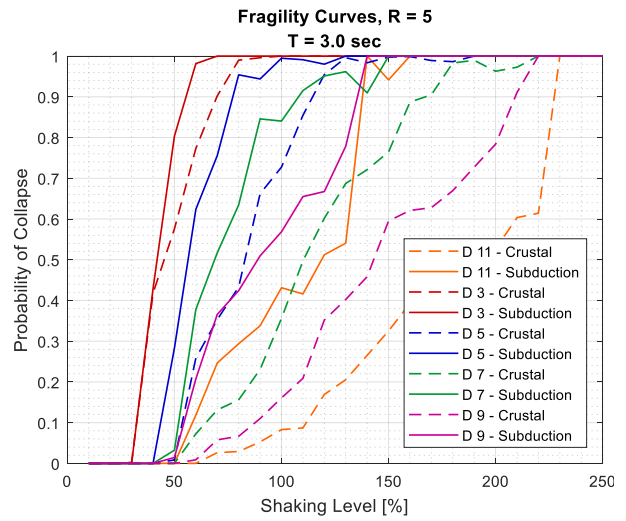


Figure B- 22: Fragility curves for T = 3.0 sec.

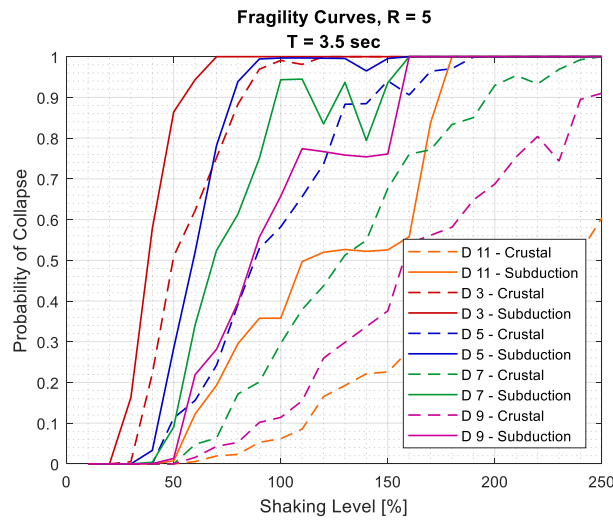


Figure B- 23: Fragility curves for T = 3.5 sec.

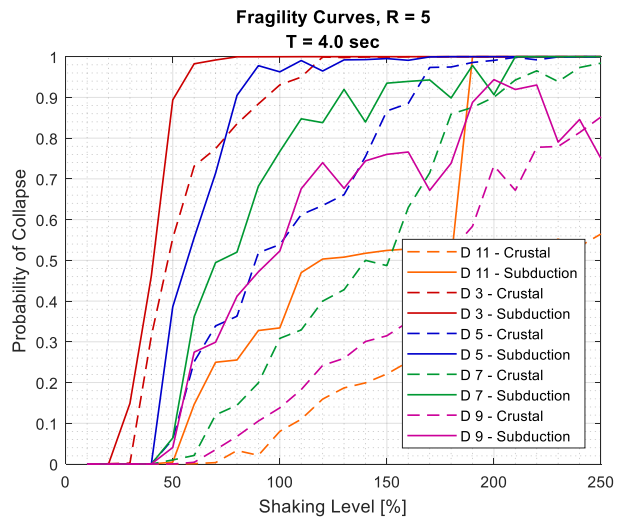


Figure B- 24: Fragility curves for T = 4.0 sec.

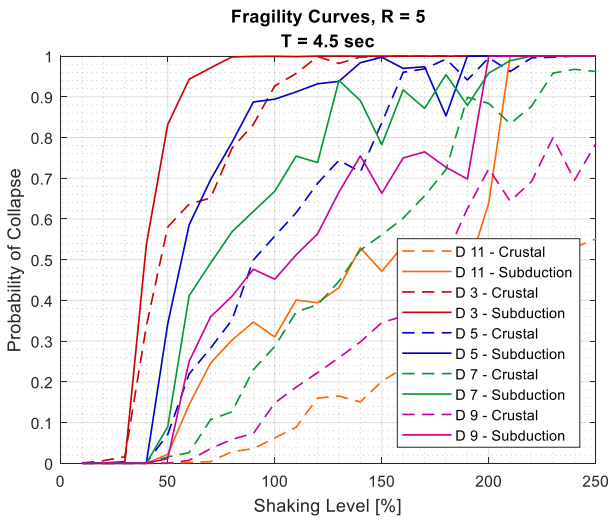


Figure B- 25: Fragility curves for T = 4.5 sec.

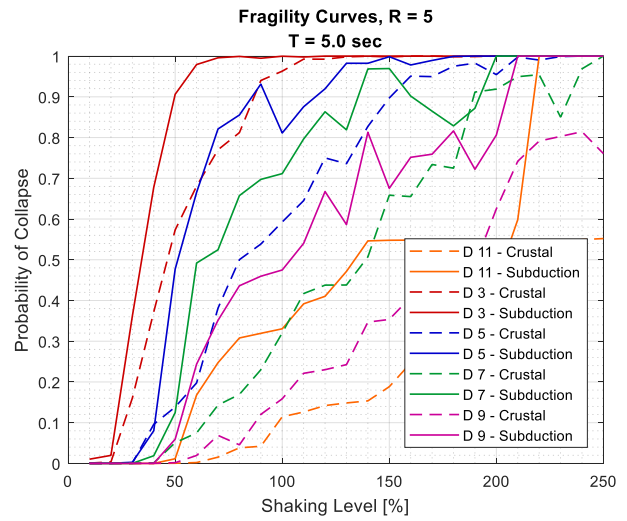


Figure B- 26: Fragility curves for T = 5.0 sec.

Appendix C Contour plots of the probability of collapse

For systems with low ductility capacity ($\mu = 3$, in Figure C-1 and Figure C-2), the first 9 contour lines, which represent probability of collapse from 10% to 90%, fall in the lower part of the plot and are located within 10 and 100% of shaking intensity. Thus, high probabilities of collapse pertain to low shaking levels. The contour lines are very close to each other, indicating a great sensitivity of the probability of collapse to increases in shaking intensity. At the 10% shaking level, the probability of collapse is below or at most equal to 10% in the whole period range, referring to a structural response that is mainly elastic. Increasing the intensity of the motions to 20-30% shaking level, the probability of collapse escalates to 60-70%, referring to structural systems that yield and suddenly reach the collapse capacity.

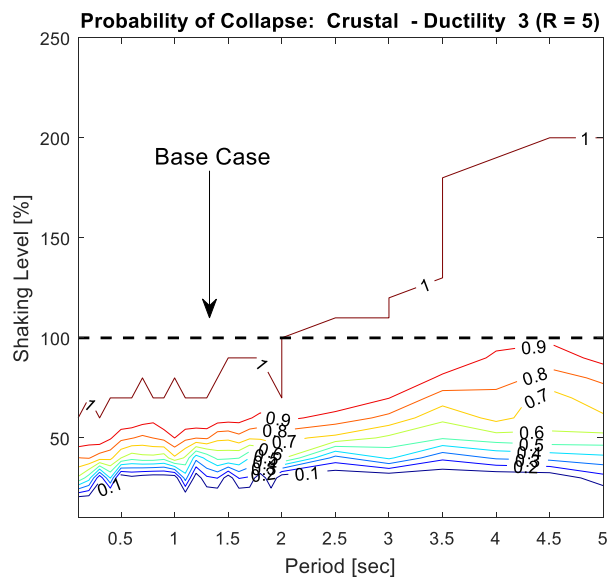


Figure C- 1: Contour plot for ductility 3 and crustal suite of motions.

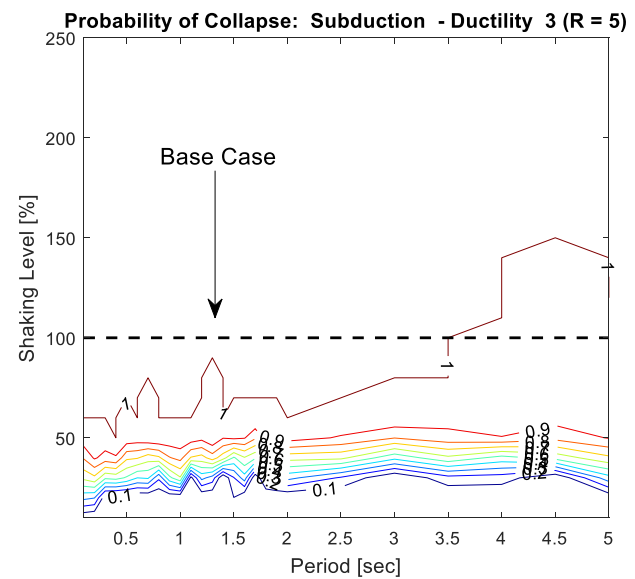


Figure C- 2: Contour plot for ductility 3 and subduction suite of motions.

This observation holds for the contour plots generated with both the crustal and subduction suite of motions results. Long duration is found not to be a crucial variable in the evaluation of the collapse probability of systems with low ductility capacity. The contour lines show a horizontal trend in the whole range of periods of interest. This shows not only that at low ductility capacities there is no variation on the structural performance due to the considered structural period, but also

that the short period performance paradox somehow vanishes, as the same performance probability is achieved regardless the structural period. Therefore, low ductility overpowers any effect due to different ground motions duration and any dependence due to structural periods. At Code Design shaking (shown as a black dashed line), both suites of motions result in probabilities of collapse above 90%.

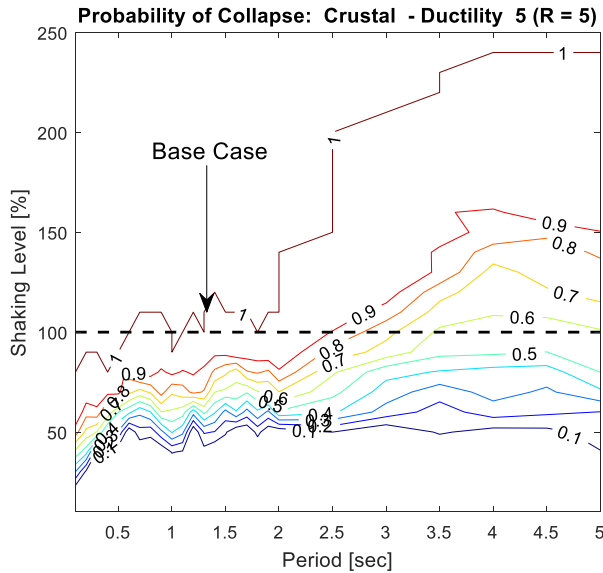


Figure C- 3: Contour plot for ductility 5 and crustal suite of motions.

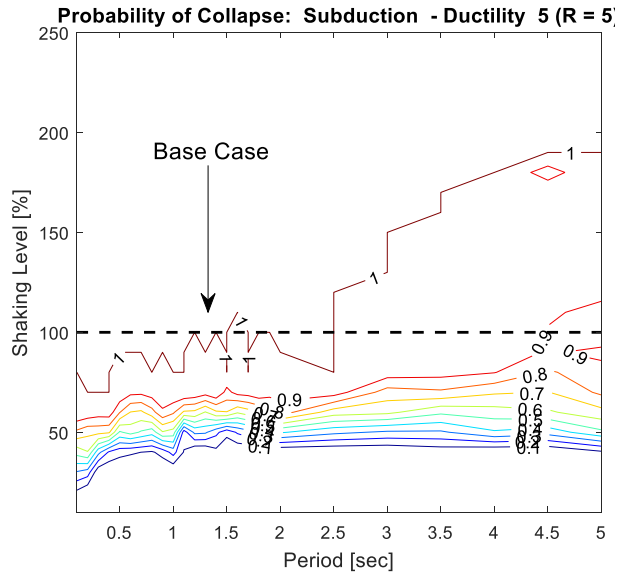


Figure C- 4: Contour plot for ductility 5 and subduction suite of motions.

For intermediate ductility capacity ($\mu = 5$, Figure C-3 and Figure C-4) the contour curves move upwards towards higher shaking intensities, indicating a better structural performance towards collapse than low ductility systems. For instance, the contour curves for equal probability of 10% correspond now to a shaking level of 40-50% of the Code design level. The difference in scatter between contour curves for subduction and crustal motions is clear. While the equal probability lines obtained with the crustal motions are more widely spaced (particularly for periods longer than 3 sec), the contour curves calculated with the subduction motions show the tight spacing and the trend is still mostly horizontal (i.e. independent of the period of the system). At 100% shaking level, subduction ground motions achieve the total probability of collapse in the whole period range. On the other hand, the collapse probability obtained with the crustal motion is above 90% up to 2.5 sec and gradually diminishes with increasing period to 55% at 5 sec. At

periods shorter than 0.5 sec, the performance paradox is visible for the contour curves generated with the crustal motions. The effect of long duration of subduction ground motions interpreted as the difference between the subduction and crustal plot can be captured, but pertains only to period longer than 2 sec and is restricted only to higher values of probability of collapse.

Moving to higher ductility capacities ($\mu = 7$, Figure C-5 and Figure C-6), the characteristics noted for ductility capacity equal to 5 are now more remarkable. The contour curves move further upwards for both crustal and subduction motions: the lower probability level (10-20%) are now associated to shaking intensity above 50%. The spacing within the crustal contour curves becomes gradually more significant in particular for structural periods between 2.5 and 5 sec. Moreover, for this period range and a 100% shaking intensity the probabilities lower significantly to values about 30-40%.

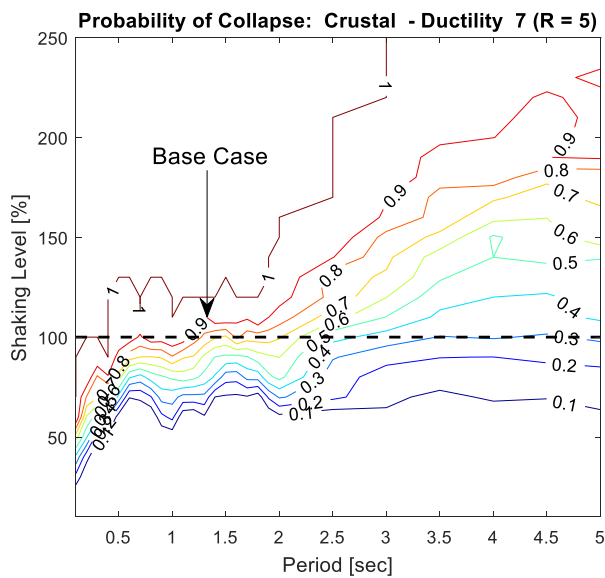


Figure C- 5: Contour plot for ductility 7 and crustal suite of motions.

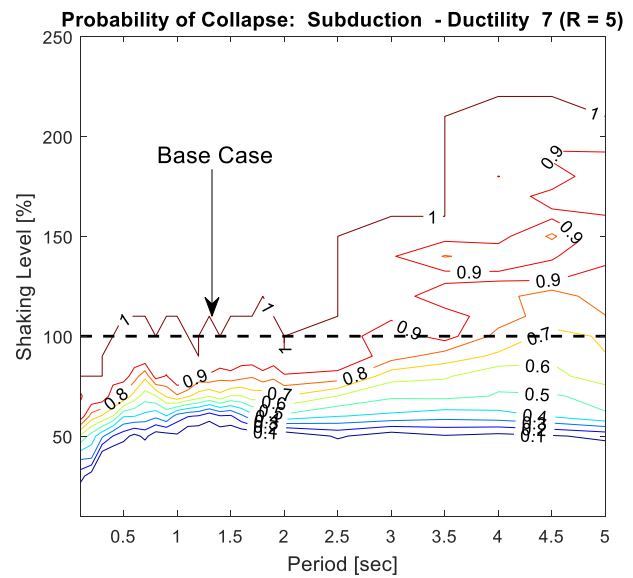


Figure C- 6: Contour plot for ductility 7 and subduction suite of motions.

As for the plot generated with the subduction suite of motions (Figure C-6), the contour curves globally move towards higher shaking intensities, implying a progressive improvement of the collapse performance. However, the curves maintain the horizontal trend previously noted at lower levels of ductility ($\mu = 3, 5$) and are still closely spaced. This means once again that the structural performance is independent from the fundamental period. It is at this level of ductility that the effect of long duration of ground motion starts to be mostly appreciated: the difference in

the distribution of probabilities between the crustal and subduction plots is particularly noticeable for a wider range of periods (from 0.5 to 5 sec).

At ductility capacity $\mu = 9$, the trends observed for ductility 7 are further emphasized. For both suites of motions, the contour curves move toward higher intensity levels (Figure C-7 and Figure C-8). The spacing of the crustal probability lines gets wider for periods above 2 sec and is unchanged at periods below 2 sec. The contour curves generated with the subduction motions start spreading apart over a wider interval of shaking intensities, from 50 to almost 150%, yet the change is minor and valid only for periods above 3.5 sec. At Base Design shaking intensity, the equal probability of collapse lines lead to probabilities of collapse above 70%.

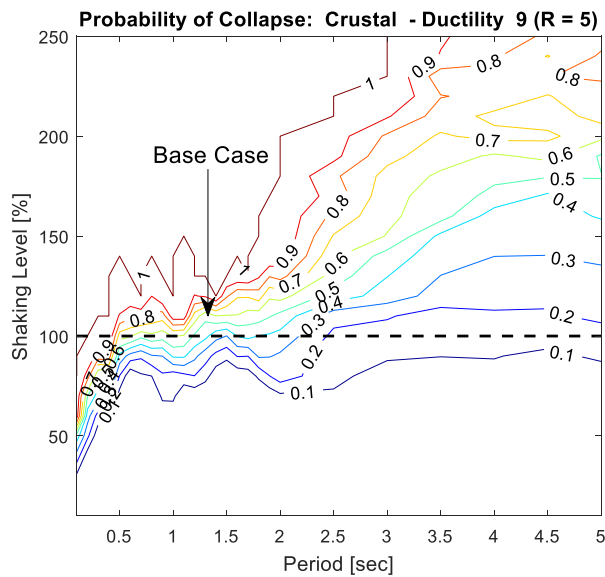


Figure C- 7: Contour plot for ductility 9 and crustal suite of motions.

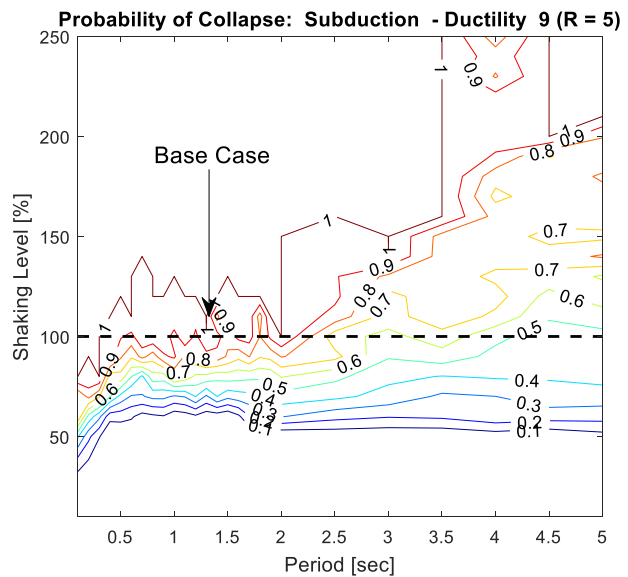


Figure C- 8: Contour plot for ductility 9 and subduction suite of motions.

Figure C- 9 and Figure C- 10 illustrate the contour curves obtained considering a ductility level equal to 11, for crustal and subduction motions respectively. Results have been discussed previously referring to Figure 5-5 and Figure 5-6.

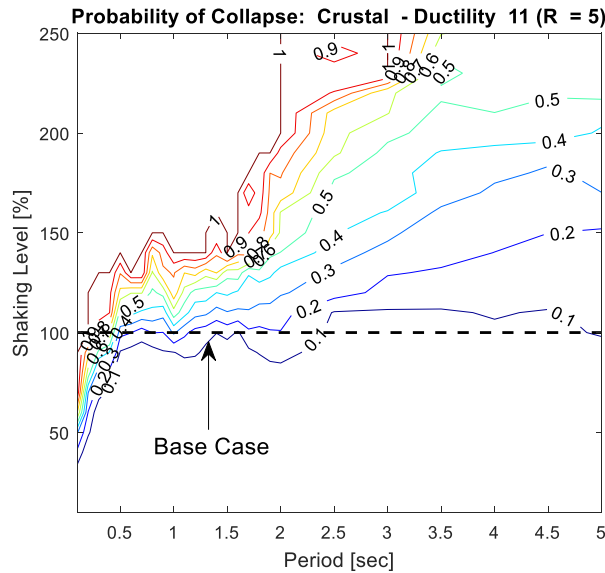


Figure C- 9: Contour plot for ductility 11 and crustal suite of motions.

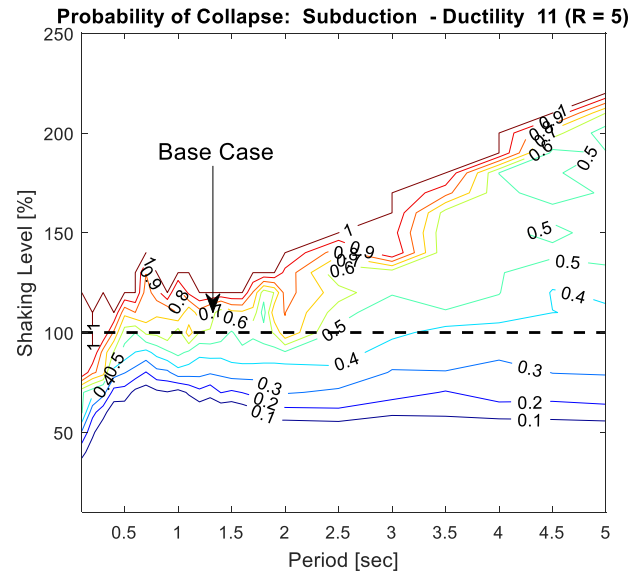


Figure C- 10: Contour plot for ductility 11 and subduction suite of motions.

The evolution of the contour plots can be summarized as follows:

- An increase in ductility capacity has the general effect of moving the contour curves towards higher levels of shaking, thus resulting in a better structural performance;
- The effect of structural period is dependent on the ductility capacity considered. While at lower ductilities the structural performance is quite similar for structures in the period range considered, as the ductility capacity increase the effect of structural period on the probability of collapse is a function of ductility and shaking intensity of the ground motions;
- For structural periods below 0.5 sec, the contour curves are very close to each other and correspond to lower shaking levels. This phenomenon refers to the paradox on the performance of short period structures and is evident at intermediate and high ductility levels;
- For structural periods between 0.5 and 2 sec, the contour curves show in general a compact horizontal trend: the structural period does not affect significantly the variation on the collapse performance which is mainly dependent on the ductility and shaking intensity of the system;

- In particular, for periods longer than 2 sec, the probability curves tend to spread out in the contour plot. This effect is magnified at higher ductility capacities and particularly for the results obtained with the crustal suite of motions.

Appendix D Duration effect plots

Appendix D includes the contour plots showing the effect of long duration represented as a difference in collapse probability calculated with subduction and crustal motions. The plots have been generated for the five different ductility capacities considered in the study. Figure D-1 and Figure D-2 shows the probability of collapse for rotational ductility equal to 3 and 5 respectively, while Figure D-3 and D-4 refer to higher ductility capacities of 7 and 9. Figure D-5 shows the effect of duration when the rotational ductility is equal to 11 and refers to Figure 5-8 of Section 5.

The same colorbar was assigned to all Figures to describe different increase increments in the probability of collapse. A *blue* color signifies that there is no difference in the calculated collapse probability with subduction and crustal motions. A color *dark red* was assigned to probability differences equal or above 60%.

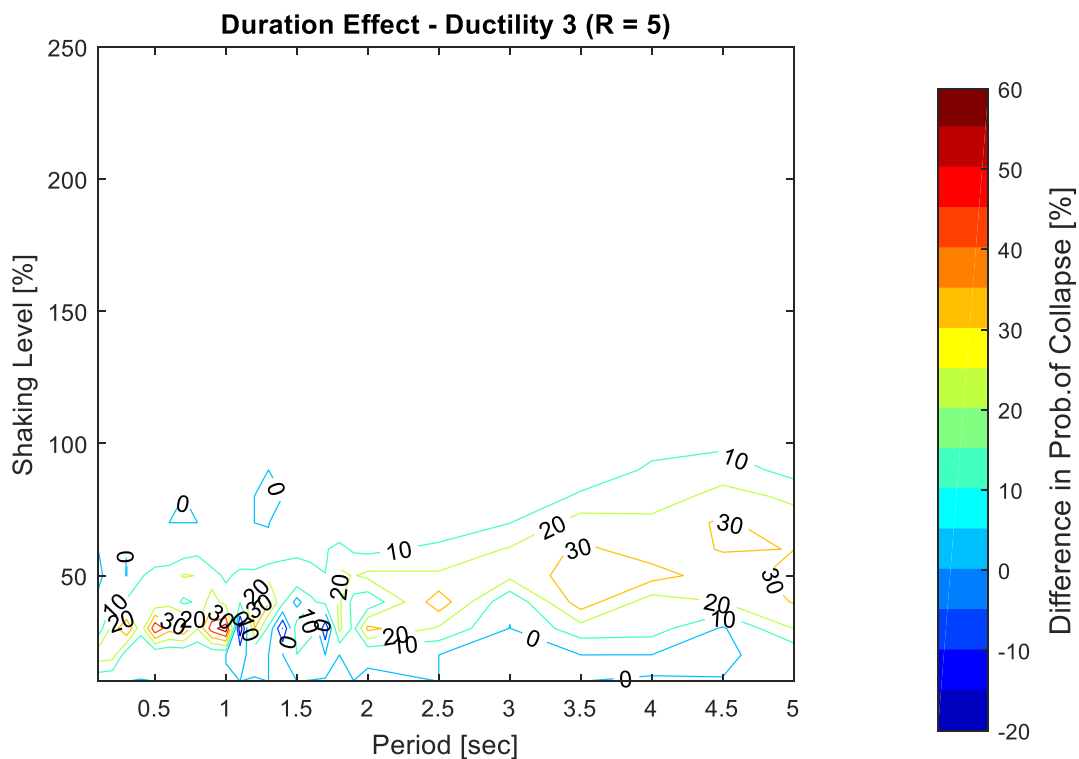


Figure D- 1: Contour plot showing the difference in probability of collapse due to long duration effect for ductility 3.

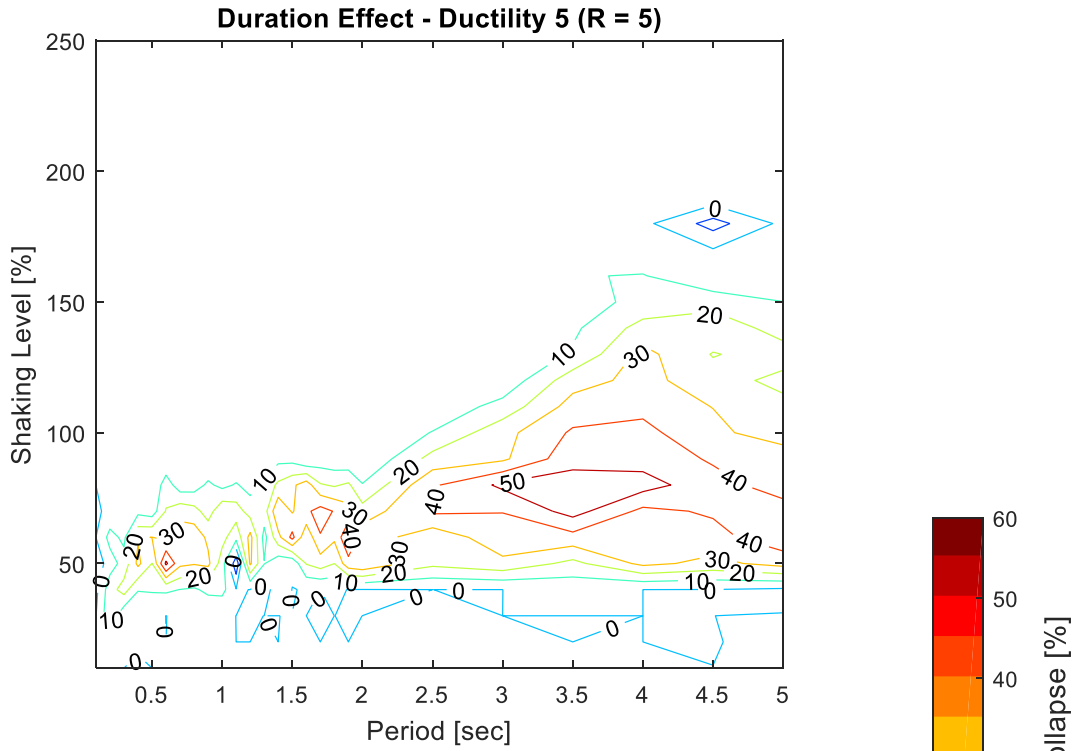


Figure D- 2: Contour plot showing the difference in probability of collapse due to long duration effect for ductility 5.

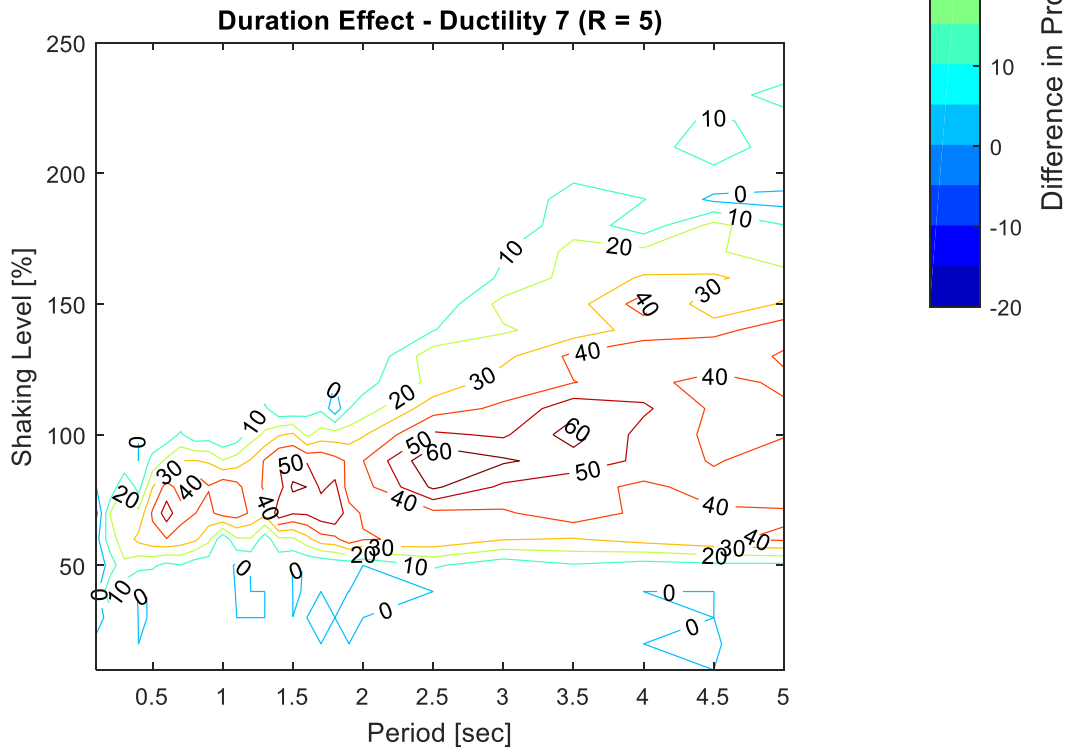


Figure D- 3: Contour plot showing the difference in probability of collapse due to long duration effect for ductility 7.

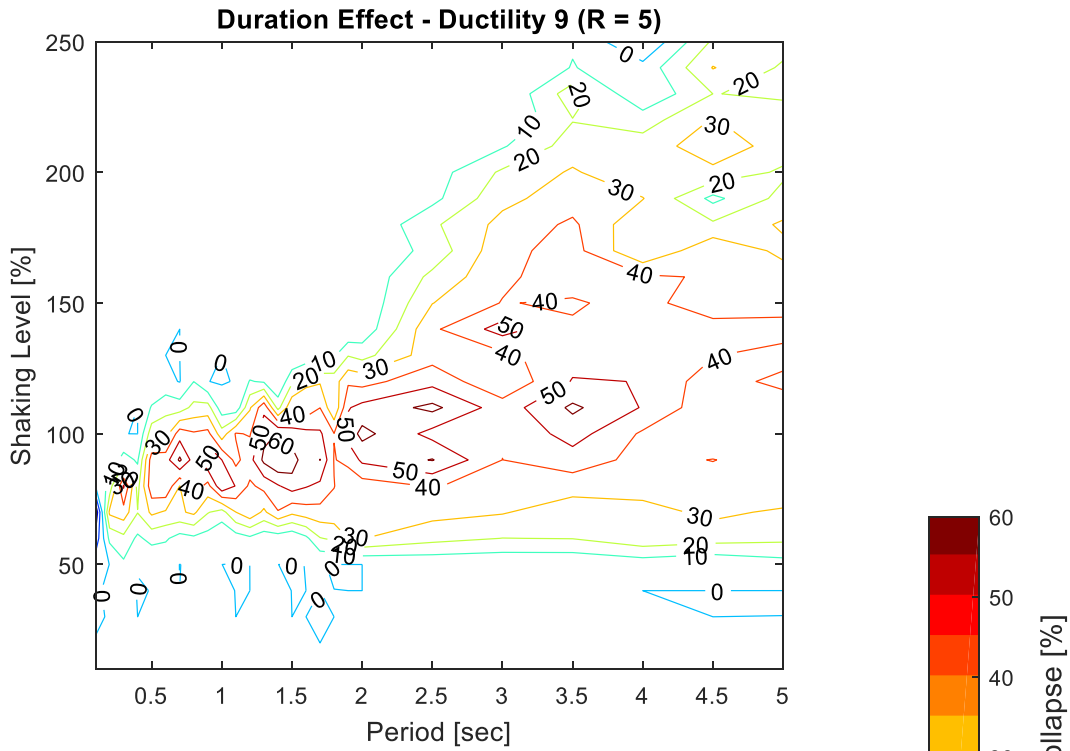


Figure D- 4: Contour plot showing the difference in probability of collapse due to long duration effect for ductility 9.

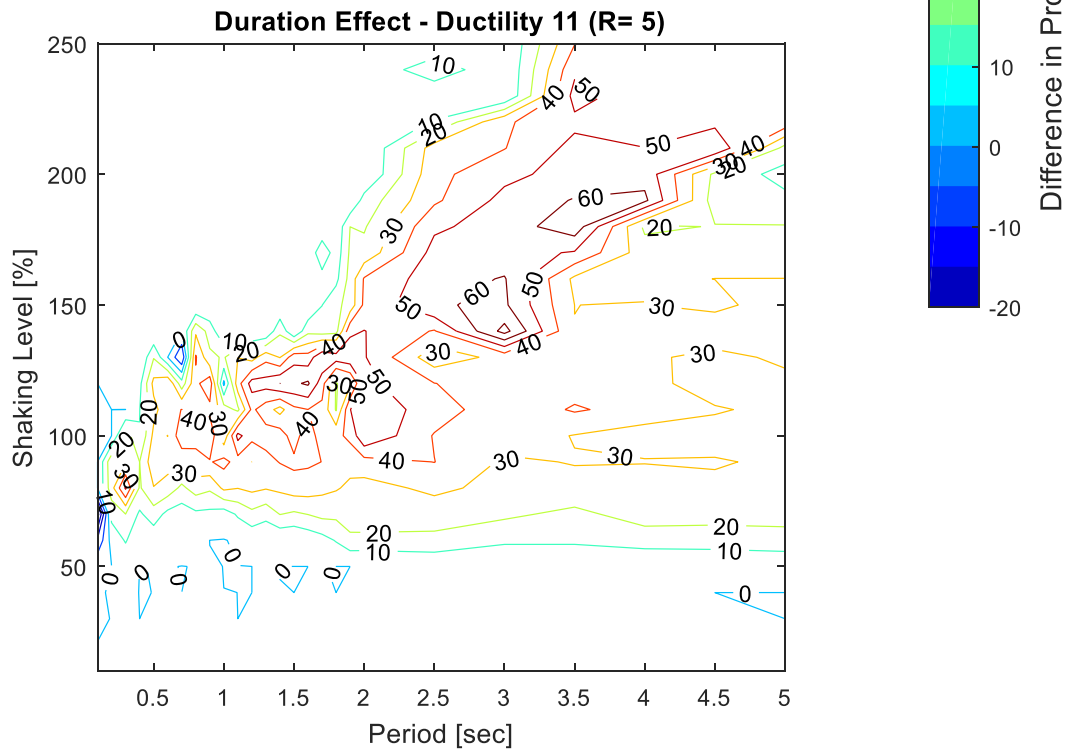


Figure D- 5: Contour plot showing the difference in probability of collapse due to long duration effect for ductility 11.